# THE INTERACTION OF A SHOCK WAVE WITH A TURBULENT SHEAR FLOW

By

Krishnan Mahesh, Parviz Moin and Sanjiva K. Lele

Prepared with the support of the
Air Force Office of Scientific Research
under AFOSR Grants 88-NA-32 and F49620-92-J-0128

Report No. TF-69

Thermosciences Division
Department of Mechanical Engineering
Stanford University
Stanford, California 94305

June 1996

# Abstract

The interaction of a shock wave with a turbulent boundary layer is a central problem in supersonic flow over wings, fins, control surfaces and inlets. This work uses direct numerical simulation and linear analysis to study the interaction of a shock wave with an idealized turbulent shear flow. Our objective is to identify and explain factors likely to be important in shock wave / boundary layer interaction.

Rapid Distortion Theory (RDT) shows the strong dependence of shock / turbulence interaction on the anisotropy of the upstream turbulence. Kinetic energy amplification of a shear flow across a shock wave is considerably higher than that of isotropic turbulence. The kinetic energy amplification across a shock is shown to be determined by the upstream values of $E_{11}(k_1)$ and $\overline{u'^2}/q^2$ ($x$ denotes the shock-normal direction). The movement of $E_{11}(k_1)$ to lower wavenumbers and increase in the upstream value of $\overline{u'^2}/q^2$ increase kinetic energy amplification. The Reynolds shear stress $\overline{u'v'}$ decreases in magnitude across a normal shock. RDT shows that amplification of the pressure-strain correlation is responsible. An argument based on the inclination angle of vortical structures is proposed to explain this decrease in magnitude of shear stress.

Reynolds stress modeling in the RDT limit shows that popular models ( *e.g.* Launder, Reece, Rodi, 1975; Speziale, Sarkar, Gatski, 1991) for the pressure-strain correlation are unable to reproduce these trends. For example, the Launder, Reece, Rodi model considerably underpredicts the amplification of kinetic energy while predicting *increase* instead of decrease in the magnitude of shear stress. The lack of dependence on upstream spectral information is likely responsible for this deficiency.

Upstream entropy fluctuations significantly influence the evolution of turbulence fluctuations across the shock wave. Both, the magnitude of (entropic) temperature fluctuations and their correlation with the velocity field affect shock / turbulence interaction. Temperature fluctuations that are negatively correlated with the shock-normal velocity component significantly increase turbulence intensity, vorticity and sound levels behind the shock wave. Positively correlated fluctuations have a suppressing effect. An argument based on the effects of bulk compression and baroclinic torque explains these trends. This explanation is further extended to derive a simple formula that predicts the amount of vorticity produced in the interaction of a shock wave with entropic temperature fluctuations.

The applicability of Morkovin's hypothesis across a shock wave is tested and found questionable. The part of the hypothesis that equates the intensity of density and temperature fluctuations seems a reasonable approximation across shocks of moderate strength ($M_1 < 2.5$). The relation between the thermodynamic and velocity field as predicted by Morkovin's hypothesis does not hold across the shock. Oscillation of the shock front is shown to be responsible.

Linear analysis is used to study the influence of acoustic waves on shock / turbulence interaction. The evolution of acoustic waves across the shock is shown to be significantly different from that of vortical fluctuations. The kinetic energy of acoustic fluctuations *decreases* across shock waves of moderate strength ($1.25 < M_1 < 1.8$). For $M_1 > 3$, the kinetic energy amplification of acoustic fluctuations significantly exceeds that of vortical fluctuations. Sound level is seen to increase across the shock. Also, acoustic fluctuations generate 'turbulence' whose contribution to the far-field kinetic energy increases with increasing shock strength.

The shear flow simulations support the predictions made by linear analysis. The evolution of turbulence kinetic energy across the shock wave is seen to depend on the upstream anisotropy and velocity-temperature correlation. Large levels of amplification (2 to 2.5) is seen when $\overline{u'T'}$ is negative upstream of the shock. Negligible amplification is observed when the upstream correlation is positive. The shear stress ($\overline{u'v'}$) decreases in magnitude across the shock. The Taylor microscales noticeably decrease across the shock wave. The fluctuations in pressure, density and temperature amplify across the shock wave, with the amplification of pressure fluctuations far exceeding those of density and temperature. The intensity of pressure fluctuations immediately behind the shock wave is non-negligible. However, due to their decay behind the shock wave, the intensity of pressure fluctuations in the far-field is significantly smaller than density and temperature; *i.e.*, the far-field thermodynamic field is dominated by entropy fluctuations.

# Acknowledgement

This work was supported by the Air Force Office of Scientific Research with Dr. Len Sakell as the technical monitor. The computational resources were provided by NASA Ames Research Center and the NAS facility. The authors have benefitted from stimulating discussions with Dr. Sangsan Lee.

# Table of contents

# List of Tables

# List of Figures

# Nomenclature

## Roman Symbols

| | |
|---|---|
| $a_1, a_2, a_3$ | Parameters in Pade expression for first derivative (§4.4) |
| $b$ | Parameter in mapping for streamwise grid (§4.3) |
| $b_1, b_2, b_3$ | Parameters in Pade expression for second derivative (§4.4) |
| $b_{ij}$ | Reynolds stress anisotropy tensor $R_{ij} - R_{ii}\delta_{ij}/3$ (§2.6.1) |
| $c$ | $\rho/\rho_0$ in RDT (§2.3.3) |
| $c(i,m)$ | Coefficient matrix in ENO scheme (§4.6.2) |
| $\overline{c}$ | Mean sound speed (§2.2) |
| $c_0^*$ | Reference sound speed (§4.2) |
| $c_p$ | Specific heat at constant pressure (§3.2.2) |
| $d$ | Parameter in mapping for streamwise grid (§4.3) |
| $f$ | $R_{11}/q^2$ (§2.6.1) |
| $f_j$ | Discrete function $f$ at node $j$ (§4.4) |
| $f'_j$ | Derivative of function $f$ at node $j$ (§4.4) |
| $f''_j$ | Second derivative of function $f$ at node $j$ (§4.4) |
| $\vec{f}_{\text{inv.}}, \vec{f}_{\text{vis.}}$ | Inviscid and viscous flux vectors in $x-$ direction (§4.6.2) |
| $\hat{f}_{j+1/2}$ | Numerical flux at $j+1/2$ cell face (§4.6.2) |
| $\vec{f}^{+/-}$ | Positive/negative split fluxes (§4.6.2) |
| $\vec{g}_{\text{inv.}}, \vec{g}_{\text{vis.}}$ | Inviscid and viscous flux vectors in $y-$ direction (§4.6.2) |
| $\vec{h}_{\text{inv.}}, \vec{h}_{\text{vis.}}$ | Inviscid and viscous flux vectors in $z-$ direction (§4.6.2) |
| $h(s)$ | $\mathrm{d}x/\mathrm{d}s$: $x$ and $s$ are the physical and computational coordinate respectively (§4.4) |
| $h'(s)$ | First derivative of $h(s)$ (§4.4) |
| $h''(s)$ | Second derivative of $h(s)$ (§4.4) |
| $k$ | Magnitude of wavenumber vector (§3.2.2) |
| $k_0$ | Peak wavenumber of initial spectrum (§3.7) |
| $\widetilde{k_i}$ | Imaginary part of wavenumber of acoustic component (§3.2.3) |
| $\widetilde{k_r}$ | Real part of wavenumber of acoustic component (§3.2.3) |

| | |
|---|---|
| $k_x, k_y$ | Wavenumber vectors in $x$ and $y$ (§4.6.3) |
| $\overline{k}$ | Wavenumber of vortical component (§3.2.3) |
| $k'$ | Modified wavenumber (§4.4) |
| $l$ | Characteristic turbulence lengthscale §2.2 |
| | Also $\sin\psi_1$ (§3.2.2) |
| $m$ | $\cos\psi_1$ (§3.2.2) |
| $n$ | Exponent in viscosity-temperature relation (§4.2) |
| $p$ | Pressure |
| $\overline{p}_0$ | Initial mean pressure in RDT (§2.3.1) |
| $q^2$ | $\overline{u_i' u_i'}$: twice the turbulence kinetic energy |
| $q_i$ | Heat flux in $i-$ th direction (§4.2) |
| $\vec{q}$ | Vector of conservative variables (§4.6.2) |
| $r$ | $U_1/U_2$ in linear analysis (§3.2.4) |
| | Also parameter in mapping for streamwise grid (§4.3) |
| $r_1, r_2$ | Constants in model solution (§2.6.1) |
| $s$ | Entropy (§3.2.2) |
| | Also computational coordinate (§4.3) |
| $t$ | Time |
| $t_0$ | Time when compression is introduced in RDT (§2.3.1) |
| $u_i'$ | Velocity fluctuation in $i-$ th direction (§2.2) |
| $u, v, w$ | Velocity in $x, y, z-$ directions |
| $u_0$ | *r.m.s.* velocity of initial isotropic field in temporal simulation (§C.3.1) |
| $x_c$ | Location of shock in initial condition (§4.7) |
| $x_i$ | Spatial coordinate in $i-$ th direction |
| $x_r$ | Coordinate in plane of disturbance in linear analysis (§3.7) |
| $x_s$ | $x$ location where sponge starts (§4.8) |
| $y_{\min}$ | Minimum value of $y$ coordinate in DNS (§4.1) |
| $A_e$ | Intensity of entropy wave (§3.2.2) |
| $A_{ij}$ | Velocity gradient tensor (§2.2) |
| $A_r$ | Amplitude ratio of entropy and vorticity waves (§3.2) |
| $A_s$ | Amplitude of sponge damping function (§C.3.1) |

| | |
|---|---|
| $A_v$ | Intensity of vorticity wave (§3.2.2) |
| $B_{ij}$ | Transformation tensor relating $\xi_i$ and $x_i$ in RDT (§2.2) |
| $C_{ij}$ | Coefficient matrix in energy spectrum equation in RDT (§2.3.1) |
| $C_M$ | Center of mass (§3.5) |
| $C_F$ | Center of force (§3.5) |
| $C_2, C_3$ | Constants in LRR pressure strain correlation model (§2.6.1) |
| $E(k)$ | Three dimensional energy spectrum |
| $E_{ij}$ | Energy spectrum tensor (§2.3.1) |
| $E_{nn}$ | Spectrum of the sum of all velocity components (§3.7) |
| $E_{rr}$ | Spectrum of $r-$ th direction velocity component (§3.7) |
| $E_{\phi\phi}$ | Spectrum of $\phi-$ th direction velocity component (§3.7) |
| $E_{\theta\theta}$ | Energy spectrum of velocity in $\theta-$ direction (§2.4.2) |
| $E_t$ | Total energy (§4.2) |
| $F, G, H$ | Coefficients in linear analysis solution (§3.2.4) |
| $I, K, Q$ | Coefficients in linear analysis solution (§3.2.4) |
| $\widetilde{F}, \widetilde{G}, \widetilde{H}$ | $F/A_v, G/A_v, H/A_v$ (Appendix A) |
| $\widetilde{I}, \widetilde{K}, \widetilde{Q}$ | $I/A_v, K/A_v, Q/A_v$ (Appendix A) |
| $L_0^*$ | Reference lengthscale used to non-dimensionalize equations (§4.2) |
| $L_x, L_y, L_z$ | Domain lengths in $x, y, z-$ directions (§4.6.1) |
| $L_i$ | Characteristic variables in outflow boundary conditions (§4.8) |
| $M_1$ | Mean Mach number upstream of shock wave (§3.2.2) |
| $M_n$ | Normal Mach number (§2.4.2) |
| $M_t$ | Fluctuation Mach number $\sqrt{q^2}/\overline{c}$ (§4.6.1) |
| $M_\infty$ | Freestream Mach number (§3.1) |
| $N_l, N_r$ | ENO zone extends from $i = N_l$ to $N_r$ (§4.6.2) |
| $N_t$ | Time steps after which inflow signal is jittered (§C.1) |
| $N_x, N_y, N_z$ | Number of points in $x, y, z-$ directions (§4.6.1) |
| $Q_{ff,\alpha}(\mathbf{r})$ | Two point correlation (§C.2) |
| $R$ | Specific gas constant (§4.2) |
| $Re$ | Reference Reynolds number (§4.2) |
| $R_{ij}$ | Reynolds stress tensor $\overline{u_i' u_j'}$ (§2.3.1) |

| | |
|---|---|
| $R_{f'g'}$ | Correlation coefficient between variables $f'$ and $g'$ |
| $R_\lambda$ | Reynolds number based on streamwise Taylor microscale $\sqrt{\overline{u'^2}}\lambda_1/\overline{\nu}$ (§4.6.1) |
| $S$ | Mean shear rate at inflow (§4.1) |
| $S_i$ | Velocity derivative skewness (§C.1) |
| $S_{ij}$ | Mean strain rate tensor $(A_{ij} + A_{ji})/2$ (§2.6.1) |
| $S^*_{ij}$ | Deviatoric part of mean strain rate tensor $S_{ij} - S_{ii}\delta_{ij}/3$ (§2.6.1) |
| $S_0$ | Initial mean shear rate in RDT (§2.3.1) |
| $T_0$ | Stagnation temperature (§3.8.6) |
| $T_0^*$ | Reference temperature used to non-dimensionalize equations (§4.2) |
| $U_c$ | Convection velocity of inflow turbulence (§4.7) |
| $U_i$ | Mean velocity in $i-$ th direction (§2.2) |
| $U_0$ | Mean velocity at bottom streamline (§4.1) |

## Greek Symbols

| | |
|---|---|
| $\alpha$ | Constant in model solution (§2.6.1) |
| $\alpha_{\text{amp.}}, c_{\text{amp.}}$ | Parameters in inflow turbulence generation (§C.1) |
| $\alpha_{\text{p}}, c_{\text{p}}$ | Parameters in inflow turbulence generation (§C.1) |
| $\beta$ | Total shear defined as $\beta = St$ (§2.3.1) |
| $\gamma$ | Ratio of specific heats |
| $\delta$ | Shock thickness (§4.6.1) |
| $\delta_{ij}$ | Unit tensor |
| $\delta_{\text{inter.}}$ | Thickness of shock as measured from time-averaged profile (§D.3.1) |
| $\delta_s$ | Measure of shock thickness in initial condition (§4.7) |
| $\delta_{\text{sponge}}$ | Width of sponge region (§C.3.1) |
| $\epsilon$ | Turbulence kinetic energy dissipation |
| $\theta$ | Dilatation<br>Also angle of oblique compression (§2.4.1)<br>Also polar angle of wavenumber vector (§2.3.1, §3.7) |
| $\kappa_i$ | Wavenumber vector in $i-$ th direction (§2.3.1) |
| $\kappa_\theta$ | Wavenumber vector in $\theta-$ direction (§2.4.2) |

| | |
|---|---|
| $\lambda$ | Taylor microscale in isotropic turbulence (§C.1) |
| | Also eigenvalue in numerical stability analysis (§4.5) |
| $\lambda_\alpha$ | Taylor microscale in $\alpha$ direction (§3.8.3) |
| $\lambda_0$ | Taylor microscale of initial isotropic field in temporal simulation (§C.3.1) |
| $\mu_0^*$ | Reference dynamic viscosity (§4.2) |
| $\nu$ | Kinematic viscosity (§4.6.1) |
| $\xi$ | Displacement of shock front (§3.2.2) |
| $\xi_i$ | Transformed coordinate in RDT (§2.2) |
| $\pi_{ij}$ | Pressure-strain correlation, $\overline{p'(u'_{i,j}+u'_{j,i})}$ (§2.3.2) |
| $\rho$ | Density |
| $\rho_0$ | Initial density in RDT (§2.3.1) |
| $\sigma(x)$ | Damping function in sponge (§4.8) |
| $\tau$ | Time variable in RDT (§2.2) |
| $\tau_{ij}$ | Viscous stress tensor (§4.2) |
| $\tau_t$ | Turbulence time-scale (§C.1) |
| $\phi$ | Polar angle of wavenumber vector (§2.3.1, §3.7) |
| $\phi_0$ | Initial phase of Fourier coefficient (§C.1) |
| $\phi_r$ | Phase difference between entropy and vorticity waves (§3.2) |
| $\psi_1$ | Disturbance incidence angle (§3.2.2) |
| $\psi_c$ | Critical angle in linear analysis (§3.2.2) |
| $\omega$ | Frequency (§3.2.3) |
| $\omega'_i$ | Vorticity fluctuations |
| $\Gamma_0$ | Initial compression rate in RDT (§2.2) |
| $\Delta m$ | Gradient Mach number (§2.2) |
| $(\Delta\rho/\rho)$ | Fractional change in mean density (§C.3.2) |
| $\Delta s$ | Spacing of computational coordinate $s$ (§4.4) |
| $\Delta t$ | Timestep (§4.5) |
| $\Delta x_{\mathrm{min}}$ | Minimum streamwise grid spacing (§4.6.1) |
| $\Delta x_{\mathrm{max}}$ | Maximum streamwise grid spacing (§4.6.1) |
| $(\Delta U/U)$ | Fractional change in mean velocity (§C.3.1) |

| | |
|---|---|
| $\Lambda$ | Mean free path (§4.6.1) |
| $\Omega_{ij}$ | Mean rotation rate tensor $(A_{ij} - A_{ji})/2$ (§2.6.1) |

## Superscripts and Subscripts

| | |
|---|---|
| $\hat{()}$ | Fourier coefficient |
| $()_0$ | Value at start of compression in RDT |
| $\vec{()}$ | Vector |
| $()^*$ | Complex conjugate |
| $()^0$ | Value at start of compression in RDT |
| $\overline{()}$ | Average over time and homogeneous directions |
| $()'$ | Fluctuation |
| $()_{1/2}$ | Value upstream/downstream of shock |
| $()^{1/2}$ | Value upstream/downstream of shock |
| $()_{\text{eddy}}$ | Value corresponding to turbulent eddy |
| $()_{\text{rms}}$ | r.m.s value |

## Abbreviations

| | |
|---|---|
| CFL | Courant, Friedrich, Lewy number |
| DNS | Direct Numerical Simulation |
| ENO | Essentially Non-Oscillatory scheme |
| LRR | Launder, Reece, Rodi model |
| RDT | Rapid Distortion Theory |
| RK3 | Third Order Runge-Kutta method |
| SRA | Strong Reynolds Analogy |
| SSG | Speziale, Sarkar, Gatski model |

# Chapter One

# Introduction

## 1.1 Motivation and background

Recent interest in high-speed civil transport aircraft and hypersonic propulsion systems has resulted in renewed research into compressible turbulent flows. At high speeds, compressibility effects become very important to the design of external and internal surfaces such as wings, fins, control surfaces and nozzle intakes. The compressibility of the medium results in large gradients in the mean thermodynamic properties, large fluctuations in the thermodynamic variables, and high levels of mean dilatation. Simple extensions of incompressible turbulence models appear unable to predict these flows, particularly phenomena associated with mean and fluctuating dilatation. Incorporating these effects of compressibility into turbulence models has motivated fundamental research into the physics of these flows.

The presence of shock waves is an important feature that distinguishes high speed flows from low speed ones. Interaction with shock waves is known to significantly alter the aerodynamics and acoustics of high speed shear layers. Shock wave/boundary layer interaction, a common flow configuration, can induce flow separation and strong fluctuating pressure loads on external surfaces. Similarly, the presence of shock waves in high speed unadapted jets is known to significantly increase the emitted noise. On the constructive side, shock waves offer the potential to increase the mixing in high speed flows. Current understanding of the physics of the interaction between shock waves and turbulent flows is limited.

This work is a fundamental study of the interaction of a shock wave with a turbulent shear flow. We use linear analysis and direct numerical simulation (DNS) to study the interaction of a normal shock wave with a turbulent shear flow. A schematic of the computed flow is provided in figure 1.1. Note that the mean velocity upstream of the shock wave has uniform velocity gradient across the mean streamlines. This mean velocity profile is motivated by studies of homogeneous turbulent flow (*e.g.* Rogers, Moin and Reynolds; 1986, Lee, Kim and Moin; 1991) which clearly bring out the importance of mean shear in a turbulent boundary layer. The mean pressure is uniform across mean streamlines; however the mean

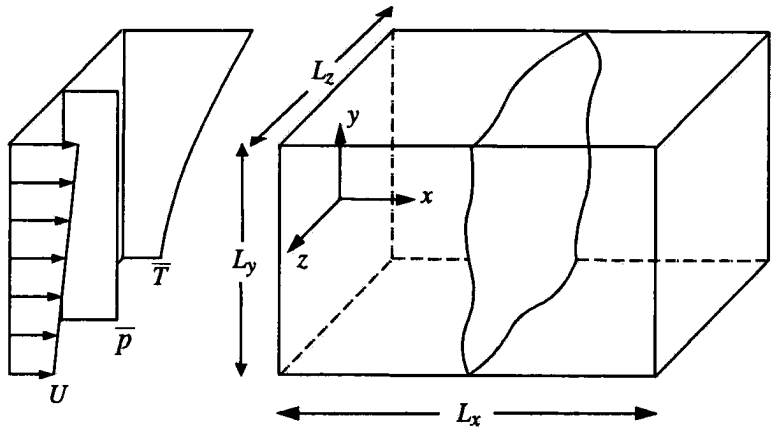


FIGURE 1.1: A schematic of the computed flow.

temperature and density vary such that the mean Mach number is uniform across the mean streamlines.

## 1.2 Review of past work

This review deals with the hydrodynamics of the interaction of shock waves, with non-reacting turbulent flows in the non-hypersonic regime. Phenomena such as detonation waves, the Richtmeyer-Meshkov instability, the regimes of shock-reflection and shock-related noise (*e.g.* 'screech') are not discussed. Experimental work, linear analysis and numerical computation are reviewed here. Experimental work and analysis of shock turbulence/interaction span about five decades. Computational work on the other hand, is very recent.

### 1.2.1 Experiments

A large body of experimental work exists on the interaction of shock waves with a turbulent boundary layer. Most experiments have examined the flow in a compression corner, with some experiments studying normal shock/boundary layer interaction and supersonic shear layers at reattachment.

Green (1970), Korkegi (1971) and Hankey and Holden (1975) provide reviews of earlier experimental work on shock wave/boundary layer interaction. The AGAR-Dograph by Fernholz and Finley (1981) provides a comprehensive summary of experiments prior to 1981. A more recent review is written by Settles and Dodson

(1994). A lot of experimental data has been gathered in the last decade. Current experiments provide data on mean velocity and wall pressure, streamwise Reynolds stress, shear stress and wall pressure fluctuations. Some information on two point correlations, spectra and PDFs is also available (*e.g.* Smits and Muck, 1987).

The flow regime covered by experiments on compression-corner flows extends from attached to separated. Amplification of the streamwise Reynolds stress ($\overline{u'^2}$), structure parameter ($\overline{u'v'}/\overline{u'^2}$), and temperature fluctuations across the shock wave was observed by Debieve, Gouin and Gaviglio (1982a, 1982b), Dussauge, Muck and Andreopoulous (1986), Smits and Muck (1987), and Selig, Andreopoulous, Muck, Dussauge and Smits (1989). Kuntz, Amaducci and Addy (1987) observed that after the interaction, the mean flow in the boundary layer accelerated near the wall as it recovered to equilibrium, and that the mean streamwise velocity profile downstream of the corner was wavy.

The unsteadiness of the shock wave in the separated regime was studied by Andreopoulous and Muck (1987). These workers analyzed wall pressure signals, and concluded that the frequency of the shock motion was controlled by the bursting frequency of the incident boundary layer. Subsequent experiments by Erengil and Dolling (1991) also show a direct correlation between the motion of the shock wave and pressure fluctuations in the upstream boundary layer. Further work aimed at correlating the motion of the shock wave to pressure fluctuations in the boundary layer was conducted by Erengil and Dolling (1990), McClure (1992) and Gramann and Dolling (1992).

One of the results of shock-induced separation is fluctuating pressure loads on the wall. Dolling and co-workers have conducted several investigations into the wall pressure fluctuations produced by shock/wave boundary layer interaction. Both two-dimensional and three dimensional flows are considered. An extensive review of experimental data is provided by Dolling (1993).

Supersonic flows at reattachment constitute another example of shock wave / boundary layer interaction. An experiment by Hayakawa *et al.* (1984) examined a reattaching supersonic flow. Strong longitudinal compression was found at reattachment, resulting in a three-fold rise in the peak level of mass flux ($\overline{\rho'u'}$). A comparable subsonic reattachment experiment by Bradshaw and Wong (1972) showed a two-fold drop in the level of $u_{\mathrm{rms}}$.

The above experiments allude to the complex nature of shock wave/boundary layer interaction. The simultaneous presence of features such as mean compression, streamline curvature, wall-induced inhomogeneity, and separation-induced unsteadiness in shock wave/boundary layer interaction has led to recent experimental work on some 'cleaner' problems. A brief review of this work is provided below. Debieve and Lacharme (1986) examined the interaction of a shock wave with the separated shear layer over a compression ramp. They concluded that turbulence levels were amplified, and Taylor microscales increase through the interaction. The effect of intermittency on turbulence statistics in the region occupied by the shock wave was also described.

The interaction of grid-generated turbulence with a shock wave was studied by Keller and Merzkirch (1990). Amplification of kinetic energy was observed along with an apparent increase in the Taylor microscale of density across the shock wave. Honkan and Andreopoulous (1990) examined the response of grid-generated turbulence to a normal shock. Considerable amplification of turbulence levels was noted. The amplification was seen to depend on the length scale and intensity of the incident flow. Another experimental investigation of the interaction of a shock wave with grid generated turbulence was conducted by Jacquin, Blin and Geffroy (1991), who noticed negligible amplification of kinetic energy across the shock wave.

A recent experiment by Barre, Alem and Bonnet (1994) has used a novel method to study the interaction of decaying turbulence with a Mach 3 normal shock wave. As opposed to placing a grid in a supersonic stream, these authors use an array of jets to produce nearly isotropic turbulence. Comparison of the results to linear analysis shows good agreement. Amplification of kinetic energy along with a clear decrease in turbulence lengthscale is observed.

Detailed experiments on the interaction of a weak shock wave with random fluctuations in density were conducted by Hesselink and Sturtevant (1988). Considerable distortion of the shock front was observed by them. They explained this distortion in terms of focusing and de-focusing of the shock front in response to density gradients in the medium.

As noted by Jacquin, Cambon and Blin (1993), experiments on grid-turbulence / shock wave interaction are not easy to conduct and certain points of contention exist. The increase in length scale that some experiments report is both counter-intuitive, and in contradiction to computation and linear analysis. Lele (1994)

observes that the inconsistency is currently unresolved. Another feature is the lower amplification of kinetic energy reported by wind-tunnel experiments as compared to shock tube experiments. Mahesh *et al.* (1995) suggest that the presence of acoustic waves in the wind-tunnel experiments is responsible; however, further data is needed to resolve this issue.

### 1.2.2 Linear analysis

The analysis of shock/turbulence interaction is based upon the decomposition of a compressible flow field into vorticity, acoustic and entropy modes as suggested by Kovasznay (1953). The independence of these modes for inviscid, uniform mean flow is used to study the interaction of each of these modes with a shock wave. Both free shock waves, and wedge-attached shocks have been considered in the literature. The analyses by different workers differ in detail, but are conceptually similar. The shock wave is modelled as an unsteady discontinuity. The linearized Euler equations are then used to describe the flow on both sides of the shock. The linearized Rankine-Hugoniot equations yield boundary conditions at the shock front. This yields a boundary value problem for the flow downstream of the shock wave. This problem is then solved for the displacement of the shock front, and the flow behind the shock wave.

The earliest studies seem to be those by Blokhintzev (Landau and Lifshitz, 1982), Burgers (1946) and Kantrowitz (1947), who examined the one-dimensional interaction of an acoustic wave with a normal shock wave. Carrier (1949) used linear analysis to study the stability of supersonic flow past a wedge. Interest in the configuration of shock waves in supersonic channel flow prompted Adams (1949) to study the steady interaction between a shock wave and an acoustic wave incident from upstream. Linear analysis was used by Chu (1952) to examine the interaction between a wedge-generated shock wave and an acoustic wave incident from downstream. The interaction between sound and a shock wave was also studied by Lighthill (1949).

Prompted by the problem of 'shock-noise', Ribner (1953) studied in detail the interaction between a vorticity wave and a shock wave. He (1954) subsequently extended his analysis to consider a spectrum of incident vorticity waves (in three dimensions) and computed for an isotropic incident spectrum, detailed statistics of the downstream flow field. Ribner appears to have been the first to predict the

interaction of isotropic turbulence with a shock wave. He noted (1953,1969) that weak levels of incident turbulence produce high levels of noise downstream of the shock. Later (1987), he extended his analysis to predict one-dimensional power spectra of the fluctuations behind the shock wave.

Around the same time as Ribner's pioneering study, Moore (1954) performed detailed analysis of the unsteady interaction of an obliquely incident acoustic wave with a shock wave of infinite extent. He studied acoustic waves that were incident from downstream as well as upstream and also outlined extension of his analysis to study the interaction of a vorticity wave with a shock wave. Other workers that have studied the interaction of unsteady disturbances with a shock wave include Kerrebrock (1956), Johnson and Laporte (1958), Lowson (1968) and McKenzie and Westphal (1968).

Most of these workers considered the interaction of vorticity and acoustic waves with a shock wave. Chang (1957) used linear analysis to examine the interaction of a plane entropy wave with an oblique shock. In addition to considering the general case of an infinite oblique shock, Chang also considered the case where the oblique shock was produced by a wedge, and accounted for reflections from the wedge. Chang's theoretical results were subsequently used by Cuadra (1968) to perform a numerical parametric study of the infinite oblique shock problem.

These earlier studies were largely motivated by issues of shock-stability and the 'shock-noise' phenomenon. Recent interest in the interaction of shock waves with turbulent flows has led to renewed interest in linear analysis. Lee, Lele and Moin (1992, 1993, 1994) repeated Ribner's (1953,1954) analysis and extended it to examine some turbulent statistics that Ribner had not considered. Mahesh, Lee, Lele and Moin (1995) extended Moore's analysis to examine the interaction of an isotropic field of acoustic waves with a shock wave. They also outlined description of the simultaneous interaction of a field of acoustic and vortical disturbances with a shock wave. Mahesh, Lele and Moin (1996) have examined the interaction of a turbulent field of vorticity and entropy fluctuations with a shock. Interest in receptivity led Duck, Lasseigne and Hussaini (1994) to study the processing of free stream disturbances by a wedge-generated shock wave. The different regimes of the pressure field behind the shock wave were discussed.

Recently, Lee, Lele and Moin (1992) have suggested that idealizing a shock wave as a homogeneous one-dimensional compression and examining the temporal

response of turbulence to this compression might approximate the spatial evolution of turbulence through a shock wave. Linear, inviscid equations, or Rapid Distortion Theory (RDT) were used to study this problem. The results (for *solenoidal* upstream turbulence) showed reasonable agreement with Ribner's analysis for shock waves whose mean Mach number was less than 2. Significant disagreement was seen for stronger shock waves. This conclusion is reiterated by Jacquin, Cambon and Blin (1993), who also compare the homogeneous compression of *compressible* turbulence to Ribner's results. They note that the difference between the two analyses is larger than that observed by Lee *et al.*

It is difficult to systematically outline the differences between the two analyses; however certain general comments can be made. Idealizing a shock wave as a one-dimensional compression prevents it from distorting in response to the incident fluctuations; as a result, RDT cannot represent the effect that shock front distortion has on the evolution of the turbulence. Also, homogeneous RDT does not incorporate the Rankine Hugoniot equations; as a result, solenoidal fluctuations do not produce all three kinds of modes upon compression. Another important difference between the two analyses is the behavior of acoustic fluctuations. The acoustic fluctuations in the spatial problem can either propagate without attenuation or decay exponentially behind the shock wave depending upon the angle of incidence of the disturbance. RDT cannot reproduce this behavior. Mahesh *et al.* (1995) compare their analysis of a shock wave interacting with acoustic fluctuations to Jacquin *et al.*'s (1993) compression of compressible turbulence, and note that the results are different over the entire range of Mach numbers. It appears that the homogeneous problem can approximate the evolution of solenoidal fluctuations across shock waves of moderate strength; however it is quite inappropriate to describe the spatial evolution as the incident turbulence becomes increasingly compressible. Similarly, the absence of mean gradients in density and temperature preclude linear baroclinic effects in the homogeneous problem. As a result, the interaction of entropy fluctuations with a shock wave cannot be predicted by the homogeneous compression problem.

There has been some recent work on the evolution of shock waves in an unsteady field of disturbances. Lele (1992a) has used Rapid Distortion Theory to calculate changes in the shock-speed caused by the interaction of isotropic turbulence with a shock wave. Kevlahan, Mahesh and Lee (1992) modelled the shock front as a

propagating surface and compared the resulting evolution to numerical simulation. Good agreement was obtained for the cases considered. A recent paper by Giddings, Rusak and Cole (1993) has developed a transonic small disturbance model to analyze the interaction of a weak shock wave with random perturbations. The model allows effects such as nonlinear steepening, focusing and the formation of caustics to be represented.

### 1.2.3 Numerical computation

Numerical computation of shock/turbulence interaction is a fairly recent undertaking. The first such computation appears to be a detailed study of isotropic turbulence interacting with a weak normal shock ($M_1 \leq 1.2$) by Lee, Lele and Moin (1992, 1993). Lee *et al.* solved the three dimensional compressible Navier Stokes equations, using a non-uniform mesh to resolve the thickness of the shock wave. Subsequently, they (1994) used a high order shock-capturing scheme to study stronger shock waves ($M_1 = 2, 3$). Their results corroborated Ribner's (1954) linear analysis. Amplification of vorticity, kinetic energy and thermodynamic fluctuations was observed along with decrease in Taylor microscale.

Subsequently, Hannappel and Friedrich (1994b) have used shock capturing to compute compressible isotropic turbulence interacting with a Mach 2 shock wave. The interaction of compressible fluctuations (kinetic energy equally distributed between solenoidal and dilatational modes) was contrasted with that of solenoidal fluctuations. The amplification of kinetic energy was seen to be lower when the incident fluctuations were compressible.

Prior to Lee *et al.*'s (1992) study, computations were largely restricted to the interaction of a shock wave with single waves of vorticity, sound and entropy or deterministic flow inhomogeneities such as hot spots and vortices. There appear to be only two detailed studies (in two dimensions) of the interaction of a shock wave with a random field of disturbances.

Zang *et al.* (1984) evaluated the linear analysis of McKenzie and Westphal (1968) by comparing it to their numerical solution of the two-dimensional Euler equations. They examined the effect of incident angle, shock-strength and the amplitude of the incident disturbance in the interaction of acoustic and vorticity waves with a shock wave. Results were presented only in the freely propagating regime. The dependence on incident angle was examined in the interaction of disturbances

of amplitude 0.1% and 10% with a Mach 8 shock wave. Good agreement was seen away from the critical angle; divergence from the linear analysis prediction was seen within about 20° of the critical angle. The linear analysis predictions were quite robust in terms of dependence on shock strength and disturbance amplitude. For an incident angle of 30°, the linear predictions were valid for disturbance amplitudes as high as 25% for acoustic waves and 100% for vorticity waves and shock waves whose Mach number was close to unity.

More recently, Mahesh, Lee, Lele and Moin (1995) have computed the interaction of a Mach 1.5 shock wave with an upstream acoustic wave. The dependence upon the incidence angle and incident amplitude was examined, and the results were compared to linear analysis. Good agreement was seen, except around the critical angles. This disagreement was explained by noting that the region around the critical angle corresponded to transonic flow in transformed coordinates and hence linear approximation would be inconsistent in that regime. Hannappel and Friedrich (1994a) have computed the interaction of a Mach 8 shock wave with vorticity and acoustic waves incident at 45° from upstream. They contrasted the evolution of these two waves. The terms in the averaged equations for the kinetic energy were also examined in their study.

Numerical calculations of the interaction of coherent flow disturbances with a shock wave have also been performed. Hussaini *et al.* (1986) studied the effect of upstream eddy motion and temperature inhomogeneity on the enhancement and production of turbulence. Meadows *et al.* (1991) examined the effect of vortex strength in a study of two-dimensional shock/vortex interaction. Several workers have computed the interaction of a shock wave with a density inhomogeneity to examine the nature of the vorticity field that is produced. A list of references may be found in a recent paper by Yang, Kubota and Zukoski (1994).

Rotman (1991) numerically solved the two-dimensional Euler equations to study the response of an isotropic random field of disturbances to a moving shock wave. Amplification of kinetic energy and decrease of length scale were observed in his study. Comparison of Rotman's results to linear analysis by Lee (Private communication) showed good agreement.

Prior to their three dimensional computation, Lee, Lele and Moin (1991) solved the two-dimensional compressible Navier Stokes equations to study the interaction of two-dimensional isotropic turbulence with a shock wave. A non-uniform mesh

was used to resolve the thickness of the shock wave. Amplification of vorticity and kinetic energy accompanied by a drop in Taylor microscale was observed.

## 1.3 Overview

Our primary objective is to study the interaction of a shock wave with a turbulent shear flow. Both linear analysis and direct numerical simulation are used for this purpose. The DNS provides a database that can be used to elucidate the flow physics as well as to test turbulence models. The linear analyses supplement the simulations in predicting the interaction.

The principal contributions and findings of this work are listed below.

- Rapid Distortion Theory was used to study the response of turbulent shear flows to rapid one-dimensional compression. Both normal and oblique compressions were considered.
- The anisotropy of shear flows (as determined by $E_{11}(\kappa_1)$ and $\overline{u'^2}/q^2$) and the obliquity of compression were shown to strongly affect the evolution of the Reynolds stresses upon compression. The Reynolds shear stress $\overline{u'v'}$ was observed to decrease in magnitude across a normal shock wave.
- Reynolds stress modelling of the normal compression problem was considered in the RDT limit. The inability of popular pressure strain models to predict the evolution of kinetic energy and the decrease in the magnitude of shear stress was demonstrated. The absence of spectral information is shown to be responsible.
- Linear analysis and direct numerical simulation of the combined interaction of vorticity and entropy fluctuations with a shock wave was carried out. The interaction of single waves as well as an isotropic turbulent field was studied.
- Significant dependence of the downstream solution on the amplitude ratio and phase difference between the incident vorticity and entropy waves was demonstrated.
- The presence of negatively correlated velocity and temperature fluctuations was shown to increase the amplification of kinetic energy and pressure fluctuations across the shock wave. Likewise, positively correlated temperature and velocity fluctuations resulted in suppression of amplification.

- A simple explanation was provided to explain these trends. Also, a scaling law to describe the production of vorticity was derived.
- The inapplicability of the Strong Reynolds Analogy (SRA) across a shock wave was demonstrated and explained.
- The interaction of a Mach 1.5 shock wave with a single acoustic wave was numerically computed and the dependence upon the incident angle examined. The results were compared to linear analysis. The requirement of transonic small disturbance equations to model the interaction around the critical angle was identified.
- Linear analysis was used to study the interaction of an isotropic field of acoustic waves with a shock wave. The evolution of kinetic energy, sound level and thermodynamic fluctuations were examined in detail.
- The spatial evolution of kinetic energy behind the shock wave was examined and the rapid non-monotonic variation immediately downstream of the shock wave explained.
- The kinetic energy of acoustic fluctuations was shown to *decrease* across the shock for Mach numbers varying from 1.25 to 1.8. For Mach numbers exceeding 3, the kinetic energy was seen to amplify by levels that far exceeded those found in the interaction of vortical fluctuations with a shock wave. These trends were explained.
- The linear analysis was used to suggest acoustic fluctuations in the upstream turbulence as a possible explanation for wind-tunnel experiments on grid turbulence/shock wave interaction reporting lower levels of kinetic energy amplification.
- Comparison of the linear analysis to Jacquin *et al.*'s analysis of the homogeneous compression of compressible turbulence revealed that the homogeneous problem was quite inappropriate to describe the spatial problem as the incident turbulence became increasingly compressible.
- Direct numerical simulation of the interaction of a shock wave with a turbulent shear flow was performed. The method of specifying inflow turbulence developed by Lee, Lele and Moin (1992) was modified to reduce the evolution length of the inflow disturbances by a factor of 4-5.

- The shear flow simulations were found to support the predictions made by linear analysis. The evolution of turbulence kinetic energy in the shear flow was found to depend on the upstream anisotropy and velocity-temperature correlation as predicted. The shear stress ($\overline{u'v'}$) decreased in magnitude across the shock. So did the '$a_1$' parameter, $\overline{u'v'}/q^2$. The Taylor microscales clearly decreased across the shock wave. The intensities of thermodynamic fluctuations changed across the shock. Acoustic fluctuations were significant immediately behind the shock. They rapidly decayed behind the shock wave leading to entropy fluctuations dominating the far-field.

This report is organized as follows. Rapid Distortion Theory is used to study the response of a homogeneous turbulent shear flow to rapid compression in Chapter 2. Chapter 3 discusses the combined interaction of vorticity and entropy fluctuations with a shock wave. Details and validation of the numerical method are presented in Chapter 4. Chapter 5 outlines the salient observations made from the simulations. Finally, Chapter 6 summarizes the important conclusions drawn. Of the four appendices, Appendix A describes details of the analysis of interaction of vorticity and entropy waves with a shock wave. Analysis of the interaction of a shock wave with an isotropic field of acoustic waves is presented in Appendix B. Next, Appendix C outlines the modified method for specification of inflow turbulence in numerical simulations. Finally, Appendix D discusses the direct numerical simulation of the interaction of a shock wave with an isotropic turbulent field of vorticity and entropy fluctuations.

# Chapter Two

# The Rapid Compression of a Turbulent Shear Flow

## 2.1 Background

This chapter uses rapid distortion theory (RDT) to examine the response of turbulent shear flows to rapid one-dimensional compression. Answers are sought to the following questions: How does the response of a turbulent shear flow to compression differ from that of isotropic turbulence ? How does a shear flow respond to oblique compression as compared to normal compression ?

One-dimensional compression is used to model the shock wave in this chapter. Also, the turbulence is constrained to be homogeneous and solenoidal. The time scale of compression is assumed small as compared to the time scale of the turbulence (a reasonable assumption in shock/turbulence interaction). RDT is then used to predict the response of the turbulence to compression. As discussed in Chapter 1, this approach is expected to yield reasonable prediction of the interaction of solenoidal turbulence with shock waves of moderate strength.

The roots of RDT applied to flows under mean compression lie in the work of Prandtl (1933), Taylor (1935), Ribner and Tucker (1953) and Batchelor and Proudman (1954). Motivated by the passage of turbulence through a wind-tunnel contraction, these workers developed RDT for turbulent flows subjected to rapid irrotational distortions. More recently, Lee (1989) has performed a detailed analysis of the response of the turbulence to axisymmetric strain and dilatation. The above studies assumed the turbulence to be incompressible; recent studies by Durbin and Zeman (1992) and Cambon, Coleman and Mansour (1992) have applied RDT to the compression of compressible turbulence. While Durbin and Zeman have examined the pressure fluctuations and the pressure-dilatation correlation in the limit of vanishing turbulent Mach Number (nearly solenoidal turbulence), Cambon *et al.* have considered finite turbulent Mach numbers and shown the negligible effect of pressure fluctuations at high turbulent Mach numbers.

All the above mentioned studies considered the compression of isotropic turbulence. To the best of our knowledge, the response of shear flows to rapid compression has not been studied before. Precedence in the use of RDT to examine the rapid

straining of anisotropic turbulence may be found in the work of Townsend (1980), Sreenivasan and Narasimha (1978), Maxey (1982) and Cambon (Private communication).

This chapter is organized as follows. A brief outline of RDT in Section 2.2 is followed in Section 2.3 by the response of turbulent shear flows to normal compression. Section 2.4 deals with the oblique compression of a turbulent shear flow. Application of the analysis to predict shock/turbulence interaction is described in Section 2.5 and Reynolds stress modeling of the normal compression problem is examined in Section 2.6. Finally, the salient results are summarized in Section 2.7. Most of the work in this chapter is described by Mahesh, Lele and Moin (1993, 1994).

## 2.2 Theoretical Procedure

Rapid Distortion Theory combines linearization of the governing equations with statistical averaging to describe the statistical evolution of turbulence under rapid mean distortion. The formal development of the RDT approximation is outlined in reviews such as those by Savill (1987) and Hunt and Carruthers (1990). When the time-scale of the mean distortion is much smaller than that of the turbulence, then the turbulence has no time to interact with itself. This allows the neglect of all terms in the governing equations that involve viscosity or the product of fluctuations yielding a set of evolution equations that are linear in the fluctuations. An alternative formulation (Pearson, 1959; Deissler, 1961) corresponding to low Reynolds number or 'weak' turbulence requires retention of the viscous terms. We neglect the viscous terms in our analysis.

Linearization of the continuity and momentum equations yields the following set of equations.

$$\frac{\partial u_i'}{\partial x_i} = 0 \tag{2.1a}$$

$$\frac{\partial u_i'}{\partial t} + U_j \frac{\partial u_i'}{\partial x_j} + u_j' \frac{\partial U_i}{\partial x_j} = -\frac{1}{\rho} \frac{\partial p'}{\partial x_i}. \tag{2.1b}$$

The variables $U_i$ and $\rho$ denote the mean velocity and density respectively; $u_i'$ and $p'$ represent the fluctuating velocity field and pressure respectively. For irrotational mean distortions, it is convenient to solve the linearized vorticity equation which reduces to Cauchy's equation.

Note that the fluctuations are assumed to be solenoidal. If the mean distortion is solenoidal, then the above equations correspond to linearization of the incompressible Navier Stokes equations. However, if the mean field is dilatational (as for a one-dimensional compression), then the governing equations are the *compressible* Navier Stokes equations and the above set of equations therefore describe evolution of the solenoidal component of the compressible flow field under the assumption that its evolution is independent of the dilatational component. (Alternatively, equations (2.1$a$) and (2.1$b$) describe the evolution of a compressible flow field with spatially uniform but time-dependent density.) The solenoidal and dilatational components are coupled even in the linear limit for rotational mean flows (Blaisdell, Mansour and Reynolds, 1991). However for irrotational mean distortions, the solenoidal component may be assumed to evolve independently in the limit $\Delta m = \Gamma_0 l/\overline{c} \ll 1$ where, $\Gamma_0$ is the mean strain rate, $l$ is a turbulence lengthscale and $\overline{c}$ is the mean speed of sound ; *i.e.*, the turbulence is nearly incompressible (Cambon, Coleman and Mansour, 1992).

The assumption of homogeneity constrains the mean velocity gradient to be uniform; *i.e.*, the mean velocity is of the form $U_i = A_{ik}(t)x_k$. For incompressible turbulence, this is the only requirement for homogeneity; since as discussed above, we consider evolution of the solenoidal component of of a compressible flow field, we constrain the mean field to satisfy homogeneity for compressible turbulent fluctuations. As a result, in addition to a uniform velocity gradient, the mean field satisfies the compressible Euler equations and has uniform pressure and density (Blaisdell, Mansour and Reynolds, 1991).

The procedure for solving equations (2.1$a$) and (2.1$b$) is fairly well established. One method of solution (Batchelor and Proudman, 1954) involves using a Fourier representation where the wavenumber changes with time as:

$$u'(\mathbf{x},t) = \sum_{\mathbf{k}} \widehat{u'}(\mathbf{k},t) e^{ik_j(t)x_j},$$

$$p'(\mathbf{x},t) = \sum_{\mathbf{k}} \widehat{p'}(\mathbf{k},t) e^{ik_j(t)x_j},$$

where:

$$\frac{\mathrm{d}k_\alpha}{\mathrm{d}t} + k_j A_{j\alpha} = 0. \tag{2.2}$$

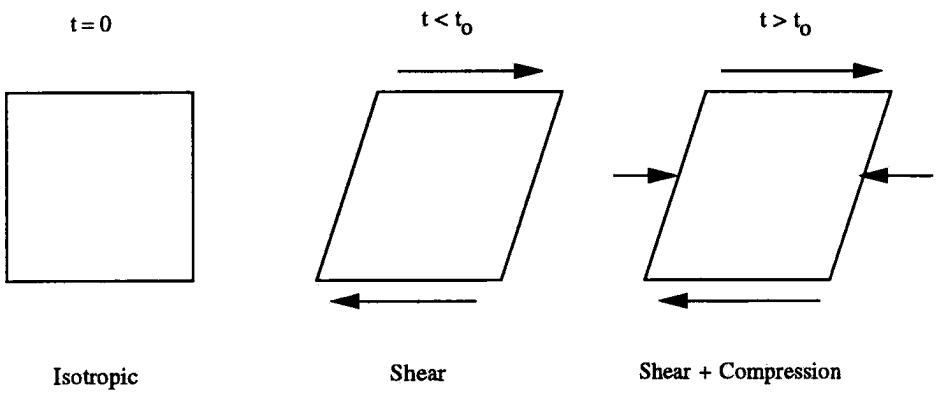


FIGURE 2.1: Schematic of the mean velocity field in the normal compression of a turbulent shear flow.

An alternative equivalent method of solution (Rogallo, 1981) is to transform coordinates to a system that deforms with the mean field; *i.e.*,

$$\xi_i = B_{ik}(t)x_k \qquad \tau = t$$

where,

$$\frac{\mathrm{d}}{\mathrm{d}t}B_{nk} + A_{jk}B_{nj} = 0. \tag{2.3}$$

The transformed equations are then solved using conventional Fourier representation. Knowledge of the Fourier coefficients enables computation of the energy spectrum tensor which is then integrated over all wavenumbers to determine the Reynolds stresses.

Homogeneous RDT being an initial-value problem, requires specification of the initial energy spectrum. As mentioned previously, earlier studies assume isotropic initial spectrum. Our analysis is different in that the compression of anisotropic turbulence is considered. Details of the analysis are presented in the following sections.

## 2.3. Normal Compression of Sheared Turbulence

The response of a turbulent shear flow to normal compression is discussed in this section. Description of the problem and the solution procedure is outlined in Section 2.3.1. Results of the analysis are presented and discussed in Sections 2.3.2 and 2.3.3 respectively.

### 2.3.1 Problem Formulation

Figure 2.1 shows a schematic of the normal compression of a turbulent shear flow. One-dimensional compression is characterized by the following mean field.

$$U_1 = \frac{\Gamma_0}{1+\Gamma_0 t} x_1, \quad U_2 = U_3 = 0, \tag{2.4a}$$

$$\rho = \frac{\rho_0}{1+\Gamma_0 t}, \tag{2.4b}$$

$$\overline{p} = \frac{\overline{p}_0}{[1+\Gamma_0 t]^\gamma}. \tag{2.4c}$$

where $U_1, U_2, U_3$ are the mean velocity components in the $x_1, x_2, x_3$ directions respectively; $\rho$ and $\overline{p}$ are the mean density and pressure respectively, and are uniform in space. $\Gamma_0$ is negative for compression and positive for expansion.

Consider isotropic turbulence that is subjected to rapid homogeneous shear *i.e.*,

$$U_1 = S_0 x_2, \quad \rho = \rho_0, \quad \overline{p} = \overline{p}_0. \tag{2.5}$$

At a non-dimensional time $\beta_0 = S_0 t_0$ during application of shear, we introduce the one-dimensional compression, *i.e.* for $t > t_0$,

$$U_1 = \frac{\Gamma_0}{1+\Gamma_0(t-t_0)} x_1 + \frac{S_0}{1+\Gamma_0(t-t_0)} x_2, \tag{2.6a}$$

$$\rho = \frac{\rho_0}{1+\Gamma_0(t-t_0)}, \tag{2.6b}$$

$$\overline{p} = \frac{\overline{p}_0}{[1+\Gamma_0(t-t_0)]^\gamma}. \tag{2.6c}$$

The shear rate changes with time during the application of compression to satisfy the compressible Euler equations. Note that the shear creates $U_1(x_2)$ while the compression creates $U_1(x_1)$; hence the terminology 'normal compression'.

Under RDT, the Reynolds stresses before compression depend only upon the total shear $\beta_0$; their subsequent evolution depends upon $\beta_0$, the ratio of shear rate to the rate of compression $(S_0/\Gamma_0)$ and the total volumetric strain $(\rho/\rho_0)$. Since our interest is in the compression of shear flows, we consider the regime where the shear sets up the initial anisotropic field and is negligible as compared to the subsequently applied compression; *i.e.*, $S_0/\Gamma_0 \ll 1$. In this report $S_0/\Gamma_0$ is 0.1 for all cases presented. Lower values of $S_0/\Gamma_0$ ( *e.g.* $S_0/\Gamma_0 = 0.01$) yielded

results identical to those shown here. Thus, we effectively consider the rapid one-dimensional compression of sheared turbulence.

The RDT equations are solved by transforming coordinates to a system that deforms with the mean field. Fourier representation in the transformed coordinates is used to derive ordinary differential equations that describe the evolution of the energy spectrum tensor. The equations are numerically advanced in time and at each time step, the energy spectrum tensor is numerically integrated over all wavenumbers to compute the Reynolds stresses.

As indicated above, the mean field is pure shear for $t < t_0$. The RDT equations for pure shear have been solved analytically (Moffatt, 1965; Townsend, 1970) and hence we do not give the evolution equations for the energy spectrum tensor. We only note that the coordinate transform used is as follows,

$$\xi_1 = x_1 - S_0 t\, x_2, \quad \xi_2 = x_2, \quad \xi_3 = x_3, \quad \tau = t. \tag{2.7}$$

At time $t_0 = \beta_0/S_0$, the coordinate transformation changes to accommodate the compression. The new transformation is given by,

$$\xi_1 = \frac{x_1}{1+\Gamma_0(t-t_0)} - [\beta_0 + S_0(t-t_0)]x_2, \quad \xi_2 = x_2, \quad \xi_3 = x_3, \quad \tau = t. \tag{2.8}$$

For $t > t_0$, the RDT equations are transformed to the above coordinate system. Using the Fourier representation,

$$u'(\xi,\tau) = \sum_{\vec{\kappa}} \widehat{u'}(\vec{\kappa},\tau) e^{i\kappa_j \xi_j}, \tag{2.9a}$$

$$p'(\xi,\tau) = \sum_{\vec{\kappa}} \widehat{p'}(\vec{\kappa},\tau) e^{i\kappa_j \xi_j}, \tag{2.9b}$$

the RDT equations take the following form for $t > t_0$:

$$\frac{\mathrm{d}\widehat{u'}_1}{\mathrm{d}\tau} = \frac{1}{1+\Gamma_0\tau'}\left[ -\Gamma_0 \widehat{u'}_1 - S_0 \widehat{u'}_2 + \kappa_1 \frac{i\widehat{p'}}{\rho} \right] \tag{2.10a}$$

$$\frac{\mathrm{d}\widehat{u'}_2}{\mathrm{d}\tau} = \left[\kappa_2 - \frac{S_0\tau'}{1+\Gamma_0\tau'}\,\kappa_1\right]\frac{i\widehat{p'}}{\rho} \tag{2.10b}$$

$$\frac{\mathrm{d}\widehat{u'}_3}{\mathrm{d}\tau} = \kappa_3 \frac{i\widehat{p'}}{\rho} \tag{2.10c}$$

$$\frac{i\widehat{p'}}{\rho} = \frac{\kappa_1\Gamma_0\ \widehat{u'}_1 + [\kappa_1 S_0 + (\kappa_1 S_0 - \kappa_2\Gamma_0)\ (1+\Gamma_0\tau')\ ]\ \widehat{u'}_2 - \kappa_3\Gamma_0\ (1+\Gamma_0\tau')\ \widehat{u'}_3}{\kappa_1^2\ [1+(S_0\tau')^2] - 2\ \kappa_1\kappa_2\ S_0\tau'\ (1+\Gamma_0\tau') + (\kappa_2^2+\kappa_3^2)\ (1+\Gamma_0\tau')^2}. \tag{2.10d}$$

where the variable $\tau' = \tau - \tau_0$. Note that the expression for pressure is obtained through elimination of the continuity equation. Also, $\Gamma_0 = 0$ in the above equations would describe the evolution for $t < t_0$ (Pure shear).

The RDT equations for a pure compression allow analytical solution as do the equations for pure shear. However, as seen above, the combination of shear and compression yields a formidable set of equations which we have not been able to solve analytically. Instead equations (2.10$a$) through (2.10$d$) were used to derive evolution equations for the energy spectrum tensor $E_{ij}(\vec{\kappa},\tau)$, defined as $E_{ij} = \widehat{u'}_i\widehat{u'}^*_j$, where the superscript '$*$' refers to the complex conjugate. For reasons of brevity, the equation for $E_{ij}$ is not reproduced here; it has the following form:

$$\frac{\mathrm{d}E_{ij}}{\mathrm{d}\tau} = C_{il}E_{lj} + C_{jl}E_{li}. \tag{2.11}$$

The above system of equations is integrated numerically to compute $E_{ij}(\vec{\kappa},\tau)$. $E_{ij}$ is then integrated over all wavenumbers to compute the Reynolds stress tensor $R_{ij}(\tau)$ defined as $R_{ij} = \overline{u'_i u'_j}$; *i.e.*,

$$R_{ij}(\tau) = \int E_{ij}(\vec{\kappa},\tau)\ \mathrm{d}^3\vec{\kappa}. \tag{2.12}$$

The integration is carried out in the polar coordinates,

$$\kappa_1 = \kappa\cos\phi, \quad \kappa_2 = \kappa\sin\phi\cos\theta, \quad \kappa_3 = \kappa\sin\phi\sin\theta, \quad \mathrm{d}^3\vec{\kappa} = \kappa^2\sin\phi\,\mathrm{d}\phi\,\mathrm{d}\theta\,\mathrm{d}\kappa$$

where, $\kappa$ varies from 0 to $\infty$, $\phi$, from 0 to $\pi$ and $\theta$, from 0 to $2\pi$. Note that since at $\tau = 0$, the energy spectrum tensor is assumed to be isotropic; *i.e.*,

$$E_{ij}(\vec{\kappa},0) = \frac{E(\kappa)}{4\pi\kappa^2}\left(\delta_{ij} - \frac{\kappa_i\kappa_j}{\kappa^2}\right),$$

it can be shown that $R_{ij}(\tau)$ is independent of the initial three-dimensional energy spectrum tensor, $E(\kappa)$ and the magnitude of the wavenumber vector.

### 2.3.2 Results

The analysis described above essentially applies RDT to the compression of a shear flow where the energy spectrum tensor of the shear flow is itself the RDT

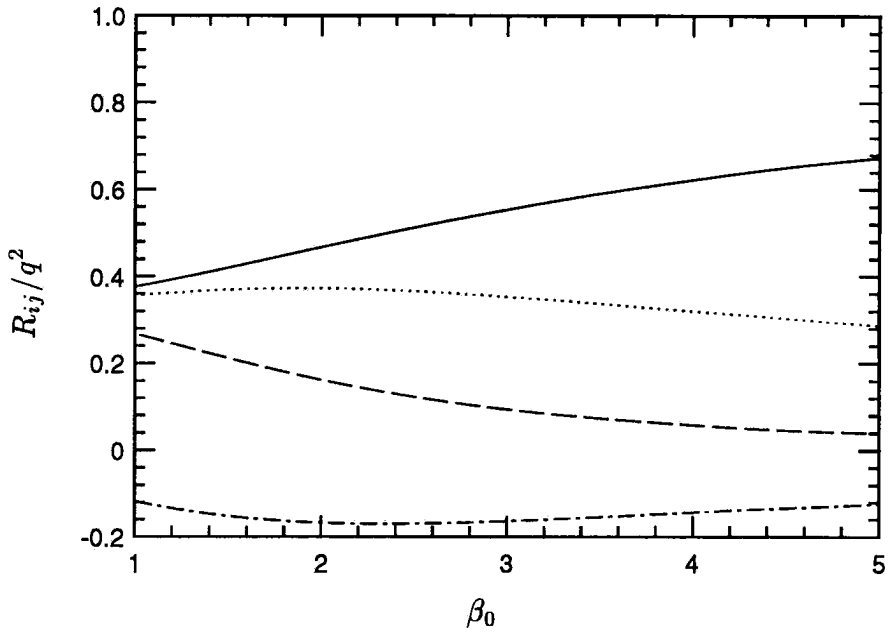


FIGURE 2.2: The evolution of $R_{ij}/q^2$ as predicted by RDT applied to the homogeneous shear of initially isotropic turbulence. ——— $(R_{11}/q^2)$, - - - - $(R_{22}/q^2)$, ····· $(R_{33}/q^2)$, —·— $(R_{12}/q^2)$.

solution to initially isotropic turbulence subjected to homogeneous shear. The use of RDT to obtain the energy spectrum tensor that characterizes a shear flow is motivated by Townsend (1970) where the RDT predictions of Reynolds stress correlations, spectra and non-dimensional Reynolds stresses in turbulent shear flows were compared to experiment and good agreement was observed.

This is illustrated in figure 2.2 where $R_{ij}/q^2$ as predicted by RDT applied to the rapid shear of initially isotropic turbulence is shown. The quantity plotted on the abscissa is the total shear $\beta$ defined as $\beta = S_0 t$. Note that after a moderate amount of total shear ($\beta$ between 2 and 3), the nondimensional Reynolds stresses are quite close to values obtained in shear flows such as homogeneous shear flow, turbulent channel flow (Moin, 1988) and boundary layers (Townsend, 1970). For example, in homogeneous shear flow (Moin, 1988), $R_{11}/q^2, R_{22}/q^2, R_{33}/q^2$ and $R_{12}/q^2$ are 0.54, 0.16, 0.31 and 0.14 respectively. For a total shear of 2.5, RDT yields values of 0.51, 0.12, 0.36 and 0.16 respectively. Townsend (1970) notes, 'The good agreement of the non-dimensional Reynolds stresses suggests that the large eddies in turbulent shear flows have very nearly the shape suggested by RDT'. This conclusion is further supported by direct numerical simulation (Lee, Kim and Moin, 1990) of turbulence

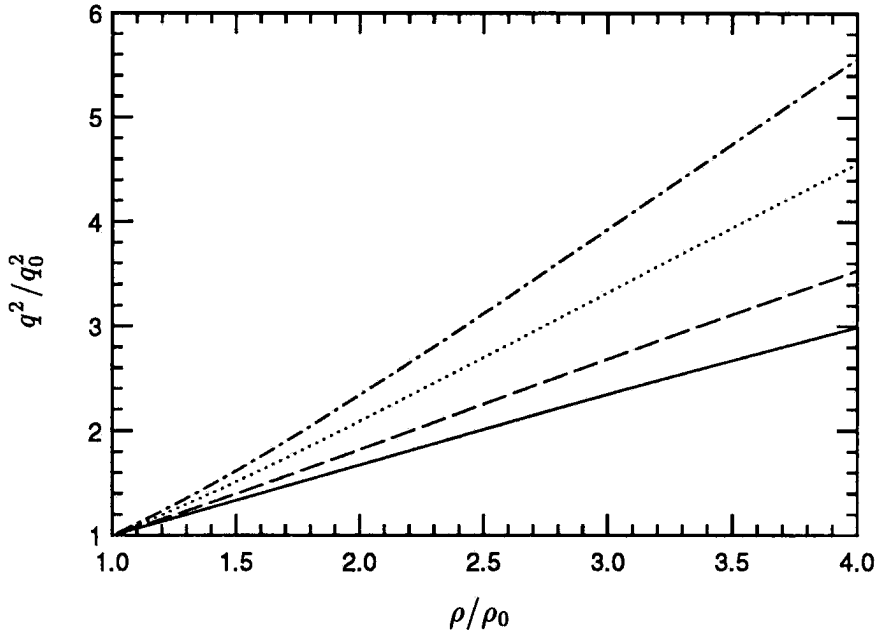


FIGURE 2.3: Evolution of $q^2$ upon the normal compression of sheared turbulence. The different curves correspond to different values of initial total shear. —— ($\beta_0 = 0$), ---- ($\beta_0 = 1$), ····· ($\beta_0 = 2$), —·— ($\beta_0 = 3$).

subjected to very high shear rates, where structures similar to near wall 'streaks' were observed.

The evolution of sheared turbulence upon compression is next examined. The abscissa in all plots shown is the total volumetric strain, $\rho/\rho_0$. $q^2$ normalized with its value at the start of compression is plotted against the total volumetric strain in figure 2.3. The different curves correspond to different values of total initial shear ($\beta_0$). $\beta_0 = 0$ corresponds to the compression of initially isotropic turbulence. $q^2$ is seen to amplify upon compression with the amplification ratio increasing as the initial total shear increases. The amplification of turbulent kinetic energy upon normal compression is thus higher for a shear flow than it is for isotropic turbulence.

The evolution of the components of turbulent kinetic energy is plotted in figure 2.4. $\beta_0$ was set to 3 for this case. All three components are seen to amplify with the $x_1$ (direction of compression) component being amplified the most. The reason for the preferential amplification of the $x_1$ component is due to the fact that it is directly 'produced' by the compression while the other components amplify through the redistributive nature of the pressure-strain correlation in the Reynolds stress

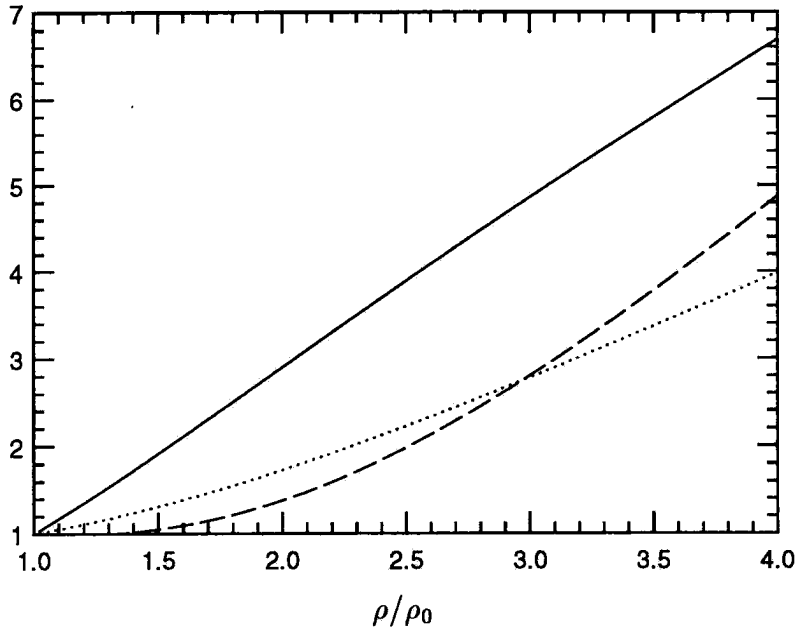


FIGURE 2.4: Evolution of the components of turbulent kinetic energy when sheared turbulence ($\beta_0 = 3$), is subjected to normal compression. ——— $(R_{11})$, - - - - $(R_{22})$, ····· $(R_{33})$.

equations. The importance of the initial anisotropy on the amplification of $\overline{u_1'^2}$ is gauged by comparing the amplification of $\overline{u_1'^2}$ of initially sheared turbulence to that of initially isotropic turbulence (figure 2.5). Note that the amplification of $\overline{u_1'^2}$ in the shear flow is much higher than that of isotropic turbulence. For example, at a density ratio of 3, the amplification ratio is 3.4 for initially isotropic turbulence and 4.85 for initially sheared turbulence - an increase of about 43 %. Shear flows in equilibrium are characterized by typical values of $R_{ij}/q^2$. It is of interest to see how these values change upon normal compression. Figure 2.6 shows the the diagonal terms of the tensor. Compression increases the contribution of $u_1'$ to the turbulent kinetic energy while decreasing that of $u_2'$ and $u_3'$. Also note (over the range of total volumetric strain shown) that the ordering of kinetic energy components ($\overline{u_1'^2} > \overline{u_3'^2} > \overline{u_2'^2}$) is retained upon normal compression.

The evolution of $R_{12}/q^2$ upon compression is plotted in figure 2.7. The three curves correspond to different values of total initial shear. Upon normal compression, $R_{12}/q^2$ decreases in magnitude and for sufficiently large total volumetric strains, it changes sign. This trend was first observed by Cambon (Private communication), and is hastened upon increasing the initial total shear. The terms in the Reynolds shear stress evolution equation provide an explanation for this behavior.

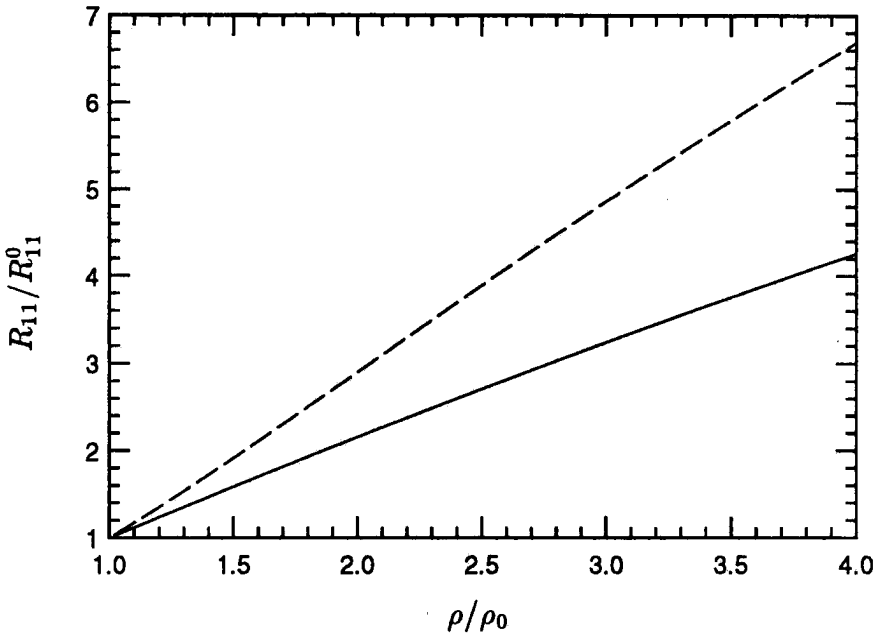


FIGURE 2.5: Comparison of the amplification of $R_{11}$ of sheared turbulence ($\beta_0 = 3$) to that of isotropic turbulence. ——— (Isotropic), ---- (Sheared).

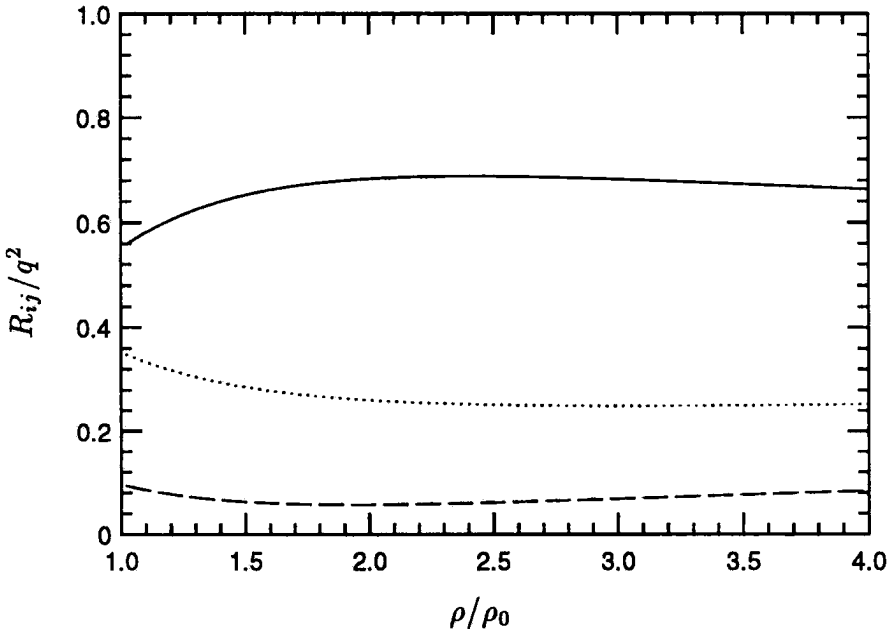


FIGURE 2.6: Evolution of $R_{ij}/q^2$ when sheared turbulence ($\beta_0 = 3$) is subjected to normal compression. ——— ($R_{11}/q^2$), ---- ($R_{22}/q^2$), ····· ($R_{33}/q^2$).

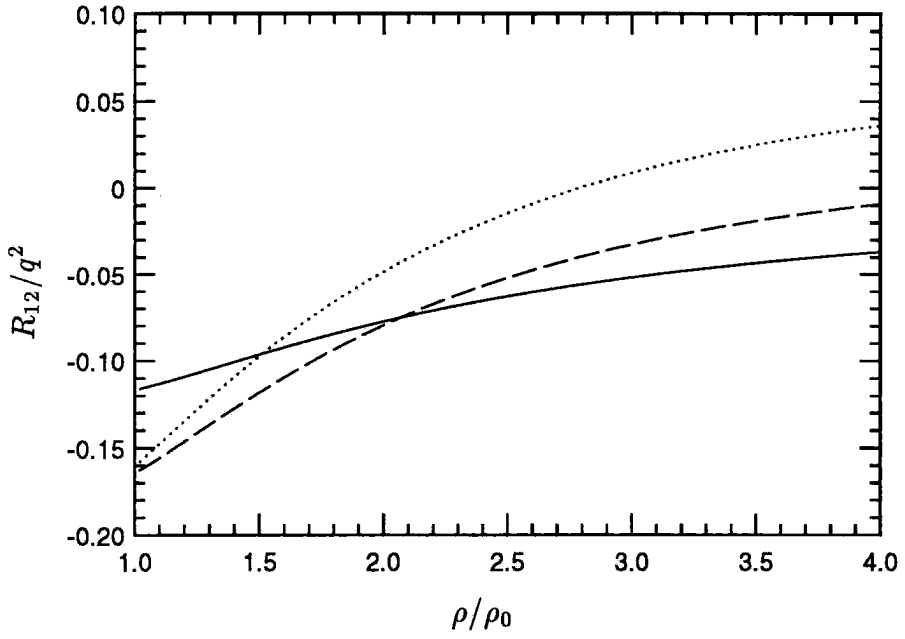


FIGURE 2.7: Evolution of $R_{12}/q^2$ when sheared turbulence is subjected to normal compression. The different curves correspond to different values of initial total shear. ——— ($\beta_0 = 1$), - - - - ($\beta_0 = 2$), ····· ($\beta_0 = 3$).

The evolution equation for $R_{12}$ is,

$$\frac{\mathrm{d}}{\mathrm{d}t}R_{12} = \underbrace{-\frac{\Gamma_0}{1+\Gamma_0 t}R_{12}}_{\text{Compression prod.}} \quad \underbrace{-\frac{S_0}{1+\Gamma_0 t}R_{22}}_{\text{Shear prod.}} \quad +\pi_{12} \tag{2.13}$$

where $\pi_{ij}$ is the pressure-strain correlation defined as $\pi_{ij} = \overline{p'(u'_{i,j} + u'_{j,i})}/\rho$. Note that both the strain and shear production terms tend to increase the magnitude of $R_{12}$ (make it more negative). The tendency of $|R_{12}|$ to decrease must therefore be due to the pressure strain correlation. Figure 2.8 illustrates the evolution of terms in the budget of $R_{12}$ for the case with $\beta_0 = 3$. We see that the tendency of $R_{12}$ to decrease upon normal compression is due to amplification of the pressure-strain correlation and the consequent upsetting of the initial balance between 'production' and the pressure-strain correlation in the shear flow.

### 2.3.3 Interpretation of the results

We have seen that the response of a shear flow to normal compression is quite different from that of isotropic turbulence. A noticeable feature is the higher am-

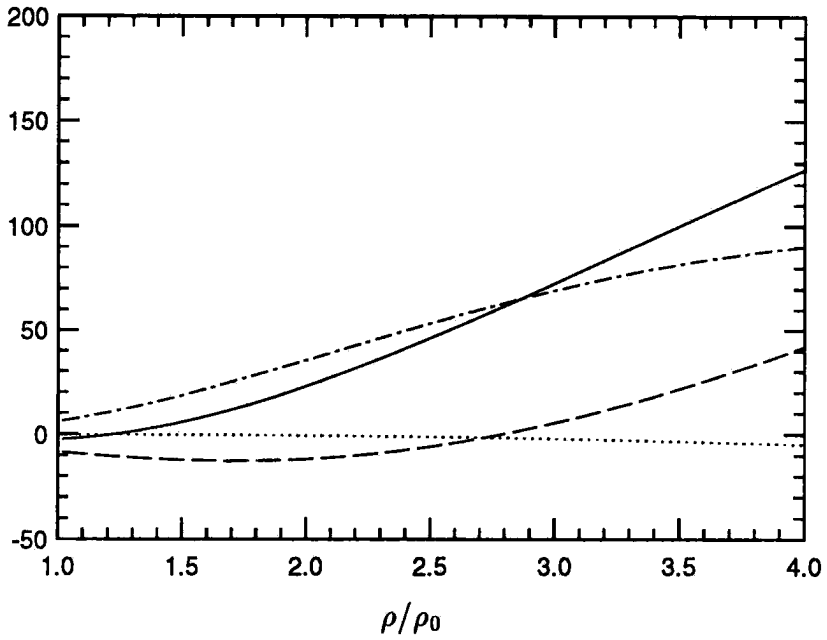


FIGURE 2.8: Budget of terms in the $R_{12}$ evolution equation during the normal compression of a shear flow ($\beta_0 = 3$). ——— (LHS), - - - - (Compression production), ····· (Shear production), —·— (Pressure-strain correlation).

plification of $\overline{u_1'^2}$ and $q^2$ in the shear flow. In this section, we attempt to explain this observation by posing the following question, 'What aspect of the initial anisotropic field is important in determining the evolution of kinetic energy during a one-dimensional compression ?'

The evolution equations for $\overline{u_1'^2}$ and $q^2$ during rapid compression are given by

$$\frac{\mathrm{d}\overline{u_1'^2}}{\mathrm{d}\tau} = -2\frac{\Gamma_0}{1+\Gamma_0\tau}\overline{u_1'^2} + \pi_{11}, \tag{2.14a}$$

$$\frac{\mathrm{d}q^2}{\mathrm{d}\tau} = -2\frac{\Gamma_0}{1+\Gamma_0\tau}\overline{u_1'^2}. \tag{2.14b}$$

When negative, the pressure-strain correlation $\pi_{11}$ 'takes' energy from $\overline{u_1'^2}$ and redistributes it among the other components. The amplification of $\overline{u_1'^2}$ and hence, $q^2$ through equation (2.14*b*), would increase if the pressure-strain correlation were to decrease. Also, since in the RDT limit, the pressure-strain correlation is the only term in the budget apart from the production term, a higher amplification rate automatically implies a lower pressure-strain correlation.

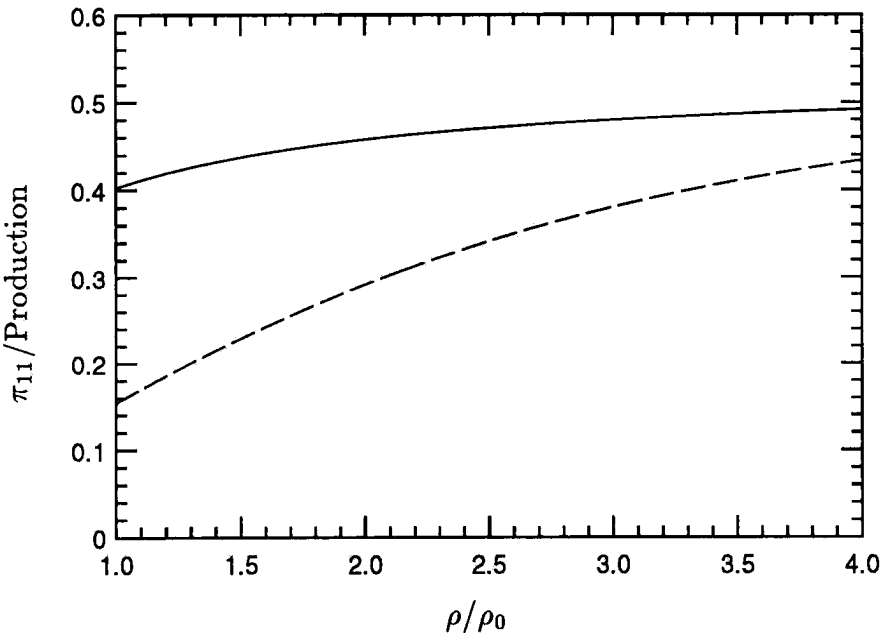


FIGURE 2.9: Evolution of the ratio of $\pi_{11}$ to the production term in the $R_{11}$ equation upon normal compression. The compression of sheared turbulence ($\beta_0 = 3$) is compared to that of isotropic turbulence. ——— (Isotropic), ---- (Sheared).

The relative magnitude of the pressure-strain term in the energy budget may be gauged from its short-time behavior. It is easily shown that in turbulence subjected to rapid one-dimensional compression, $\pi_{11}$ is given by:

$$\pi_{11} = -2\Gamma_0 c \int \frac{c^2\kappa_1^2}{c^2\kappa_1^2 + \kappa_2^2 + \kappa_3^3} E_{11}(\vec{\kappa}) \mathrm{d}^3\kappa \tag{2.15}$$

where, $c = \rho/\rho_0$. $\pi_{11}$ thus strongly depends upon the spectral distribution of the $u_1'$ component of velocity. Note that as the energy distribution in $u_1'$ moves to smaller $\kappa_1$, the magnitude of $\pi_{11}$ decreases. The small time evolution of $\pi_{11}$ may be estimated by replacing $E_{11}$ in equation (2.15) with its initial value, $E_{11}^0$. This small time evolution shows how the spectral distribution of $u_1'$ in the initial field affects the rate of change of $\overline{u_1'^2}$ when anisotropic turbulence is compressed.

Since mean shear tends to stretch the turbulence in the streamwise direction, $\widehat{u'}_1$ in a shear flow has energy at smaller $\kappa_1$ as compared to isotropic turbulence and hence according to equation (2.15), a lower initial value of $\pi_{11}$. This is shown in figure 2.9, where the ratio of $\pi_{11}$ to the production term in the $R_{11}$ equation is plotted. The pressure-strain correlation is indeed seen to be smaller when shear flow is compressed.

As one continues the compression, the energy in $u_1'$ is moved to larger $\kappa_1$ and hence, the pressure-strain correlation would progressively become more important. Analysis shows that, in the limit of infinite $\rho/\rho_0$, the ratio of $\pi_{11}$ to the production term is independent of the initial energy spectrum; it is equal to 1. This is shown as follows. For turbulence subjected to one-dimensional compression, under RDT,

$$E_{11}(\vec{\kappa}) = \frac{c^2 E_{11}^0(\vec{\kappa})}{c^2(\kappa_1/\kappa)^2 + (\kappa_2/\kappa)^2 + (\kappa_3/\kappa)^2} \tag{2.16}$$

where, $c = \rho/\rho_0$.

Denoting the denominator in the above expression by $D$, the rate of change of $E_{11}$ is given by,

$$\frac{\mathrm{d}E_{11}}{\mathrm{d}\tau} = \frac{E_{11}^0}{D^2}\left(D\frac{\mathrm{d}c^2}{\mathrm{d}\tau} - c^2\frac{\mathrm{d}D}{\mathrm{d}\tau}\right). \tag{2.17}$$

Noting that $\mathrm{d}c/\mathrm{d}t = -\Gamma_0 c^2$ and considering very large compressions, it can be shown that,

$$\lim_{c\to\infty} \frac{\mathrm{d}E_{11}}{\mathrm{d}\tau} = 0. \tag{2.18}$$

Since $E_{11}$ when integrated over all wavenumbers yields $R_{11}$, the above equation implies that in the limit of very large $c$, $\mathrm{d}\overline{u_1'^2}/\mathrm{d}\tau = 0$. Substitution into equation (2.14$a$) shows that asymptotically, $\pi_{11} = -$Production. Note that this relation is independent of the initial energy spectrum. The asymptotic behavior shows the diminishing effect of initial anisotropy upon the pressure-strain correlation as time progresses. This is supported by figure 2.9 where the two curves tend towards each other as $c$ increases. Integration to larger time shows that the two curves do indeed asymptote to 1.

We see that when anisotropic turbulence is compressed (in the $x_1$ direction), the feature of the initial field that determines kinetic energy evolution is $E_{11}^0(\kappa_1)$. As the energy in ${u_1'}^0$ moves to smaller $\kappa_1$, the relative importance of $\pi_{11}$ decreases, resulting in larger amplification of $\overline{u_1'^2}$. The amplification of $q^2$, in addition to being influenced by $E_{11}^0$, is also influenced by the initial value of $\overline{u_1'^2}/q^2$. This is shown as follows. The kinetic energy equation for a one-dimensional compression (Equation 2.14$b$) may be rewritten as,

$$\frac{1}{2q_0^2}\frac{\mathrm{d}q^2}{\mathrm{d}\tau} = -\frac{\Gamma_0}{1+\Gamma_0\tau}\,\frac{R_{11}}{R_{11}^0}\,\frac{R_{11}^0}{q_0^2}. \tag{2.19}$$

Note that as $R_{11}^0/q_0^2$ increases, the rate of amplification of $q^2$ increases. This explains the trend seen in figure 2.3. In addition to having energy at lower $\kappa_1$, a shear flow

that is subjected to normal compression also has a larger fraction of its energy along the direction of compression, resulting in a higher amplification of $q^2$ as compared to isotropic turbulence.

## 2.4. Oblique Compression of Sheared Turbulence

Thus far, we have examined the effect of compression on sheared turbulence normal to the direction of shear. Since shear flows are anisotropic, one would expect the direction of compression relative to the shear to be an important parameter; *i.e.*, the oblique compression of a shear flow would yield results different from normal compression. In the section that follows, we discuss the procedure (Section 2.4.1) and results (Section 2.4.2) of RDT applied to the problem of oblique compression.

### 2.4.1. Problem Formulation

Under RDT, the obliquity of compression may be characterized by the angle $\theta$ between the direction of compression and the direction of the upstream shear flow. Note that $\theta = 0$ corresponds to the normal compression discussed in the previous section. Recall that the normal compression problem was formulated by considering sheared turbulence subjected to simultaneous shear and compression in the regime where the compression rate was much higher than the rate of shear. The sole reason for retention of the shear during compression was to avoid the destruction of vorticity. However, one might adopt the point of view that if the mean shear is not important during the process of compression, then it may be ignored except for its effect on the initial spectrum. This is the approach adopted in this section in applying RDT to the oblique compression of sheared turbulence. We essentially repeat RDT for turbulence subjected to a one-dimensional compression. However the initial energy spectrum instead of being isotropic is the RDT solution to isotropic turbulence subjected to homogeneous shear. Also as mentioned, the initial mean shear is assumed to be at angle $\theta$ to the subsequently applied compression. The validity of this approach was verified by comparison of the results for $\theta = 0$ to the more completely formulated normal compression problem.

Figure 2.10 shows a schematic of the the oblique compression problem. Note that the shear is assumed to be in the $x_2$ direction. For reasons of convenience, the time-dependent wavenumber approach (Batchelor and Proudman, 1954) was used to solve the RDT equations. The RDT solution to the oblique compression problem requires knowledge of the evolution of the energy spectrum tensor when isotropic

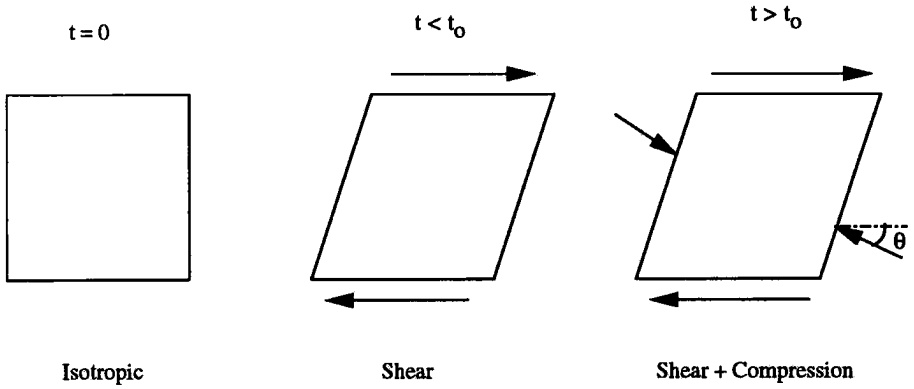


FIGURE 2.10: Coordinate system used in the analysis of oblique compression of sheared turbulence.

turbulence is subjected to homogeneous shear and the transfer function of the vorticity spectrum tensor when turbulence (not necessarily isotropic) is subjected to a one-dimensional compression. As indicated earlier, these problems have been solved analytically. Assuming knowledge of these transfer functions, the procedure for RDT applied to the oblique compression problem is as follows:

1. Consider isotropic turbulence that is subjected to homogeneous shear in the $x_2$ direction. Denote the wavenumber vector at $t = 0$ by $\vec{k}_0$. For a given total shear (defined in the previous section), compute the energy spectrum tensor at the end of shear.
2. With reference to figure 2.10, rotate the energy spectrum tensor and wavenumber vector by the angle $\theta$. This aligns the field with the compression.
3. From the rotated energy spectrum tensor and the wavenumber vector, obtain the vorticity spectrum tensor in the rotated coordinates.
4. Using the transfer functions for the compression problem, obtain the vorticity spectrum tensor and wavenumber vector after compression.
5. Using the inverse of the relation in 3, obtain the energy spectrum tensor after compression in the rotated coordinates. Integrate the energy spectrum tensor over $\mathbf{k_0}$ to obtain the Reynolds stress tensor in rotated coordinates.
6. Rotate the Reynolds stress tensor back by the angle $\theta$. This yields the Reynolds stress tensor after compression in the original coordinate system.

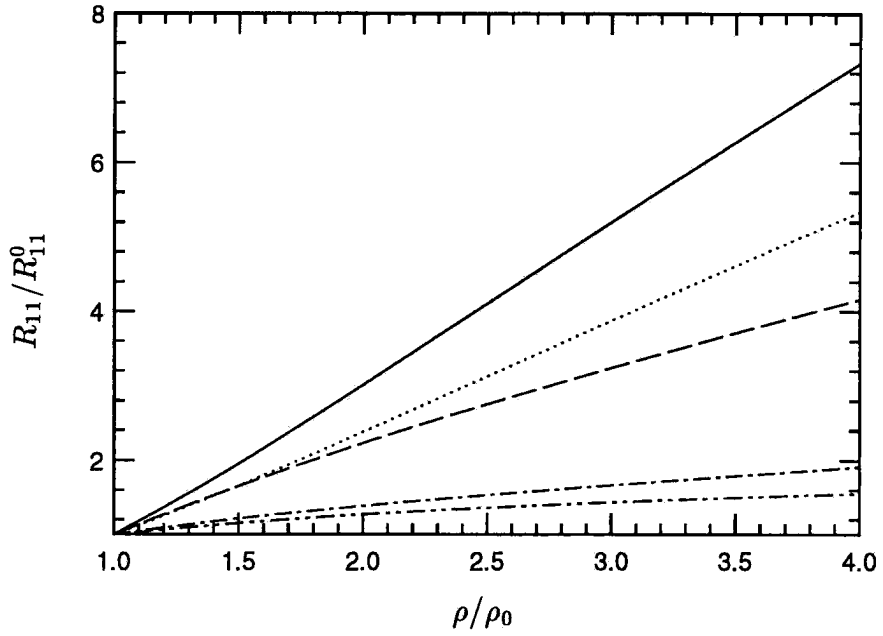


FIGURE 2.11: Evolution of $R_{11}$ upon the oblique compression of sheared turbulence ($\beta_0 = 3$). The different curves correspond to different values of oblique angle. ——— ($\theta = 0°$), - - - - ($\theta = 30°$), ····· ($\theta = -30°$), —·— ($\theta = 60°$), —··— ($\theta = -60°$).

## 2.4.2. Results

We describe in this section some of the results of RDT applied to the oblique compression of sheared turbulence. The effect of the oblique angle $\theta$, is gauged by comparison to the previously discussed normal compression problem. The amplification of the streamwise component of turbulent kinetic energy upon compression is shown in figure 2.11 for different angles of obliquity.

The initial condition corresponds to sheared turbulence with $\beta_0 = 3$. Recall that $\theta = 0$ corresponds to normal compression. Note the decrease in amplification ratio with increasing magnitude of oblique angle. The effect of oblique compression on $q^2$ is shown in figure 2.12. Once again, the amplification of $q^2$ decreases as the oblique angle increases. In the previous section, we emphasized the importance of the $E_{11}(\kappa_1)$ and $\overline{u_1'^2}/q^2$ on the amplification of kinetic energy. If oblique compression is viewed in a coordinate system aligned with the compression, we see that the effect of oblique compression may be explained by the initial value of $E_{\theta\theta}(\kappa_\theta)$ and $\overline{u_\theta'^2}/q^2$, where $\theta$ refers to the direction of compression.

In the previous section, we noted how normal compression could significantly

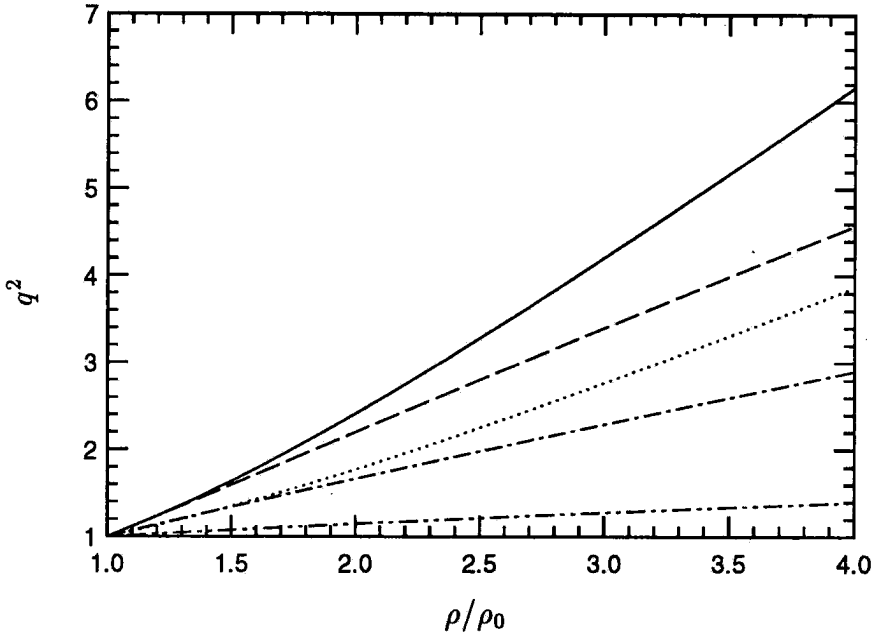


FIGURE 2.12: Evolution of $q^2$ upon the oblique compression of sheared turbulence ($\beta_0 = 3$). The different curves correspond to different values of oblique angle. —— ($\theta = 0°$), ---- ($\theta = 30°$), ····· ($\theta = -30°$), —·— ($\theta = 60°$), —···— ($\theta = -60°$).

change the nondimensional Reynolds stresses of a shear flow. The effect of oblique compression on the diagonal elements of $R_{ij}/q^2$ is shown in figures 2.13,2.14 and 2.15. It is clear that obliquity of compression has a significant effect on the evolution of the Reynolds stresses. The qualitative difference in the curves for different oblique angles is striking to note.

Figure 2.16 shows the evolution of the nondimensional Reynolds shear stress upon oblique compression. Recall the effect of normal compression to decrease $R_{12}/q^2$ and even change its sign. In comparison, we see that this trend decreases as the compression becomes more oblique and for large oblique angles, $R_{12}/q^2$ slightly amplifies.

## 2.5 Application to shock/turbulence interaction

We illustrate application of the analysis to shock/turbulence interaction. Recall that the Reynolds stress tensor during compression of a shear flow is of the form:

$$R_{ij} = R_{ij}\ (\rho/\rho_0; \beta_0, \theta). \tag{2.20}$$

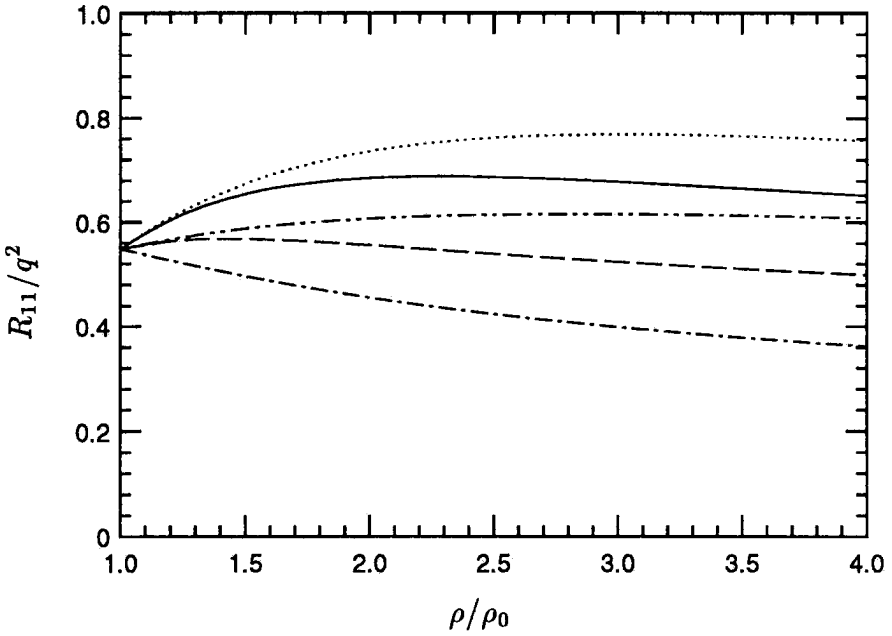


FIGURE 2.13: Evolution of $R_{11}/q^2$ upon the oblique compression of sheared turbulence ($\beta_0 = 3$). The different curves correspond to different values of oblique angle. —— ($\theta = 0°$), ---- ($\theta = 30°$), ····· ($\theta = -30°$), —-— ($\theta = 60°$), —··— ($\theta = -60°$).

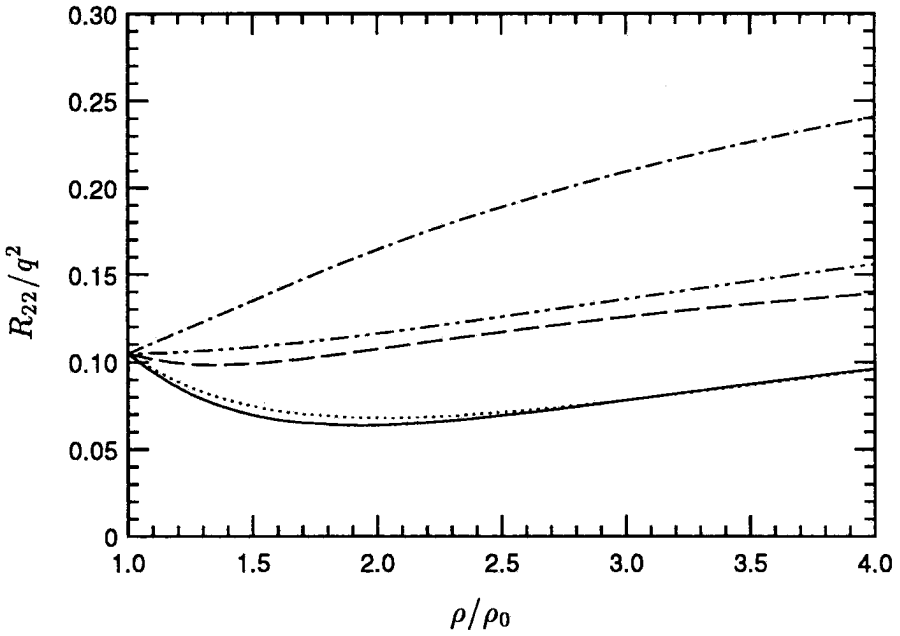


FIGURE 2.14: Evolution of $R_{22}/q^2$ upon the oblique compression of sheared turbulence ($\beta_0 = 3$). The different curves correspond to different values of oblique angle. —— ($\theta = 0°$), ---- ($\theta = 30°$), ····· ($\theta = -30°$), —-— ($\theta = 60°$), —··— ($\theta = -60°$).

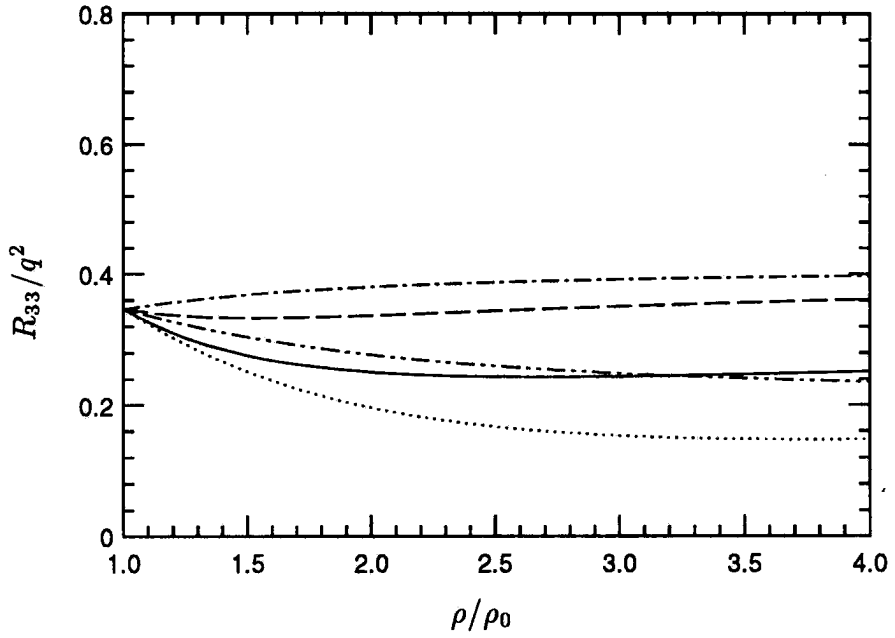


FIGURE 2.15: Evolution of $R_{33}/q^2$ upon the oblique compression of sheared turbulence ($\beta_0 = 3$). The different curves correspond to different values of oblique angle. ——— ($\theta = 0°$), ---- ($\theta = 30°$), ····· ($\theta = -30°$), —·— ($\theta = 60°$), —··— ($\theta = -60°$).

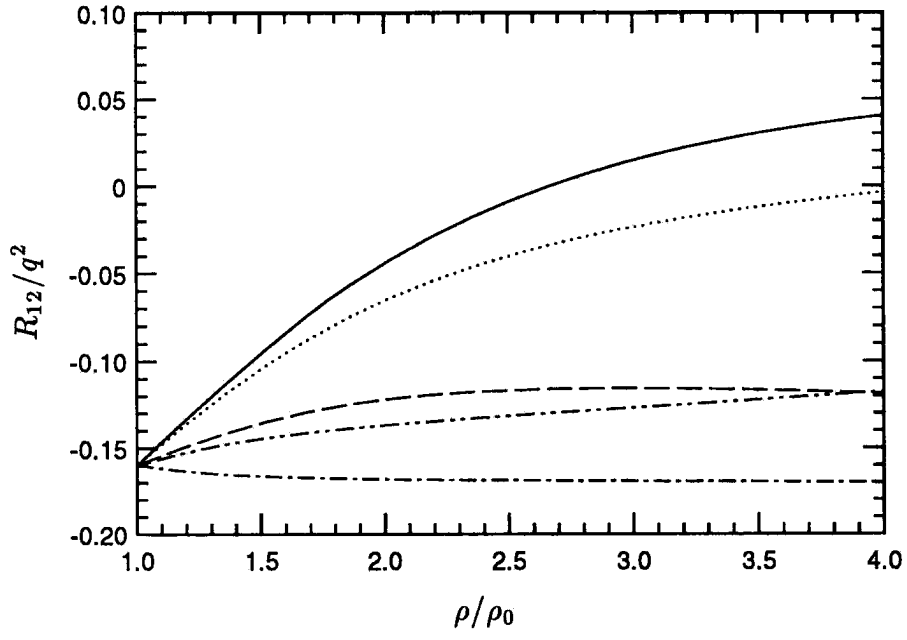


FIGURE 2.16: Evolution of $R_{12}/q^2$ upon the oblique compression of sheared turbulence ($\beta_0 = 3$). The different curves correspond to different values of oblique angle. ——— ($\theta = 0°$), ---- ($\theta = 30°$), ····· ($\theta = -30°$), —·— ($\theta = 60°$), —··— ($\theta = -60°$).

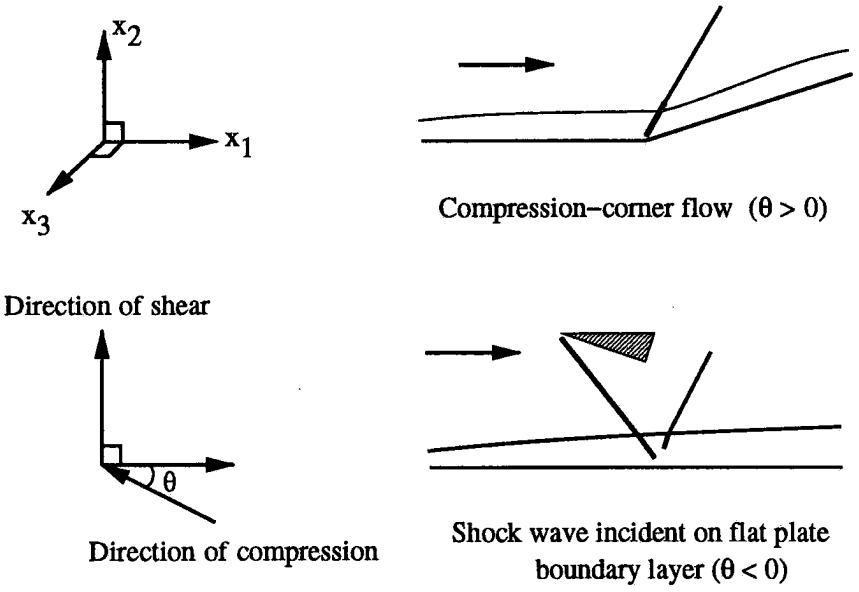


FIGURE 2.17: Examples of the oblique compression of a shear flow.

Note that $S_0/\Gamma_0$ is assumed negligible in writing the above expression. The parameter $\theta$ in the above expression is determined by the oblique angle of the shock wave. Figure 2.17 illustrates a couple of examples that correspond to positive and negative $\theta$. The choice of $\beta_0$ depends upon the extent of shear (quantified by $Sq^2/\epsilon$) in the flow upstream of the shock wave. As discussed before, $\beta_0 = 2.5$ seems appropriate for shear flows in equilibrium. Higher values of $\beta_0$ may be chosen for strongly sheared flows. The variable $\rho/\rho_0$ in the above expression is the total amount of compression the shear flow experiences. It is equated to the density ratio across the shock wave which the Rankine-Hugoniot equations relate to the shock-normal Mach number, $M_n$. *i.e.*,

$$\frac{\rho}{\rho_0} = \frac{(\gamma+1)M_n^2}{2+(\gamma-1)M_n^2}. \tag{2.21}$$

Thus, once the strength and inclination angle of the shock wave is known, its effect on the shear flow can be predicted.

Consider the following two examples: the interaction of a shear flow with a Mach 1.5 normal shock and shock/turbulence interaction in a compression corner with free-stream Mach number 2.9 and wedge angle 8°. The compression corner corresponds to an experiment by Smits and Muck (1987).

The evolution of $R_{ij}$ and $R_{ij}/q^2$ is predicted for both cases. The incident turbulence is assumed to be in equilibrium and hence $\beta_0$ was taken as 2.5. For the

normal shock problem, it is clear that $M_n$ and $\theta$ are 1.5 and 0° respectively. In the case of the compression corner, these parameters are obtained by assuming that the flow is turned across a single shock wave. Solution of the corresponding oblique shock equations yields $M_n = 1.29$ and $\theta = 63.65°$. Another point to be noted is that the coordinate system in our analysis was aligned with the direction of mean shear. However experimental coordinate systems are aligned with the local wall direction. As a result, the compression corner problem requires that the Reynolds stresses predicted by our analysis be rotated by the wedge angle to be consistent with experiments. The results are tabulated below.

| | $R_{11}$ | $R_{22}$ | $R_{33}$ | $R_{11}/q^2$ | $R_{22}/q^2$ | $R_{33}/q^2$ | $R_{12}/q^2$ |
|---|---|---|---|---|---|---|---|
| Normal | 2.60 | 1.30 | 1.60 | 0.64 | 0.08 | 0.28 | -0.07 |
| Oblique | 1.05 | 2.22 | 1.40 | 0.40 | 0.22 | 0.38 | -0.21 |

TABLE 2.1: The Reynolds stresses as predicted by RDT for two representative cases of shock/turbulence interaction.

The complexity of the flow in a compression-corner prevents quantitative comparison between the analysis and the experimental flow. Comparison (Mahesh, Lele and Moin, 1993) shows qualitative agreement, thereby underscoring the importance of upstream anisotropy and shock wave obliquity in compression-corner flow.

## 2.6 Application to Reynolds Stress modeling

The analysis described in the preceding sections reveals significant effects of anisotropy on the response of shear flows to compression. The spectral distribution of energy prior to compression is seen to strongly influence the Reynolds stresses through the pressure-strain correlation. In this section, we consider Reynolds stress modeling of the normal compression problem to see if the model equations reproduce the evolution as predicted by RDT. Since the pressure-strain correlation is the only term that needs to be modelled, the RDT limit is a natural choice to evaluate models for the rapid pressure-strain correlation.

We evaluate models of the form, $\pi_{ij} = \pi_{ij}(b_{ij}, S^*_{ij}, \Omega_{ij})$ where $b_{ij}$ denotes the Reynolds stress anisotropy tensor, $S^*_{ij}$ denotes the deviatoric part of the mean strain rate tensor and $\Omega_{ij}$ denotes the mean rotation rate tensor. Linear, quadratic and cubic forms of these models exist. We only consider two representative versions of these models.

### 2.6.1 Launder, Reece, Rodi (LRR) model

Consider the model,

$$\pi_{ij} = q^2\left[\frac{2}{5}S^*_{ij} + C_2\left(S^*_{il}b_{lj} + S^*_{jl}b_{li} - \frac{2}{3}S^*_{lm}b_{ml}\delta_{ij}\right) + C_3\left(\Omega_{il}b_{lj} + \Omega_{jl}b_{il}\right)\right]. \quad (2.22)$$

The models of several workers; *e.g.* Launder, Reece and Rodi (1975) and Naot, Shavit and Wolfshtein (1970) are of the above form, differing only in the constants $C_2$ and $C_3$.

During simultaneous shear and compression (Section 2.3.1), $S^*_{ij}$ and $\Omega_{ij}$ are given by,

$$S^*_{ij} = \frac{\Gamma_0}{1+\Gamma_0 t'}\begin{pmatrix} \frac{2}{3} & \frac{1}{2}\frac{S_0}{\Gamma_0} & 0 \\ \frac{1}{2}\frac{S_0}{\Gamma_0} & -\frac{1}{3} & 0 \\ 0 & 0 & -\frac{1}{3} \end{pmatrix}, \quad \Omega_{ij} = \frac{\Gamma_0}{1+\Gamma_0 t'}\begin{pmatrix} 0 & \frac{1}{2}\frac{S_0}{\Gamma_0} & 0 \\ -\frac{1}{2}\frac{S_0}{\Gamma_0} & 0 & 0 \\ 0 & 0 & 0 \end{pmatrix} \quad (2.23)$$

where $t' = t - t_0$. In the limit $S_0/\Gamma_0 \ll 1$,

$$S^*_{ij} = \frac{\Gamma_0}{1+\Gamma_0 t'}\begin{pmatrix} \frac{2}{3} & 0 & 0 \\ 0 & -\frac{1}{3} & 0 \\ 0 & 0 & -\frac{1}{3} \end{pmatrix}, \quad \Omega_{ij} = 0. \quad (2.24)$$

We consider the evolution of $R_{11}$ and $R_{12}$. Substitution of $S^*_{ij}$ and $\Omega_{ij}$ into equation (2.22) yields,

$$\pi_{11} = \frac{2}{3}q^2\,\frac{\Gamma_0}{1+\Gamma_0 t'}\left[\frac{2}{5} + C_2 b_{11}\right]. \quad (2.25)$$

Note that the trace-free property of $b_{ij}$ is used to obtain the above expression. Also,

$$\pi_{12} = \frac{1}{3}q^2\,\frac{\Gamma_0}{1+\Gamma_0 t'}\,C_2 b_{12}. \quad (2.26)$$

The modeled equations may be solved analytically in the RDT limit to obtain the Reynolds stresses. Consider,

$$\frac{\mathrm{d}R_{11}}{\mathrm{d}t'} = -2\,\frac{\Gamma_0}{1+\Gamma_0 t'}\,R_{11} + \pi_{11}, \quad (2.27a)$$

$$\frac{\mathrm{d}q^2}{\mathrm{d}t'} = -2\,\frac{\Gamma_0}{1+\Gamma_0 t'}\,R_{11}. \quad (2.27b)$$

Defining a variable $f = R_{11}/q^2 = b_{11} + 1/3$, the above equations may be manipulated to obtain,

$$\frac{\mathrm{d}f}{\mathrm{d}t'} = 2\,\frac{\Gamma_0}{1+\Gamma_0 t'}\,(f^2 - f) + \frac{\pi_{11}}{q^2}. \quad (2.28)$$

Substituting for $\pi_{11}/q^2$,

$$\frac{\mathrm{d}f}{\mathrm{d}t'} = 2\,\frac{\Gamma_0}{1+\Gamma_0 t'}\left[f^2 + f\left(\frac{C_2}{3}-1\right) + \frac{1}{3}\left(\frac{2}{5}-\frac{C_2}{3}\right)\right]. \tag{2.29}$$

Denoting $f$ at $t'=0$ by $f_0$, the above equation may be integrated to yield

$$f = \frac{r_1 - \alpha r_2}{1-\alpha} \tag{2.30}$$

where, $\alpha$ is defined as

$$\alpha = \frac{f_0 - r_1}{f_0 - r_2}\,(1+\Gamma_0 t')^{2(r_1-r_2)}. \tag{2.31}$$

$r_1$ and $r_2$ are the roots of $f^2 + f\left(\frac{C_2}{3}-1\right) + \frac{1}{3}\left(\frac{2}{5}-\frac{C_2}{3}\right) = 0$ and are given by,

$$r_{1,2} = \frac{1}{2}\left[-\left(\frac{C_2}{3}-1\right) \pm \sqrt{\left(\frac{C_2}{3}-1\right)^2 - \frac{4}{3}\left(\frac{2}{5}-\frac{C_2}{3}\right)}\;\right]. \tag{2.32}$$

Once $f$ is known, $q^2$ may be calculated as follows. We rewrite equation (2.27*b*) as,

$$\frac{dq^2}{dt'} = -2\,\frac{\Gamma_0}{1+\Gamma_0 t'}\,fq^2. \tag{2.33}$$

Substituting for $f$ and integrating, we get,

$$\frac{q^2}{q_0^2} = \frac{1-\alpha}{1-\alpha_0}\left(\frac{\alpha_0}{\alpha}\right)^{\frac{r_1}{r_1-r_2}} \tag{2.34}$$

where, the subscript '0' corresponds to time $t'=0$. Note that $\alpha$ may be expressed in terms of the total volumetric strain ; *i.e.*,

$$\alpha = \frac{f_0 - r_1}{f_0 - r_2}\left(\frac{\rho}{\rho_0}\right)^{-2(r_1-r_2)}. \tag{2.35}$$

We next compare the predicted values of $R_{11}$ and $q^2$ with the RDT evolution. Our choice of $C_2$ in the above equations is dictated by the asymptotic behavior of the model solution. Equations (2.32) and (2.35) show that in the limit of infinite volumetric strain, $\alpha \to \infty$ and hence $f \to r_2$. Since $r_2$ depends only upon $C_2$, this suggests that the asymptotic value of $R_{11}/q^2$ as predicted by the model is independent of the initial anisotropy. This behavior is in agreement with RDT.

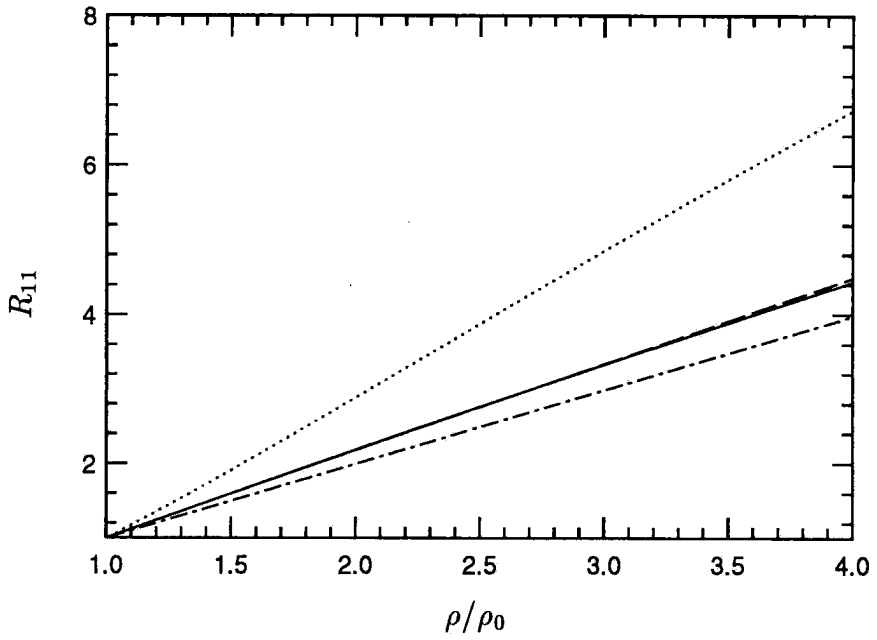


FIGURE 2.18: Comparison of model solution to RDT prediction of $R_{11}$. —— (Isotropic; RDT), - - - - (Isotropic; model), ····· (Sheared; RDT), —·— (Sheared; model).

This independence of $R_{11}/q^2$ of the initial condition allows the asymptotic values to be determined from the compression of isotropic turbulence. It can be shown (Lee, 1989) that $R_{11}/q^2$ asymptotes to 1/2. Equating $r_2$ to 1/2 and solving the resulting equation for $C_2$, we get

$$C_2 = \frac{21}{10}. \tag{2.36}$$

Figure 2.18 compares the predicted evolution of $R_{11}$ to the RDT solution. The compression of isotropic turbulence ($\beta_0 = 0$) and sheared turbulence ($\beta_0 = 2.5$) are both plotted. Note that the model predicts $R_{11}$ quite well when the initial state is isotropic. However, the amplification of $R_{11}$ in the shear flow is considerably underpredicted. Similar behavior is observed in figure 2.19, where the evolution of $q^2$ is plotted. The evolution of isotropic turbulence is predicted well while the amplification of kinetic energy in the shear flow is underpredicted. This behavior of the model solution is attributed to the lack of spectral information which prevents it from reproducing the suppression of $\pi_{11}$ in the shear flow.

Similarly, the model is unable to reproduce the drop and change in sign of Reynolds shear stress. This is shown as follows. The evolution of $R_{12}$ is given by

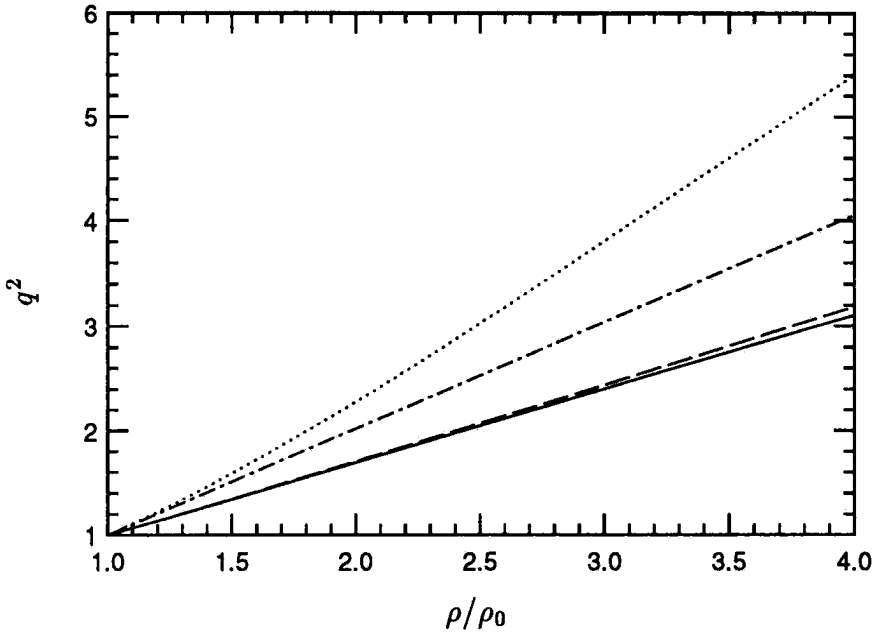


FIGURE 2.19: Comparison of model solution to RDT prediction of $q^2$. ——— (Isotropic; RDT), - - - - (Isotropic; model), ····· (Sheared; RDT), —·— (Sheared; model).

equation (2.13) as

$$\frac{\mathrm{d}}{\mathrm{d}t'}R_{12} = \frac{\Gamma_0}{1+\Gamma_0 t'}\left[-R_{12} - \frac{S_0}{\Gamma_0}R_{22}\right] + \pi_{12}. \tag{2.37}$$

Using the model expression for $\pi_{12}$ as given in equation (2.26) we get,

$$\frac{\mathrm{d}}{\mathrm{d}t'}R_{12} = \frac{\Gamma_0}{1+\Gamma_0 t'}\left[-R_{12} - \frac{S_0}{\Gamma_0}R_{22} + \frac{C_2}{3}R_{12}\right]. \tag{2.38}$$

In the limit $S_0/\Gamma_0 \ll 1$, this becomes,

$$\frac{\mathrm{d}}{\mathrm{d}t'}R_{12} = \frac{\Gamma_0}{1+\Gamma_0 t'}\left(\frac{C_2}{3} - 1\right)R_{12}. \tag{2.39}$$

Integration of the above equation yields'

$$R_{12} = R_{12}^0\,(1+\Gamma_0 t')^{C_2/3-1}. \tag{2.40}$$

Since $\Gamma_0$ is negative, the above equation predicts an *increase* in the Reynolds shear stress upon normal compression. Thus, presence of spectral information seems to be particularly important in predicting the evolution of $R_{12}$.

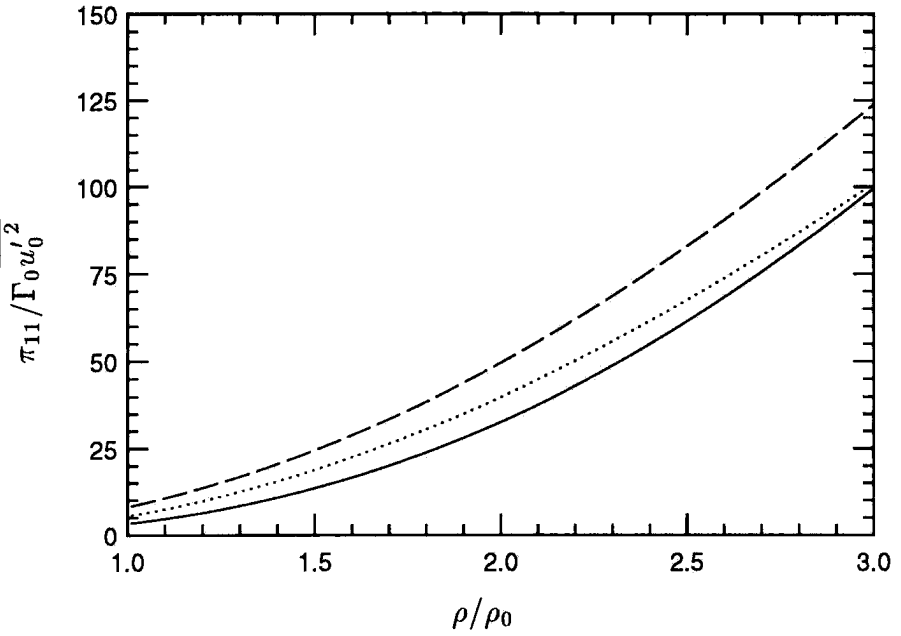


FIGURE 2.20: Comparison of model prediction of $\pi_{11}$ to RDT prediction in the normal compression of a shear flow ($\beta_0 = 3$). —— (RDT), - - - - (LRR), ····· (SSG).

## 2.6.2 Speziale, Sarkar, Gatski (SSG) model

The more recent model developed by Speziale, Sarkar and Gatski (1991) is evaluated in this section. Unlike the LRR model, where the solution to the Reynolds stress equations was analytically obtained, we only conduct an *a priori* evaluation of the SSG model; *i.e.*, we test the ability of the model to predict the pressure strain correlation, given the RDT values for the Reynolds stresses. The rapid pressure strain correlation according to the SSG model is given by the expression,

$$\pi_{ij} = -C_1^* P b_{ij} + (C_3 - C_3^* II_b^{1/2})\frac{q^2}{2}S_{ij}^* + C_4\frac{q^2}{2}\left(b_{ik}S_{jk}^* + b_{jk}S_{ik}^* - \frac{2}{3}b_{kl}S_{kl}^*\delta_{ij}\right) + C_5\frac{q^2}{2}(b_{ik}\Omega_{jk} + b_{jk}\Omega_{ik}) \tag{2.41}$$

where $P = -\overline{u_i'u_j'}\partial U_i/\partial x_j$ is the turbulence production, $II_b = b_{ij}b_{ij}$ and the constants,

$$C_1^* = 1.8, \quad C_3 = 0.8, \quad C_3^*1.3, \quad C_4 = 1.25, \quad C_5 = 0.4. \tag{2.42}$$

In the limit $S_0/\Gamma_0 \ll 1$, the production

$$P = -\frac{\Gamma_0}{1+\Gamma_0 t'}R_{11}. \tag{2.43}$$

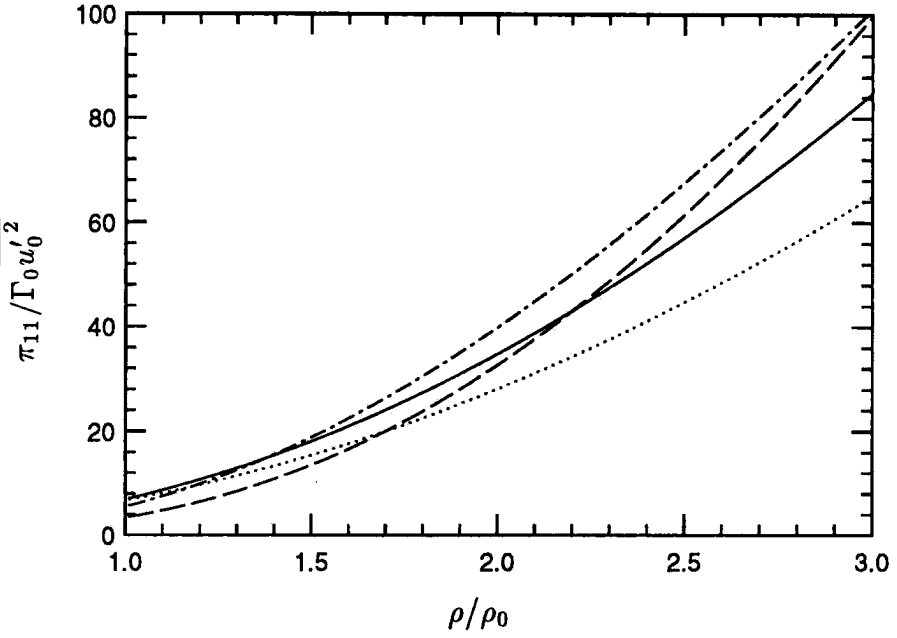


FIGURE 2.21: Comparison of the SSG model prediction of $\pi_{11}$ to RDT in the normal compression of isotropic turbulence and shear flow ($\beta_0 = 3$). —— (RDT:Isotropic), ---- (RDT:Sheared), ····· (SSG:Isotropic), —·— (SSG: Sheared).

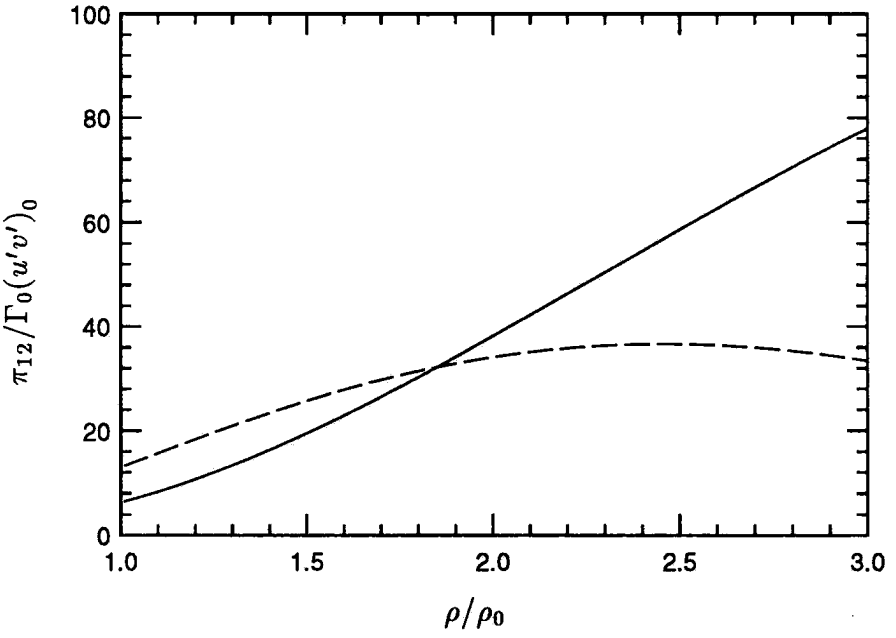


FIGURE 2.22: Comparison of SSG model prediction of $\pi_{12}$ to RDT prediction in the normal compression of a shear flow ($\beta_0 = 3$). —— (RDT), ---- (SSG).

Using equation 2.24 to obtain $S_{ij}^*$, this yields the following expression for $\pi_{11}$ according to the SSG model.

$$\pi_{11} = \frac{\Gamma_0}{1+\Gamma_0 t'}\left[C_1^* R_{11} b_{11} + (C_3 - C_3^* I I_b^{1/2})\frac{q^2}{3} + C_4 \frac{q^2}{3} b_{11}\right]. \qquad (2.44)$$

Figure 2.20 compares the prediction of $\pi_{11}$ of the SSG and LRR models with the RDT solution for the case where the shear flow ($\beta_0 = 3$) is subjected to normal compression. The SSG model is seen to be closer to the RDT solution. The ability of the model to predict the suppressed level of $\pi_{11}$ in the shear flow is evaluated in figure 2.21. Interestingly, the SSG model does predict an initial suppression of $\pi_{11}$ in compression of the shear flow. However, the extent of suppression is smaller than the RDT solution. By contrast, the LRR model predicts a higher value of $\pi_{11}$ in the shear flow (equation 2.25).

The ability of the model to predict the shear stress evolution is next evaluated. $\pi_{12}$ according to the SSG model is given by,

$$\pi_{12} = \frac{\Gamma_0}{1+\Gamma_0 t'}\left[C_1^* R_{11} + C_4 \frac{q^2}{6}\right] b_{12}. \qquad (2.45)$$

The model prediction of $\pi_{12}$ is compared to the RDT value in figure 2.22. Significant deviation is observed beyond a total volumetric strain of about 2. Thus, it appears that while the SSG model is an improvement over the LRR model, the absence of spectral information still hinders its ability to predict the response of the shear flow to normal compression.

## 2.7. Summary

Homogeneous rapid distortion theory was used to examine the response of sheared turbulence to rapid one-dimensional compression. Both normal and oblique compressions (with respect to the shear) were considered. The response of shear flows to compression was found to be quite different from the previously studied, compression of isotropic turbulence. The differences were interpreted in a more general framework and the relevant parameters influencing kinetic energy amplification were identified.

$E_{11}(\kappa_1)$ of the initial field was found to determine the evolution of the streamwise (the direction of compression) component of kinetic energy. Flows with $u_1'$ at

lower $\kappa_1$ have a reduced effect of pressure during compression and hence a higher amplification of $u_1'$. The evolution of $q^2$ upon compression is influenced by the initial fraction of kinetic energy in the direction of compression ($\overline{u_1'^2}/q^2$), in addition to the initial $E_{11}(\kappa_1)$. Flows with a larger value of initial $\overline{u_1'^2}/q^2$ and $u_1'$ at lower $\kappa_1$ have a larger amplification of $q^2$.

Upon normal compression, all components of turbulent kinetic energy of shear flow are amplified with the streamwise component being amplified the most. The amplification of $\overline{u_1'^2}$ and $q^2$ is higher than that in isotropic turbulence. Normal compression decreases the turbulent shear stress and for large enough compressions changes its sign. Examination of the terms in the shear stress evolution equation showed that amplification of the pressure-strain correlation upon compression is responsible for this behavior.

The oblique angle between the directions of shear and compression was seen to affect the response of sheared turbulence to compression significantly. The effect of angle of obliquity on the evolution of kinetic energy may be explained by the initial distribution of $E_{\theta\theta}(\kappa_\theta)$ and $\overline{u_\theta'^2}/q^2$, where $\theta$ is the direction of compression. Over a range of obliquity angles varying from $-60°$ to $60°$, the amplification of $\overline{u_1'^2}$ and $q^2$ was seen to decrease with increasing magnitude of oblique angle. Also oblique compression reduces the tendency of the shear stress to decrease in magnitude; for large oblique angles, the shear stress is amplified.

With respect to shock/turbulence interaction, our results suggest that, besides shock strength (defined in terms of the normal Mach number), the anisotropy of the turbulence and the shock inclination angle are important parameters in determining the evolution of turbulence across the shock. It is striking that the evolution of the Reynolds stresses upon oblique compression is qualitatively different for different oblique angles. These important effects of initial anisotropy and the shock inclination angle should be accounted for in the modeling of shock/turbulence interaction.

# Chapter Three

# The Influence of Entropy Fluctuations on Shock / Turbulence Interaction

## 3.1 Introduction

The preceding chapter identified the anisotropy of the incident turbulence to be an important element in shock/turbulence interaction. Recall that the analysis that was performed constrained the turbulence to be homogeneous and solenoidal. As mentioned in Chapter 1, turbulent fluctuations in a compressible medium have acoustic and entropy fluctuations in addition to vortical fluctuations. The influence that these modes exert on the interaction of the turbulence with a shock wave is therefore of interest.

Morkovin (1961) hypothesized that the turbulent fluctuations in compressible boundary layers are essentially composed of vorticity and entropy modes; *i.e.* the acoustic mode is negligible. This hypothesis along with the assumption of negligible fluctuations in stagnation temperature leads to the following relation between the thermodynamic and velocity field,

$$\frac{\rho'}{\overline{\rho}} = -\frac{T'}{\overline{T}} = (\gamma - 1)M^2 \frac{u'}{U}. \tag{3.1}$$

A considerable body of experimental evidence supports the above hypothesis. In fact, Bradshaw (1977) states 'There is little point in taking turbulence measurements in constant pressure boundary layers at $M_\infty < 5$ to check Morkovin's hypothesis, except possibly for intermittency measurements'.

Morkovin's hypothesis suggests that in addition to being correlated, the intensity of vorticity and entropy fluctuations in a turbulent boundary layer are of comparable magnitude. In this chapter, we seek to identify the quantitative influence that entropy fluctuations exert on the evolution of a turbulent flow across a shock wave. We use inviscid linear analysis to study the combined interaction of vorticity and entropy fluctuations with a shock wave. We have in addition, conducted direct numerical simulation of the interaction of a shock wave with an isotropic turbulent field of vorticity and entropy fluctuations: details of the simulations are discussed

in Appendix D. Also, the influence of upstream acoustic waves on shock/turbulence interaction is studied separately in Appendix B.

As discussed in Chapter 1, Ribner (1953, 1954, 1969, 1987) has examined in detail the interaction of a field of vortical fluctuations with a shock wave. The study of the influence of entropy fluctuations on shock/turbulence interaction seems to have been restricted to the analysis of plane entropy waves interacting with a shock (Morkovin; 1960, Chang; 1957, Cuadra; 1968). Apparently, the interaction of a field of entropy fluctuations with a shock wave has not been considered before. Nor has the effect of the correlation between vorticity and entropy fluctuations been emphasized.

This chapter is organized as follows. The simultaneous interaction of a shock wave with a vorticity and entropy wave (henceforth referred to as vorticity-entropy wave) is formulated in Section 3.2. Results of the interaction are presented in Section 3.3. The analysis is compared to numerical simulation in Section 3.4. Sections 3.5 and 3.6 provide an explanation for the influence of entropy fluctuations and suggest a scaling for the evolution of vorticity across the shock. The analysis is extended in Section 3.7 to consider the evolution of an isotropic field of vorticity-entropy waves across a shock wave. Section 3.8 discusses the results. The chapter is concluded with a summary of the important conclusions in Section 3.9. Some of the work in this chapter is discussed by Mahesh, Lele and Moin (1996).

## 3.2 The interaction of a vorticity-entropy wave with a shock wave

### 3.2.1 The three modes in a compressible medium

Kovasznay (1953) showed that fluctuations of small amplitude in a compressible medium could be decomposed into vorticity, acoustic and entropy modes. These modes were shown to evolve independently in the inviscid limit for uniform mean flow. The vorticity mode as defined by Kovasznay has no pressure or density fluctuations. It has a solenoidal velocity field that is convected by the mean flow. The acoustic mode travels at the speed of sound relative to the mean flow, has isentropic pressure and density fluctuations and a corresponding irrotational velocity field that satisfies the acoustic wave equation. The entropy mode is convected by the mean flow and has no velocity or pressure fluctuations; it has only density and temperature fluctuations.

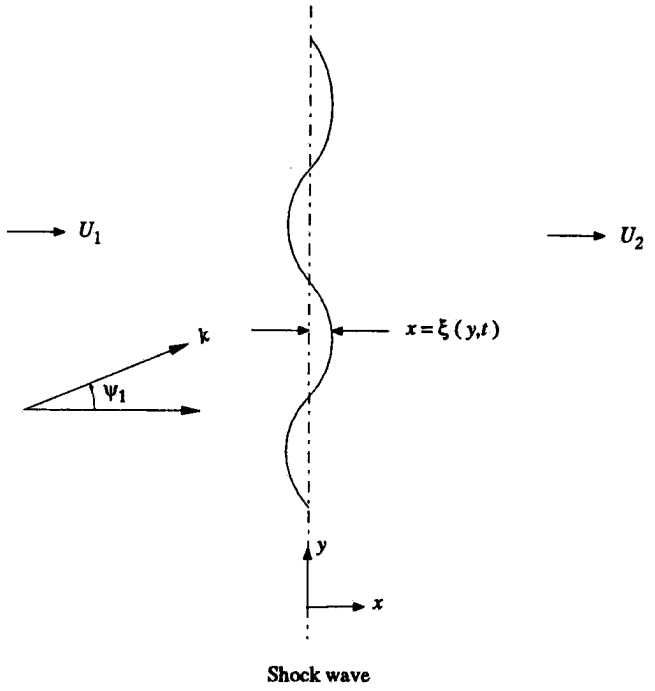


FIGURE 3.1: Schematic of the interaction of a vorticity-entropy wave with a shock wave.

The independent evolution of these modes in the inviscid limit implies that the fluctuating velocity field is a linear superposition of acoustic and vortical modes. Similarly, the density and temperature fields are superpositions of acoustic and entropic components. The pressure field is associated solely with the acoustic mode.

## 3.2.2 Formulation of the problem

The two-dimensional interaction of a shock wave with a plane vorticity-entropy wave is schematically illustrated in figure 3.1. The two-dimensional problem will be extended to describe the interaction of the shock with a three-dimensional field of turbulence in Section 3.7. Note that the shock wave is stationary in the mean. The variables $U, \overline{p}, \overline{\rho}, \overline{T}$ and $M$ denote the mean velocity, pressure, density, temperature and Mach number respectively and subscripts 1 and 2 denote the upstream and downstream states. The flow upstream of the shock wave is perturbed by the weak disturbance field of the incident vorticity-entropy wave which is assumed to be a plane wave that makes angle $\psi_1$ with the $x$ axis. The variables $u', v', p', \rho'$ and $T'$ represent the fluctuating velocities, pressure, density and temperature. The incident

field has the following form:

$$\frac{u_1'}{U_1} = lA_v \; e^{ik(mx+ly-U_1 mt)} \tag{3.2a}$$

$$\frac{v_1'}{U_1} = -mA_v \; e^{ik(mx+ly-U_1 mt)} \tag{3.2b}$$

$$\frac{\rho_1'}{\overline{\rho}_1} = A_e \; e^{ik(mx+ly-U_1 mt)} \tag{3.2c}$$

$$\frac{T_1'}{\overline{T}_1} = -\frac{\rho_1'}{\overline{\rho}_1} \tag{3.2d}$$

$$p_1' = 0 \tag{3.2e}$$

where the variables $m = \cos\psi_1$ and $l = \sin\psi_1$. The shock wave deforms in response to the incident disturbance; the displacement is denoted by $x = \xi(y,t)$. The analysis involves solution of a boundary-value problem for the shock displacement and the flow field behind the shock wave. The governing equations behind the shock wave are the Euler equations that are linearized about the uniform flow behind the shock. *i.e.*,

$$\rho_t' + U\ \rho_x' = -\overline{\rho}\ (u_x' + v_y') \tag{3.3a}$$

$$u_t' + U\ u_x' = -\frac{1}{\overline{\rho}}\ p_x' \tag{3.3b}$$

$$v_t' + U\ v_x' = -\frac{1}{\overline{\rho}}\ p_y' \tag{3.3c}$$

$$s_t' + U\ s_x' = 0. \tag{3.3d}$$

Also,

$$\frac{p'}{\overline{p}} = \frac{\rho'}{\overline{\rho}} + \frac{T'}{\overline{T}} \quad \text{and} \quad \frac{s'}{c_p} = \frac{p'}{\gamma\overline{p}} - \frac{\rho'}{\overline{\rho}}. \tag{3.3e}$$

The variables $s'$ and $c_p$ in the above equations represent entropy fluctuations and the specific heat at constant pressure respectively.

The above equations are solved on the domain $x \geq 0$ subject to boundary conditions imposed at $x = 0$ (the mean position of the shock wave). The boundary conditions are obtained by linearizing the Rankine-Hugoniot equations in a frame of reference that moves at the instantaneous speed of the shock wave. This yields the following equations that describe the flow field immediately behind the shock

wave; *i.e.* at $x = 0$,

$$\frac{u_2' - \xi_t}{U_1} = \frac{(\gamma-1)M_1^2 - 2}{(\gamma+1)M_1^2}\left(\frac{u_1' - \xi_t}{U_1}\right) + \frac{2}{(\gamma+1)M_1^2}\left(\frac{T_1'}{\overline{T}_1}\right) \tag{3.4a}$$

$$\frac{v_2'}{U_1} = \frac{v_1'}{U_1} + \frac{2(M_1^2-1)}{(\gamma+1)M_1^2}\,\xi_y \tag{3.4b}$$

$$\frac{\rho_2'}{\overline{\rho}_2} = \frac{4}{(\gamma-1)M_1^2+2}\left(\frac{u_1' - \xi_t}{U_1}\right) - \frac{(\gamma-1)M_1^2+4}{(\gamma-1)M_1^2+2}\left(\frac{T_1'}{\overline{T}_1}\right) \tag{3.4c}$$

$$\frac{p_2'}{\overline{p}_2} = \frac{4\gamma M_1^2}{2\gamma M_1^2 - (\gamma-1)}\left(\frac{u_1' - \xi_t}{U_1}\right) - \frac{2\gamma M_1^2}{2\gamma M_1^2 - (\gamma-1)}\left(\frac{T_1'}{\overline{T}_1}\right). \tag{3.4d}$$

The governing equations and boundary conditions suggest that the solution could be obtained by superposing the solutions to the interaction of the shock with a vorticity (Ribner, 1953) and entropy wave (Chang, 1957) independently. It is simpler however, to directly solve the combined problem. The independent interaction of the shock with vorticity and entropy waves become special cases of our analysis and will be used as baseline cases for comparison. Our solution in these limiting cases is of course identical to that of the above workers.

### 3.2.3 The two regimes behind the shock wave

The solution to equations (3.3) has two different regimes that differ in the nature of the pressure field. The incidence angle of the disturbance and the Mach number of the shock wave determine the regime that the solution lies in. The two regimes are demarcated by a critical angle of incidence that we denote as $\psi_c$. If $0 < \psi_1 < \psi_c$, the pressure field behind the shock wave (and hence its associated velocity and thermodynamic field) is a plane wave. If however, $\psi_c < \psi_1 < \pi/2$, the pressure field behind the shock wave corresponds to an evanescent wave and decays exponentially. The vorticity and entropy fields behind the shock wave correspond to plane waves over both regimes.

The existence of the two regimes is illustrated as follows. The pressure field behind the shock wave satisfies the wave equation; *i.e.*,

$$p_{tt}' + 2U_2\, p_{xt}' - (a_2^2 - U_2^2)\, p_{xx}' - a_2^2\, p_{yy}' = 0. \tag{3.5}$$

Continuity at the shock wave requires that the solution behind the shock wave have the same transverse wave number and frequency as the incident disturbance. The pressure may therefore be expressed as ,

$$p' = F(x)\, e^{ik(ly - mU_1 t)}. \tag{3.6}$$

Substituting the above expression for pressure into equation (3.5) yields the following equation for $F$.

$$\left[\frac{a_2^2}{U_1^2} - \frac{U_2^2}{U_1^2}\right] F'' + i\ 2km\frac{U_2}{U_1}\ F' + k^2\left[m^2 - l^2\frac{a_2^2}{U_1^2}\right] F = 0. \tag{3.7}$$

Assume that the pressure field is a plane wave; *i.e.* $F \sim e^{i\widetilde{k}x}$. Substitution into equation (3.7) yields the following equation for $\widetilde{k}$.

$$\left[\frac{a_2^2}{U_1^2} - \frac{U_2^2}{U_1^2}\right] \widetilde{k}^2 + 2km\frac{U_2}{U_1}\ \widetilde{k} - k^2\left[m^2 - l^2\frac{a_2^2}{U_1^2}\right] = 0. \tag{3.8}$$

The discriminant of the above quadratic equation determines if $\widetilde{k}$ is real or imaginary. A real valued $\widetilde{k}$ would ensure that the pressure field is indeed a plane wave. The discriminant is given by,

$$\begin{aligned} \text{Discriminant} &= 2k\sqrt{m^2\frac{a_2^2}{U_1^2} - l^2\frac{a_2^2}{U_1^2}\left(\frac{a_2^2}{U_1^2} - \frac{U_2^2}{U_1^2}\right)} \\ &= 2kl\frac{a_2}{U_1}\sqrt{\frac{m^2}{l^2} - \left(\frac{a_2^2}{U_1^2} - \frac{U_2^2}{U_1^2}\right)}. \end{aligned} \tag{3.9}$$

Recall that $m = \cos\ \psi_1$ and $l = \sin\ \psi_1$. The requirement for real $\widetilde{k}$ is therefore,

$$\cot^2\ \psi_1 > \left(\frac{a_2^2}{U_1^2} - \frac{U_2^2}{U_1^2}\right). \tag{3.10}$$

*i.e.*, $0 < \psi_1 < \psi_c$ where $\psi_c$ is a root of,

$$\cot^2\ \psi_c = \left(\frac{a_2^2}{U_1^2} - \frac{U_2^2}{U_1^2}\right). \tag{3.11}$$

Note that $\psi_c$ is a function of the Mach number of the shock wave. If the incidence angle exceeds $\psi_c$, $\widetilde{k}$ becomes imaginary. Denoting the real and imaginary parts of $\widetilde{k}$ by $\widetilde{k}_r$ and and $\widetilde{k}_i$ respectively, the function $F$ is now given by,

$$F \sim e^{-\widetilde{k}_i x}\ e^{i\widetilde{k}_r x}. \tag{3.12}$$

*i.e.* the pressure field decays exponentially behind the shock wave.

The existence of two regimes of the pressure field is a common feature of problems involving acoustic wave propagation. Classical examples include the scattering

of sound by a vortex sheet and the propagation of sound generated by a flexural wall.

### 3.2.4 The solution behind the shock wave

The functional form of the solution behind the shock wave is derived in this section. Recall that the preceding section had outlined the two regimes of the solution. The arguments of the vorticity, entropy and acoustic modes over both regimes are derived below.

It was noted that the vorticity and entropy fluctuations were plane waves over both regimes. Since vorticity and entropy fluctuations are both convected by the mean flow, they are of the same form which is given by:

$$e^{i\overline{k}x}e^{ik(ly-mU_1t)}. \tag{3.13}$$

Note that the transverse wavenumber and frequency have been matched to that of the incident disturbance. The variable $\overline{k}$ is obtained as follows. Convection by the mean flow requires that the vorticity and entropy fluctuations have the following dispersion relation:

$$\omega = U_1 km = U_2\overline{k}.$$

*i.e.*,

$$\overline{k} = km\frac{U_1}{U_2} = kmr. \tag{3.14}$$

The vorticity and entropy fields are therefore of the form:

$$e^{ik(mrx+ly-mU_1t)}. \tag{3.15}$$

The form of the pressure field was derived in the previous section. However, explicit expressions were not derived for the variables $\widetilde{k}, \widetilde{k}_i$ and $\widetilde{k}_r$. Evaluation of these variables would completely determine the functional form of the pressure field. Recall that $\widetilde{k}$ was defined as the root of equation (3.8); *i.e*,

$$\widetilde{k} = \frac{-2km\frac{U_2}{U_1} + 2kl\frac{a_2}{U_1}\sqrt{\frac{m^2}{l^2} - \left(\frac{a_2^2}{U_1^2} - \frac{U_2^2}{U_1^2}\right)}}{2\left(\frac{a_2^2}{U_1^2} - \frac{U_2^2}{U_1^2}\right)}. \tag{3.16}$$

The other root is rejected on the grounds that it leads to a physically unacceptable solution that grows exponentially behind the shock wave. This yields,

$$\frac{\widetilde{k}}{k} = \frac{-m\frac{U_2}{U_1} + l\frac{a_2}{U_1}\sqrt{\frac{m^2}{l^2} - \left(\frac{a_2^2}{U_1^2} - \frac{U_2^2}{U_1^2}\right)}}{\left(\frac{a_2^2}{U_1^2} - \frac{U_2^2}{U_1^2}\right)}$$

$$= \frac{U_1}{U_2}\frac{M_2}{1-M_2^2}\left[-mM_2 + l\sqrt{\frac{m^2}{l^2} - \frac{U_2^2}{U_1^2}\left(\frac{1}{M_2^2} - 1\right)}\right]. \tag{3.17}$$

The above expression is real only if $0 < \psi_1 < \psi_c$. If the angle of incidence exceeds $\psi_c$, $\widetilde{k}$ is complex. Equation 3.16 shows that the real and imaginary parts of $\widetilde{k}$ are given by:

$$\frac{\widetilde{k_r}}{k} = -m\frac{U_2}{U_1}\frac{1}{\left(\frac{a_2^2}{U_1^2} - \frac{U_2^2}{U_1^2}\right)} = -m\frac{U_1}{U_2}\frac{M_2^2}{1-M_2^2}. \tag{3.18}$$

$$\frac{\widetilde{k_i}}{k} = \frac{l\frac{a_2}{U_1}\sqrt{\left(\frac{a_2^2}{U_1^2} - \frac{U_2^2}{U_1^2}\right) - \frac{m^2}{l^2}}}{\left(\frac{a_2^2}{U_1^2} - \frac{U_2^2}{U_1^2}\right)} = l\frac{U_1}{U_2}\frac{M_2}{1-M_2^2}\sqrt{\frac{U_2^2}{U_1^2}\left(\frac{1}{M_2^2} - 1\right) - \frac{m^2}{l^2}}. \tag{3.19}$$

The argument of the vorticity, entropy and acoustic modes behind the shock wave are now completely determined over both regimes of the solution. Expressions for the velocity and thermodynamic field behind the shock wave follow and are given below.

$$\begin{aligned}
\frac{u_2'}{U_1} &= F\, e^{i\widetilde{k}x} e^{ik(ly - mU_1 t)} + G\, e^{ik(mrx + ly - mU_1 t)} \\
\frac{v_2'}{U_1} &= H\, e^{i\widetilde{k}x} e^{ik(ly - mU_1 t)} + I\, e^{ik(mrx + ly - mU_1 t)} \\
\frac{p_2'}{\overline{p}_2} &= K\, e^{i\widetilde{k}x} e^{ik(ly - mU_1 t)} \\
\frac{\rho_2'}{\overline{\rho}_2} &= \frac{K}{\gamma}\, e^{i\widetilde{k}x} e^{ik(ly - mU_1 t)} + Q\, e^{ik(mrx + ly - mU_1 t)} \\
\frac{T_2'}{\overline{T}_2} &= \frac{\gamma - 1}{\gamma} K\, e^{i\widetilde{k}x} e^{ik(ly - mU_1 t)} - Q\, e^{ik(mrx + ly - mU_1 t)}.
\end{aligned} \tag{3.20}$$

The boundary conditions across the shock wave yield the following expressions for the velocity and slope of the shock front:

$$\frac{\xi_t}{U_1} = L\, e^{ik\,(ly - mU_1 t)}; \quad \xi_y = -\frac{l}{m} L\, e^{ik\,(ly - mU_1 t)}. \tag{3.21}$$

The coefficients $F, H$ and $K$ in the above expressions are associated with the acoustic component. The vortical component is represented by $G$ and $I$. The variable $Q$ represents the entropy component.

The above expressions for the solution are next substituted into the governing equations behind the shock wave and the boundary conditions at the mean position of the shock front. Since the argument of the solution has been matched to that of the incident disturbance this yields a set of equations relating the coefficients. This system of equations is analytically solved thereby completing the solution. Details of this procedure are not particularly enlightening and are deferred to Appendix A. The coefficients thus obtained are functions of the mean upstream Mach number $M_1$, the incidence angle of the disturbance $\psi_1$ and the amplitude ratio $(A_r)$ and phase difference $(\phi_r)$ between the vorticity and entropy waves; *i.e.* $A_r e^{i\phi_r} = A_e/A_v$.

## 3.3 Results

Expressions are now derived to describe the streamwise evolution of statistics behind the shock wave. Consider for example the streamwise component of velocity. The kinetic energy associated with this component is denoted by $\overline{u_2'^2} = \overline{u_2' u_2'^*}$ where the overbar implies averaging over the transverse direction and time and the '*' denotes complex conjugate. The following expression is obtained for $\overline{u_2'^2}$ from Equation 3.20:

$$\frac{\overline{u_2'^2}}{U_1^2} = [\ |\widetilde{F}|^2\ e^{i(\widetilde{k}-\widetilde{k}^*)x} + |\widetilde{G}|^2 + \widetilde{F}\widetilde{G}^* e^{i(\widetilde{k}-kmr)x} + \widetilde{F}^*\widetilde{G} e^{-i(\widetilde{k}^*-kmr)x}\ ]\ |A_v|^2. \quad (3.22)$$

The spatial variation of $\overline{u_2'^2}$ is different over the two regimes. The wavenumber $\widetilde{k}$ is real over the propagating regime and hence

$$\frac{\overline{u_2'^2}}{U_1^2} = [\ |\widetilde{F}|^2 + |\widetilde{G}|^2 + 2(\widetilde{F}_r\widetilde{G}_r + \widetilde{F}_i\widetilde{G}_i)\cos(\widetilde{k}-kmr)x - 2(\widetilde{F}_i\widetilde{G}_r - \widetilde{F}_r\widetilde{G}_i)\sin(\widetilde{k}-kmr)x]\ |A_v|^2. \quad (3.23)$$

where the subscripts '$r$' and '$i$' denote the real and imaginary parts respectively. The kinetic energy thus has spatially uniform contributions from the vortical and acoustic components of the velocity field and an oscillating component whose argument is the phase difference between them. Similar expressions may be written for

quantities such as $\overline{v_2'^2}$, density and temperature in the propagating regime. Variables such as vorticity,dilatation and pressure that depend on only one component (see equation 3.20) are of course spatially uniform. *e.g.*,

$$\frac{\overline{p_2'^2}}{\overline{p}_2^2} = |\widetilde{K}|^2 \, |A_v|^2. \tag{3.24}$$

The evolution of $\overline{u_2'^2}$ over the decaying regime may be shown to be given by:

$$\frac{\overline{u_2'^2}}{U_1^2} = [\, e^{-2\widetilde{k}_i x}|\widetilde{F}|^2 + |\widetilde{G}|^2 + 2e^{-\widetilde{k}_i x}(\widetilde{F}_r\widetilde{G}_r + \widetilde{F}_i\widetilde{G}_i)\cos(\widetilde{k}_r - kmr)x - 2e^{-\widetilde{k}_i x}(\widetilde{F}_i\widetilde{G}_r - \widetilde{F}_r\widetilde{G}_i)\sin(\widetilde{k}_r - kmr)x] \, |A_v|^2 \tag{3.25}$$

The corresponding equation for pressure is:

$$\frac{\overline{p_2'^2}}{\overline{p}_2^2} = e^{-2\widetilde{k}_i x}|\widetilde{K}|^2 \, |A_v|^2. \tag{3.26}$$

The kinetic energy over this regime is seen to have a spatially uniform vortical component, an acoustic component that decays exponentially behind the shock wave and a damped oscillating component due to the correlation between the acoustic and vortical modes that the shock wave introduces. In describing the flow-field behind the shock wave, $x = 0$ is referred to as the 'near-field' and $x \to \infty$ is called the 'far-field'. We will see that the far-field values are attained over a distance comparable to the lengthscale of the incident disturbance. As a result, it is the far-field values that are of practical importance.

The analysis is now applied to the interaction of a vorticity-entropy wave with a Mach 1.5 shock wave. Incidence angles of 45° and 75° are considered so that behavior over both regimes is illustrated. (The critical angle is 61.36°). The objective here is to demonstrate the influence of entropy fluctuations and their correlation with the incident vorticity fluctuations. The interaction of the vorticity-entropy waves is therefore contrasted with the independent interaction of the shock with a vorticity wave and entropy wave at the same angle of incidence. These two limiting cases are referred to as the 'pure vorticity' and 'pure entropy' limits.

The normalization of the curves in the pure entropy limit deserves clarification. There is no incident velocity field in the pure entropy limit; *i.e.*, $q_1^2 = \overline{\omega_1'^2} = 0$. The

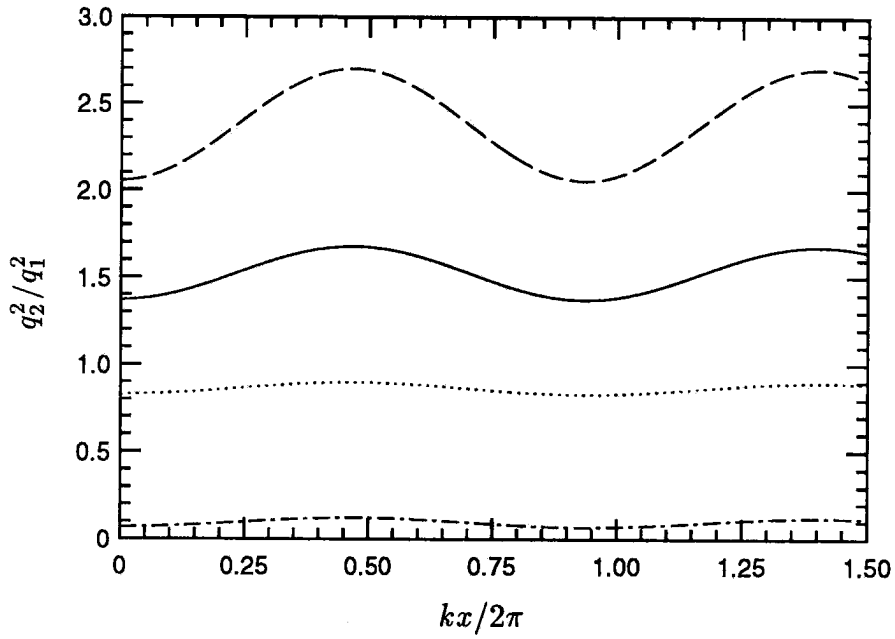


FIGURE 3.2: Evolution of $q^2$ behind the shock wave in the propagating regime. The incidence angle is 45° and the mean Mach number is 1.5. ——— (Pure vorticity), - - - - ($A_r = 1; \phi_r = 0$), ····· ($A_r = 1; \phi_r = 180°$), —·—·— (Pure entropy).

appropriate normalization in this limit is $(q_2^2/U_1^2)/(\overline{\rho_1'^2}/\overline{\rho}_1^2)$. We set the intensity $\rho_1'/\overline{\rho}_1$ in the pure entropy limit to equal its value in the vorticity-entropy wave; *i.e.*, $(\rho_1'/\overline{\rho}_1)_{\text{pure ent.}} = A_r(\sqrt{q_1^2}/U_1)_{\text{vort.-ent.}}$. This allows a consistent comparison between the pure entropy limit and the other curves.

Figure 3.2 shows the evolution of kinetic energy behind the shock wave over the propagating regime ($\psi_1 = 45°$). All three curves are normalized by the incident kinetic energy. The presence of entropy fluctuations is seen to significantly affect the amplification of kinetic energy across the shock wave. The evolution of $q^2$ is strongly affected by both the amplitude ratio and phase difference between the vorticity and entropy waves. Dependence upon the amplitude is monotonic. Entropy fluctuations that are in phase with the vorticity fluctuations ($u_1'$ and $T_1'$ are negatively correlated) enhance the amplification of kinetic energy. Suppression of amplification is observed when $u_1'$ and $T_1'$ are positively correlated. The pressure fluctuations behind the shock wave are similarly affected.

The decaying regime ($\psi_1 = 75°$) as shown in figure 3.3 displays similar influence of the entropy fluctuations. Both near-field and far-field levels of kinetic energy are

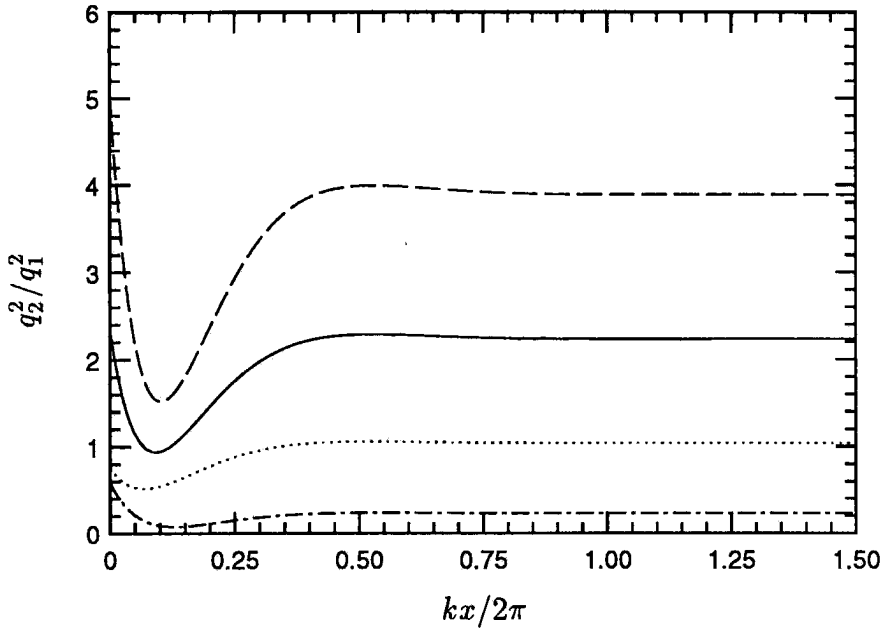


FIGURE 3.3: Evolution of $q^2$ behind the shock wave in the decaying regime. The incidence angle is 75° and the mean Mach number is 1.5. ——— (Pure vorticity), - - - - ($A_r = 1; \phi_r = 0$), ····· ($A_r = 1; \phi_r = 180°$), —·— (Pure entropy).

affected. The dependence upon amplitude ratio and phase difference is identical to that seen in the propagating regime. Also note that the curves asymptote to the far-field levels within a wavelength of the incident disturbance.

This influence of the entropy fluctuations is not limited to the two angles considered above; it extends over all angles of incidence. This is illustrated in figure 3.4 where the far-field levels of amplification of $q^2$ are plotted against the angle of incidence. The Mach number of the shock wave is 1.5. Note that the notion of far-field is introduced into the propagating regime by ignoring the oscillating component in Equation 3.25. Reason for this neglect is statistical cancellation of this component in the far-field for an incident turbulent field. Also shown in figure 3.5 is the amplification of vorticity across the shock wave. Negative correlation between $u'$ and $T'$ is clearly seen to increase the amplification while positive correlation suppresses it.

## 3.4. Comparison to numerical solution

The analysis makes the assumptions of linearity and inviscid flow. Its validity is therefore evaluated by comparison to numerical solution where nonlinear and

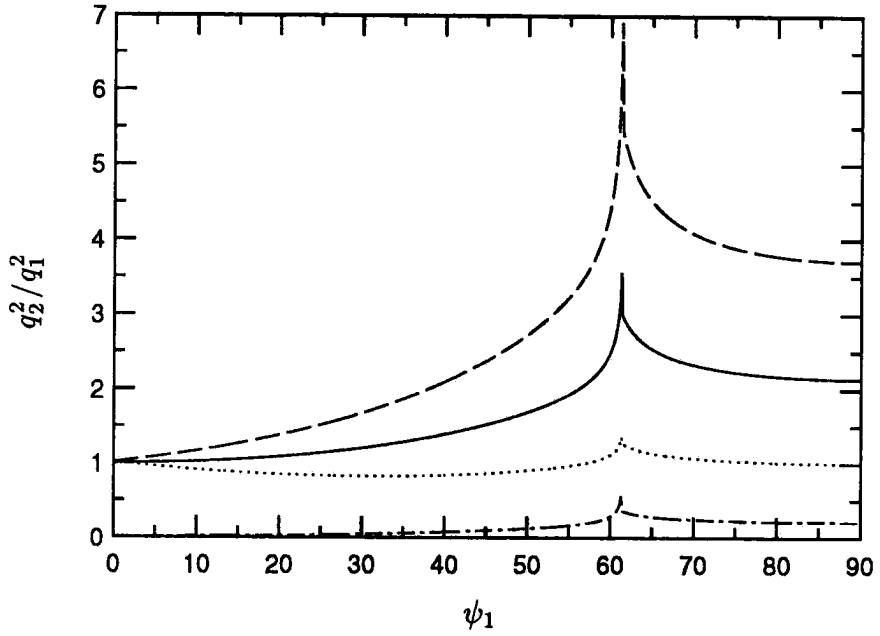


FIGURE 3.4: The amplification of kinetic energy across the shock wave as a function of the angle of incidence. Far-field kinetic energy levels are plotted and the mean Mach number is 1.5. ——— (Pure vorticity), ---- ($A_r = 1; \phi_r = 0$), ····· ($A_r = 1; \phi_r = 180°$), —·— (Pure entropy).

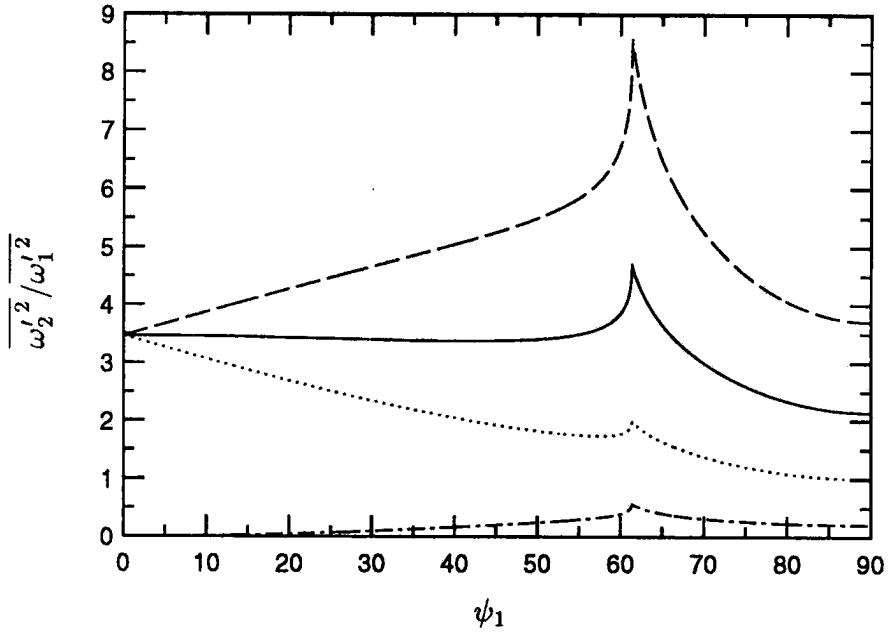


FIGURE 3.5: The amplification of vorticity across the shock wave as a function of the angle of incidence. The mean Mach number is 1.5. ——— (Pure vorticity), ---- ($A_r = 1; \phi_r = 0$), ····· ($A_r = 1; \phi_r = 180°$),—·— (Pure entropy).

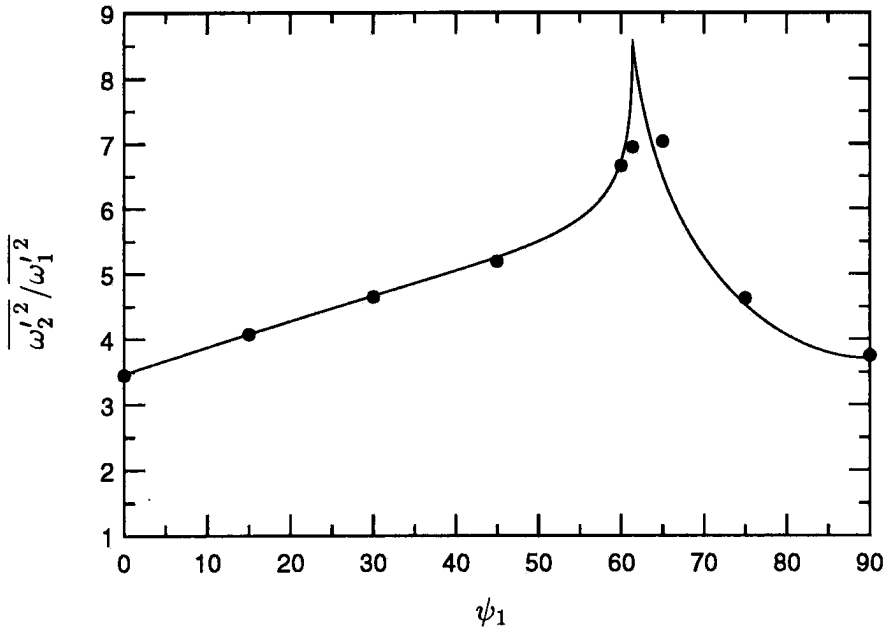


FIGURE 3.6: The amplification of vorticity across the shock wave as a function of the angle of incidence. The mean Mach number is 1.5. The line corresponds to linear analysis while the symbols are from numerical solution.

viscous effects are retained. We present numerical results of the interaction of a sinusoidal vorticity-entropy wave with a Mach 1.5 shock wave. The governing equations are the discretized two-dimensional unsteady compressible Navier Stokes equations. Details of the discretization are discussed in Chapter 4. The shock wave is stationary at the center of the domain in the mean. The shock structure is a result of molecular viscosity; no shock capturing or shock -fitting is used. A structured mesh that is non-uniform in the streamwise direction is used to resolve the shock wave. About 7 mesh points are located inside the shock wave.

Periodic boundary conditions are imposed transverse to the shock. The disturbance field corresponding to a vorticity-entropy wave is superposed onto the supersonic mean flow at the inflow boundary. Approximately non-reflecting boundary conditions (Poinsot and Lele, 1992) are used at the outflow boundary. The initial condition is a numerically computed steady shock wave. The vorticity-entropy wave is then introduced through the inflow boundary condition. The transients set up by the initial period of adjustment are allowed to exit the domain. Statistics are then gathered over a period of the inflow disturbance.

The computations examine the dependence of the interaction upon the inci-

dence angle of the disturbance. The incidence angle was varied from 0 to 90 degrees while the amplitudes $A_v$ and $A_e$ were fixed at 0.05. We compare in figure 3.6 the computed values of amplification of vorticity fluctuations to the linear analysis predictions. The vorticity fluctuations in the computation decay on both sides of the shock wave. The plotted values of vorticity amplification use the values of vorticity immediately outside the intermittent region associated with shock oscillation. Depending upon the incidence angle, the width of the intermittent region and the decay rate of vorticity behind the shock could be large enough for the decay of vorticity over the width of the intermittent region to be significant. Extrapolation of the downstream decay rate is then used to calculate the 'inviscid' vorticity amplification. Such correction for viscous effects was used for the 15° and 30° incidence angles. Note however that these viscosity corrections are less than 5% of the uncorrected values of vorticity amplification. As shown in figure 3.6, excellent agreement is seen away from the critical angles. Appreciable deviation is observed around the critical angle (the maximum deviation is about 20% at the critical angle).

As noted by Ribner (1953) and Chang (1954), within linear analysis the *unsteady* interaction of an oblique wave with a normal shock may be transformed into the *steady* interaction of an oblique wave with an oblique shock. The transformation involves defining the coordinates $x_s = x, y_s = y - U_1 t \cot \psi_1$. The governing equations in the transformed coordinates are the steady Euler equations linearized about uniform mean flow at a Mach number:

$$M_e^2 = \frac{U_2^2 + \cot^2 \psi_1 U_1^2}{a_2^2}.$$

$M_e^2$ equals unity at the critical angle whose vicinity therefore corresponds to transonic mean flow in transformed coordinates. It is likely that the inconsistency of linear equations in the transonic regime causes the deviation between computation and linear analysis around the critical angle.

## 3.5 A simple explanation

An explanation is provided for the influence of entropy fluctuations on the evolution of a turbulent flow across a shock wave. Consider the following idealization of the mean field associated with the shock:

$$U = U(x); \quad \overline{p} = \overline{p}(x); \quad \overline{\rho} = \overline{\rho}(x). \tag{3.27}$$

Linearization of the Euler equations about the above mean flow yields the following governing equations for the fluctuations:

$$\overline{\rho}\,(u'_t + Uu'_x + u'U_x) + \rho'\,U\,U_x = -p'_x \tag{3.28}$$

$$\overline{\rho}\,(v'_t + Uv'_x) = -p'_y. \tag{3.29}$$

Denoting the fluctuating vorticity by $\omega'$, the following equation may be derived for $\omega'$:

$$\omega'_t + U\omega'_x = -\omega' U_x - \frac{\rho'_y}{\overline{\rho}^2}\,\overline{p}_x + \frac{p'_y}{\overline{\rho}^2}\,\overline{\rho}_x. \tag{3.30}$$

The above set of equations represents the effects of bulk change across the shock wave. Effects due to shock distortion are absent. The motivation to examine the above set of equations is that, although the interaction of a vortical field with a shock wave generates acoustic waves, the contribution of these acoustic waves to the downstream kinetic energy is not significant. It will be seen in Section 3.8.2 that amplification and generation of vortical fluctuations accounts for most of the kinetic energy (99%) behind the shock wave.

The evolution of the vorticity fluctuations can therefore be related to that of kinetic energy. Equation 3.30 shows three terms that modify the vorticity field. The first term $(-\omega' U_x)$ represents the effect of bulk compression. The drop in mean velocity across the shock wave indicates that this term would enhance vorticity fluctuations. The second and third terms in equation 3.30 represent baroclinic contributions to the change in vorticity across the shock wave.

If the incident disturbance comprises of vorticity and entropy fluctuations, then $p' = 0$ and hence,

$$\omega'_t + U\omega'_x = -\omega'\,U_x - \frac{\rho'_y}{\overline{\rho}^2}\,\overline{p}_x. \tag{3.31}$$

The incident vorticity fluctuations are thus enhanced by bulk compression. The incident entropy fluctuations produce vorticity at the shock wave through the baroclinic term. The baroclinic contribution can enhance or oppose the effect of bulk compression. The phase difference between the vorticity and entropy waves determines whether enhancement or opposition is observed.

Consider for example the plane vorticity-entropy wave represented by equation (3.2). It is easily shown that,

$$-\omega' U_x - \frac{\rho'_y}{\overline{\rho}^2}\,\overline{p}_x \sim A_v\,UU_x - A_e\,l\frac{\overline{p}_x}{\overline{\rho}}. \tag{3.32}$$

Since $U_x$ is negative and $\overline{p}_x$ is positive across a shock wave, the two sources of vorticity are of the same sign if $A_e$ and $A_v$ are of the same sign. They oppose each other if $A_e$ and $A_v$ are of opposite sign. Thus, if $u'$ and $T'$ are negatively correlated the entropy field enhances the amplification of fluctuating vorticity. On the other hand, a positive correlation between $u'$ and $T'$ suppresses the amplification of vorticity across the shock wave.

Further insight is gained from a schematic illustration of this effect. Figure 3.7 shows a fluid element of circular cross-section passing through a shock wave. The geometric center of this element is denoted by $C_F$, while $C_M$ denotes the center of mass. The disturbance field associated with the fluid element is that of a vorticity-entropy wave. The element therefore exhibits solid body rotation (with associated vorticity $\omega'$) which is assumed positive in the direction shown. Also, the density gradient associated with the entropy wave causes the centre of mass to differ from the centre of force (the geometric centre). Note that $C_M$ is below $C_F$, if the correlation between $u'$ and $T'$ is negative.

Bulk compression compresses the element in the streamwise direction thereby enhancing the rotation. In addition, the shock wave exerts a pressure force (associated with the adverse pressure gradient) that passes through $C_F$. This pressure force would exert a torque about the centre of mass. This torque manifests itself as the baroclinic source of vorticity. Note that if $C_M$ is below $C_F$, the baroclinic rotation is in the same direction as the rotation due to bulk compression. It is in the opposite direction, if $C_M$ is above $C_F$ (positive correlation between $u'$ and $T'$). The upstream correlation between $u'$ and $T'$ thus determines the location of $C_M$ with respect to $C_F$, and thereby the relative sense of rotation that the baroclinic torque produces.

## 3.6 Scaling of the evolution of vorticity across a shock wave

Equation (3.31) is used to derive approximate expressions for the evolution of vorticity fluctuations across the shock. The expressions are evaluated by comparing to the linear analysis predictions. Equation (3.31) is rewritten as:

$$D_t(U\omega') = -\frac{\rho'_y}{\overline{\rho}^2}\, U\overline{p}_x. \tag{3.33}$$

where $D_t$ denotes the material derivative $\partial/\partial t + U\partial/\partial x$.

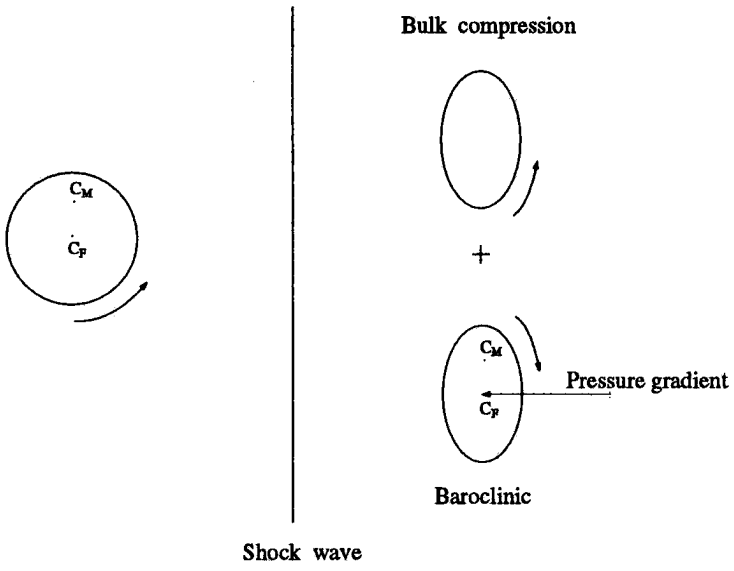


(a)

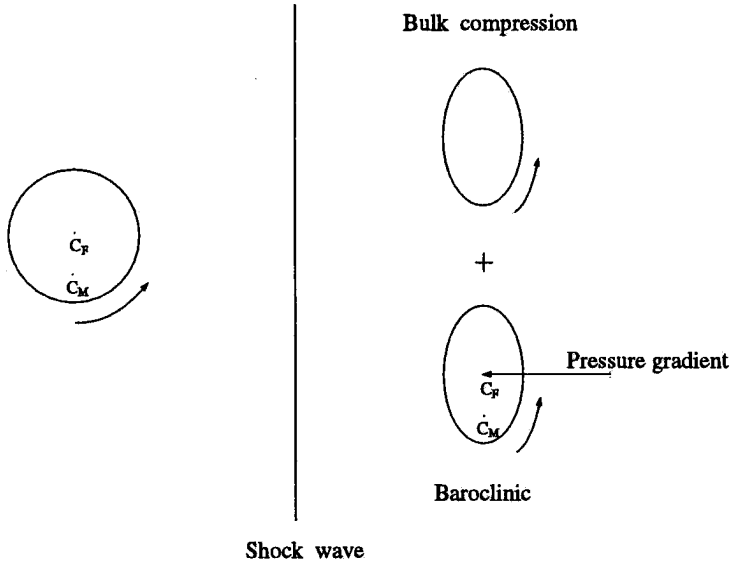


(b)

FIGURE 3.7: A spherical element of fluid passing through a shock wave. The effects of bulk compression and baroclinic vorticity production are shown. $u'$ and $T'$ are negatively correlated upstream of the shock wave in $(a)$ while $(b)$ corresponds to positive correlation between $u'$ and $T'$.

Using the relation $\overline{p}_x = -\overline{\rho} U U_x$ in the above equation yields:

$$D_t(U\omega') = \frac{\rho'_y}{\overline{\rho}}\, U^2 U_x = \frac{\rho'_y}{3\overline{\rho}}\, (U^3)_x. \tag{3.34}$$

The shock wave is approximated as a discontinuity. $(U^3)_x$ is expressed as $\Delta U^3 \delta(x)$, where $\Delta(U^3)$ represents the difference in $U^3$ across the shock wave, and $\delta(x)$ denotes the Dirac delta function. An approximate solution to the above equation is obtained by setting $\rho'_y$ equal to its upstream value. Transforming coordinates to $x' = x - Ut, \tau = t$ and integrating yields the following expression for the change in vorticity across the shock wave:

$$U_2\omega'_2 - U_1\omega'_1 \sim \frac{ikl}{3} A_e \frac{(U_2^3 - U_1^3)}{U_1}. \tag{3.35}$$

which yields:

$$\omega'_2 \sim r\omega'_1 + \frac{ikl}{3}\, A_e\, U_1\, \frac{1 - r^3}{r^2} \tag{3.36}$$

where $r = U_1/U_2$ is obtained from the Rankine-Hugoniot equations. Equation (3.36) suggests that the incident vorticity fluctuations amplify by an amount equal to the mean density ratio across the shock. The vorticity produced by the incident entropy fluctuations is predicted to scale as $kA_e l(1 - r^3)/r^2$.

These expressions are next, evaluated in figures 3.8 and 3.9. Figure 3.8 shows the amplification of vorticity in the interaction of a vorticity wave with a shock. Mean Mach numbers from 1.25 to 2.5 are considered. Both scaled and unscaled values of *rms* vorticity behind the shock wave are plotted as a function of incidence angle. The interaction of an entropy wave with a shock is examined in figure 3.9. The proposed scaling seems to yield reasonable collapse of the curves for the incident entropy waves, especially in the propagating regime. Validity of the scaling for a turbulent field would depend upon the fraction of incident waves in the propagating regime. The scaling is less satisfactory for the incident vorticity waves. It performs well for incidence angles near zero, however a systematic deviation is seen with incidence angle and Mach number.

## 3.7 The interaction of a shock with an isotropic field of vorticity and entropy fluctuations

The analysis is extended to describe the evolution of a turbulent flow across a shock wave. In light of Morkovin's hypothesis, the turbulence is represented as a random three-dimensional field of vorticity-entropy waves.

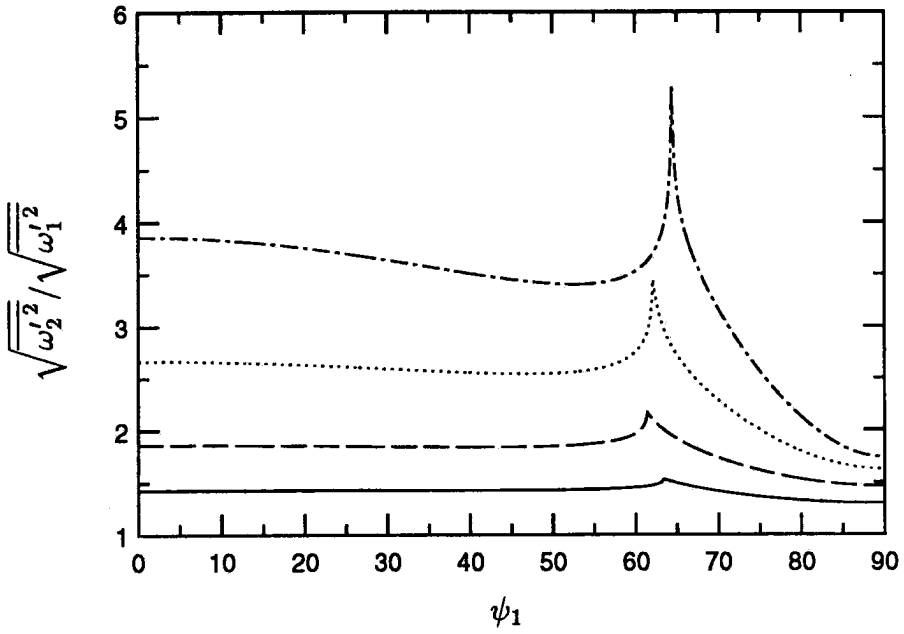


FIGURE 3.8a: Unscaled amplification of the *rms* level of vorticity in the interaction of a vorticity wave with a shock wave. ——— $(M_1 = 1.25)$, - - - - $(M_1 = 1.5)$, ····· $(M_1 = 2)$, — - — $(M_1 = 2.5)$.

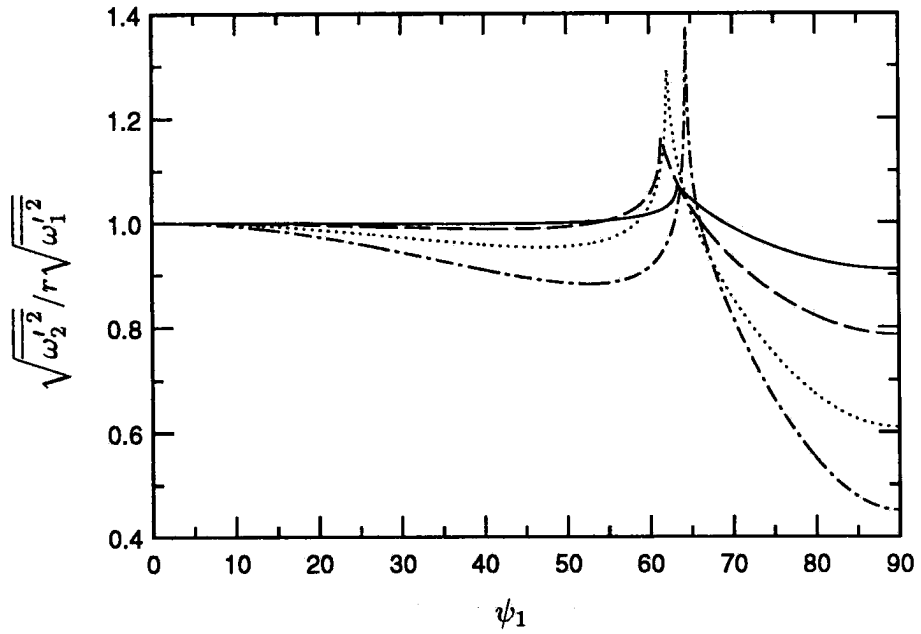


FIGURE 3.8b: Scaled amplification of the *rms* level of vorticity in the interaction of a vorticity wave with a shock wave. ——— $(M_1 = 1.25)$, - - - - $(M_1 = 1.5)$, ····· $(M_1 = 2)$, — - — $(M_1 = 2.5)$.

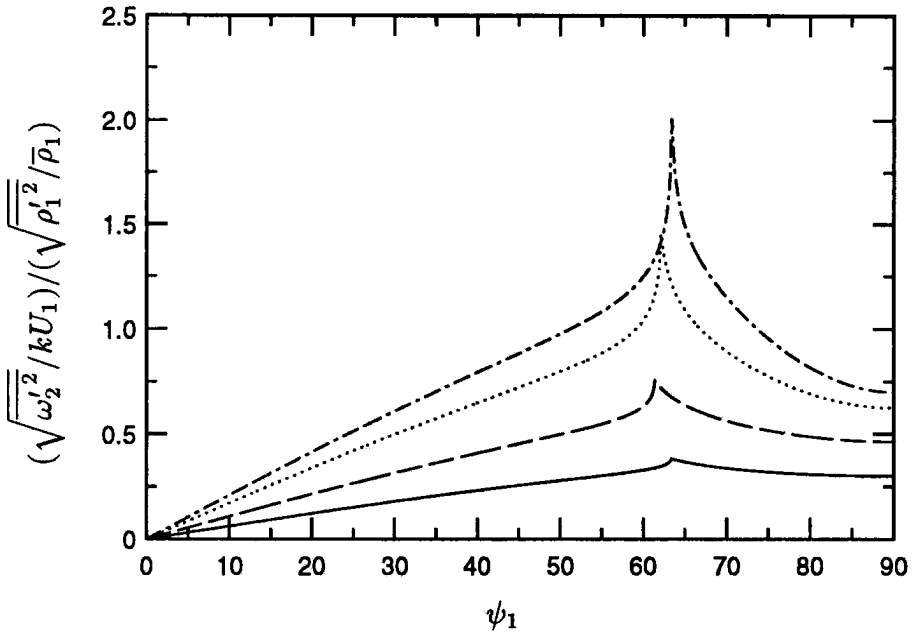


FIGURE 3.9a: Unscaled *rms* level of vorticity produced in the interaction of an entropy wave with a shock wave. ——— ($M_1 = 1.25$), ---- ($M_1 = 1.5$), ····· ($M_1 = 2$), —·— ($M_1 = 2.5$).

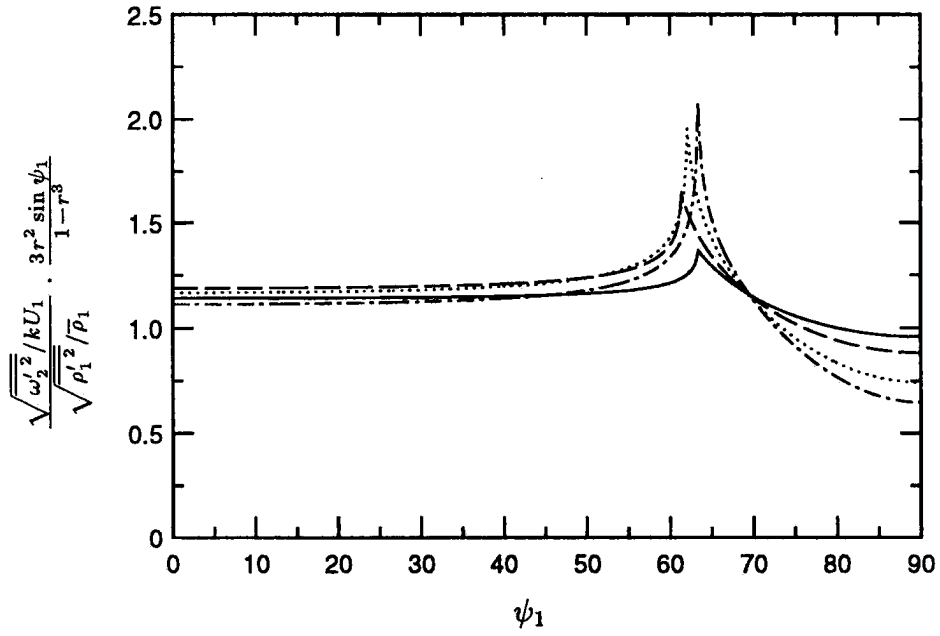


FIGURE 3.9b: Scaled *rms* level of vorticity produced in the interaction of an entropy wave with a shock wave. ——— ($M_1 = 1.25$), ---- ($M_1 = 1.5$), ····· ($M_1 = 2$), —·— ($M_1 = 2.5$).

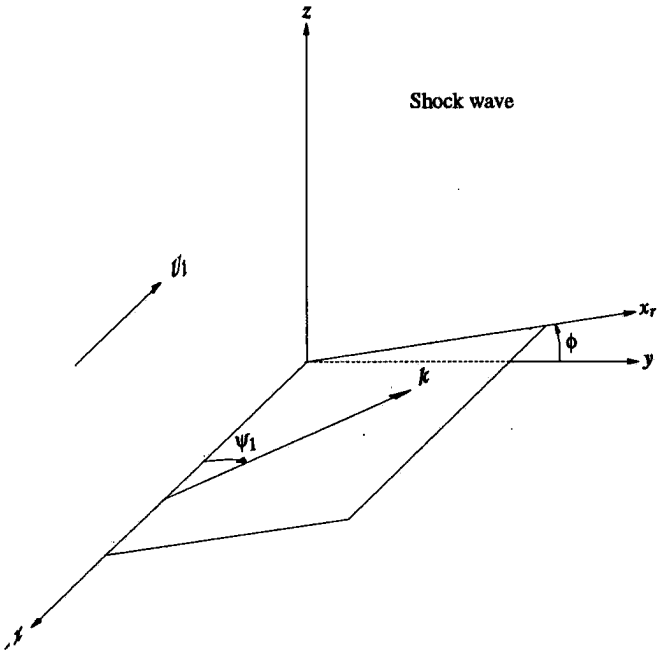


FIGURE 3.10: Coordinate system used in the interaction of isotropic turbulence with a shock wave.

The turbulent field upstream of the shock wave, is assumed to be isotropic. It will be seen however, that the procedure is easily extended to consider anisotropic turbulence.

The incident turbulent field is represented as a superposition of plane vorticity-entropy waves (Fourier modes) in three dimensions. Each of these waves would interact independently with the shock wave under linear analysis. For a given upstream spectrum, the interaction of each of these waves with the shock wave is predicted. Integration over all waves behind the shock wave yields turbulence statistics behind the shock.

The three dimensional problem is related to the two dimensional analysis of the preceding section as follows. Consider an incident plane wave in three dimensions. As shown in figure 3.10, the wavenumber vector of the wave lies in a plane that makes angle $\phi$ with the $y$ axis. In this plane which we call the $x - x_r$ plane, the wave makes angle $\psi_1$ with the $x$ axis. It is readily seen that the $x - x_r$ plane is identical to the plane of interaction in the two-dimensional problem.

The solenoidal nature of the incident velocity field requires the velocity vector

of the wave to be normal to the wavenumber vector. The velocity field may therefore be expressed as a sum of two components: one normal to the wavenumber vector in the $x - x_r$ plane and the other normal to the $x - x_r$ plane (the $\phi$ direction). It is intuitively clear that the $\phi$ component of velocity would pass unchanged through the shock wave. As a result, the three dimensional problem may be solved using results of the two dimensional analysis in the $x - x_r$ plane. The following discussion uses subscripts '$r$' and '$\phi$' to denote the components in the $r$ and $\phi$ directions respectively. Equations 3.20 and 3.22 allow the following expressions to be written for the components of kinetic energy behind the shock wave:

$$\frac{E_{11}}{U_1^2} = [\ |\widetilde{F}|^2 + |\widetilde{G}|^2 + \widetilde{F}\widetilde{G}^* e^{i(\widetilde{k}-kmr)x} + \widetilde{F}^*\widetilde{G} e^{-i(\widetilde{k}-kmr)x}\ ]\ |A_v|^2. \tag{3.37}$$

$$\frac{E_{rr}}{U_1^2} = [\ |\widetilde{H}|^2 + |\widetilde{I}|^2 + \widetilde{H}\widetilde{I}^* e^{i(\widetilde{k}-kmr)x} + \widetilde{H}^*\widetilde{I} e^{-i(\widetilde{k}-kmr)x}\ ]\ |A_v|^2. \tag{3.38}$$

Recall that the variables in parentheses depend upon $M_1, \psi_1, A_e/A_v$ and $k$. The term $|A_v|$ represents the magnitude of the velocity vector *in the* $x - x_r$ *plane.* It is related to the cartesian components of kinetic energy as follows. Figure 3.10 shows that,

$$|A_v| = \frac{|u_1'|}{l}. \tag{3.39}$$

This implies that

$$|A_v|^2 = \frac{E_{11}^1}{l^2}. \tag{3.40}$$

where the superscript '1' denotes the state upstream of the shock. Since the incident turbulence is isotropic, it has an energy spectrum of the form,

$$E_{ij}^1 = \frac{E(k)}{4\pi k^2}\left(\delta_{ij} - \frac{k_i k_j}{k^2}\right) \tag{3.41}$$

where $E(k)$ is the three dimensional energy spectrum tensor such that $\int E(k)\ dk = q_1^2/2$. The wavenumbers in cartesian coordinates are given by:

$$k_1 = k\cos\psi_1; \quad k_2 = k\sin\psi_1\cos\phi; \quad k_3 = k\sin\psi_1\sin\phi. \tag{3.42}$$

Using the above expression to obtain $E_{11}^1$, we see that,

$$|A_v|^2 = \frac{E(k)}{4\pi k^2}. \tag{3.43}$$

Alternatively, $|A_v|^2$ could be obtained using,

$$|A_v|^2 = E^1_{11} + E^1_{rr} = E^1_{nn} - E^1_{\phi\phi}. \tag{3.44}$$

where $E^1_{rr}$ and $E^1_{\phi\phi}$ may be obtained from,

$$v' = u'_r \cos\phi - u'_\phi \sin\phi; \quad w' = u'_r \sin\phi + u'_\phi \cos\phi. \tag{3.45a}$$

$$u'_r = v' \cos\phi + w' \sin\phi; \quad u'_\phi = w' \cos\phi - v' \sin\phi. \tag{3.45b}$$

$E_{11}$ and $E_{rr}$ behind the shock wave will be completely determined once $E(k)$ and $A_e/A_v$ are specified. We use the following form for $E(k)$:

$$E(k) \sim \left(\frac{k}{k_0}\right)^4 e^{-2(\frac{k}{k_0})^2}. \tag{3.46}$$

The quantity $A_e/A_v$ may be represented as $A_r e^{i\phi_r}$ where $A_r$ and $\phi_r$ are both functions of the wavenumber vector. Appropriate functional dependencies may be assumed depending upon the flow being considered. This report presents results for $\phi_r = 0$ and $\pi$; *i.e.* the density field is either perfectly correlated or perfectly anti-correlated with the velocity field. Also, two forms of the upstream density spectrum are considered. One case assumes the density field to be isotropic with the same three-dimensional spectrum as the velocity field; *i.e.* $A_r$ is assumed constant. For this case it is easily shown that

$$A_r = \sqrt{2}\frac{\rho'_1/\overline{\rho_1}}{\sqrt{q_1^2}/U_1}. \tag{3.47a}$$

The second case assumes that the density field satisfies Morkovin's hypothesis at every wavenumber. For isotropic velocity field, it is easily seen that the resulting density field is axisymmetric; *i.e.*

$$A_r = (\gamma - 1)M_1^2 \sin\psi_1. \tag{3.47b}$$

Once $E(k)$ and $A_e/A_v$ are specified, equations 3.37 and 3.38 are used to obtain $E_{11}$ and $E_{rr}$ behind the shock wave. The following expressions for $E_{22}$ and $E_{33}$ are obtained from equation 3.45*a*:

$$E_{22} = \cos^2\phi\ E_{rr} + \sin^2\phi\ E_{\phi\phi} - \sin 2\phi\ E_{r\phi}. \tag{3.48a}$$

$$E_{33} = \sin^2\phi\ E_{rr} + \cos^2\phi\ E_{\phi\phi} + \sin 2\phi\ E_{r\phi}. \tag{3.48b}$$

Recognizing that turbulence behind the shock wave will be axisymmetric, we solve for $E_{22} + E_{33}$. The above set of equations show that,

$$E_{22} + E_{33} = E_{rr} + E_{\phi\phi}. \tag{3.49}$$

$E_{\phi\phi}$ was noted to remain unchanged across the shock wave and hence is equated to its upstream value. Equation 3.44 is used to obtain the upstream value of $E_{\phi\phi}$; *i.e.*,

$$E^1_{\phi\phi} = E^1_{nn} - |A_v|^2 = \frac{E(k)}{4\pi k^2}. \tag{3.50}$$

This yields,

$$E_{22} + E_{33} = E_{rr} + \frac{E(k)}{4\pi k^2}. \tag{3.51}$$

The spectra are then integrated over all wavenumbers to obtain statistics as a function of distance behind the shock wave. The elemental volume of integration is given by the expression:

$$\mathrm{d}^3\mathbf{k} = k^2 \sin\psi_1\ \mathrm{d}\psi_1\ \mathrm{d}\phi\ \mathrm{d}k \tag{3.52}$$

where $k$ varies from 0 to $\infty$, $\psi_1$ varies from $-\pi/2$ to $\pi/2$ and $\phi$ varies from 0 to $2\pi$.

The following expressions are obtained for the streamwise variation of kinetic energy behind the shock wave:

$$\frac{\overline{u_2'^2}}{U_1^2} = \int_{k=0}^{\infty}\int_{\psi_1=-\pi/2}^{\pi/2}\int_{\phi=0}^{2\pi} E_{11}\ k^2 \sin\psi_1\ \mathrm{d}\phi\ \mathrm{d}\psi_1\ \mathrm{d}k. \tag{3.53}$$

Recall the problem is symmetric about $\psi_1 = 0$. Also the transfer functions that yield $E_{11}$ are independent of $\phi$. As a result,

$$\frac{\overline{u_2'^2}}{U_1^2} = 4\pi \int_{k=0}^{\infty}\int_{\psi_1=0}^{\pi/2} E_{11}\ k^2 \sin\psi_1\ \mathrm{d}\psi_1\ \mathrm{d}k. \tag{3.54}$$

The integration over $k$ and $\psi_1$ is performed numerically. Similar expressions are obtained for the transverse components of kinetic energy. *i.e.*,

$$\frac{\overline{v_2'^2}}{U_1^2} = \frac{\overline{w_2'^2}}{U_1^2} = \frac{4\pi}{2}\int_{k=0}^{\infty}\int_{\psi_1=0}^{\pi/2}\left[E_{rr} + \frac{E(k)}{4\pi k^2}\right] k^2 \sin\psi_1\ \mathrm{d}\psi_1\ \mathrm{d}k. \tag{3.55}$$

The evaluation of scalar quantities behind the shock wave is considerably simpler. For example the pressure field behind the shock is given by the following expression (Equations 3.24 and 3.26) :

$$\frac{\overline{p_2'^2}}{\overline{p}_2^2} = 4\pi \int_{k=0}^{\infty} \int_{\psi_1=0}^{\pi/2} E_{pp}\, k^2 \sin\psi_1 \, \mathrm{d}\psi_1 \, \mathrm{d}k. \tag{3.56}$$

where $E_{pp} = |\widetilde{K}|^2 |A_v|^2$ in the propagating regime and $e^{-2k_i x}|\widetilde{K}|^2|A_v|^2$ in the decaying regime respectively.

## 3.8 Results

The evolution of turbulence statistics across the shock wave is examined in this section. The spatial variation of kinetic energy behind the shock wave is discussed in Section 3.8.1. Dependence of the far-field levels of kinetic energy on the mean Mach number are examined in Section 3.8.2. Section 3.8.3 presents the evolution of fluctuating vorticity and Taylor microscales across the shock wave. The influence of the incident fluctuations on the oscillation of the shock front is discussed in Section 3.8.4. Section 3.8.5 examines the spatial evolution and far-field levels of the thermodynamic fluctuations behind the shock. The influence of entropy fluctuations on the interaction is emphasized throughout. Finally, Section 3.8.6 examines the validity of Morkovin's hypothesis behind the shock wave.

### 3.8.1 The spatial evolution of kinetic energy

The variation of $q^2$ with distance behind a Mach 1.5 shock wave is plotted in figure 3.11. The combined interaction of vorticity and entropy fluctuations is compared to that of vorticity and entropy fluctuations alone. As mentioned before, two representative cases of combined interaction are considered: one where $u'$ and $T'$ are negatively correlated upstream of the shock ($A_r = 0.58, \phi_r = 0$) and the other where $u'$ and $T'$ are positively correlated ($A_r = 0.58, \phi_r = \pi$). The value of 0.58 was (arbitrarily) chosen to satisfy Morkovin's hypothesis at a Mach number of 1.35. All four curves are normalized with the incident value of $q^2$. As discussed in Section 3.3, $q_2^2/q_1^2$ in the pure entropy limit corresponds to 0.17 $(q_2^2/U_1^2)/(\overline{\rho_1'^2}/\overline{\rho_1^2})$ where the factor 0.17 equals $(\overline{\rho_1'^2}/\overline{\rho_1^2})/(q_1^2/U_1^2)$ for $A_r = 0.58$.

Similar spatial variation is exhibited by all three curves. Amplification of $q^2$ across the shock wave is followed by rapid drop and rise immediately downstream

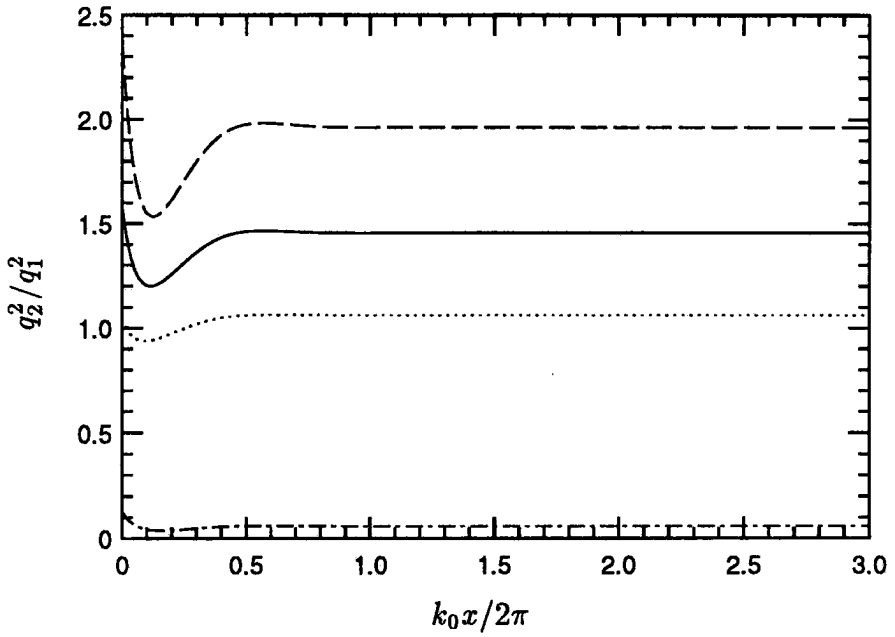


FIGURE 3.11: Evolution of $q^2$ behind a Mach 1.5 shock wave. —— (Pure vorticity), ---- ($A_r = 0.58; \phi_r = 0$), ····· ($A_r = 0.58; \phi_r = 180°$), —·— (Pure entropy).

of the shock wave. Temperature fluctuations that are negatively correlated with $u'$ yield higher levels of kinetic energy at all streamwise locations while positively correlated temperature fluctuations have the opposite effect.

The rapid variation of kinetic energy behind the shock wave is a fundamental feature of shock/turbulence interaction. DNS of isotropic vortical fluctuations interacting with a shock wave (Lee, Lele and Moin, 1993) exhibits this feature, as does linear analysis of acoustic fluctuations (Mahesh, Lee, Lele and Moin, 1995) interacting with a shock. The discussion (Section 3.3) of single vorticity-entropy waves interacting with a shock reveals that waves incident at angles greater than the critical angle (decaying regime) produce this rapid variation through the damped oscillatory correlation between acoustic and vortical fluctuations behind the shock wave.

This correlation was overlooked by Lee, Lele and Moin (1993) in their linear analysis of a shock wave interacting with isotropic vortical fluctuations. This led them to erroneously conclude that linear analysis could not reproduce this rapid variation of kinetic energy seen in their computations. This error was subsequently corrected by them (Lee, Lele and Moin, 1993). Equations 3.23 and 3.25 suggest

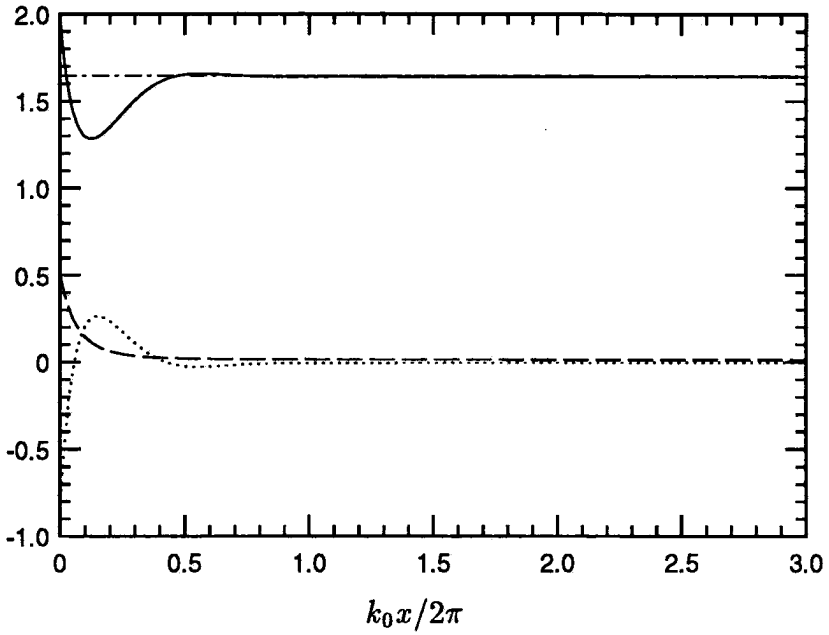


FIGURE 3.12: The streamwise variation of terms in Equation 3.57 behind a Mach 1.5 shock wave. The incident fluctuations correspond to $A_r = 0.58$ and $\phi_r = 0$. All terms are non-dimensionalized as indicated in Equation 3.57 and normalized with $\sqrt{q_1^2}/U_1$. —— $(q^2)$, ---- $(\overline{p'^2})$, ····· $(\overline{p'u'})$, —·— $(I_{\text{total}})$.

that $q^2$ behind the shock wave may be decomposed into four components: a spatially uniform vortical component, an acoustic component that decays exponentially and non-monotonic components corresponding to the correlation between acoustic and vortical fluctuations over both regimes of the solution. This decomposition, was performed by Mahesh, Lee, Lele and Moin (1995) in their analysis of acoustic fluctuations interacting with a shock wave. The correlation between acoustic and vortical fluctuations produced by waves in the decaying regime of the solution were seen to produce the rapid variation of kinetic energy.

The variation of kinetic energy behind the shock wave may be further clarified by examination of the equations governing its evolution. Rearrangement of equations 3.3 shows that the quantity,

$$I_{\text{total}} = \frac{\gamma M}{2}\left[\frac{q^2}{a^2} + \frac{\overline{p'^2}}{\gamma^2\overline{p}^2}\right] + \frac{\overline{p'u'}}{\overline{p}a}. \tag{3.57}$$

is conserved along a mean streamline. $I_{\text{total}}$ changes across the shock wave and remains constant downstream. As will be seen in the next section, $\overline{p'^2}$ decays exponentially behind the shock wave. The rapid non-monotonic variation of $q^2$ may

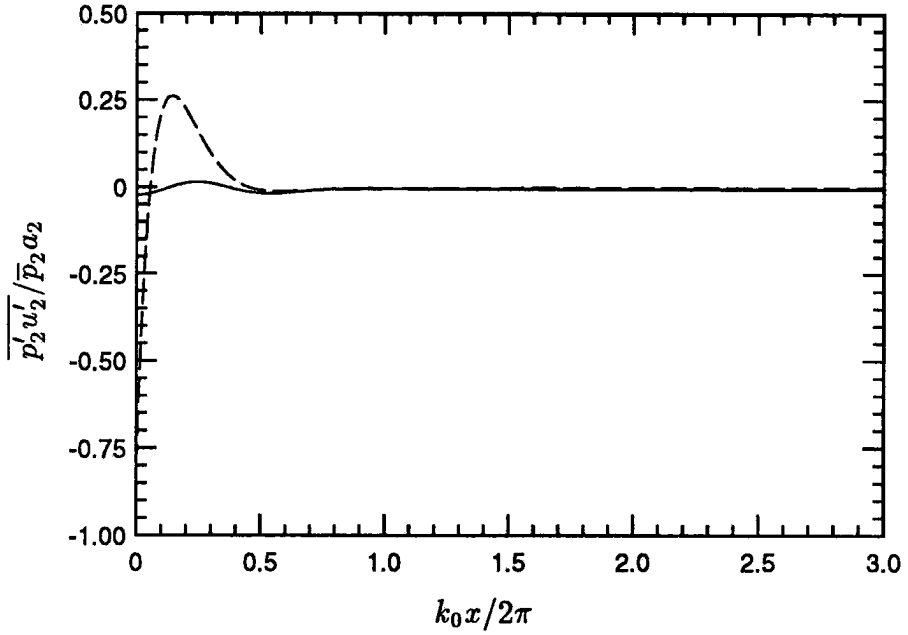


FIGURE 3.13: Decomposition of $\overline{p_2' u_2'}$ behind a Mach 1.5 shock wave. The incident fluctuations correspond to $A_r = 0.58$ and $\phi_r = 0$. Both terms are normalized with $\sqrt{q_1^2}/U_1$. —— $(\overline{p_2' u_2'}_{\text{prop}})$, ---- $(\overline{p_2' u_2'}_{\text{decay}})$.

therefore be explained as a result of partitioning between potential and kinetic energy brought about by the correlation between acoustic fluctuations and the shock-normal component of fluctuating velocity. This is illustrated in figure 3.12 where the terms in Equation 3.57 are plotted.

The $\overline{p'u'}$ correlation may be decomposed into two components as follows:

$$\overline{p'u'} = \overline{p'u'}_{\text{prop}} + \overline{p'u'}_{\text{decay}}. \tag{3.58}$$

where the subscripts 'prop' and 'decay' refer to the propagating and decaying regimes respectively. The above decomposition is performed in figure 3.13 and reveals that the correlation between acoustic fluctuations and the velocity field in the decaying regime causes the rapid variation of $q^2$ behind the shock wave. Note that the pressure-velocity correlation in the far-field is solely due to the incident fluctuations in the propagating regime. The far-field levels of $q^2$ are therefore determined by the correlation between pressure and acoustic component of the velocity field in the propagating regime.

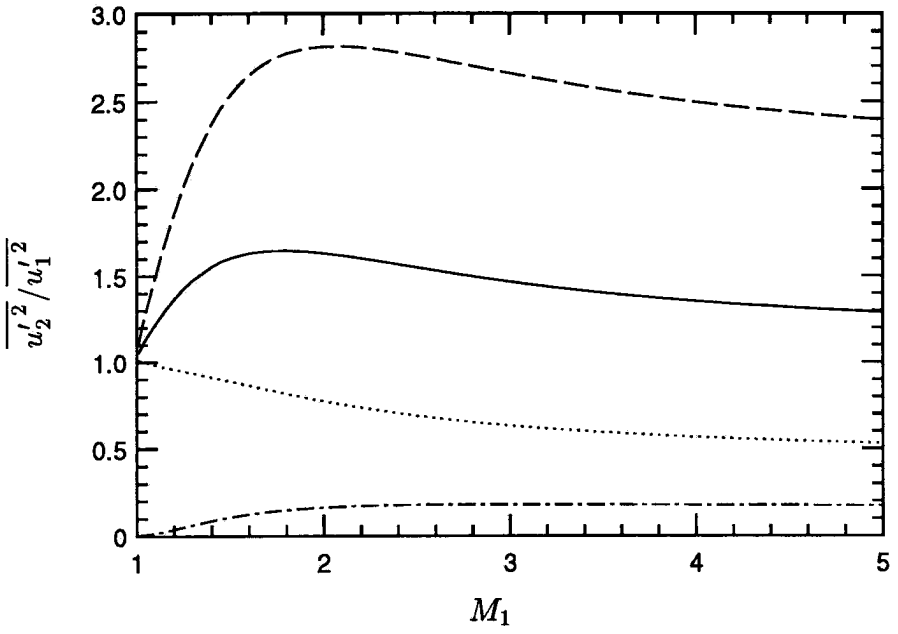


FIGURE 3.14: The amplification of $\overline{u'^2}$ across the shock wave in the far-field. ——— (Pure vorticity), ---- ($A_r = 0.58; \phi_r = 0$), ····· ($A_r = 0.58; \phi_r = 180°$),—·— (Pure entropy).

## 3.8.2 Far-field kinetic energy

The influence of entropy fluctuations on far-field levels of kinetic energy amplification is examined as a function of mean Mach number. If $A_e/A_v$ is independent of $k$, it is easily shown that turbulence statistics in the far-field are independent of the upstream energy spectrum. Equation 3.54 outlined the expression for $\overline{u_2'^2}$. Substituting for $E_{11}$ from equations 3.23 and 3.25 into equation 3.54, the following expression is obtained:

$$\left(\frac{\overline{u_2'^2}}{U_1^2}\right)_{\text{far-field}} = \left[\int_0^{\psi_c} (|\widetilde{F}|^2+|\widetilde{G}|^2)\sin\psi_1 \mathrm{d}\psi_1 + \int_{\psi_c}^{\pi/2} |\widetilde{G}|^2 \sin\psi_1 \mathrm{d}\psi_1\right] \int_0^{\infty} E(k)\mathrm{d}k. \tag{3.59}$$

In writing the above expression, use is made of the fact that the correlation term in the propagating regime integrates to zero in the far-field. Since $\int_0^{\infty} E(k)\mathrm{d}k = q_1^2/2$, the above expression is independent of the upstream energy spectrum. The above discussion holds also for the other components of kinetic energy and the thermodynamic fluctuations. Thus if $A_e/A_v$ is independent of $k$, the far-field levels depend only upon $M_1$ and $A_e/A_v$.

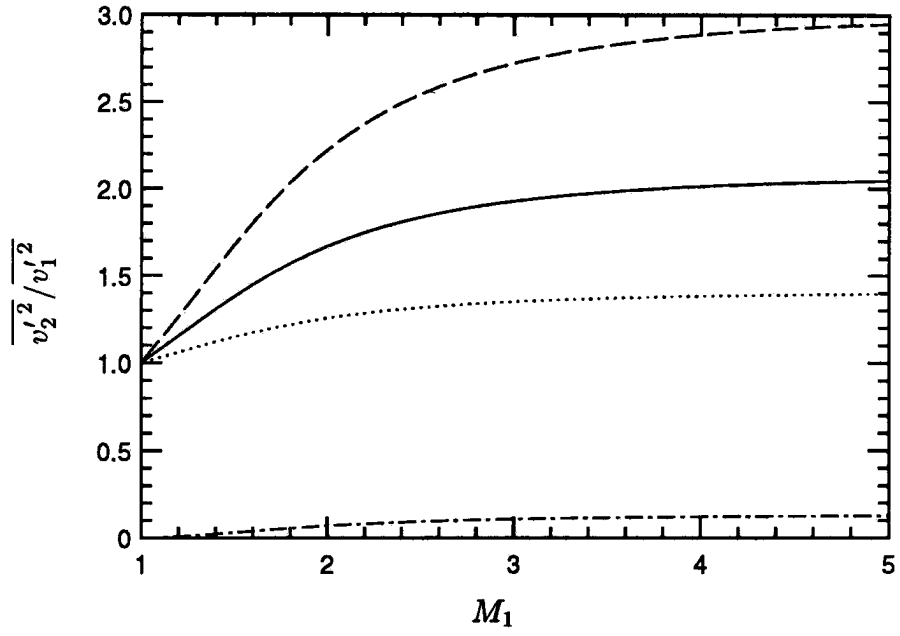


FIGURE 3.15: The amplification of $\overline{v'^2}$ across the shock wave in the far-field. ——— (Pure vorticity), ---- ($A_r = 0.58; \phi_r = 0$), ····· ($A_r = 0.58; \phi_r = 180°$),—·— (Pure entropy).

The far-field levels of kinetic energy amplification are plotted in figures 3.14 and 3.15 respectively. The presence of entropy fluctuations is seen to significantly influence the levels of kinetic energy behind the shock wave. Recall that the far-field kinetic energy may be decomposed into vortical and acoustic components. Figure 3.16 illustrates that while acoustic waves are generated at the shock wave, their contribution to the kinetic energy is not very significant; amplification and generation of vortical fluctuations accounts for most of the kinetic energy behind the shock wave.

Entropy fluctuations also influence the anisotropy of the turbulence behind the shock. As shown in figure 3.17, negatively correlated fluctuations of $u'$ and $T'$ upstream of the shock wave increase the fraction of energy in the streamwise direction behind the shock. On the other hand, positively correlated fluctuations tend to decrease the fraction of turbulence kinetic energy in the streamwise direction.

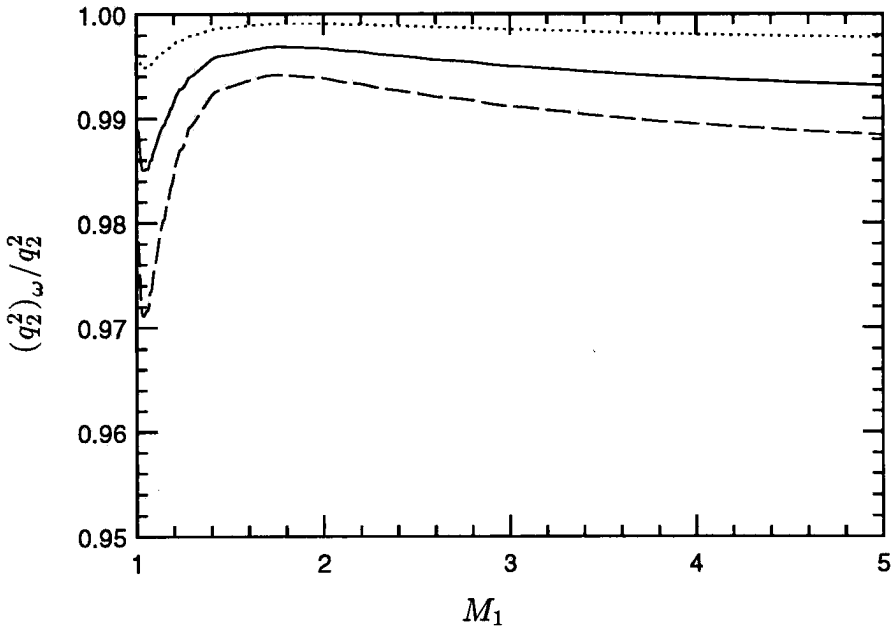


FIGURE 3.16: Vortical contribution to kinetic energy in the far-field behind the shock. —— (Pure vorticity), ---- ($A_r = 0.58; \phi_r = 0$), ····· ($A_r = 0.58; \phi_r = 180°$).

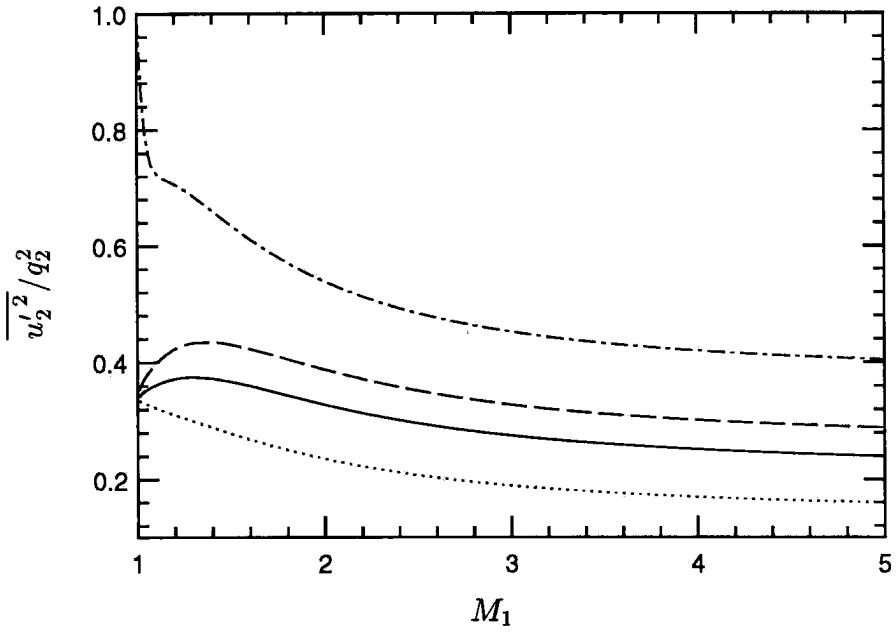


FIGURE 3.17: Far-field values of $\overline{u'^2}/q^2$ behind the shock wave. —— (Pure vorticity), ---- ($A_r = 0.58; \phi_r = 0$), ····· ($A_r = 0.58; \phi_r = 180°$),—-— (Pure entropy).

### 3.8.3 Vorticity fluctuations and Taylor microscale

The evolution of vorticity fluctuations and Taylor microscale of the vortical component of the flow is examined in this section. Equations 3.20 and 3.45 may be used to derive expressions for the vorticity behind the shock wave. The streamwise component of vorticity is observed to remain unchanged across the shock wave. The transverse components are altered by the shock and are given by the following expression:

$$\frac{\overline{\omega_2'^2}}{U_1^2} = \frac{\overline{\omega_3'^2}}{U_1^2} = 2\int_{\phi=0}^{2\pi}\int_{\psi_1=0}^{\pi/2}\int_{k=0}^{\infty}\{\cos^2\phi\ [m^2r^2|\widetilde{I}|^2 + l^2|\widetilde{G}|^2 - 2mrl(\widetilde{I}_r\widetilde{G}_r + \widetilde{I}_i\widetilde{G}_i)\ ] + m^2\sin^2\phi\}\ k^4|A_v|^2\ \sin\psi_1\ \mathrm{d}k\ \mathrm{d}\psi_1\ \mathrm{d}\phi \quad (3.60).$$

Substituting for $|A_v|^2$ and integrating over $\phi$, we get:

$$\frac{\overline{\omega_2'^2}}{U_1^2} = \frac{\overline{\omega_3'^2}}{U_1^2} = \int_{\psi_1=0}^{\pi/2}[\ m^2r^2|\widetilde{I}|^2 + l^2|\widetilde{G}|^2 - 2mrl(\widetilde{I}_r\widetilde{G}_r + \widetilde{I}_i\widetilde{G}_i) + m^2\ ]\ \sin\psi_1\ \mathrm{d}\psi_1 \times \int_{k=0}^{\infty}\frac{k^2E(k)}{2}\mathrm{d}k. \quad (3.61)$$

For isotropic incident spectrum, it is easily shown that the incident vorticity is given by the following expression:

$$\frac{\overline{\omega_2'^2}}{U_1^2} = \frac{\overline{\omega_3'^2}}{U_1^2} = \int_{\psi_1=0}^{\pi/2}(2-l^2)\sin\psi_1\ \mathrm{d}\psi_1\int_{k=0}^{\infty}\frac{k^2E(k)}{2}\mathrm{d}k. \quad (3.62)$$

The amplification of vorticity fluctuations across the shock wave is therefore independent of the incident energy spectrum if $A_e/A_v$ is independent of $k$. As expected, the amplification of transverse components of vorticity is considerably affected by the presence of entropy fluctuations. As shown in figure 3.18, negative correlation between $u'$ and $T'$ upstream of the shock increases vorticity levels behind the shock. Positively correlated fluctuations yield lower levels of amplification.

Equations 3.20 and 3.45 may be used to derive expressions for the Taylor microscale behind the shock wave. The influence of entropy fluctuations on the Taylor microscale of the vortical component is examined in figure 3.19. The incident entropy fluctuations are seen to have negligible effect on the drop of the streamwise Taylor microscale across the shock wave.

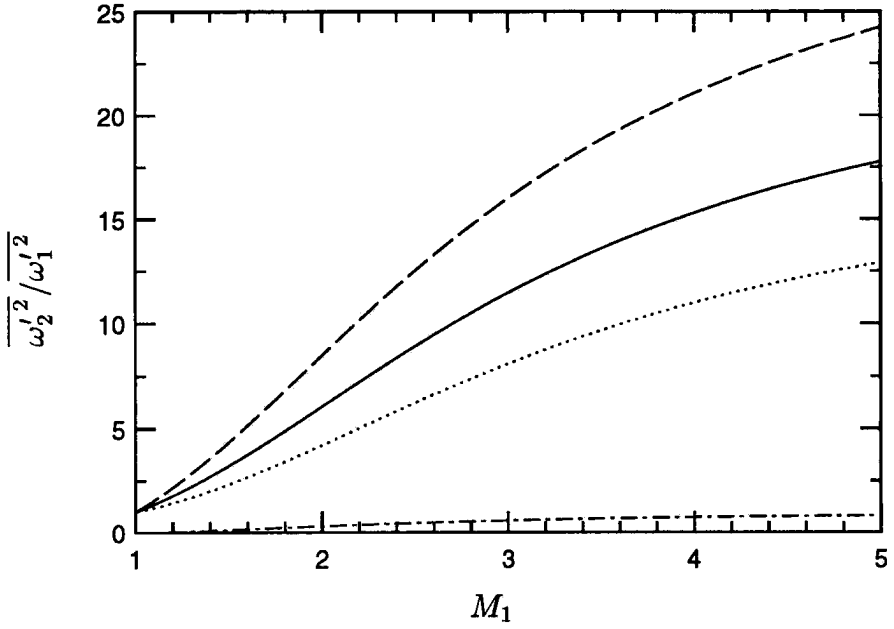


FIGURE 3.18: Amplification of transverse components of vorticity across the shock wave. —— (Pure vorticity), ---- ($A_r = 0.58; \phi_r = 0$), ····· ($A_r = 0.58; \phi_r = 180°$), —·— (Pure entropy).

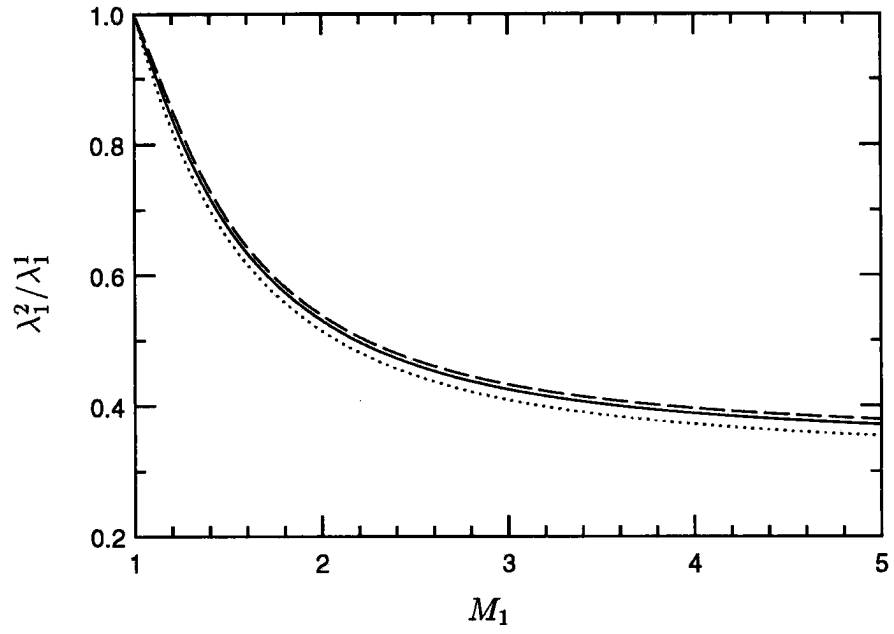


FIGURE 3.19: The evolution of shock-normal Taylor microscale across the shock wave. —— (Pure vorticity), ---- ($A_r = 0.58; \phi_r = 0$), ····· ($A_r = 0.58; \phi_r = 180°$).

### 3.8.4 Statistics of the shock front

The oscillation of the shock wave is considerably affected by the presence of entropy fluctuations in the incident field of disturbances. Results for the velocity and amplitude of oscillation of the shock front are presented below.

From equation (3.21), the *rms* level of the oscillation velocity is given by:

$$\frac{\overline{\xi_t^2}}{U_1^2} = 4\pi \int_{k=0}^{\infty} \int_{\psi_1=0}^{\pi/2} |\widetilde{L}|^2 \, |A_v|^2 \, k^2 \sin\psi_1 \, \mathrm{d}k \, \mathrm{d}\psi_1. \tag{3.63}$$

Substitution for $|A_v|^2$ from equation 3.43 yields:

$$\frac{\overline{\xi_t^2}}{U_1^2} = \int_{\psi_1=0}^{\pi/2} |\widetilde{L}|^2 \sin\psi_1 \, \mathrm{d}\psi_1 \int_{k=0}^{\infty} E(k) \, \mathrm{d}k. \tag{3.64}$$

*i.e.*, the *rms* velocity of oscillation of the shock wave is independent of the incident energy spectrum if $A_e/A_v$ does not depend upon $k$. The influence on incident entropy fluctuations on the *rms* level of $\xi_t$ is illustrated in figure 3.20. The oscillation velocity is seen to be of the order of the incident velocity fluctuation. Entropy fluctuations with negatively correlated $u'$ and $T'$ enhance the oscillation velocity of the shock wave. Positively correlated fluctuations are observed to suppress it.

The amplitude of oscillation of the shock wave is similarly affected. Integration of equation (3.21) yields the following expression for the *rms* oscillation amplitude:

$$\overline{\xi^2} = 4\pi \int_{k=0}^{\infty} \int_{\psi_1=0}^{\pi/2} \frac{|\widetilde{L}|^2}{m^2 k^2} \, |A_v|^2 \, k^2 \sin\psi_1 \, \mathrm{d}k \, \mathrm{d}\psi_1. \tag{3.65}$$

Substituting for $|A_v|^2$ from equation (3.43) we get:

$$\overline{\xi^2} = \int_{\psi_1=0}^{\pi/2} \frac{|\widetilde{L}|^2}{m^2} \sin\psi_1 \, \mathrm{d}\psi_1 \int_{k=0}^{\infty} \frac{E(k)}{k^2} \, \mathrm{d}k. \tag{3.66}$$

Unlike the oscillation velocity, the amplitude of oscillation is dependent upon the incident spectrum. As shown in figure 3.21, the oscillation amplitude is increased by the incidence of temperature fluctuations that are negatively correlated with $u'$. Decrease in the amplitude of oscillation is observed when $u'$ and $T'$ in the incident field are positively correlated.

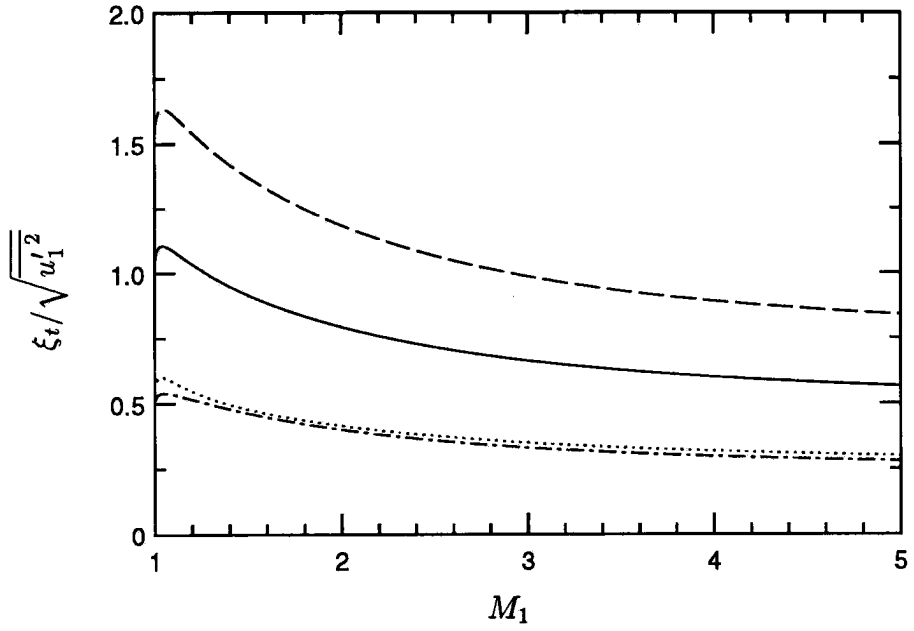


FIGURE 3.20: The *rms* level of fluctuations in shock speed. ——— (Pure vorticity), ---- ($A_r = 0.58; \phi_r = 0$), ····· ($A_r = 0.58; \phi_r = 180°$), —·— (Pure entropy).

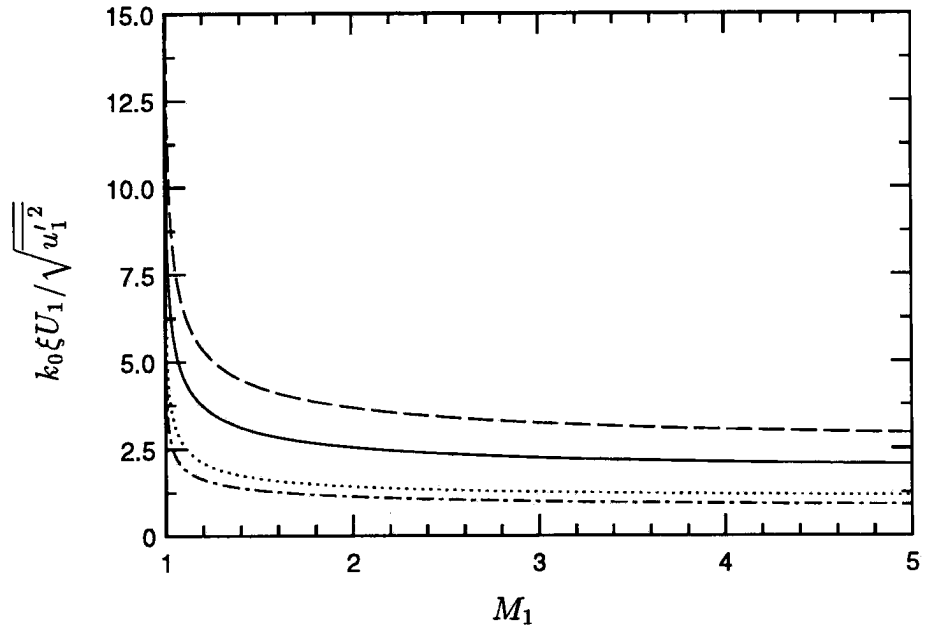


FIGURE 3.21: The *rms* level of displacement of the shock front. ——— (Pure vorticity), ---- ($A_r = 0.58; \phi_r = 0$), ····· ($A_r = 0.58; \phi_r = 180°$), —·— (Pure entropy).

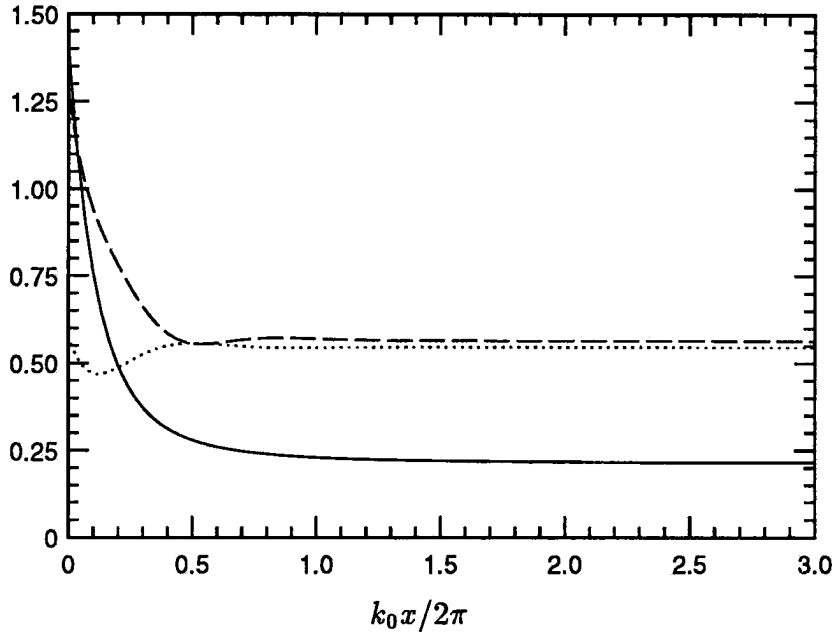


FIGURE 3.22: The variation of thermodynamic fluctuations behind a Mach 1.5 shock wave.The incident fluctuations correspond to $A_r = 0.58$ and $\phi_r = 0$. All three curves are normalized with $\sqrt{q_1^2}/U_1$. —— $(\sqrt{\overline{p_2'^2}}/\overline{p}_2)$, ---- $(\sqrt{\overline{\rho_2'^2}}/\overline{\rho}_2)$, ····· $(\sqrt{\overline{T_2'^2}}/\overline{T}_2)$.

## 3.8.5 Thermodynamic fluctuations

The streamwise variation of pressure, density and temperature fluctuations behind a Mach 1.5 shock wave is shown in figure 3.22. The incident field comprises of vorticity and entropy fluctuations ($A_r = 0.58, \phi_r = 0$). Pressure fluctuations decay exponentially behind the shock wave while density and temperature fluctuations exhibit non-monotonic behavior. The pressure fluctuations in the near-field are seen to be intense while the far-field intensity is smaller than those of density and temperature.

The preceding sections showed how entropy fluctuations affect the vortical part of the flow-field. Figure 3.23 shows that this influence extends to the acoustic component. The far-field intensity of pressure is plotted as a function of Mach number. The combined interaction of vorticity and entropy fluctuations is compared to that of vortical fluctuations alone. Fluctuations with a negative correlation between $u'$ and $T'$ are seen to increase the level of sound in the far-field while positively correlated fluctuations suppress it. Over the range of Mach numbers shown, this difference in sound level is calculated to be between 4 and 5 decibels.

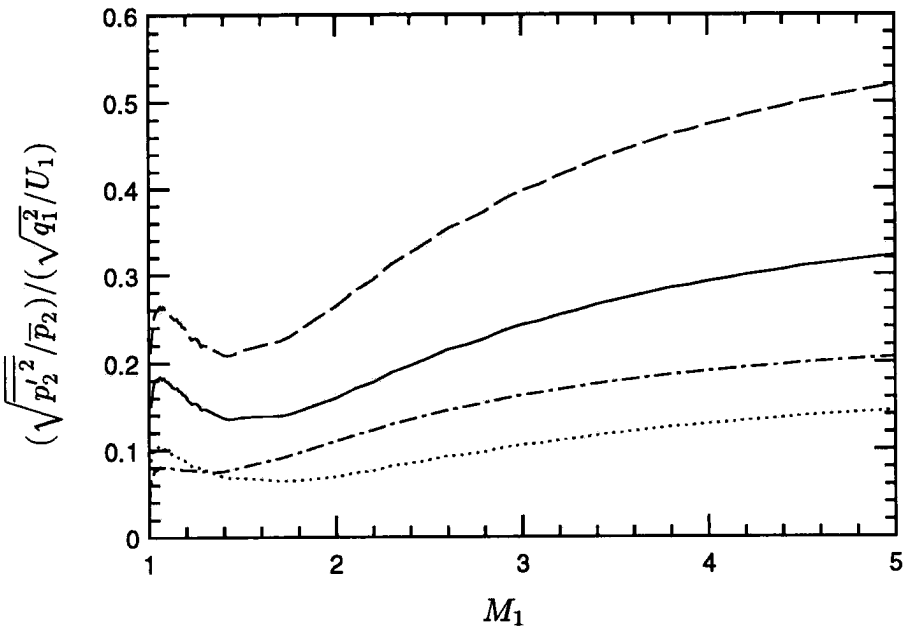


FIGURE 3.23: Intensity of pressure fluctuations in the far-field of the shock. ——— (Pure vorticity), ---- ($A_r = 0.58; \phi_r = 0$), ····· ($A_r = 0.58; \phi_r = 180°$),—·— (Pure entropy).

## 3.8.6 Morkovin's hypothesis across a shock wave

The applicability of Morkovin's hypothesis (Equation 3.1) across a shock wave is examined in this section. The incident field of vorticity and entropy fluctuations is constrained to satisfy Morkovin's hypothesis *i.e.*, $A_r$ is chosen (Equation 3.47b) such that the relation,

$$\frac{\rho_1'}{\overline{\rho}_1} = (\gamma - 1)M_1^2 \frac{u_1'}{U_1} \tag{3.67}$$

is satisfied at every wavenumber. The fluctuations in the far-field behind the shock are then examined to see if the hypothesis holds in the *rms* sense. The results (figure 3.24) show that the first part of the hypothesis *i.e.*, $\rho'/\overline{\rho} = -T'/\overline{T}$ is still a good approximation behind the shock wave especially, if the mean Mach number is less than 2. However the part of the hypothesis that relates $T'$ to $u'$ exhibits large deviation with Mach number. This behavior is explained below.

The equation, $\rho'/\overline{\rho} = -T'/\overline{T}$ is obtained by setting $p'$ to zero in the linearized equation of state. It amounts to neglecting the acoustic mode in comparison to the entropy mode. As seen from equation 3.2*d* it is an identity as far as the initial disturbance field is concerned. Upon interaction with the shock, the incident

field of vorticity and entropy fluctuations generate acoustic waves. The generation of acoustic waves is however accompanied by amplification of the incident entropy fluctuations. Also a fraction of the acoustic waves decays behind the shock. As a result the acoustic contribution in the far-field to the thermodynamic fluctuations becomes significant only at the larger Mach numbers. The first part of Morkovin's hypothesis is therefore a good approximation behind shock waves of moderate strength.

The relation,

$$\frac{T'}{\overline{T}} = -(\gamma - 1)M^2 \frac{u'}{U} \tag{3.68}$$

is obtained by assuming negligible fluctuations in stagnation temperature in the linear limit. Denoting the stagnation temperature by $T_0$,

$$\begin{aligned} T_0 &= T + \frac{u^2 + v^2 + w^2}{2c_p} \\ &= \overline{T} + T' + \frac{(U + u')^2 + v'^2 + w'^2}{2c_p}. \end{aligned} \tag{3.69}$$

Linearizing the above equation yields the following expression for fluctuations in stagnation temperature:

$$T_0' = T' + \frac{Uu'}{c_p}. \tag{3.70}$$

Setting $T_0'$ to zero and rearranging yields equation 3.68.

In the linear limit, fluctuations in stagnation temperature obey the relation, $DT_0'/Dt = \partial p'/\partial t$ behind the shock wave. Decomposing the temperature field into acoustic and entropic components, and the velocity into acoustic and vortical components allows decomposition of $T_0'$ into $T_{0\text{ent}}'$ and $T_{0\text{acous}}'$ such that $DT_{0\text{ent}}'/Dt = 0$ and $DT_{0\text{acous}}'/Dt = \partial p'/\partial t$.The Rankine-Hugoniot equations may then be used to show that equation 3.68 cannot be valid behind a shock wave if it is assumed to hold upstream of the shock. The energy equation requires the stagnation temperature to be constant across the shock in a frame of reference that moves at the instantaneous speed of the shock wave. *i.e.*,

$$\overline{T}_1 + T_1' + \frac{(U_1 + u_1' - \xi_t)^2 + v_1'^2 + w_1'^2}{2c_p} = \overline{T}_2 + T_2' + \frac{(U_2 + u_2' - \xi_t)^2 + v_2'^2 + w_2'^2}{2c_p}. \tag{3.71}$$

Linearization of the above equation yields:

$$T_1' + \frac{U_1(u_1' - \xi_t)}{c_p} = T_2' + \frac{U_2(u_2' - \xi_t)}{c_p}. \tag{3.72}$$

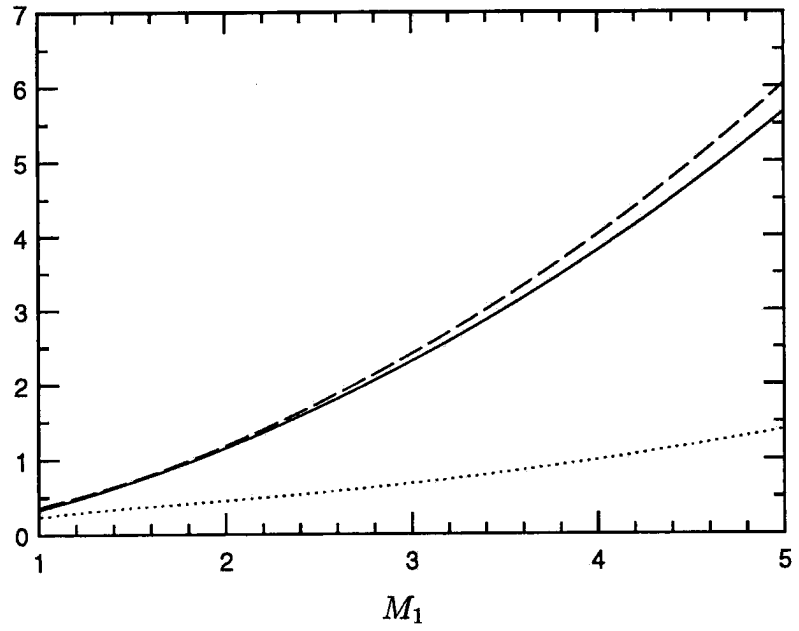


FIGURE 3.24: Evaluation of Morkovin's hypothesis in the far-field of the shock wave. —— $(\sqrt{\overline{\rho_2'^2}}/\overline{\rho}_2)$, ---- $(\sqrt{\overline{T_2'^2}}/\overline{T}_2)$, ····· $(\gamma-1)M_2^2\sqrt{\overline{u_2'^2}}/U_2$.

Upon rearrangement,

$$T_1' + \frac{U_1 u_1'}{c_p} = T_2' + \frac{U_2 u_2'}{c_p} + \frac{\xi_t}{c_p}(U_1 - U_2). \tag{3.73}$$

The validity of Morkovin's hypothesis upstream of the shock wave requires that:

$$T_1' + \frac{U_1 u_1'}{c_p} = 0. \tag{3.74}$$

This implies:

$$T_2' + \frac{U_2 u_2'}{c_p} = -\frac{\xi_t}{c_p}(U_1 - U_2). \tag{3.75}$$

*i.e.*, the fluctuations of stagnation temperature are not zero behind the shock wave. Dividing through by $\overline{T}_2$ and rearranging, we get:

$$\frac{T_2'}{\overline{T}_2} + (\gamma-1)M_2^2\frac{u_2'}{U_2} = -(\gamma-1)M_2\left(\frac{U_1}{U_2} - 1\right)\frac{\xi_t}{a_2}. \tag{3.76}$$

The applicability of Morkovin's hypothesis immediately behind the shock wave requires that,

$$(\gamma-1)M_2\left(\frac{U_1}{U_2} - 1\right)\frac{\xi_t}{a_2} \sim 0. \tag{3.77}$$

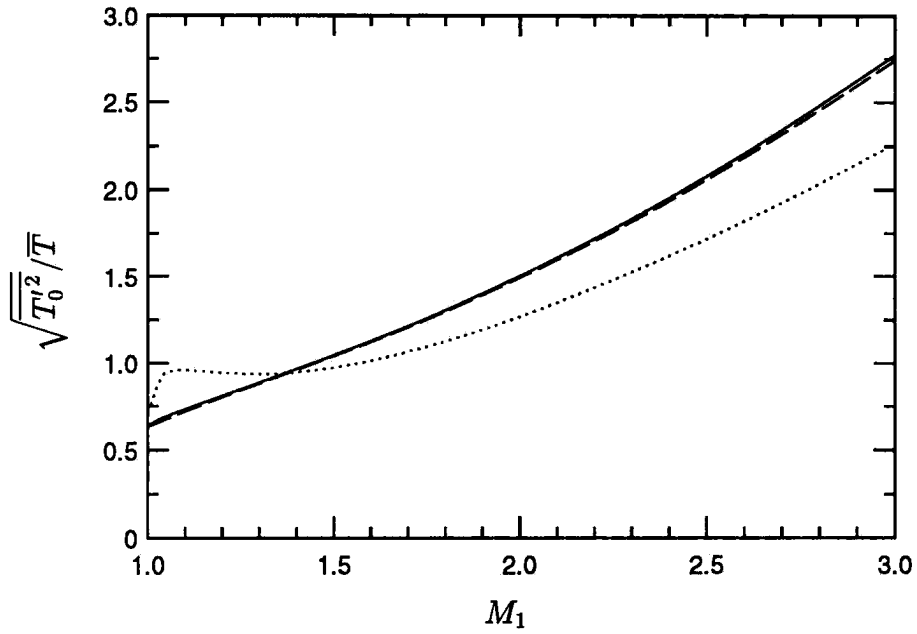


FIGURE 3.25: Decomposition of stagnation temperature fluctuations using linear analysis. All the curves are nondimensionalized by the upstream value of $u_{\text{rms}}/U$. ——— , far field value; - - - - , contribution due to vorticity and entropy fluctuations; ····· , near field value.

The *rms* values of the near-field stagnation temperature are plotted in figure 3.25 as a function of mean Mach number. The plotted values are seen to be comparable to the terms in Morkovin's hypothesis (figure 3.24) leading to inapplicability of the hypothesis *immediately behind* the shock wave. The above argument may next be extended to show why the hypothesis does not hold in the *far-field.* Decomposition of the stagnation temperature fluctuations into vorticity-entropy and acoustic components shows that both near and far field values of the stagnation temperature fluctuations are dominated by the vorticity-entropy component. As shown in figure 3.25, the vorticity-entropy component is indistinguishable from the total level in the far-field, while its contribution to the near-field level is greater than 80% over the range of Mach numbers shown. Figure 3.25 and equation 3.76 therefore show that appreciable level of stagnation temperature fluctuations are generated immediately behind the shock wave due to oscillation of the shock front. Most of these fluctuations arise from vorticity-entropy fluctuations, which convect downstream to generate an appreciable level of stagnation temperature fluctuations in the far-field of the shock wave. This leads to inapplicability of Morkovin's hypothesis in the far-field.

## 3.9 Summary

Inviscid linear analysis was used to study the simultaneous interaction of vorticity and entropy fluctuations with a shock wave. The two-dimensional interaction of a shock wave with a plane vorticity-entropy wave was initially considered. Expressions were derived for the flow-field behind the shock and the displacement of the shock front. The statistics of kinetic energy and thermodynamic fluctuations behind the shock wave were examined. The amplitude ratio and phase difference between the incident entropy and vorticity fluctuations were shown to significantly influence the statistics. Dependence upon the amplitude ratio was monotonic. Entropy fluctuations in phase with the incident vorticity fluctuations ($u'$ and $T'$ negatively correlated) were observed to enhance levels of kinetic energy and thermodynamic fluctuations behind the shock. Positively correlated fluctuations were observed to have a suppressing effect.

An explanation was provided to explain these trends. The evolution of fluctuating vorticity across the shock wave was noted to have two important contributions: bulk compression of incident vorticity and baroclinic production of vorticity through the incident entropy fluctuations. The upstream correlation between vorticity and entropy fluctuations was shown to determine whether these two sources of vorticity enhance or oppose each other thereby determining kinetic energy levels behind the shock wave. A scaling was then proposed for the evolution of vorticity across the shock wave.

The analysis was extended to consider the interaction of a shock wave with an isotropic field of vorticity and entropy fluctuations. Both spatial variation behind the shock and far-field levels of turbulence statistics were examined. The presence of entropy fluctuations was shown to significantly affect the levels of kinetic energy, vorticity and thermodynamic fluctuations behind the shock. Higher levels of kinetic energy and vorticity were observed when $u'$ and $T'$ in the incident fluctuations were negatively correlated. Positive correlation had the opposite effect. Acoustic waves were produced through the interaction. The level of sound behind the shock wave was enhanced by the incidence of fluctuations with negative correlation between $u'$ and $T'$. Suppression of sound level was observed if the incident fluctuations were positively correlated. The incidence of entropy fluctuations was observed to affect the oscillation of the shock front. Negatively correlated fluctuations of $u'$ and $T'$ increased the velocity and amplitude of oscillation while positively correlated

fluctuations suppressed it.

The applicability of Morkovin's hypothesis behind a shock wave was examined. Statistics in the far-field indicate that neglect of the acoustic mode is a good approximation in the far-field of shock waves of moderate strength ($M_1 < 2$). The part of the hypothesis relating $u'$ and $T'$ was seen to be invalid behind the shock. Non-negligible oscillation of the shock front was shown to be responsible.

# Chapter Four

# Direct Numerical Simulation: Numerical Procedure

## 4.1 Introduction

This chapter discusses the numerical computation of the interaction of a turbulent shear flow with a normal shock wave. A schematic of the problem is shown in figure 4.1. Note that the mean flow upstream of the shock wave is supersonic and has uniform velocity gradient across the mean streamlines. Also, a mean temperature gradient that maintains uniform mean Mach number across the mean streamlines is imposed. The mean flow at the inflow is approximately given by the relations,

$$U_1(y) = U_0 + S(y - y_{\min}), \qquad \overline{p}_1(y) = \frac{1}{\gamma}, \qquad \overline{T}_1(y) = \frac{U_1^2(y)}{(\gamma - 1)M_1^2}. \tag{4.1}$$

The following sections describe the procedure used to numerically compute the interaction of this shear flow with a normal shock wave. Section 4.2 describes the governing equations that were solved. Details of the computational grid are provided in section 4.3. The methods to compute the spatial derivatives and the time advancement scheme are outlined in sections 4.4 and 4.5 respectively. Section 4.6 describes details of how the shock wave was treated. This is followed in sections 4.7 and 4.8 by a description of the initial and boundary conditions.

## 4.2 Governing equations

The governing equations are the three-dimensional, unsteady, compressible continuity, energy and Navier Stokes equations. The equations are solved in Cartesian coordinates for the conservative variables; *i.e.*,

$$\frac{\partial \rho^*}{\partial t^*} + \frac{\partial}{\partial x_i^*}(\rho^* u_i^*) = 0 \tag{4.2a}$$

$$\frac{\partial}{\partial t^*}(\rho^* u_i^*) + \frac{\partial}{\partial x_j^*}(\rho^* u_i^* u_j^* + p^* \delta_{ij}) = \frac{\partial \tau_{ij}^*}{\partial x_j^*} \tag{4.2b}$$

$$\frac{\partial E_t^*}{\partial t^*} + \frac{\partial}{\partial x_i^*}[(E_t^* + p^*)u_i^*] = -\frac{\partial q_i^*}{\partial x_i^*} + \frac{\partial}{\partial x_j^*}(u_i^* \tau_{ij}^*). \tag{4.2c}$$

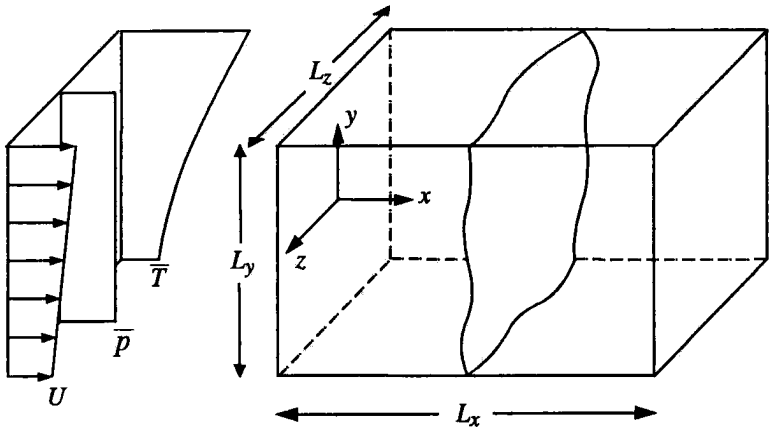


FIGURE 4.1: A schematic of the computational domain. Also shown is the mean flow at the inflow of the domain.

The superscript '*' is used to indicate that the variables are in dimensional form. The variables $\rho^*, u_i^*, p^*, \tau_{ij}^*$ and $q_i^*$ denote the density, velocity, thermodynamic pressure, viscous stress tensor and heat flux respectively. $E_t^*$ denotes the total energy which is defined as the sum of internal energy and kinetic energy; *i.e.*,

$$E_t^* = \rho^*(e^* + \frac{u_i^* u_i^*}{2}), \tag{4.3}$$

where the variable $e^*$ represents the specific internal energy. The viscous stress and heat flux are modeled using Stokes hypothesis and Fourier's law of heat conduction; *i.e.*,

$$\tau_{ij}^* = \mu^* \left( \frac{\partial u_i^*}{\partial x_j^*} + \frac{\partial u_j^*}{\partial x_i^*} - \frac{2}{3} \frac{\partial u_k^*}{\partial x_k^*} \delta_{ij} \right), \tag{4.4a}$$

$$q_i^* = -k^* \frac{\partial T^*}{\partial x_i^*}, \tag{4.4b}$$

where the variables $\mu^*$ and $k^*$ denote the molecular viscosity and thermal conductivity respectively. Note that the bulk viscosity of the fluid is assumed to be zero. The fluid is assumed to be a perfect gas; *i.e.*,

$$p^* = \rho^* R T^* \tag{4.5}$$

where $R$ is the specific gas constant. Also the specific internal energy and enthalpy ($h^*$) are given by:

$$e^* = c_v T^* \qquad \text{and} \qquad h^* = c_p T^*, \tag{4.6}$$

where the variables $c_v$ and $c_p$ denote the specific heats at constant volume and constant pressure respectively. The ratio of specific heats, $\gamma = c_p/c_v$ is assumed to be 1.4 in our computations. Note that the variation of viscosity with temperature is neglected in the turbulent calculations. Instead of the commonly used power law

$$\mu^* \propto T^{*n}, \tag{4.7}$$

we set $\mu^*$ to be constant. The desire to reduce the variation in turbulence Reynolds number across mean streamlines prompted this approximation. If in addition to the gradient in mean density across mean streamlines, $\mu^*$ were allowed to vary with temperature, then the variation in turbulence Reynolds number across the mean streamlines would be large. Setting $\mu^*$ to be constant reduces the variation in turbulence Reynolds number.

The thermal conductivity is related to molecular viscosity through the assumption of constant Prandtl number:

$$Pr = \frac{\mu^* c_p}{k^*}. \tag{4.8}$$

The Prandtl number was assumed to be 0.7 in our calculations.

The governing equations are non-dimensionalized prior to solution. An arbitrary length $L_0^*$ and reference speed of sound $c_0^*$ are chosen as length and velocity scales respectively. The density and viscosity at the reference state are then used to nondimensionalize density and viscosity. This yields the following non-dimensional variables:

$$x_i = \frac{x_i^*}{L_0^*}, \quad t = \frac{t^* c_0^*}{L_0^*}, \quad u_i = \frac{u_i^*}{c_0^*}, \quad \rho = \frac{\rho^*}{\rho_0}.$$

$$\mu = \frac{\mu^*}{\mu_0^*}, \quad p = \frac{p^*}{\rho_0^* c_0^{*2}} = \frac{p^*}{\gamma p_0^*}, \quad T = \frac{1}{\gamma - 1}\frac{T^*}{T_0^*}, \quad e = \frac{e^*}{c_0^{*2}}. \tag{4.9}$$

The non-dimensional form of the governing equations is as follows:

$$\frac{\partial \rho}{\partial t} = -\frac{\partial}{\partial x_i}(\rho u_i) \tag{4.10a}$$

$$\frac{\partial}{\partial t}(\rho u_i) = -\frac{\partial}{\partial x_j}(\rho u_i u_j + p\delta_{ij}) + \frac{\partial \tau_{ij}}{\partial x_j} \tag{4.10b}$$

$$\frac{\partial E_t}{\partial t} = -\frac{\partial}{\partial x_i}[(E_t + p)u_i] - \frac{\partial q_i}{\partial x_i} + \frac{\partial}{\partial x_j}(u_i \tau_{ij}). \tag{4.10c}$$

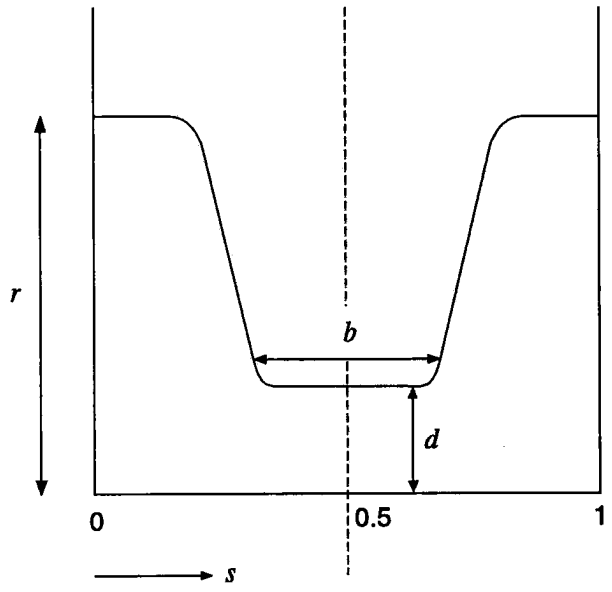


FIGURE 4.2: A schematic of the desired slope ($\mathrm{d}x/\mathrm{d}s$) in the mapping between non-uniform ($x$) and uniform ($s$) grid.

The constitutive relations are given by:

$$\tau_{ij} = \frac{\mu}{Re}\left(\frac{\partial u_i}{\partial x_j} + \frac{\partial u_j}{\partial x_i} - \frac{2}{3}\frac{\partial u_k}{\partial x_k}\delta_{ij}\right)$$

$$q_i = -\frac{\mu}{RePr}\frac{\partial T}{\partial x_i}. \tag{4.11}$$

where $Re$ is a Reynolds number defined as:

$$Re = \frac{\rho_0^* c_0^* L_0^*}{\mu_0^*}. \tag{4.12}$$

Similarly, the perfect gas law in non-dimensional form is given by:

$$p = \frac{\gamma - 1}{\gamma}\rho T. \tag{4.13}$$

## 4.3 Computational mesh

The governing equations are discretized on a structured mesh that is non-uniform in the streamwise direction and uniform in the $y$ and $z$ directions. The streamwise nonuniformity is designed to cluster points around the shock wave. An analytical transformation is used for this purpose.

Using the variable $s$ to denote a coordinate that varies uniformly from 0 to 1, a transformation $x = x(s)$ is derived to cluster points around the center of the domain (since the shock wave is around the center). $x$ varies from 0 to 1 initially; it is subsequently rescaled to vary from 0 to $L_x$ where $L_x$ is the streamwise extent of the computational domain. Recognizing that $\mathrm{d}x/\mathrm{d}s$ is representative of $\Delta x/\Delta s$ and hence the mesh spacing, the derivation is initiated by assuming a suitable form for $\mathrm{d}x/\mathrm{d}s$. The variation shown in figure 4.2 was considered desirable. The variables $d$ and $r$ approximately represent the mesh size at the shock wave and the boundaries respectively. The extent of the domain that has a fine mesh is controlled by the variables $b$ and $d$. Superposition of two hyperbolic tangent profiles was used to achieve the desired profile; *i.e.*,

$$\frac{1}{C}\frac{\mathrm{d}x}{\mathrm{d}s} = r + \left(\frac{r-d}{2}\right)\Big[\tanh b(s-3/4) - \tanh b(s-1/4)\Big] \tag{4.14}$$

where $C$ is an undetermined constant. Integrating the above equation and using the conditions $x(0) = 0, x(1) = 1$ yields the following expression:

$$x = \frac{rs + \left(\frac{r-d}{2b}\right)\ln\left[\frac{\cosh b(s-3/4)\cosh b/4}{\cosh b(s-1/4)\cosh 3b/4}\right]}{r + \left(\frac{r-d}{b}\right)\ln\left[\frac{\cosh b/4}{\cosh 3b/4}\right]}. \tag{4.15}$$

The above equation is rescaled to allow $x$ to vary from 0 to $L_x$ such that points are clustered around $L_x/2$. This yields the following expression for the nonuniform mesh:

$$\frac{x}{L_x} = \frac{rs + \left(\frac{r-d}{2b}\right)\ln\left[\frac{\cosh b(s-3/4)\cosh b/4}{\cosh b(s-1/4)\cosh 3b/4}\right]}{r + \left(\frac{r-d}{b}\right)\ln\left[\frac{\cosh b/4}{\cosh 3b/4}\right]} \tag{4.16}$$

Equation 4.16 is differentiated to obtain the metrics, $\mathrm{d}x/\mathrm{d}s$ and $\mathrm{d}^2x/\mathrm{d}s^2$. Typical values for the parameters $b, r$ and $d$ are 10, 1.9 and 0.15 respectively. For example, a grid of 191 points and the above choice of parameters is used to compute a Mach 1.5 shock wave. Figure 4.3 illustrates the streamwise variation of the grid spacing that results.

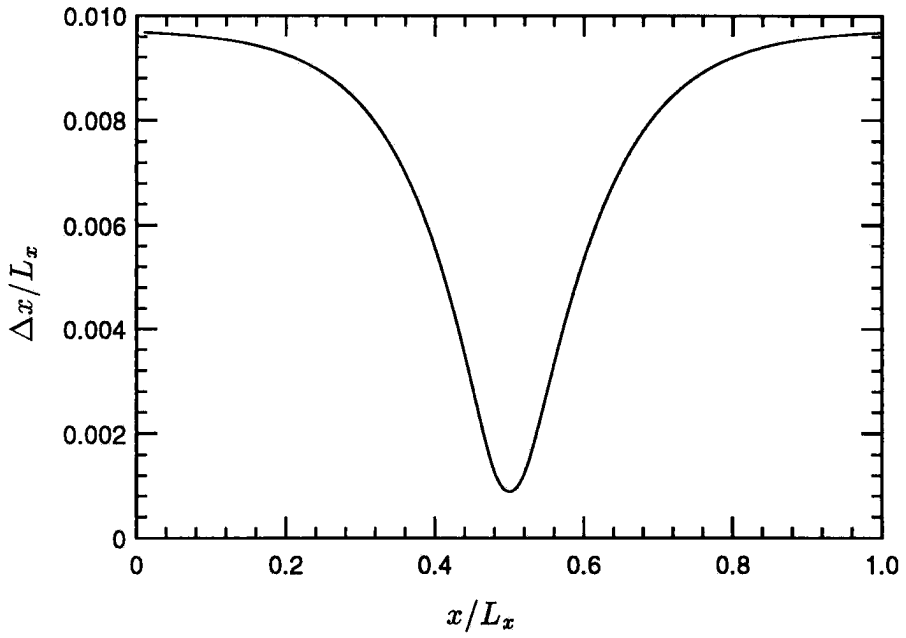


FIGURE 4.3: An example of the non-uniform mesh in the streamwise direction. The mesh spacing is plotted against streamwise distance.

## 4.4 Computation of spatial derivatives

The spatial derivatives in the governing equations are computed using a modified Pade scheme developed by Lele (1992b). The first derivative on a uniform mesh is given by the following implicit equation:

$$f'_{j-1} + a_1 f'_j + f'_{j+1} = a_2 \frac{(f_{j+1} - f_{j-1})}{\Delta s} + a_3 \frac{(f_{j+2} - f_{j-2})}{\Delta s} \tag{4.19}$$

where the coefficients $a_2$ and $a_3$ are expressed in terms of $a_1$ as:

$$a_2 = \frac{1 + 2a_1}{3}; \qquad a_3 = \frac{4 - a_1}{12}. \tag{4.20}$$

The above equation with the parameter $a_1$ set to equal 3 is applied to the interior nodes ($j$=4 to $N - 3$). Along the periodic directions, the above equation is also applied to the boundary nodes. In the non-periodic directions, expressions are derived for the nodes at the boundary to close the system. These expressions are constrained to satisfy discrete global conservation when coupled to the scheme applied in the interior. Also the tridiagonal aspect of the scheme is preserved. The details are described by Lele (1992b) and are not repeated here. These additional equations are given by:

$$2f'_1 + 4f'_2 = \frac{-5f_1 + 4f_2 + f_3}{\Delta s}; \qquad j = 1 \tag{4.21a}$$

$$f'_1 + 4f'_2 + f'_3 = 3\frac{f_3 - f_1}{\Delta s}; \qquad j = 2 \tag{4.21b}$$

$$f'_2 + \tilde{a}_1 f'_3 + f'_4 = \tilde{a}_2\frac{(f_4 - f_2)}{\Delta s} + \tilde{a}_3\frac{(f_5 - f_1)}{\Delta s}; \qquad j = 3. \tag{4.21c}$$

The variables $\tilde{a}_1, \tilde{a}_2$ and $\tilde{a}_3$ are defined as:

$$\tilde{a}_1 = 16\frac{1 + 2a_1}{40 - a_1}; \quad \tilde{a}_2 = \frac{1 + 2\tilde{a}_1}{3}; \quad \tilde{a}_3 = \frac{4 - \tilde{a}_1}{12}. \tag{4.22}$$

Similar expressions are written for the nodes $j = N - 2$ to $N$. The resulting system of equations is then solved following LDU decomposition. Note that the derivatives are computed on a uniform mesh. The transformation derived in the preceding section is used to obtain derivatives at the non-uniformly spaced nodes in the $x$ direction; *i.e.*,

$$\frac{\partial f}{\partial x} = \frac{1}{h(s)}\frac{\partial f}{\partial s} \tag{4.23}$$

where $h(s) = \mathrm{d}x/\mathrm{d}s$. Taylor's series analysis (Lele, 1992b) shows that the scheme used in the interior is sixth order accurate. The equations used at the boundaries are less accurate; equations (4.21*a*) and (4.21*b*, *c*) are third and fourth order accurate respectively.

A similar compact scheme is used to compute the second derivatives. The following expression is used at the interior points ($j = 3$ to $N - 2$):

$$f''_{j-1} + b_1 f''_j + f''_{j+1} = b_2\frac{f_{j+1} - 2f_j + f_{j-1}}{\Delta s^2} + b_3\frac{f_{j+2} - 2f_j + f_{j-2}}{\Delta s^2} \tag{4.24}$$

where $b_2$ and $b_3$ are given by:

$$b_2 = 4\frac{(b_1 - 1)}{3}; \qquad b_3 = \frac{10 - b_1}{12}. \tag{4.25}$$

The variable $b_1$ is set to $11/2$ thereby yielding sixth order accuracy (Lele, 1992b). Along non-periodic directions, the system of equations is closed by the following expressions near the boundaries:

$$f''_1 + 11f''_2 = \frac{13f_1 - 27f_2 + 15f_3 - f_4}{\Delta s^2}; \qquad j = 1 \tag{4.26a}$$

$$f''_1 + 10f''_2 + f''_3 = \frac{12(f_3 - 2f_2 + f_1)}{\Delta s^2}; \qquad j = 2. \tag{4.26b}$$

Equations (4.26*a*) and (4.26*b*) are third and fourth order respectively. Similar expressions are written for the nodes at the other boundary. The system of equations

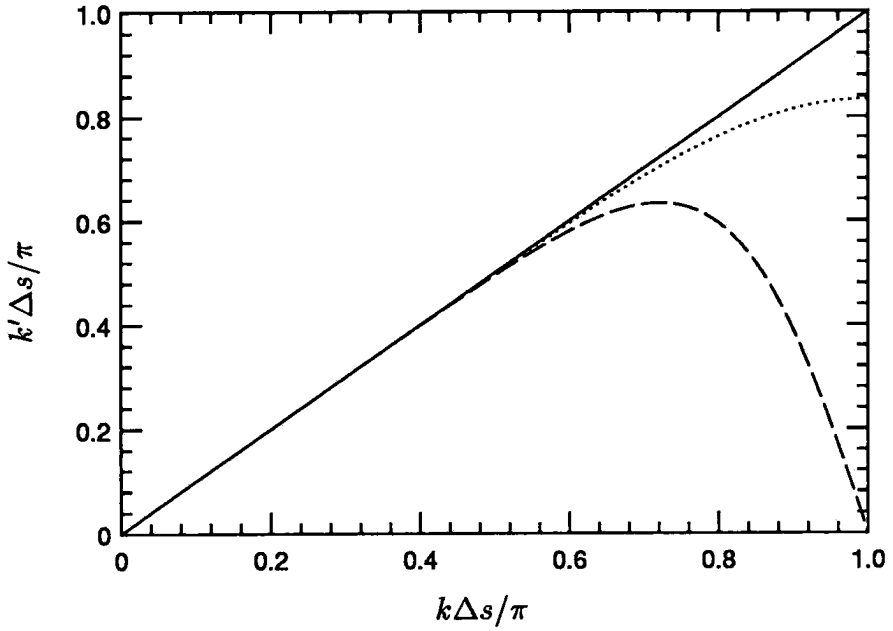


FIGURE 4.4: The modified wavenumber of the sixth order Pade scheme. ——— (Exact), - - - - (First derivative), ····· (Second derivative). Note that $\sqrt{k'^2}$ is plotted for the second derivative.

is then solved to obtain the second derivatives on the uniform mesh. Analytical expressions for the metrics (section 4.3) are then used to obtain the second derivatives on the nonuniformly distributed points in the streamwise direction; *i.e.*,

$$\frac{\partial^2 f}{\partial x^2} = \frac{1}{h^2}\frac{\partial^2 f}{\partial s^2} - \frac{h'}{h^2}\frac{\partial f}{\partial x}. \tag{4.27}$$

The schemes used to compute the derivatives in the interior have good resolution properties in addition to being sixth order accurate. Fourier analysis and the 'modified wavenumber' provide an effective means of quantifying the resolution characteristics. Consider differentiating the function $e^{ikx}$. The exact solution is $ike^{ikx}$. Numerical differentiation on the other hand will yield a solution of the form $ik'e^{ikx}$. The variable $k'$ is a function of $k$ and is called the modified wavenumber. The closeness of $k'$ to $k$ provides a measure of the resolution characteristics of the scheme.

For the differencing scheme described by equation (4.19) the modified wavenumber is given by:

$$k'\Delta s = 2\frac{(a_2 \sin k\Delta s + a_3 \sin 2k\Delta s)}{a_1 + 2\cos k\Delta s}. \tag{4.28}$$

A similar procedure can be followed for the second derivative. Numerical differentiation would yield an expression of the form $-k'^2 e^{ikx}$ as compared to the exact solution of $-k^2 e^{ikx}$. Once again the modified wavenumber may be examined as a function of $k$. For the scheme described by equation (4.24) the modified wavenumber is given by:

$$k'\Delta s = 2\sqrt{\frac{b_2 \sin^2 k\Delta s/2 + b_3 \sin^2 k\Delta s}{b_1 + 2\cos k\Delta s}}. \tag{4.29}$$

The resolution properties of the spatial scheme are illustrated in figure 4.4 where the modified wavenumber is compared to the exact solution. Note that about 55% of the range of wavenumbers is very accurately represented.

## 4.5 Time advancement

An explicit scheme is used for time advancement. The third order compact storage Runge-Kutta scheme (Wray, 1986) is used to advance the conservative variables $(\rho, \rho u_i, E_t)$. When applied to the equation, $dy/dt = f(y,t)$, this scheme has the following predictor-corrector form (we advance from $t_n$ to $t_{n+1}$):

$$y_{n+1/3} = y_n + \frac{8}{15}\Delta t f(y_n, t_n) \tag{4.30a}$$

$$y_{n+2/3} = y_n + \frac{1}{4}\Delta t f(y_n, t_n) + \frac{5}{12}\Delta t f(y_{n+1/3}, t_{n+1/3}) \tag{4.30b}$$

$$y_{n+1} = y_n + \frac{1}{4}\Delta t f(y_n, t_n) + \frac{3}{4}\Delta t f(y_{n+2/3}, t_{n+2/3}) \tag{4.30c}$$

where:

$$t_{n+1/3} = t + \frac{8}{15}\Delta t; \qquad t_{n+2/3} = t_n + \frac{2}{3}\Delta t. \tag{4.30d}$$

The time step is constrained by the following requirements of convective and viscous stability. Convective stability is determined by the wave equation:

$$\frac{\partial f}{\partial t} + (u+c)\frac{\partial f}{\partial x} = 0 \tag{4.31}$$

where the variables $u$ and $c$ represent the velocity and speed of sound respectively. $u+c$ is used as the convection velocity since it is the largest of the three eigenvalues of the one-dimensional Euler equations. Using the transformation $x = x(s)$ the above equation is rewritten as:

$$\frac{\partial f}{\partial t} + \frac{u+c}{h(s)}\frac{\partial f}{\partial s} = 0. \tag{4.32}$$

Recognizing that the time step will be constrained by the maximum value of $(u + c)/h(s)$, we approximate the above equation by:

$$\frac{\partial f}{\partial t} + \frac{u+c}{h_{\min}} \frac{\partial f}{\partial s} = 0 \tag{4.33}$$

Assuming periodic boundary conditions and Fourier transforming yields the following equation for the Fourier coefficients:

$$\frac{d\widehat{f}}{dt} = -i \frac{u+c}{h_{\min}} k' \widehat{f}. \tag{4.34}$$

where the variables $\widehat{f}$ and $k'$ denote the Fourier transform of $f$ and the modified wavenumber respectively.

The above equation is of the form $y' = \lambda y$ where the variable $\lambda$ is imaginary. Numerical stability requires that:

$$\lambda \Delta t < \sqrt{3} \tag{4.35}$$

when RK3 is used to integrate the above equation. Thus,

$$\frac{u+c}{h_{\min}} k' \Delta t < \sqrt{3}. \tag{4.36}$$

The maximum value of $k'$ as given by equation (4.28) is $1.989/\Delta s$. The stability criterion is therefore:

$$\frac{(u+c)\Delta t}{h_{\min} \Delta s} < \frac{\sqrt{3}}{1.989}. \tag{4.37}$$

Since $h_{\min}\Delta s$ equals $\Delta x_{\min}$ to a very good approximation, the above equation may be expressed as:

$$(u+c)\frac{\Delta t}{\Delta x_{\min}} < 0.871. \tag{4.38}$$

The corresponding criterion that we use in the three dimensional computations is:

$$\left[\frac{|u_1|+c}{\Delta x_1} + \frac{|u_2|+c}{\Delta x_2} + \frac{|u_3|+c}{\Delta x_3}\right]_{\max} \Delta t < 0.871 \tag{4.39}$$

where the maximum value is computed over the entire domain. Defining a CFL number as,

$$CFL = \left[\frac{|u_1|+c}{\Delta x_1} + \frac{|u_2|+c}{\Delta x_2} + \frac{|u_3|+c}{\Delta x_3}\right]_{\max} \Delta t, \tag{4.40}$$

the time step is given by $CFL < 0.871$.

The viscous terms in the Navier Stokes equations impose a similar restriction on the time step. Consider the diffusion equation:

$$\frac{\partial f}{\partial t} = \nu \frac{\partial^2 f}{\partial s^2}. \tag{4.41}$$

Assuming periodic boundary conditions and Fourier transforming we get:

$$\frac{d\widehat{f}}{dt} = -\nu k'^2 \widehat{f} \tag{4.42}$$

which is of the form $y' = \lambda y$ where $\lambda$ is real and $k'$ is the modified wavenumber for the second derivative approximation (equation 4.29). The use of RK3 to integrate the above equation requires that:

$$|\lambda|\Delta t = \nu k'^2 \Delta t < 2.5. \tag{4.43}$$

The modified wavenumber for the second derivative approximation has a maximum value of $2.619/\Delta s$. Substitution into equation (4.43) yields the following stability criterion:

$$\frac{\nu \Delta t}{\Delta s^2} < 0.365. \tag{4.44}$$

The variable $\Delta s$ is replaced by $\Delta x_{\min}$ in computing the time step for a nonuniform mesh. The stability criterion in three dimensions is:

$$\Delta t \left( \frac{\nu}{\Delta x_1^2} + \frac{\nu}{\Delta x_2^2} + \frac{\nu}{\Delta x_3^2} \right)_{\max} < 0.365. \tag{4.45}$$

The convective criterion is the more restrictive of the two criteria for the computations reported. In practice either a constant time step is specified or the $CFL$ number is specified which is then used to compute the time step from equation (4.40). Typically accuracy requirements restrict the $CFL$ number (as defined in equation 4.40) to be less than 0.5.

## 4.6 Treatment of the shock wave

### 4.6.1 Resolving the thickness of the shock wave

The thickness of a shock wave in a viscous (Navier Stokes) fluid represents a balance between inertial forces, viscous forces and compressibility. As a result, typical shock thicknesses in a turbulent medium are considerably smaller than typical

lengthscales of the turbulence. To illustrate this, consider the following expression for the thickness of a weak laminar shock derived by Taylor (for details see Thompson, 1984):

$$\frac{\delta}{\Lambda} = \frac{3}{4}\frac{A}{M_1 - 1} \tag{4.46}$$

where $\delta$ is the shock thickness, $\Lambda$ is the mean free path of the medium and $A$ is a constant that depends on the precise definition of the shock thickness. $A$ has the value 9.19 if the edges of the shock wave are defined to lie at $U - U_2 = 0.99(U_1 - U_2)$ and $U - U_2 = 0.01(U_1 - U_2)$. The mean free path may be approximated by the relation:

$$\Lambda = \frac{\mu_1}{\rho_1 c_1}. \tag{4.47}$$

This yields the following expression for shock thickness:

$$\frac{c_1 \delta}{\nu_1} = \frac{6.89}{M_1 - 1} \tag{4.48}$$

where $M_1$ denotes the shock-normal upstream Mach number. In assessing the thickness of a shock wave in a turbulent medium, $M_1 \sim (\overline{U}_1 + u_1')/(\overline{c}_1 + c_1')$, which upon linearizing equals $M_1(1 + u_1'/\overline{U}_1 - c_1'/\overline{c}_1)$. The above estimate is expected to be adequate as long as the change in Mach number caused by the turbulent fluctuations is small compared to the mean Mach number. Typically, this is a good assumption for mean Mach numbers exceeding 1.15. In our calculations the mean Mach number exceeds 1.2. Also, the *rms* values of $u_1'/\overline{U}_1$ and $c_1'/\overline{c}_1$ are about 2.5%. $M_1(1 + u_1'/\overline{U}_1 - c_1'/\overline{c}_1)$ is therefore equal to $M_1$ to a very good approximation.

The shock thickness is therefore given by:

$$\frac{c_1 \delta}{\nu_1} = \frac{6.89}{M_1 - 1}. \tag{4.49}$$

The thickness of the shock wave is related to the turbulence lengthscale through the turbulence Reynolds number. Defining a Reynolds number based on the streamwise Taylor microscale as,

$$R_\lambda = \frac{\sqrt{\overline{u_1'^2}}\lambda_1}{\nu_1} \tag{4.50}$$

equations (4.49) and (4.50) may be combined to obtain the following expression relating the turbulence lengthscale to the shock wave thickness:

$$\frac{\lambda_1}{\delta}\frac{\sqrt{\overline{u_1'^2}}}{\overline{c}_1} = R_\lambda \frac{(M_1 - 1)}{6.89}. \tag{4.51}$$

Now,

$$\frac{\sqrt{\overline{u_1'^2}}}{\overline{c}_1} = \frac{\sqrt{\overline{u_1'^2}}}{q_1}\frac{q_1}{\overline{c}_1} = M_t\sqrt{\frac{\overline{u_1'^2}}{q_1^2}}. \tag{4.52}$$

where the fluctuation Mach number $M_t$ is defined as $M_t = q_1/\overline{c}_1$. The quantity, $\overline{u_1'^2}/q_1^2$ has a typical value of 0.55 in incompressible shear flows (Townsend, 1976), implying that:

$$\frac{\sqrt{\overline{u_1'^2}}}{\overline{c}_1} \sim 0.74M_t. \tag{4.53}$$

Substituting into equation (4.51) we get,

$$\frac{\lambda_1}{\delta} = \frac{R_\lambda}{5.1}\frac{(M_1 - 1)}{M_t}. \tag{4.54}$$

Typical values for $R_\lambda$ and $M_t$ in our calculations are 30 and 0.03 respectively. For these values of $R_\lambda$ and $M_t$, we tabulate below the ratio of streamwise Taylor microscale to shock thickness as a function of the mean upstream Mach number.

| $M_1$ | $\lambda_1/\delta$ |
|---|---|
| 1.2 | 39 |
| 1.5 | 98 |
| 2.0 | 196 |
| 3.0 | 392 |

TABLE 4.1: The ratio of the upstream streamwise Taylor microscale to shock thickness as a function of the mean upstream Mach number.

This disparity in lengthscale results in the number of points in the streamwise direction increasing with Mach number if the shock wave is to be resolved. Also the system of equations becomes increasingly stiff. These effects are estimated below.

The smallest grid spacing in the streamwise direction is determined by the shock thickness. Typically about 10 points are needed to resolve the shock wave thickness. The smallest grid spacing $\Delta x_{\min}$ is therefore approximately $\delta/10$. Although a stretched mesh is used in the streamwise direction, accuracy requirements impose an upper bound on the rate of stretching. The total number of points and the rate of stretching determine the maximum grid spacing $\Delta x_{\max}$. In our shock-resolving

calculations, $\Delta x_{\max}/\Delta x_{\min} \sim 20$. This maximum grid spacing which occurs at the boundaries is required to resolve the turbulent fluctuations. The length of the domain upstream of the shock wave is determined by the distance taken by the inflow fluctuations to evolve into a 'realistic' state. Since the shock is around the center of the domain, the domain length downstream of the shock is the same as that upstream. Typically, the length of the domain in our calculations is about $10\lambda_1$ in the streamwise direction. *i.e.*,

$$\begin{aligned} L_x \sim 10\lambda_1 &= 10\frac{\lambda_1}{\delta}\delta \\ &= 10\frac{R_\lambda}{5.1}\frac{(M_1-1)}{M_t}\delta \\ &\sim 1961(M_1-1)\delta \end{aligned} \tag{4.55}$$

where $R_\lambda$ and $M_t$ are taken as 30 and 0.03 respectively. A crude estimate of the number of points in the streamwise direction is provided. We assume that the non-uniform mesh is such that the mesh spacing is approximately $\Delta x_{\max}$ on both sides of the shock and $\Delta x_{\min}$ inside the shock wave. Note that this assumption provides an optimistic estimate of the number of streamwise points. The actual number of points would be higher if the variation in mesh spacing is properly represented. The number of points in the streamwise direction is given by:

$$\begin{aligned} N_x &\sim \frac{L_x}{\Delta x_{\max}} + 10 \\ &= 1961(M_1-1)\underbrace{\frac{\delta}{\Delta x_{\min}}}_{10}\underbrace{\frac{\Delta x_{\max}}{\Delta x_{\min}}}_{1/20} + 10 \\ &= 980(M_1-1) + 10. \end{aligned} \tag{4.56}$$

| $M_1$ | $N_x$ |
|---|---|
| 1.2 | 206 |
| 1.5 | 500 |
| 2.0 | 990 |
| 3.0 | 1970 |

TABLE 4.2: The approximate number of streamwise points in a shock-resolving computation as a function of the upstream Mach number.

$N_x$ is tabulated as a function of $M_1$ in Table 4.2. It becomes apparent that it would be impractical to exceed a mean Mach number of 1.5 while trying to resolve the thickness of the shock wave.

The increase in numerical stiffness with Mach number is illustrated next. As noted in Section 4.5, the time step is determined by the time scale of acoustic wave propagation over the smallest grid spacing. *i.e.*,

$$\Delta t = \frac{CFL}{\left[\frac{|u_1|+c}{\Delta x_1} + \frac{|u_2|+c}{\Delta x_2} + \frac{|u_3|+c}{\Delta x_3}\right]_{\max}} \tag{4.57}$$

which may be approximated as:

$$\Delta t \sim \frac{\Delta x_{\min}}{c} \frac{CFL}{M_1 + 1 + \underbrace{\frac{\Delta x_{\min}}{\Delta x_2}}_{\sim 0.05} + \underbrace{\frac{\Delta x_{\min}}{\Delta x_3}}_{\sim 0.05}} \tag{4.58}$$

where $c = \bar{c}_1$ is the mean sound speed upstream of the shock. This yields the following expression for the time step:

$$\Delta t = CFL \, \frac{\Delta x_{\min}}{c(M_1 + 1.1)}. \tag{4.59}$$

Substituting $\delta/10$ for $\Delta x_{\min}$ and using equation (4.54) for $\delta$, we get:

$$\frac{R_\lambda}{M_t} \frac{c\Delta t}{\lambda_1} \frac{1}{CFL} = \frac{0.51}{(M_1 - 1)(M_1 + 1.1)}. \tag{4.60}$$

| $M_1$ | Timestep |
|---|---|
| 1.2 | 1.11 |
| 1.5 | 0.39 |
| 2.0 | 0.16 |
| 3.0 | 0.06 |

TABLE 4.3: The variation of the timestep with the mean upstream Mach number in a shock-resolving computation.

This non-dimensional time step is tabulated in Table 4.3 as a function of Mach number. The total amount of time taken for statistics to converge is determined

by the timescale of the upstream turbulence and is not significantly affected by Mach number. As a result, the decrease in time step with Mach number causes the total number of timesteps to increase. Our preliminary (unreported) Mach 1.2 calculations took about 350 hours on the Cray C-90. Based on Table 4.3 the corresponding run times for the stronger shock waves are estimated below.

| $M_1$ | Cray C90 Single Processor hours |
|---|---|
| 1.2 | 350 |
| 1.5 | 987 |
| 2.0 | 2428 |
| 3.0 | 6420 |

TABLE 4.4: The approximate run-time of a turbulent shock-resolving simulation as a function of the mean upstream Mach number.

The impracticality of computing flows with Mach numbers exceeding 1.5 with an explicit time advancement scheme, while resolving the thickness of the shock is obvious.

### 4.6.2 Shock Capturing

A practical alternative to resolving the thickness of the shock wave is 'shock capturing': where numerical viscosity is used to smoothen the shock wave. A wide body of literature exists on the subject (see for example Hirsch, 1990). A brief summary leading up to the scheme used in our computations is provided below.

The classical approach to shock capturing adds a linear diffusion term to the governing equations. Such schemes do not ensure non-linear stability and can therefore result in instability or oscillatory solutions when applied to strong shock waves. More recently, shock capturing schemes have been designed for non-linear conservative hyperbolic equations. These schemes are equivalent to adding a non-linear viscous term to the equations, ensuring non-linear stability in the process.

The development of shock capturing schemes relies on the Lax-Wendroff theorem (Lax and Wendroff, 1960) which shows that the limit solution of a consistent conservative finite difference approximation of the equations satisfies the Rankine-Hugoniot equations across a shock wave. An entropy inequality (Leroux, 1977;

Majda and Osher, 1979) is further needed to ensure that the scheme captures the physically relevant solution of the Euler equations *i.e.*, 'expansion' shocks are not obtained. The term 'shock capturing scheme' refers to the numerical scheme used to approximate the inviscid flux terms in the governing equations. Standard (usually central difference) schemes are used for the viscous terms (in our case the sixth order Pade scheme is used).

A brief introduction to shock capturing is given below. The Navier Stokes equations are first expressed in the form:

$$\frac{\partial \vec{q}}{\partial t} = -\frac{\partial \vec{f}_{\text{inv.}}}{\partial x} - \frac{\partial \vec{g}_{\text{inv.}}}{\partial y} - \frac{\partial \vec{h}_{\text{inv.}}}{\partial z} + \frac{\partial \vec{f}_{\text{visc.}}}{\partial x} + \frac{\partial \vec{g}_{\text{visc.}}}{\partial y} + \frac{\partial \vec{h}_{\text{visc.}}}{\partial z}. \tag{4.61}$$

where the subscripts 'inv.' and 'visc.' refer to the inviscid and viscous fluxes respectively, and $\vec{q} = (\rho, \rho u, \rho v, \rho w, E_t)^T$, $\vec{f}_{\text{inv.}} = u\vec{q} + p(0,1,0,0,u)^T$, $\vec{g}_{\text{inv.}} = v\vec{q} + p(0,0,1,0,v)^T$ and $\vec{h}_{\text{inv.}} = w\vec{q} + p(0,0,0,1,w)^T$. The viscous fluxes may be similarly obtained by comparison to equations 4.2.

Truly multi-dimensional shock-capturing schemes, where the conservative properties of all three inviscid flux terms are simultaneously enforced, are still a topic of research. A popular alternative is to approximate the three inviscid flux terms separately. The core of a shock capturing scheme is therefore a one-dimensional approximation to each of the flux terms. Consider the following one-dimensional conservative hyperbolic equation:

$$\frac{\partial u}{\partial t} + \frac{\partial}{\partial x} f(u) = 0 \tag{4.62}$$

where $f(u)$ is a non-linear flux term. In accordance with the Lax-Wendroff theorem, the spatial derivative is approximated as:

$$\frac{\hat{f}_{j+1/2} - \hat{f}_{j-1/2}}{\Delta x} \tag{4.63}$$

where $\hat{f}_{j+1/2}$ and $\hat{f}_{j-1/2}$ are *numerical fluxes* that are functions of the nodal values of $u$. The numerical fluxes are required to be consistent with the governing equation in the sense:

$$\hat{f}(....u, u, u, ....) = f(u). \tag{4.64}$$

Upon integrating in time, most schemes are expressible in the form:

$$u_j^{n+1} = G(...u_{j-1}^n, u_j^n, u_{j+1}^n ...). \tag{4.65}$$

The form of the numerical flux term and the function $G$, distinguishes one shock capturing scheme from another. The hierarchy of shock capturing schemes includes monotone, total variation diminishing (TVD), total variation bounded (TVB) and essentially non-oscillatory (ENO) schemes. A comprehensive review of monotone and TVD schemes is provided by Yee (1987). Monotone schemes are necessarily first order accurate. While TVD schemes may be of high order, their constraint on the total variation limits them to first order at the extrema of discontinuities. TVB schemes recover high order accuracy at extrema by relaxing the constraint on the total variation; however, their fixed stencil causes excessive smearing of the shock and the solution in its vicinity (Shu and Osher, 1988). These methods are therefore unsuitable to compute shock waves in flows where small scale features are important; turbulence being a prime example.

The ENO schemes are promising candidates to compute shock waves in turbulent flows. An adaptive stencil (based on difference tables) in these schemes uses the smooth parts of the solution to approximate derivatives around a discontinuity. ENO schemes were first introduced by Harten and Osher (1987) and Harten, Enquist, Osher and Chakravarthy (1987). Subsequent modifications by Shu and Osher (1988, 1989) have considerably increased the efficiency and simplicity of these schemes. Computations that evaluate the accuracy of the ENO schemes have been conducted by Shu (1990) and Shu, Erlebacher, Zang, Whitaker and Osher (1991). Details of the development of the ENO scheme may be found in these references and will not be repeated here. The final form of the ENO scheme that is used in our computations is summarized below.

Consider approximation of the flux term $\partial \vec{f}/\partial x$ (the subscript 'inv.' is dropped for notational brevity). It may be approximated either in terms of the characteristic variables (Shu *et al.*, 1991) or each of its component elements may be approximated individually. The latter approach is chosen for its ease of implementation. Also, the global Lax-Friedrichs flux splitting is used for upwinding. The flux is first split into two parts as follows:

$$\vec{f}(\vec{q}) = \vec{f}^{+}(\vec{q}) + \vec{f}^{-}(\vec{q}) \tag{4.66}$$

where the fluxes $\vec{f}^{+}$ and $\vec{f}^{-}$ are defined as follows:

$$\vec{f}^{\pm} = (\vec{f} \pm \alpha \vec{q})/2 \tag{4.67}$$

where $\alpha$ is the maximum value of $|u| + c$ in the $x$ direction. Note that this decomposition ensures that the eigenvalues of $\vec{f}^{+}$ are positive while those of $\vec{f}^{-}$ are

negative. Upwinding (in the appropriate direction) is then used to compute the spatial derivatives of both fluxes.

Denoting a component of either $\vec{f}^+$ or $\vec{f}^-$ by $f$, the derivative of $f$ (as indicated in equation 4.63) is approximated as:

$$\left.\frac{\partial f}{\partial x}\right|_{x=x_j} = \frac{\hat{f}_{j+1/2} - \hat{f}_{j-1/2}}{\Delta x} \tag{4.68}$$

where the numerical fluxes are defined as:

$$\hat{f}_{j+1/2} = \sum_{m=0}^{r} c(i-j,m)\ f[i,m] \tag{4.69}$$

where $i$ is the leftmost point in the stencil used to approximate the flux and $f[j,k]$ represents the (undivided) difference of $f$ defined as:

$$\begin{aligned} &f[j,0] = f(u_j) \\ &f[j,k] = f[j+1,k-1] - f[j,k-1]; \qquad k = 1,...,r \end{aligned} \tag{4.70}$$

where the variable $r$ denotes the spatial order of the scheme. ENO schemes of arbitrary order may thus be constructed. Note that the above representation satisfies the consistency requirement of equation 4.64. The coefficient matrix $c(s,m)$ is given by the following relation:

$$c(s,m) = \frac{1}{(m+1)!} \sum_{l=s}^{s+m} \prod_{\substack{p=s \\ p\neq l}}^{s+m} (-p+1). \tag{4.71}$$

The matrix $c$ is computed once and stored. An adaptive procedure is then used to determine the index $i$. Having decided upon the overall order of the scheme, the variable $i$ in equation 4.69 is chosen to yield the smallest absolute value of the undivided difference at every order $k$; *i.e.*, having started with $i = j$ or $i = j+1$ (depending upon the direction of upwinding), the following logic is implemented:

$$i = i-1 \ \text{ if } \ |\, f[i,k] \,| \ > \ |\, f[i-1,k] \,| \,; \qquad k = 1....r. \tag{4.72}$$

The above algorithm tends to strongly inhibit differencing across a discontinuity. This is the base form of the ENO scheme as described by Shu *et al.* (1991). The above scheme was found to have an unexpected degeneracy in the accuracy of the

solution with increasing order of the scheme or increasing number of points by Rogerson and Meiburg (1990). Shu (1990) attributed this degeneracy to choice of linearly unstable stencils during the adaptive procedure. Biasing the adaptive choice of stencil towards the linearly stable stencil (central differencing in our case) was advocated by him as a cure. This bias is achieved by the following modification to equation 4.72:

$$i = i - 1 \text{ if } 2 \mid f[i,k] \mid > \mid f[i-1,k] \mid ; \qquad k = 1....r. \tag{4.73}$$

The ENO scheme described above was used by Lee (1992) and Lee, Lele and Moin (1994) to compute the interaction of isotropic turbulence with shock waves of Mach numbers 2 and 3. The scheme was first evaluated by computing spatially decaying isotropic turbulence. Results of a sixth order ENO scheme were found to be in good agreement with results obtained using the sixth order Pade scheme. In computing shock/turbulence interaction, use was made of *a priori* knowledge of the approximate location of the shock wave. The ENO scheme was only applied locally around the shock; the sixth order Pade scheme was used everywhere else. This was done primarily to improve code performance, since the adaptive nature of the ENO scheme makes it more expensive to compute derivatives than the Pade scheme.

The interaction of two dimensional turbulence with a Mach 1.2 and Mach 2 shock was then computed using this hybrid scheme. Comparison to simulations where the thickness of the shock was resolved showed very good agreement. The smallest grid spacing using ENO was about 5 - 6 times that using shock-resolving. In computing three dimensional shock/turbulence interaction, application of ENO in all three coordinate directions was found to significantly increase the dissipation of turbulent kinetic energy. To alleviate this effect, ENO was used to only compute the flux terms in the streamwise (shock-normal) direction; the Pade scheme was applied to the transverse directions. The interaction of a Mach 1.2 shock wave with isotropic turbulence was then computed using this scheme. The results were in very good agreement with their simulations where the shock wave was resolved.

We use the same scheme as Lee *et al.* The sixth order ENO scheme biased towards central differencing is applied in the streamwise direction in the immediate vicinity of the shock wave. The sixth order Pade scheme is applied everywhere else. The zone over which ENO ($r = 6$) is applied is defined *a priori* by $N_l \leq i \leq N_r$

where,

$$N_l = \frac{Nx+1}{2} - 5r; \qquad N_r = \frac{Nx+1}{2} + 5r. \tag{4.74}$$

### 4.6.3 Evaluation of the shock-capturing scheme

The hybrid scheme described above, is evaluated in this section. A steady one-dimensional normal shock is first computed using both shock capturing and by resolving the shock thickness. The results are then contrasted. The ability of shock capturing schemes to compute shock waves in turbulent flows is then tested by computing the interaction of a Mach 1.5 shock wave with a plane vorticity-entropy wave at varying angles of incidence. The results are evaluated by comparison to linear analysis. Parameters such as domain length, viscosity, mesh and amplitude of the incident disturbance in these test problems are matched to those in the shear flow/shock wave simulation. These test problems are therefore used to determine the computational parameters of the turbulent simulation.

A steady Mach 1.5 normal shock is first computed. The initial condition ( a one-dimensional version of equations 4.80) ensures that the shock is at the center of the domain whose length $L_x$ is $3\pi$. The reference Reynolds number ($Re$ in equations 4.2) is set equal to 750. The flow is advanced at a CFL number of 0.4 till steady state is reached. A non-uniform mesh is used for both computations. The parameters $b, r$ and $d$ of the mesh are 15, 1.9 and 0.1 when the shock wave is resolved while the shock capturing calculation has values of 10,1.9 and 0.15 respectively. This choice of mesh parameters is made by trial and error. Also, the number of points was progressively increased until the solution obtained was found acceptable. The two computations are compared in Table 4.5. Note that shock capturing reduces the number of points from 447 to 191. This is accompanied by an increase in the time step; $\Delta t_{\text{shock cap.}} = 3.9\ \Delta t_{\text{shock resolv.}}$. The thickness of the shock wave is increased by a factor of 2.4 while the number of points inside the shock wave decreases from 10 to 6.

The quality of the solution obtained is illustrated in figure 4.5 where the velocity, pressure, density and temperature are plotted. Both solutions seem to smoothly transition through the shock wave to their downstream values. However, closer examination reveals the presence of small streamwise oscillations behind the shock wave when shock capturing is used. These oscillations are largest in the density and temperature; they are imperceptibly small in the velocity and pressure profiles.

In contrast to standard central difference schemes, these oscillations are bounded; they do not lead to instability. This behavior of the ENO schemes is documented in the literature (Meadows *et al.*, 1993, Woodward and Collela; 1984, Roberts; 1990, Lindquist and Giles; 1991). Shock capturing schemes (not necessarily ENO) are known to produce spurious oscillations in entropy (reflected in density and temperature) when applied to slowly moving shock waves.

| | Shock resolving | Shock capturing |
|---|---|---|
| $N_x$ | 447 | 191 |
| $\Delta x_{\max}$ | $4.01 \times 10^{-2}$ | $9.13 \times 10^{-2}$ |
| $\Delta x_{\min}$ | $2.16 \times 10^{-3}$ | $8.39 \times 10^{-3}$ |
| $\Delta x_{\max}/\Delta x_{\min}$ | 19 | 11 |
| $\Delta t$ | $0.35\times10^{-3}$ | $0.14\times10^{-2}$ |
| Shock thickness | 0.018 | 0.043 |
| Points inside shock | 10 | 6 |

TABLE 4.5: Comparison between shock-capturing and shock-resolving in the computation of a Mach 1.5 laminar shock wave.

Meadows *et al.* show that the approximate frequency of these oscillations is $u_s/\Delta x$ where $u_s$ is the velocity of the shock wave with respect to the grid. Thus strictly speaking, shock capturing does not yield a steady solution. They use the above frequency to estimate the wavelengths of the pressure and entropy waves behind the shock as $(u_2 + a_2)\Delta x/u_s$ and $u_2\Delta x/u_s$ respectively. Increasing shock speed or decreasing the mesh spacing decreases the magnitude of these oscillations. As suggested by Meadows *et al.*, both these factors increase the frequency and hence decrease the wavelength of the oscillations. This allows the dissipation inherent in the shock capturing scheme to eliminate the oscillations. While Meadows *et al.* examined a moving shock wave, the source of shock velocity in our computations is less clear. Switching of the stencil by the adaptive algorithm is the most likely cause of change in shock location and hence shock velocity. To allow computation of shock/turbulence interaction, we ensure that the magnitude of the oscillations in density behind the shock wave is small with respect to the magnitude of density fluctuations behind the shock wave in the turbulent simulation. Since we have no

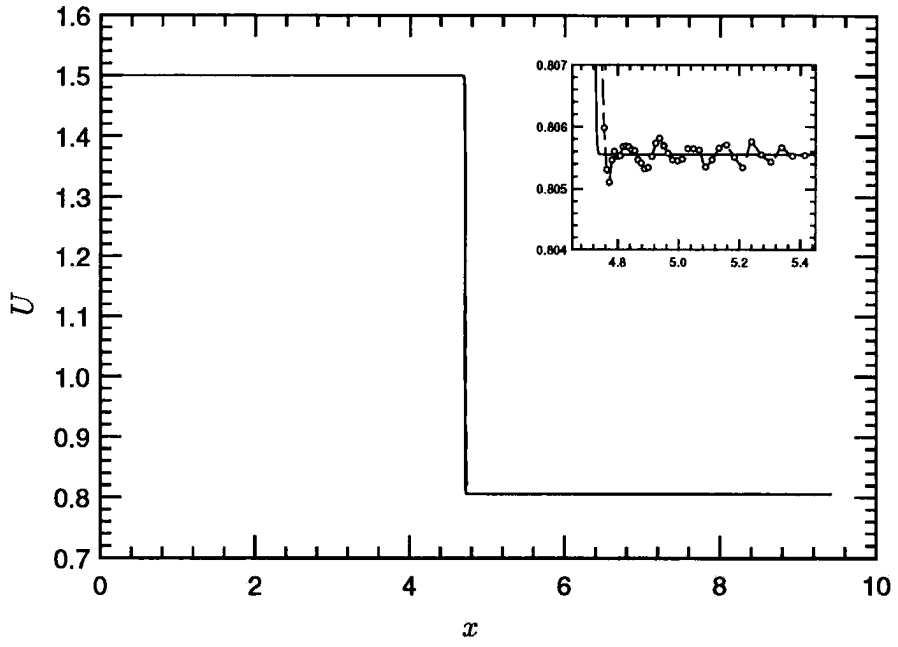


(a)

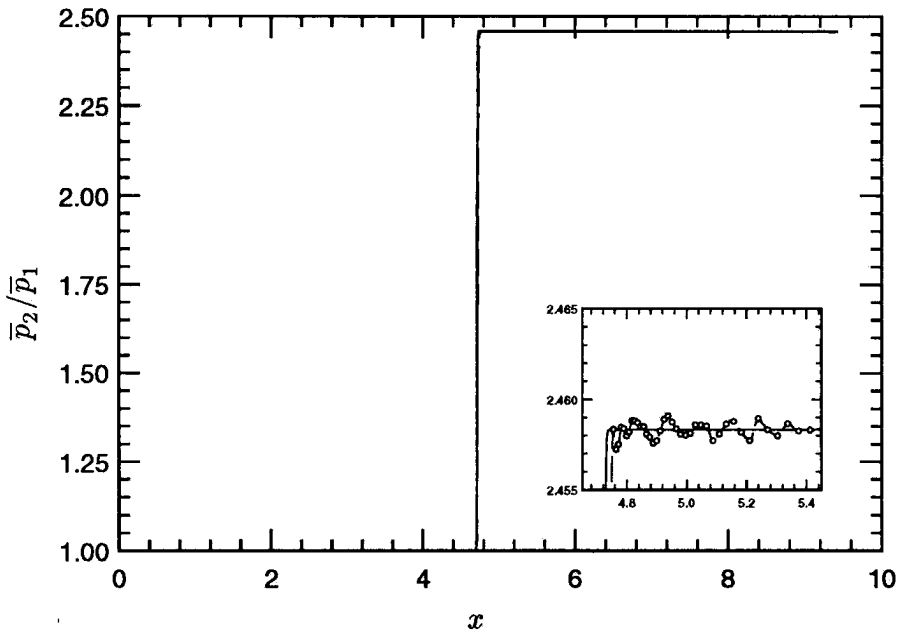


(b)

FIGURE 4.5: Comparison between shock-resolving and shock-capturing in the computation of a Mach 1.5 normal shock. ——— (Shock-resolving), ---- (Shock capturing). $(a)$ : Velocity, $(b)$ : Pressure, $(c)$ : Density, $(d)$ : Temperature. The solid line in the insert is from shock-resolving while the dashed line with circles is from shock-capturing

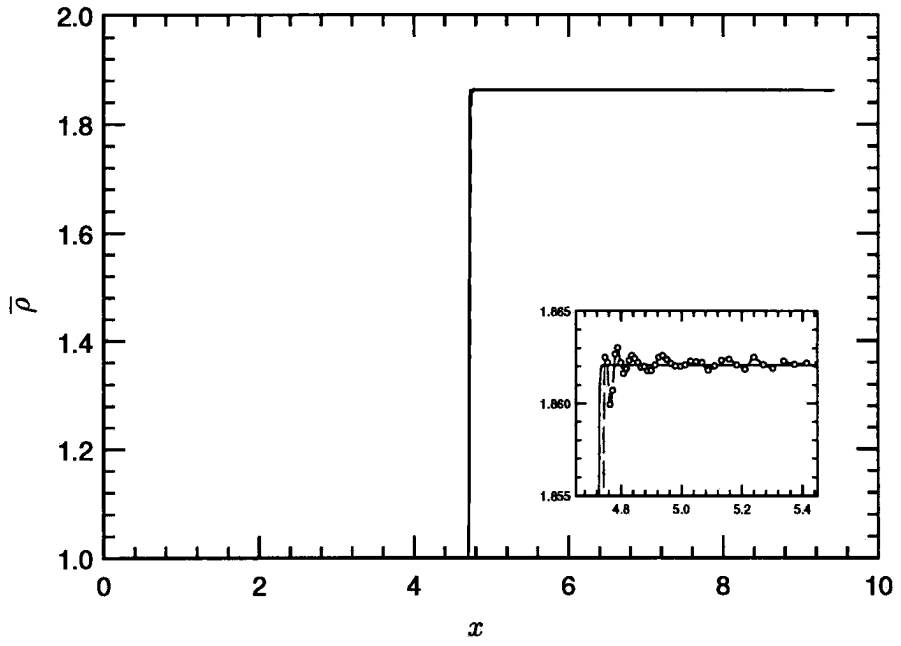


(*c*)

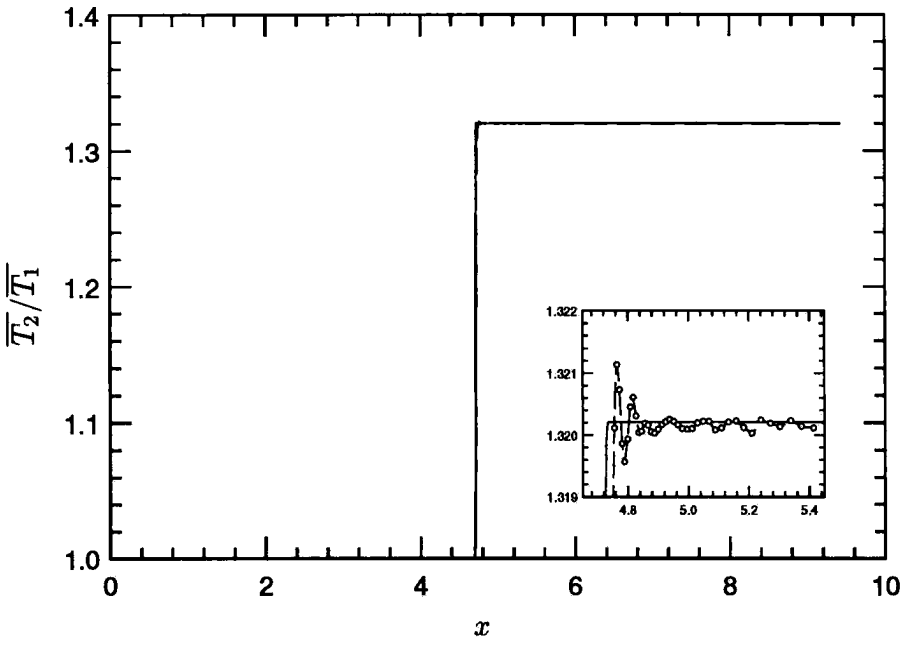


(*d*)

FIGURE 4.5 continued: See previous page for caption.

control over the shock speed, iteration on the mesh is necessary until the oscillations are acceptably small. The numerically induced oscillations in density are about 0.02% of the mean density behind the shock wave. By comparison, the intensity of density fluctuations in the turbulent simulation are about 2.5% upstream of the shock wave; the downstream values will be higher. The above level of numerical oscillation in density is therefore considered acceptable.

The unsteady two-dimensional interaction of a Mach 1.5 shock wave with a plane vorticity-entropy wave at varying angles of incidence is next computed. The results are compared to the linear analysis described in Chapter 3. Recall that a similar computation where the shock wave was resolved was performed in Section 3.4. The results were found to agree well with linear analysis. The computational domain has dimensions of $3\pi$ and $2\pi$ in the streamwise and transverse directions respectively. The streamwise mesh is identical to that used to compute the steady one-dimensional shock. A uniform mesh of 33 points is used in the $y$ direction. The mean flow parameters are identical to those in the steady shock wave computation. Periodic boundary conditions are imposed at the $y$ boundaries. All the flow variables are specified at the inflow boundary and non-reflecting boundary conditions (Section 4.8) are used at the outflow boundary. The flow is initialized by a steady normal shock wave over which the fluctuating vorticity-entropy wave is superposed; *i.e.*, at $t = 0$,

$$\begin{aligned} u &= U + U_1 A_v \sin\psi_1 \cos(k_x x + k_y y) \\ v &= U_1 A_v \cos\psi_1 \cos(k_x x + k_y y); \qquad p = \overline{p} \\ \rho &= \overline{\rho} + \overline{\rho}_1 A_e \cos(k_x x + k_y y) \end{aligned} \tag{4.75}$$

where the overbars denote mean quantities and the subscript '1' refers to the state upstream of the shock wave.

The wavenumbers $k_x$ and $k_y$ are given by:

$$k_x = k\cos\psi_1; \qquad k_y = k\sin\psi_1 \tag{4.76}$$

where $k$ is the magnitude of the wavenumber vector and $\psi_1$ denotes the angle the wavenumber vector makes with the $x$ axis. The variables $A_v$ and $A_e$ denote the intensity of velocity and density upstream of the shock wave and are both equal to 2.5%. The unsteadiness associated with the incident wave is specified through the inflow boundary condition; *i.e.*, at $(x = 0)$,

$$u = U_1 + U_1 A_v \sin\psi_1 \cos(k_y y - U_1 k_x t)$$

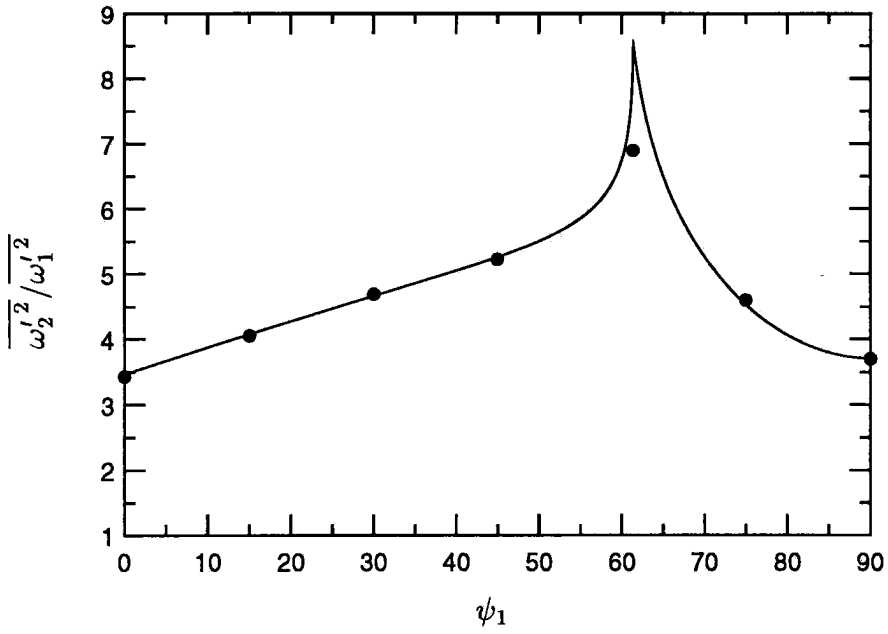


FIGURE 4.6: The amplification of vorticity across a Mach 1.5 shock wave in its interaction with a plane vorticity-entropy wave. The line corresponds to linear analysis while the symbols are from numerical solution.

$$v = U_1 A_v \cos\psi_1 \cos(k_y y - U_1 k_x t); \qquad p = \overline{p}$$

$$\rho = \overline{\rho} + \overline{\rho}_1 A_e \cos(k_y y - U_1 k_x t). \tag{4.77}$$

The parameters $k$ and $\psi_1$ are selected so that we have one wavelength in the $y$ direction *i.e.*,

$$k_y = k \sin\psi_1 = 1. \tag{4.78}$$

The solution is advanced at a $CFL$ number of 0.4 until initial transients exit the domain. Statistics are then gathered over a period of the inflow disturbance, $2\pi/\overline{U}_1 k_x$.

The incidence angle $\psi_1$ is varied from 0 to $\pi/2$ and the results are compared to linear analysis. The amplification of vorticity across the shock wave is the least ambiguous to compare to analysis since vorticity varies monotonically on both sides of the shock. We tabulate below (and plot in figure 4.6) the computed amplification of vorticity across the shock. Also listed are predictions of the linear analysis. The two values are seen to agree to about 1% away from the critical angle (the error is computed with respect to linear analysis prediction). As explained in Chapter 3, the deviation around the critical angle is a limitation of the linear analysis, not the computation. These computations also help in assessing the performance of the exit

boundary conditions. The performance of the non-reflecting conditions are known to degrade as the angle of the acoustic waves with the normal to the exit boundary increases. This results in some reflection that corrupts the dilatational component of the flow near the boundary. Vorticity is unaffected. The incident waves around 0° and 90° are unaffected by the outflow boundary conditions while some corruption is seen for the other angles. The decaying regime is more benign in this respect since the amplitude of the acoustic wave decays exponentially behind the shock wave. Note that the length scale of the upstream fluctuations are smaller in the turbulent calculation as compared to the single mode computation. Also, reflected acoustic waves would not travel upstream uninterrupted in a turbulent flow. The influence on the solution inside the domain will therefore be smaller in the turbulent calculation. Similar observations were made by Lee, Lele and Moin (1992) on the exit boundary conditions in their computations of isotropic turbulence/shock wave interaction.

| $\psi_1$ (degrees) | Computation | Linear analysis | Error |
|---|---|---|---|
| 0 | 3.43 | 3.45 | 0.6% |
| 15 | 4.05 | 4.07 | 0.5% |
| 30 | 4.69 | 4.66 | 0.6% |
| 45 | 5.22 | 5.26 | 0.8% |
| 61.36 | 6.89 | 8.5 | 19% |
| 75 | 4.60 | 4.53 | 1.55% |
| 90 | 3.70 | 3.71 | 0.3% |

TABLE 4.6: Vorticity amplification factors from simulation compared to linear analysis in the interaction of a Mach 1.5 shock with a plane vorticity-entropy wave.

Besides statistics, instantaneous fields are examined for spurious oscillations. Increased distortion of the shock wave could generate spurious oscillations due to our use of the Pade scheme in the $y$ direction. Figure 4.7 shows the $v$ component of velocity for incident angles of 45°, 75° and 90° respectively. The smooth change in the angle of propagation and wavelength of the incident wave is noted over the propagating regime. Some small amplitude periodic oscillations are observed for the incidence angle of 75°. These spurious oscillations are generated at the shock front around the region of maximum slope and are subsequently convected downstream.

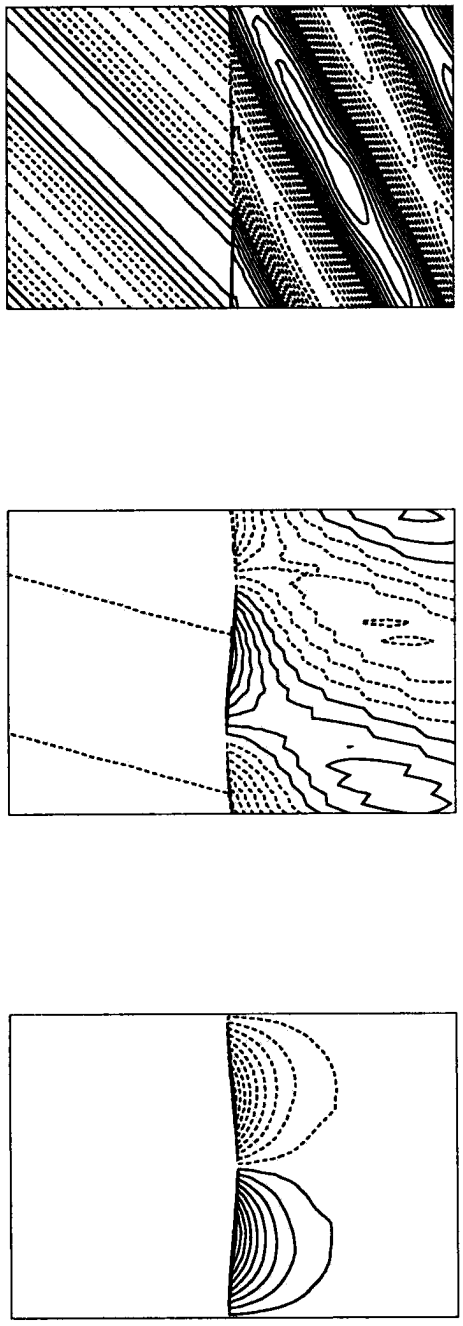


FIGURE 4.7: Contours of $v$ in the interaction of a vorticity-entropy wave with a Mach 1.5 shock. Figures $(a), (b)$ and $(c)$ correspond to incidence angles of $45°, 75°$ and $90°$ respectively. The solid and dashed lines denote positive and negative values respectively.

Their amplitude is small as reflected in the statistics of vorticity amplification shown in Table 4.6. In summary, while the shock-capturing scheme is not perfect, it does represent the interaction accurately for most of the incidence angles. It is therefore expected to be quite adequate in predicting the interaction of the turbulent field with the shock wave.

## 4.7 Initial conditions

The turbulent simulations are initialized by superposing turbulent fluctuations onto the steady laminar solution of the shock wave in the shear flow. The laminar solution is obtained from a two-dimensional computation where the extent of the domain and the mesh were the same as the turbulent simulation. The two-dimensional computation is performed in two stages as follows. The domain is first initialized as a one-dimensional normal shock at every $y$ location; *i.e.*, given the following state at the inflow:

$$U_1(y) = U_0 + S(y - y_{\min}), \qquad V_1 = 0$$

$$\overline{p}_1(y) = \frac{1}{\gamma}, \qquad \overline{T}_1(y) = \frac{U_1^2(y)}{(\gamma-1)M_1^2}, \tag{4.79}$$

the rest of the domain is initialized as follows:

$$U(x,y) = \frac{U_1(y)+U_2(y)}{2} + \frac{U_2(y)-U_1(y)}{2}\tanh\frac{(x-x_c)}{\delta_s}, \qquad V(x,y) = 0$$

$$\overline{T}(x,y) = \overline{T}_1(y) + \frac{U_1^2(y)}{2} - \frac{U^2(x,y)}{2}, \qquad \overline{\rho}(x,y) = \frac{1}{(\gamma-1)\overline{T}_1(y)}\frac{U_1(y)}{U(x,y)}. \tag{4.80}$$

The subscript '2' in the above equations denotes the state behind the shock wave and is obtained from the Rankine-Hugoniot relations; *i.e.*,

$$\frac{U_2(y)}{U_1(y)} = \frac{2+(\gamma-1)M_1^2}{(\gamma+1)M_1^2}. \tag{4.81}$$

The variable $x_c$ denotes the location of the shock wave and is set equal to $L_x/2$. The parameter $\delta_s$ is a measure of the distance over which the initial field varies between upstream and downstream states. It is typically set equal to 2.

The one-dimensional Navier Stokes equations are then advanced at each $y$ location. The purpose of this one-dimensional calculation is to provide shock profiles that can be used to specify boundary conditions at the $y$ boundaries in the turbulent

calculation. The flow is advanced till a steady state is obtained. The inflow boundary being supersonic, all flow variables are specified there. Non-reflecting boundary conditions ( Section 4.8) are specified at the outflow boundary. No boundary conditions are needed at the $y$ boundaries since the calculation is one-dimensional.

The steady solution that is obtained is used to initialize a computation on the same mesh where the two-dimensional Navier-Stokes equations are solved. The one-dimensional steady solution that was obtained is used to specify boundary conditions at the $y$ boundaries. Quantities that vary across the shock wave ($U, \rho$ and $\overline{p}$) are set to equal the values obtained at the boundary from the one-dimensional solution. The velocity in the $y$ direction is obtained by advancing the $y$ momentum equation. The boundary conditions at the inflow and outflow boundaries are the same as those in the one-dimensional computation. The flow is then advanced in time until a steady state is obtained. This steady solution is then used as the mean field to initialize the three-dimensional turbulent simulation.

The turbulent fluctuations (see Section 4.8) are obtained from a temporal computation of a shear flow. The mean flow in the temporal simulations matches that at the inflow of the shock wave computation. The temporal simulation has periodic boundary conditions in the $x$ and $z$ directions. Non-reflecting boundary conditions are specified at the $y$ boundaries. The spatial extent and grid in the $y$ and $z$ directions matches that of the shock wave computation. An instantaneous realization (the same as that used to generate inflow turbulence; see section 4.8) of the temporal simulation is used to compute fluctuations of the primitive variables ($u_i, \rho, p$).

The two-dimensional steady solution is first specified over all $x-z$ planes. The turbulent signal obtained from the temporal simulation is then interpolated onto the grid used in the spatial calculations and then superposed onto the mean flow. Note that the temporal turbulent field is only representative of the flow upstream of the shock wave. As a result, it is specified only over the part of the domain upstream of the shock. This is achieved by applying a smoothing function to the turbulent signal in the streamwise direction. The smoothing function is based on the hyperbolic tangent profile and smoothly varies from one near the inflow to zero a bit upstream of the shock wave. A primitive variable, $f(x, y, z)$ is therefore

computed as follows:

$$f(x,y,z) = \overline{f} + \frac{1-\tanh[b_{\text{init.}}(x-L_x/4)]}{2} \sum_{k_1,k_3} \widehat{f}(k_1,y,k_3) \exp i(k_1 x + k_3 z). \tag{4.82}$$

where the variable $\overline{f}$ is obtained from the steady laminar solution. The variable $b_{\text{init.}}$ determines the rate at which the smoothing function varies from zero to one; it was set to equal 5. Absence of the smoothing function would result in the specification of turbulent fluctuations over the entire length of the computational domain. Such initial fields were found to generate severe transients in the vicinity of the shock wave. Numerical instability was a consequence. This effect was found to be more pronounced as the shock strength increased. The use of the smoothing function was therefore found essential to generate tolerable transients.

## 4.8 Boundary conditions

### 4.8.1 Inflow boundary

Since flow at the inflow boundary is supersonic, all flow variables are prescribed there. Unsteady fluctuations representative of the turbulence in the shear flow are specified. Details of the procedure and validation of this method of generating turbulent fluctuations at the inflow are provided in Appendix C. A brief summary is provided below.

Essentially, an instantaneous realization of a developed temporal simulation is used to generate inflow turbulence. The fluctuations in primitive variables of the temporal field are first Fourier transformed in the $x$ and $z$ directions; *i.e.*, $f(x,y,z)$ is transformed into $\widehat{f}(k_1,y,k_3)$. Taylor's hypothesis is then used to convert the streamwise wavenumber $k_1$ into frequency $\omega$. Inverse Fourier transforming then yields $f(t,y,z)$; *i.e.*, $x = U_c t$ is used to express $f(t,y,z)$ as $\sum_{k_1,k_3} \widehat{f}(k_1,y,k_3) \exp(ik_1 U_c t)$ $\exp(ik_3 z)$. This amounts to convecting a temporal realization into the spatial domain at a convection velocity $U_c$. To ensure randomness in time, the amplitude and phase of the Fourier coefficients are randomly jittered with time. The fluctuations thus obtained are superposed onto the mean field at the inflow. This method of specifying inflow turbulence is a considerable improvement over that proposed by Lee, Lele and Moin (1992).

### 4.8.2 Outflow boundary

Approximately non-reflecting boundary conditions are specified at the subsonic outflow boundary. The boundary conditions comprise of a 'sponge layer' in the streamwise direction, followed by a characteristics-based boundary condition (Poinsot & Lele, 1992) at the outflow plane. Boundary conditions involving a sponge layer have been used in the past in a variety of problems: e.g. Givoli (1991), Israeli & Orszag (1981), Colonius, Moin & Lele (1995). The boundary conditions with a sponge were shown (Colonius *et al.*) to yield significantly better results than boundary conditions without the sponge layer.

Accordingly, a 'cooling term' of the form, $-\sigma(\mathbf{U} - \mathbf{U}_{\text{ref}})$ is added to the right-hand side of the governing equations *over the sponge layer alone.* $\mathbf{U}_{\text{ref}}$ denotes the vector of reference variables towards which the solution in the sponge layer is forced. It is set to equal the steady laminar solution that was used to specify the initial condition. The coefficient $\sigma(x)$ is a polynomial function; i.e.

$$\sigma(x) = A_s \frac{(x - x_s)^n}{(L_x - x_s)^n} \tag{4.83}$$

where, $x_s$ and $L_x$ denotes the start of the sponge and the length of the domain respectively. Typical values of $A_s$, $n$ and $(L_x - x_s)/L_x$ used in our simulations are 5, 3 and 0.14 respectively.

The formulation proposed by Poinsot and Lele (1992) is used at the exit plane. These boundary conditions are an extension of the formulation proposed by Thompson (1987). Given the hyperbolic nature of the Euler equations, the solution at the boundary supports waves that propagate out and into the domain. While the amplitudes of the outgoing waves are determined by the solution inside the domain, the incoming waves need to be specified. For lack of a better approximation, the amplitude of the incoming waves is set to zero.

The implementation of these boundary conditions is equivalent to specifying conditions on the derivatives of some flow variables normal to the boundary. Details of the boundary conditions may be found in Poinsot and Lele (1992). The Navier Stokes equations are expressed as follows:

$$\frac{\partial \vec{q}}{\partial t} + \frac{\partial \vec{f}}{\partial x} = \text{RHS} \tag{4.84}$$

where RHS contains the viscous terms and inviscid terms involving derivatives parallel to the boundary. The RHS is therefore computed using the solution in the domain. The propagation of waves across the boundary is determined by the one-dimensional equation:

$$\frac{\partial \vec{q}}{\partial t} + \frac{\partial \vec{f}}{\partial x} = 0. \tag{4.85}$$

The above equation is expressed in terms of the primitive variables and diagonalized (Thompson; 1987, Poinsot and Lele; 1992). This equation has five eigenvalues $u, u, u, u + c, u - c$. In the linear limit, these eigenvalues correspond to the propagation of vorticity, entropy and acoustic waves. The diagonalization relates the amplitudes of the characteristic variables to the spatial derivatives of the physical variables as follows (the notation used by Poinsot and Lele is retained):

$$\frac{\partial}{\partial x}\rho u = [L_2 + (L_5 + L_1)/2]/c^2 \tag{4.86a}$$

$$\frac{\partial}{\partial x}c^2\rho u = (L_5 + L_1)/2 \tag{4.86b}$$

$$u\frac{\partial u}{\partial x} = (L_5 - L_1)/2\rho c \tag{4.86c}$$

$$u\frac{\partial v}{\partial x} = L_3 \tag{4.86d}$$

$$u\frac{\partial w}{\partial x} = L_4 \tag{4.86e}$$

where the $L_i$'s are defined as:

$$L_1 = (u - c)\left(\frac{\partial p}{\partial x} - \rho c\frac{\partial u}{\partial x}\right) \tag{4.87a}$$

$$L_2 = u\left(c^2\frac{\partial \rho}{\partial x} - \frac{\partial p}{\partial x}\right) \tag{4.87b}$$

$$L_3 = u\frac{\partial v}{\partial x} \tag{4.87c}$$

$$L_4 = u\frac{\partial w}{\partial x} \tag{4.87d}$$

$$L_5 = (u + c)\left(\frac{\partial p}{\partial x} + \rho c\frac{\partial u}{\partial x}\right). \tag{4.87e}$$

$L_i$ denotes the amplitude of the characteristic variables in the linear limit. The number of boundary conditions that are specified is equal to the number of incoming waves. The sign of the eigenvalues determines whether a wave is incoming or

outgoing. Since the exit boundary is subsonic, the only negative eigenvalue is $u - c$. The exit boundary condition is therefore to set the amplitude of the corresponding incoming waves to zero. *i.e.*,

$$L_1 = 0. \tag{4.88}$$

The other $L_i$'s are computed using equations (4.87) and the solution in the domain. This yields the derivatives normal to the boundary which are then substituted into equations (4.2) (Poinsot and Lele, 1992).

### 4.8.3 Top and bottom boundaries

Boundary conditions at the top and bottom boundaries pose a formidable challenge since the flow is not compact. These boundary conditions are required to have a non-reflecting character while fixing the mean location of the shock wave. These dual requirements are hard to achieve. Several variants of the characteristic based non-reflecting conditions were tried. The boundary conditions were evaluated by computing a steady two-dimensional laminar solution to the shock wave in the shear flow. The shock wave was either found to travel upstream or, numerical instability resulted when these boundary conditions were used.

The dual requirements of shock stationarity and non-reflecting character were achieved through use of 'sponge' regions near the top and bottom boundaries. As done near the outflow boundary, a term of the form, $\sigma(\mathbf{U} - \mathbf{U}_{\text{ref.}})$ is added to the governing equations near the top and bottom boundaries. The variable $\sigma$ is increased from zero at the start of the sponge region to a finite value at the boundary. The reference solution $\mathbf{U}_{\text{ref.}}$ is set to equal the laminar solution that is used to specify the initial condition. The solution in the sponge region is thus gently damped towards the steady laminar solution. Hence, at the top and bottom planes ($j = 1, N_y$), $u, \rho$ and $\overline{p}$ are set to equal their laminar values while the transverse velocity components are obtained from the $y$ and $z$ momentum equations.

## 4.9 Simulations performed

Results from two simulations are discussed in this report. The mean upstream Mach number in the two computations is 1.2 and 1.5 respectively. Apart from the difference in the shock strengths, there is one important difference between the two simulations: the sign of the upstream velocity-temperature correlation is different. Also, the 'sponge' regions discussed above were not implemented in the Mach 1.5 computation. Section 4.8.1 and Appendix C discussed the procedure

used to generate inflow turbulence for the Mach 1.2 computation. Recall that the temporal simulation used to generate inflow turbulence was initialized with an isotropic velocity field and zero thermodynamic fluctuations. The temporal evolution of $R_{u'T'}$ and $R_{v'T'}$ (figure C.11) showed that $R_{u'T'}$ was positive while $R_{v'T'}$ was negative. The linearized equations governing the evolution of the velocity-temperature correlation (equations C.14-C.16) were used to show that $\overline{u'T'}$ was positive because the mean velocity and temperature both increase with increasing $y$ in the computations.

However, Morkovin's hypothesis (equation C.1) and experimental measurements show that $\overline{u'T'}$ in an adiabatic boundary layer is negative; $R_{u'T'}$ is nearly -1. As a result, it was decided to ensure that the turbulence upstream of the Mach 1.5 shock wave had negative $\overline{u'T'}$. This was achieved through the initial conditions used in the temporal simulation to generate inflow turbulence for the Mach 1.5 simulation. The linear equations governing the evolution of the velocity-temperature correlation are reproduced below from Appendix C:

$$\frac{\partial}{\partial t}\overline{v'T'} + U\underbrace{\frac{\partial}{\partial x}\overline{v'T'}}_{0} = \underbrace{-\overline{v'^2}\frac{\mathrm{d}\overline{T}}{\mathrm{d}y}}_{\text{negative}} + \underbrace{\overline{Tv'\theta'} - \frac{1}{\overline{\rho}}\overline{T'\frac{\partial p'}{\partial y}}}_{\text{neglect}}. \qquad (4.88a)$$

$$\frac{\partial}{\partial t}\overline{u'T'} + U\underbrace{\frac{\partial}{\partial x}\overline{u'T'}}_{0} = \underbrace{-\overline{u'v'}\frac{\mathrm{d}\overline{T}}{\mathrm{d}y}}_{\text{positive}} - \overline{v'T'}\frac{\mathrm{d}U}{\mathrm{d}y} + \underbrace{\overline{Tu'\theta'} - \frac{1}{\overline{\rho}}\overline{T'\frac{\partial p'}{\partial x}}}_{\text{neglect}}. \qquad (4.88b)$$

Of the three 'production' terms, $-\overline{v'^2}\mathrm{d}\overline{T}/\mathrm{d}y$ is always negative. Since the initial turbulence is isotropic, $\overline{u'v'}$ is initially zero; as the turbulence evolves, it becomes negative, and the term $-\overline{u'v'}\mathrm{d}\overline{T}/\mathrm{d}y$ becomes positive. The remaining production term is $-\overline{v'T'}\mathrm{d}U/\mathrm{d}y$. If $\overline{v'T'}$ were negative, then equation (4.88) shows that this would tend to decrease $\overline{u'T'}$. Equation 4.88a shows that if the initial thermodynamic field were zero, then $\overline{v'T'}$ would be negative. However, if $\overline{v'T'}$ was *initially positive*, then there would be a transient period of time when $\overline{v'T'}$ would remain positive and $\overline{u'T'}$ would be negative (since its initial value is zero).

This was the procedure used to generate the initial thermodynamic field for the Mach 1.5 temporal simulation. In addition to an isotropic velocity field, an initial field of entropy fluctuations with positive $\overline{v'T'}$ (*i.e.*, negative $\overline{v'\rho'}$ ) was specified; *i.e.*, initially,

$$p' = 0; \qquad \frac{\rho'}{\overline{\rho}} = -\beta\frac{v'}{\overline{U}}. \qquad (3.89)$$

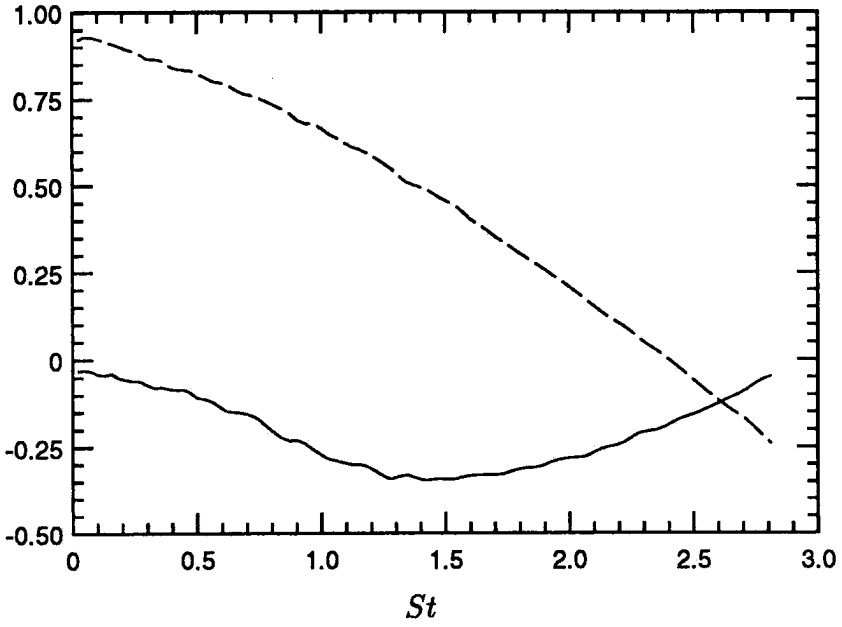


FIGURE 4.8: The evolution of velocity-temperature correlation at the centerline in the Mach 1.5 temporal simulation. —— $(R_{u'T'})$, ---- $(R_{v'T'})$.

The variable $\beta$ is a constant that was by trial and error set to 18. Increasing $\beta$ ensures that $\overline{u'T'}$ stays negative for longer periods of time, thereby allowing the velocity field to develop further. Figure 4.8 shows the temporal evolution of the velocity-temperature correlation in the Mach 1.5 simulation. An instantaneous realization at $St = 2.8$ was taken and used to generate inflow turbulence. The properties of the resulting turbulence immediately upstream of the Mach 1.5 shock wave are tabulated below. Corresponding values for the Mach 1.2 shock are reported in Chapter 5.

| | | | |
|---|---|---|---|
| $R_\lambda$ | 29.0 | $M_t$ | 0.03 |
| $\overline{u'^2}/q^2$ | 0.53 | $\overline{v'^2}/q^2$ | 0.23 |
| $\overline{w'^2}/q^2$ | 0.24 | $\overline{u'v'}/q^2$ | -0.22 |
| $\sqrt{q^2}/\overline{U_1}$ | 0.025 | $\rho_{\rm rms}/\overline{\rho_1}$ | 0.03 |
| $T_{\rm rms}/\overline{T_1}$ | 0.03 | $p_{\rm rms}/\gamma\overline{P_1}$ | 0.0014 |
| $\overline{u'T'}/u_{\rm rms}T_{\rm rms}$ | -0.1 | $\overline{v'T'}/v_{\rm rms}T_{\rm rms}$ | -0.24 |
| $\overline{\rho'T'}/\rho_{\rm rms}T_{\rm rms}$ | -1.0 | | |

TABLE 4.7: Parameters upstream of the Mach 1.5 shock wave at the center streamline.

# Chapter Five

# Direct Numerical Simulation: Results

## 5.1 Introduction

This chapter presents the results obtained from direct numerical simulation of the interaction of the turbulent shear flow with a normal shock wave. The relevant parameters of the computations are first outlined. Properties of the turbulent flow upstream of the shock wave are then discussed in section 5.2. Section 5.3 outlines the evolution of the mean flow across the shock wave. This is followed in section 5.4, by a discussion of the evolution of the turbulence kinetic energy. The influence of the shock wave on the Reynolds shear stress of the turbulence is then presented in section 5.5. Section 5.6 discusses the evolution of the thermodynamic fluctuations across the shock. The chapter is then concluded with a discussion of the turbulence length scales in section 5.7.

| | Mach 1.2 | Mach 1.5 |
|---|---|---|
| $M_1$ | 1.2 | 1.5 |
| $L_x$ | 12 | $3\pi$ |
| $L_y$ | $5\pi$ | $3\pi$ |
| $L_z$ | $5\pi$ | $3\pi$ |
| $N_x$ | 191 | 191 |
| $N_y$ | 121 | 81 |
| $N_z$ | 121 | 81 |
| $b$ | 12 | 10 |
| $r$ | 1.9 | 1.9 |
| $d$ | 0.25 | 0.15 |
| $U_0$ | 2 | 2 |
| $S$ | 0.2 | 0.1 |

TABLE 5.1: Numerical parameters in the simulations conducted.

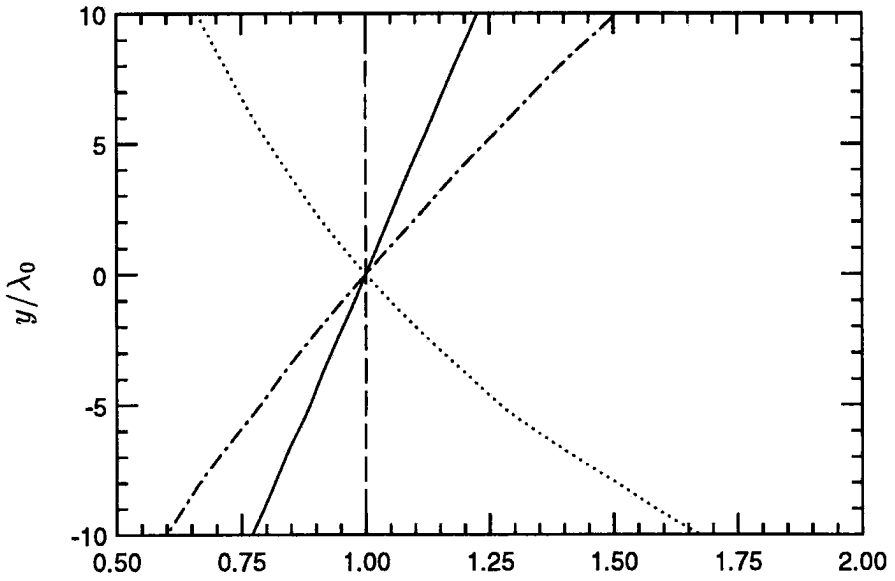


FIGURE 5.1: The mean profiles upstream of the Mach 1.2 shock wave ($x/\lambda_0 = 14.5$). ——— $(U)$, - - - - $(\overline{p})$, ····· $(\overline{\rho})$, —·— $(\overline{T})$. All the variables are normalized by their value at the center streamline ($y/\lambda_0 = 0$).

Results from two simulations are presented in this chapter. The two computations differ in the shock strength, which is Mach 1.2 and Mach 1.5 respectively. Also, as discussed in Chapter 4, the upstream correlation between the velocity and temperature fluctuations is different between the two simulations. Results from the Mach 1.2 simulation will be discussed in detail, with the Mach 1.5 results supplementing the discussion. The relevant parameters of the computations are tabulated in Table 5.1. Note that $M_1$ denotes the mean upstream Mach number, $L_x, L_y$ and $L_z$ denote the length of the domain in the $x, y$ and $z$ directions, the number of points used in the three coordinate directions is represented by $N_x, N_y$ and $N_z$, the variables $b, r$ and $d$ denote the parameters involved in the streamwise nonuniform mesh and $U_0$ and $S$ determine the mean upstream velocity profile.

## 5.2 The flow upstream of the shock wave

Profiles of the mean velocity, pressure, density and temperature measured immediately upstream of the Mach 1.2 shock wave ($x/\lambda_0 = 14.5$) are plotted in figure 5.1. Note that the 'sponge' regions are not shown. Also, $\lambda_0$ is the Taylor microscale of the initial isotropic field in the temporal simulation used to generate inflow turbulence (Appendix C).

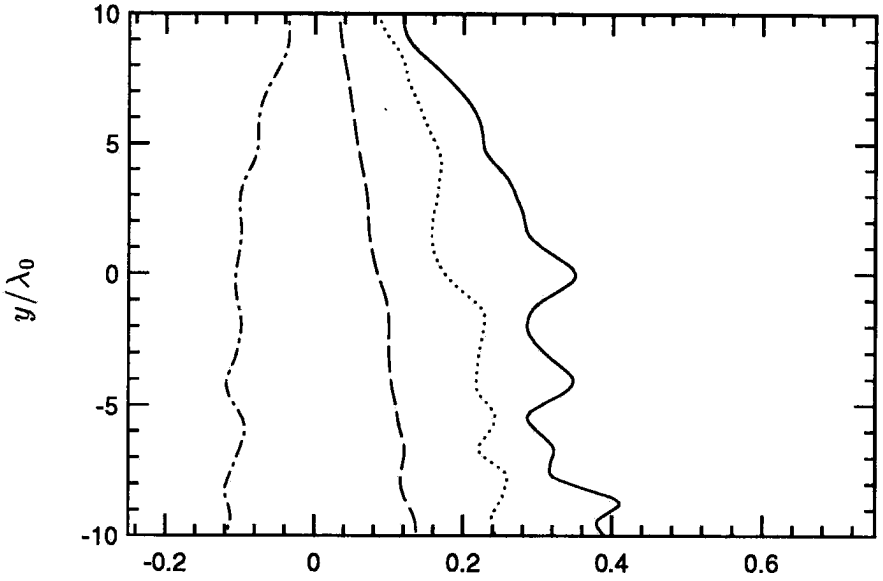


FIGURE 5.2: Turbulence Reynolds stresses upstream of the Mach 1.2 shock wave ($x/\lambda_0 = 14.5$). All the curves are normalized by $\overline{u_0^2}$. —— $(\overline{u'^2})$, ---- $(\overline{v'^2})$, ····· $(\overline{w'^2})$, —·— $(\overline{u'v'})$.

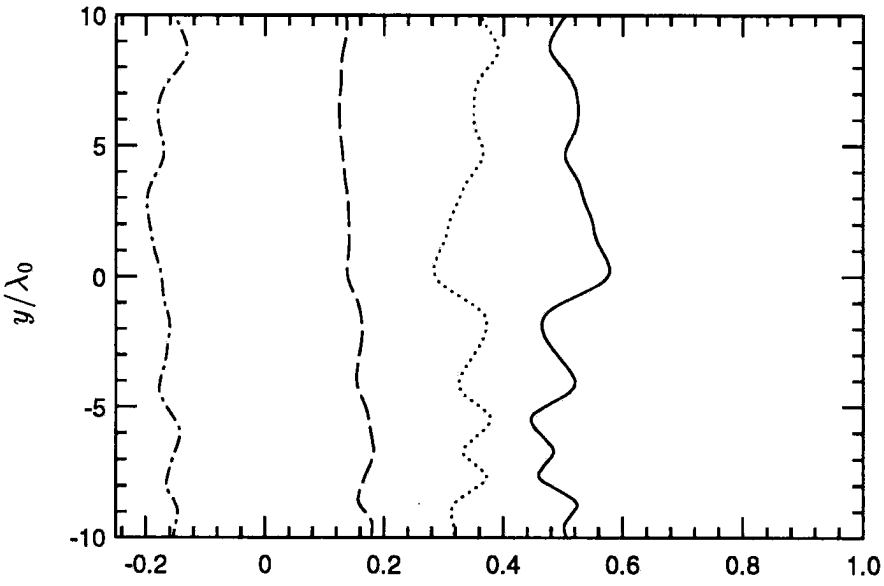


FIGURE 5.3: The non-dimensional Reynolds stresses upstream of the Mach 1.2 shock wave ($x/\lambda_0 = 14.5$). —— $(\overline{u'^2}/q^2)$, ---- $(\overline{v'^2}/q^2)$, ····· $(\overline{w'^2}/q^2)$, —·— $(\overline{u'v'}/q^2)$.

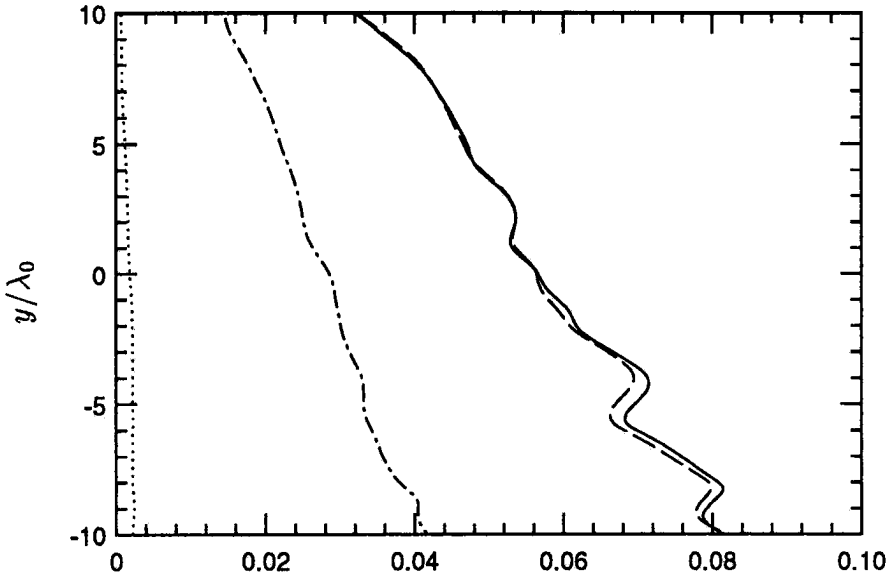


FIGURE 5.4: Intensity of the thermodynamic field upstream of the Mach 1.2 shock wave ($x/\lambda_0 = 14.5$). —— $(\rho_{\rm rms}/\overline{\rho})$, ---- $(T_{\rm rms}/\overline{T})$, ····· $(p_{\rm rms}/\gamma\overline{p})$, —·— $(\sqrt{q^2}/U)$.

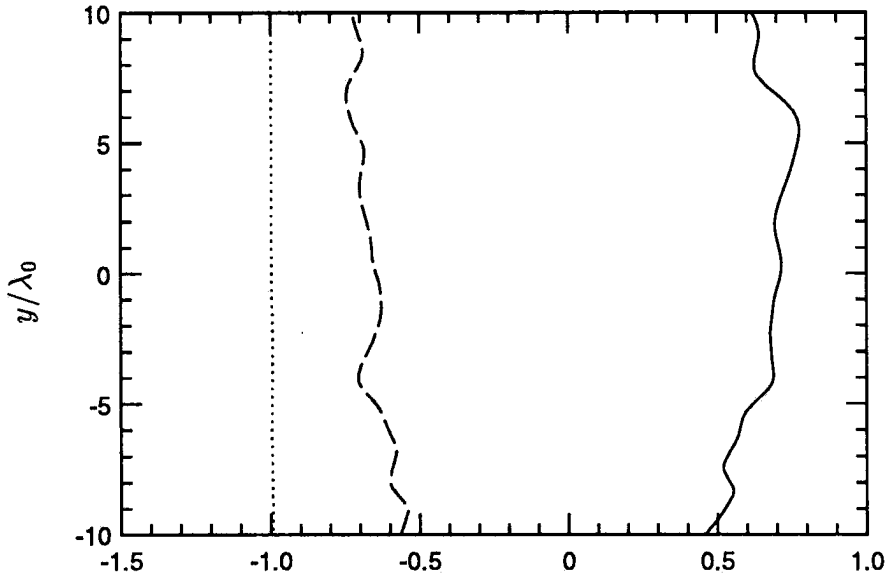


FIGURE 5.5: The correlation of the temperature fluctuations with the velocity and density fluctuations upstream of the Mach 1.2 shock wave ($x/\lambda_0 = 14.5$). —— $(\overline{u'T'}/u_{\rm rms}T_{\rm rms})$, ---- $(\overline{v'T'}/v_{\rm rms}T_{\rm rms})$, ····· $(\overline{\rho'T'}/\rho_{\rm rms}T_{\rm rms})$.

| | | | |
|---|---|---|---|
| $R_\lambda$ | 24.5 | $M_t$ | 0.034 |
| $\overline{u'^2}/q^2$ | 0.57 | $\overline{v'^2}/q^2$ | 0.14 |
| $\overline{w'^2}/q^2$ | 0.29 | $\overline{u'v'}/q^2$ | -0.17 |
| $\sqrt{q^2}/\overline{U_1}$ | 0.029 | $\rho_{\rm rms}/\overline{\rho_1}$ | 0.057 |
| $T_{\rm rms}/\overline{T_1}$ | 0.056 | $p_{\rm rms}/\gamma\overline{P_1}$ | 0.0018 |
| $\overline{u'T'}/u_{\rm rms}T_{\rm rms}$ | 0.71 | $\overline{v'T'}/v_{\rm rms}T_{\rm rms}$ | -0.65 |
| $\overline{\rho'T'}/\rho_{\rm rms}T_{\rm rms}$ | -0.996 | | |

TABLE 5.2: Parameters upstream of the Mach 1.2 shock wave at the center streamline.

As anticipated, the mean velocity varies linearly across streamlines, the mean pressure is uniform and the mean temperature varies quadratically. The transverse components of mean velocity, while not plotted, were examined and found to be negligible; $\overline{v}$ is four orders lower than $U$.

Profiles of the turbulence Reynolds stresses ($\overline{u_i'u_j'}$) at the same streamwise location (figure 5.2) show the ordering ($\overline{u'^2} > \overline{w'^2} > \overline{v'^2}$) that is commonly observed in two-dimensional shear flows (Townsend, 1976). The kinetic energy is observed to decrease in magnitude with increasing $y$ location. As noted in Appendix C, this behavior is consistent with viscous effects increasing in the $y$ direction due to the decreasing mean density in that direction. Also, as shown in figure 5.3, the Reynolds stresses normalized by $q^2$ are nearly uniform across the mean streamlines.

The turbulence results show some oscillations, suggesting limited statistical sample. Note that the plotted results were obtained by averaging over the $z-$direction and time. After initial transients were allowed to exit the domain, a total of 95 time samples were obtained over 8550 timesteps (3.8 time units). For reference, it takes 4.4 time units to convect a single realization of inflow turbulence at the inflow plane and about 3.9 time units for a particle at the centerline to travel the length of the domain. The computational cost is approximately 225 single processor Cray C90 hours per flow-through time based on the centerline velocity. The cost of obtaining statistical convergence to the extent possible in computations with at least two homogeneous directions was estimated to be prohibitive. As a result, some oscillation in the results was tolerated.

The intensity of the density, temperature and pressure field upstream of the

Mach 1.2 shock wave is plotted in figure 5.4. The value of $\rho_{\rm rms}/\overline{\rho}$ is seen to be nearly equal to that of $T_{\rm rms}/\overline{T}$. By comparison, the value of $p_{\rm rms}/\overline{p}$ is seen to be noticeably smaller. The correlation coefficient between the density and temperature fluctuations ($\overline{\rho' T'}/\rho_{\rm rms} T_{\rm rms}$) is plotted in figure 5.5 and is equal to approximately -0.99 at all $y-$ locations. In light of Kovasznay's (1953) modal decomposition, this suggests that the thermodynamic field upstream of the shock is dominated by entropy fluctuations. Also, the intensity of the density and temperature fluctuations are comparable to that of the velocity fluctuations. As shown in figure 5.4, $\rho_{\rm rms}/\overline{\rho}$ and $T_{\rm rms}/\overline{T}$ are approximately twice $\sqrt{q^2}/U$. The correlation between the velocity and temperature fluctuations is shown in figure 5.5. As anticipated from Appendix C, $\overline{u'T'}$ is seen to be positive on all streamlines.

The relevant non-dimensional parameters of the turbulence upstream of the Mach 1.2 shock wave are tabulated in Table 5.2. All quantities tabulated, are measured at the center streamline ($y/\lambda_0 = 0$) immediately upstream of the shock wave ($x/\lambda_0 = 14.5$). The upstream turbulence is seen to be at low Reynolds number, low fluctuation Mach number, and dominated by vortical and entropy fluctuations that are correlated such that $\overline{u'T'}$ is positive.

## 5.3 The mean flow across the shock wave

The mean flow undergoes noticeable change across the shock wave, which appears to be predicted quite accurately by the Rankine Hugoniot relations for a steady laminar shock. Figure 5.6 shows profiles of the mean streamwise velocity on both sides of the shock. The upstream profile is measured at the location, $x/\lambda_0 = 14.5$ while the downstream profile is measured at $x/\lambda_0 = 25$. The velocity profiles are seen to be quite linear on both sides of the shock, with the shear rate being lower on the downstream side.

The velocity ratio across a steady laminar shock is known to be given by the relation,

$$\frac{U_2}{U_1} = \frac{2 + (\gamma - 1)M_1^2}{(\gamma + 1)M_1^2}. \tag{5.1}$$

Figure 5.6 tests the validity of the above equation across the shock wave on each mean streamline in the shear flow. The downstream velocity profile is divided by the velocity ratio across a laminar shock and the resulting profile is compared to

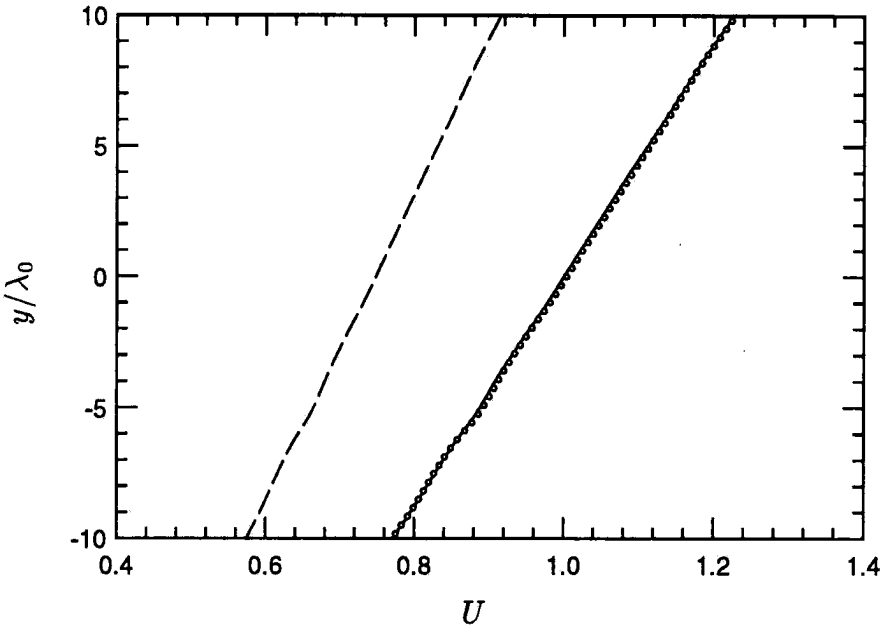


FIGURE 5.6: The mean velocity upstream and downstream of the Mach 1.2 shock wave. —— $(x/\lambda_0 = 14.5)$, ---- $(x/\lambda_0 = 25)$. The symbols are obtained by dividing the downstream velocity profile by the jump across a laminar shock.

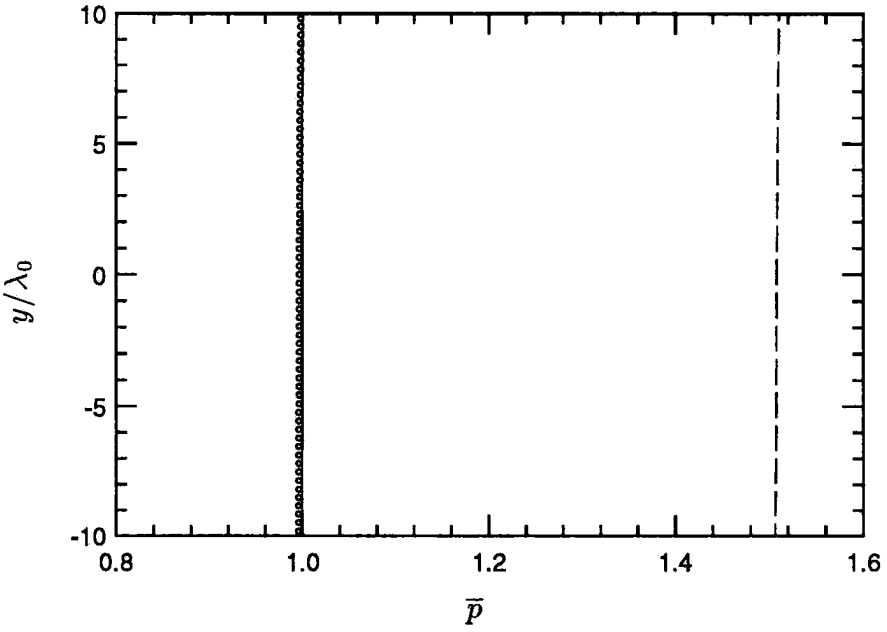


FIGURE 5.7: The mean pressure upstream and downstream of the Mach 1.2 shock wave. —— $(x/\lambda_0 = 14.5)$, ---- $(x/\lambda_0 = 25)$. The symbols are obtained by dividing the downstream pressure profile by the jump across a laminar shock.

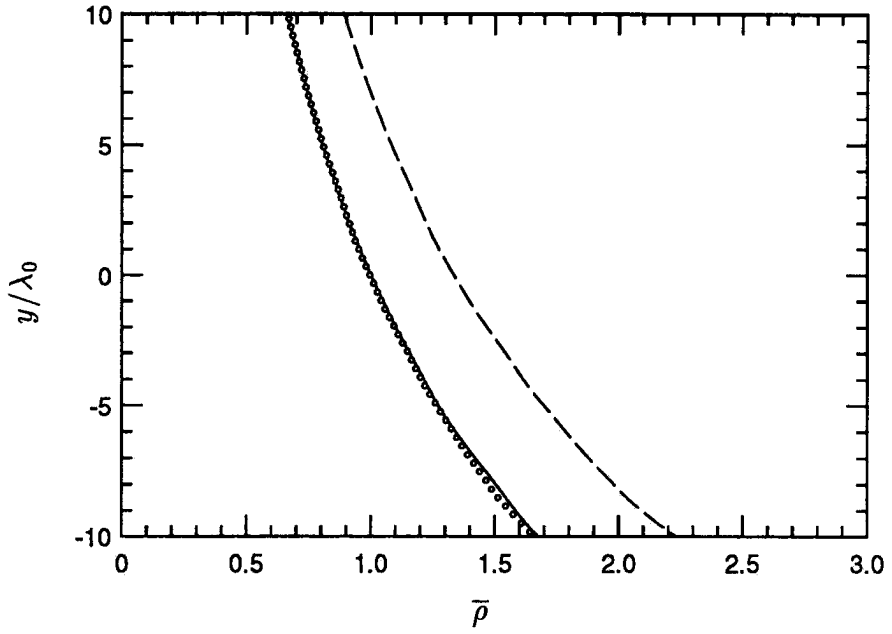


FIGURE 5.8: The mean density upstream and downstream of the Mach 1.2 shock wave. ——— $(x/\lambda_0 = 14.5)$, ---- $(x/\lambda_0 = 25)$. The symbols are obtained by dividing the downstream density profile by the jump across a laminar shock.

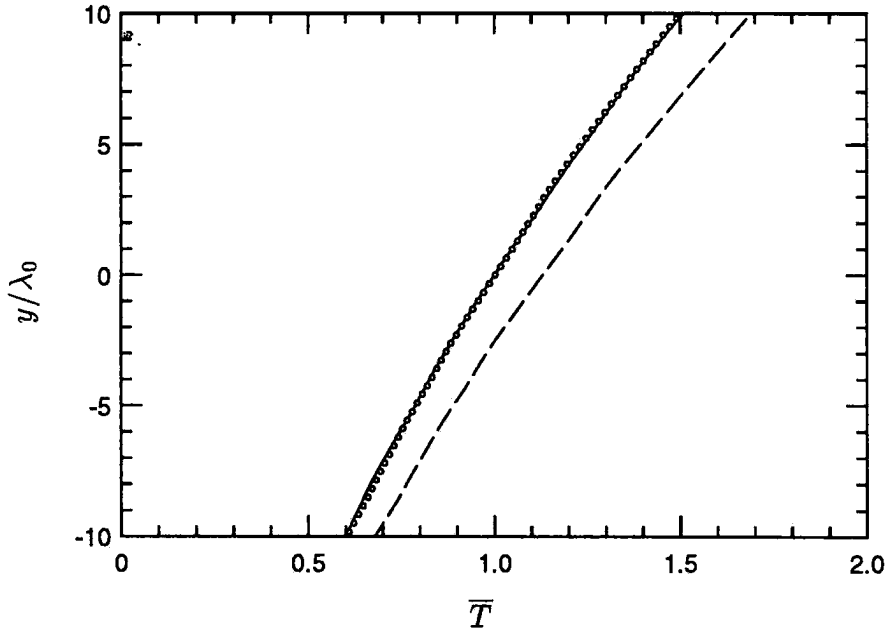


FIGURE 5.9: The mean temperature upstream and downstream of the Mach 1.2 shock wave. ——— $(x/\lambda_0 = 14.5)$, ---- $(x/\lambda_0 = 25)$. The symbols are obtained by dividing the downstream temperature profile by the jump across a laminar shock.

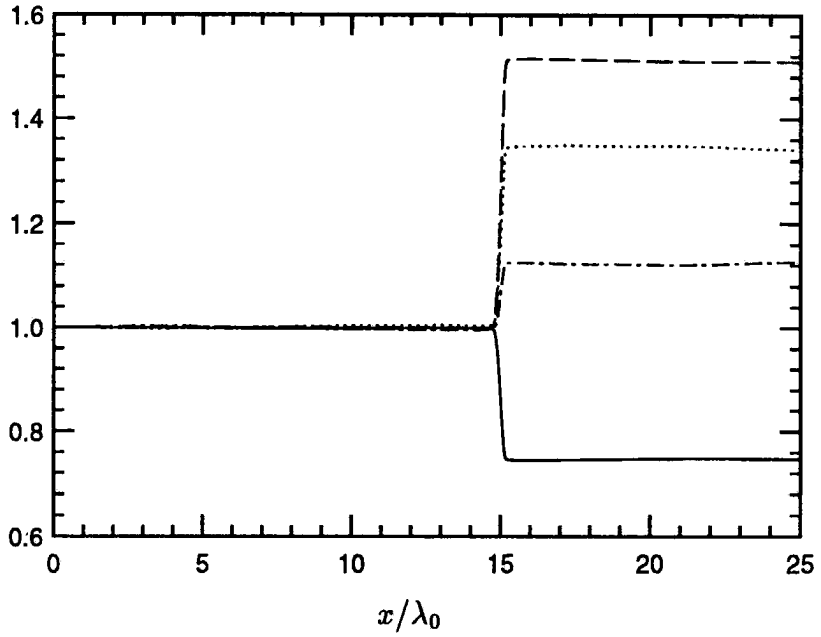


FIGURE 5.10: Streamwise variation of the mean flow at the center streamline ($y/\lambda_0 = 0$). All curves are normalized with their value at the inflow. ——— ($U$), ---- ($\overline{p}$), ····· ($\overline{\rho}$), —·— ($\overline{T}$).

the upstream profile. As seen in figure 5.6, the comparison is quite good, suggesting that the laminar normal shock equations predict the jump in the mean velocity profile quite accurately. The mean pressure, density and temperature profiles show similar behavior. As shown in figures 5.7 through 5.9, dividing the downstream profiles by the corresponding jump for a laminar shock shows good agreement with the upstream profiles.

## 5.4 Turbulence kinetic energy

Interaction with the Mach 1.2 shock wave is observed to decrease the kinetic energy of the turbulence in the shear flow. As shown in figure 5.11, the streamwise component of kinetic energy $\overline{u'^2}$ drops across the shock wave, $\overline{v'^2}$ increases slightly, while the spanwise component $\overline{w'^2}$ remains nearly constant. The net result is a slight drop in the total kinetic energy $q^2$ across the shock wave. This result appears intriguing at first glance. Past studies of isotropic solenoidal turbulence interacting with a shock wave (Ribner; 1954, Lee, Lele and Moin;. 1992) show increase in turbulence kinetic energy across the shock. In addition, rapid distortion theory used in Chapter 2 predicted the amplification of kinetic energy in the shear flow to

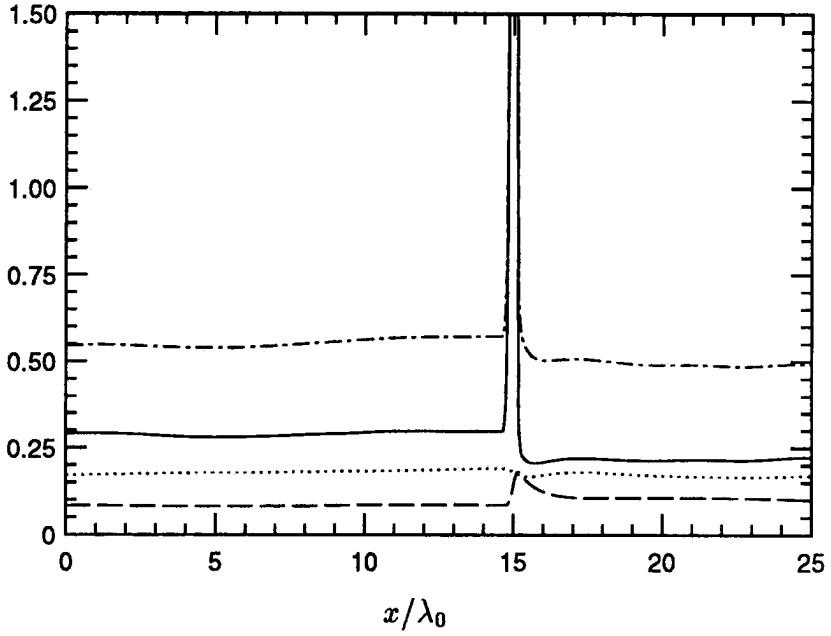


FIGURE 5.11: Streamwise variation of the turbulence Reynolds stresses at the center streamline ($y/\lambda_0 = 0$). All curves are normalized with $u_0^2$. —— $(\overline{u'^2})$, ---- $(\overline{v'^2})$, ····· $(\overline{w'^2})$, —·— $(q^2)$.

be even higher than that of isotropic turbulence. As shown in Table 5.3, the DNS results do not follow the trends predicted by linear analysis.

| Amplification of | Ribner: Isotropic | RDT: Shear | DNS: Shear |
|---|---|---|---|
| $\overline{u'^2}$ | 1.37 | 1.60 | 0.78 |
| $\overline{v'^2}$ | 1.15 | 1.00 | 1.05 |
| $\overline{w'^2}$ | 1.15 | 1.19 | 0.98 |

TABLE 5.3: Amplification of turbulence kinetic energy across the Mach 1.2 shock wave. Linear analysis prediction for isotropic turbulence (Ribner 1954) and shear flow (RDT: $\beta_o = 3$) is compared to the DNS value.

The difference can however be reconciled by recalling that the analyses of Ribner and Chapter 2 do not allow for the presence of upstream entropy fluctuations. As noted from section 5.2, the upstream shear flow has an appreciable level of entropy fluctuations (twice the intensity of the velocity fluctuations). The influence of the upstream entropy fluctuations on the evolution of turbulence kinetic energy across the shock wave would therefore be quite significant.

We recall that the linear analysis performed in Chapter 3 showed that upstream entropy fluctuations with positive $\overline{u'T'}$ would suppress kinetic energy amplification across the shock wave. More specifically, figure 3.14 showed that $\overline{u'^2}$ *decreases* across the shock wave if the intensity of the entropy fluctuations is comparable to that of the velocity fluctuations. The transverse component $\overline{v'^2}$ still increases across the shock wave, although by smaller levels (figure 3.15).

These trends are in agreement with those observed in DNS of the shear flow. Although the analysis performed in Chapter 3 considered isotropic turbulence upstream of the shock, it can be argued that the observed trends should extend to the shear flow. Denoting the shock thickness by $\delta$, the turbulence is strained by the shock wave on a time-scale $\delta/U_1$. The turbulence is simultaneously strained by the mean shear on a time-scale $1/S$, where $S = dU/dy$. Using the variable $l$ to denote the lengthscale of the turbulence, the turbulence turn-over time scale is approximately equal to $l/q$. Since, $\delta/l \ll 1$, and $Sl/q$ (Appendix C) is typically between 5 and 10, the effect of the mean shear is expected to be small as the turbulence passes through the shock wave. As a result, as argued in section 3.5, bulk compression and baroclinic torque are expected to be the primary factors that influence the evolution of the vorticity fluctuations across the shock. The positive correlation between $u'$ and $T'$ upstream of the shock wave is therefore expected to suppress kinetic energy amplification in the shear flow.

Morkovin's hypothesis and experimental observations show strong evidence that $u'$ and $T'$ are negatively correlated in supersonic boundary layers with the correlation coefficient varying between -0.8 and -1. The analysis performed in Chapter 3 suggested that this negative correlation would result in strong kinetic energy amplification across a shock wave. To test this assertion, DNS of the Mach 1.5 shock wave interacting with a shear flow was performed. In contrast to the Mach 1.2 simulation, the turbulence upstream of the shock wave had negative $\overline{u'T'}$ on all the streamlines. This was made possible by the initial conditions used in the temporal simulation to generate inflow turbulence. Details of this procedure are discussed in section 4.8.

The evolution of turbulence kinetic energy across the Mach 1.5 shock wave is plotted in figure 5.12. All components of kinetic energy are seen to undergo noticeable amplification across the shock wave. Using the downstream value at $x/\lambda_0 = 19$, the kinetic energy amplification across the Mach 1.5 shock wave is

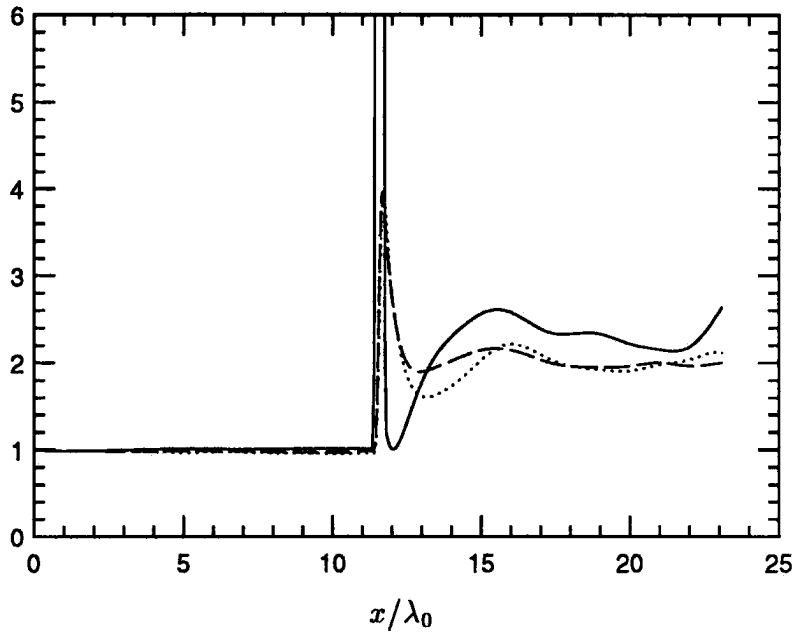


FIGURE 5.12: Variation of the turbulence kinetic energy across the Mach 1.5 shock wave. All curves are normalized with their value at the inflow. —— $(\overline{u'^2})$, ---- $(\overline{v'^2})$, ····· $(\overline{w'^2})$.

compared in Table 5.4 to linear analysis predictions. The amplification levels are seen to be uniformly higher than that of isotropic turbulence. Also, the amplification of the transverse components is higher than predicted by RDT, which is consistent with the absence of entropy fluctuations in the analysis. However, the amplification of the streamwise kinetic energy is lower than predicted by RDT, suggesting that RDT tends to overpredict the streamwise kinetic energy amplification. A similar conclusion regarding RDT was reached by Lee, Lele and Moin (1992) in their study of the interaction of isotropic turbulence with a shock wave.

| Amplification of | Ribner | RDT: Shear flow | DNS: Shear flow |
|---|---|---|---|
| $\overline{u'^2}$ | 1.6 | 2.6 | 2.3 |
| $\overline{v'^2}$ | 1.38 | 1.25 | 1.9 |
| $\overline{w'^2}$ | 1.38 | 1.59 | 2.0 |

TABLE 5.4: Amplification of turbulence kinetic energy across the Mach 1.5 shock wave. Linear analysis prediction for isotropic turbulence (Ribner 1954) and shear flow (RDT: $\beta_o = 3$) is compared to the DNS value.

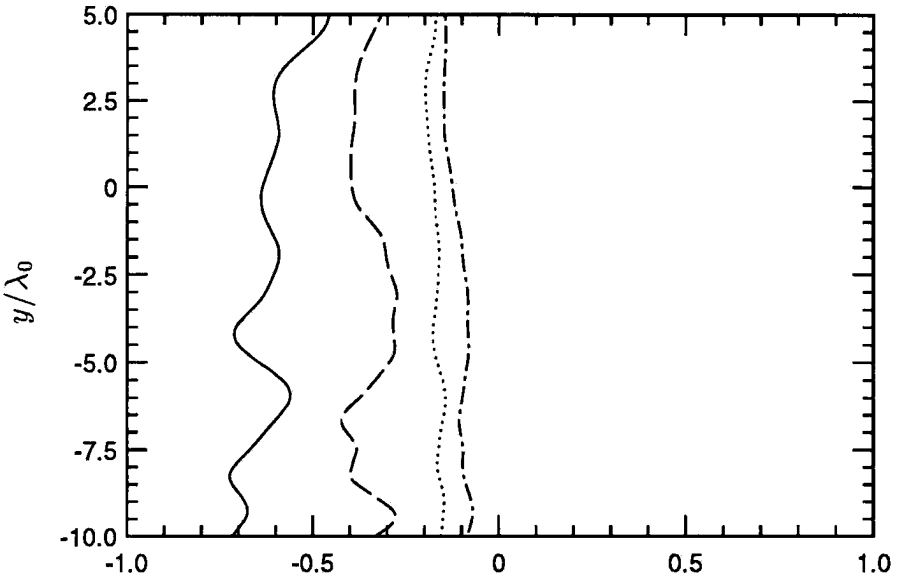


FIGURE 5.13: Profiles of Reynolds shear stress on both sides of the shock wave. ——— ($\overline{u'v'}$ upstream), - - - - ($\overline{u'v'}$ downstream), ····· ($\overline{u'v'}/q^2$ upstream), —·— ($\overline{u'v'}/q^2$ downstream). The upstream and downstream profiles are measured at $x/\lambda_0 = 14.5$ and 25 respectively.

Note that the turbulence kinetic energy increases rapidly immediately *behind* the Mach 1.5 shock wave, similar to the trend observed when the upstream turbulence is isotropic. In contrast, this rapid rise in kinetic energy is not observed behind the Mach 1.2 shock wave (figure 5.11). This difference between the two simulations may be explained by the different signs of the upstream velocity-temperature correlation. Linear analysis applied to the interaction of isotropic turbulence interacting with a shock wave shows a similar trend. Figure 3.11 shows noticeable rise in $q^2$ behind a Mach 1.5 shock wave if $\overline{u'T'}$ is negative upstream. On the other hand, this downstream rise in energy is strongly suppressed if the velocity temperature correlation is positive.

## Section 5.5 Reynolds shear stress

The influence of the shock wave on the Reynolds shear stress, $\overline{u'v'}$ is considered in this section. Figures 5.13 and 5.14 show the evolution of $\overline{u'v'}$ and the non-dimensional shear stress $\overline{u'v'}/q^2$ across the Mach 1.2 shock wave. Both quantities are seen to undergo a decrease in magnitude across the shock. Using values measured at $x/\lambda_0 = 14.5$ and 25 respectively, the change in shear stress across the Mach 1.2

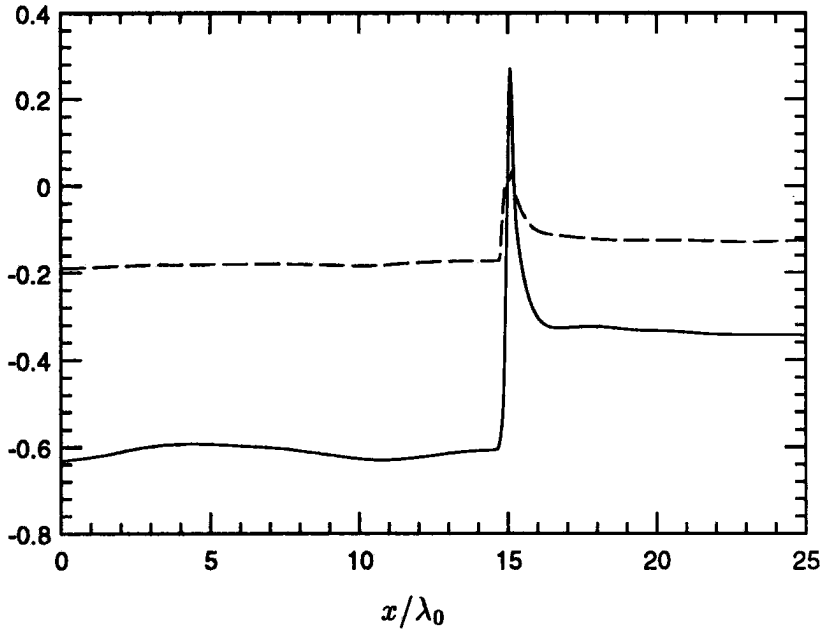


FIGURE 5.14: Streamwise variation of the turbulence Reynolds shear stress for the Mach 1.2 shock ($y/\lambda_0 = 0$). —— $(\overline{u'v'})$, ---- $(\overline{u'v'}/q^2)$. $\overline{u'v'}$ is normalized by the value of $u_{\rm rms}v_{\rm rms}$ at the inflow.

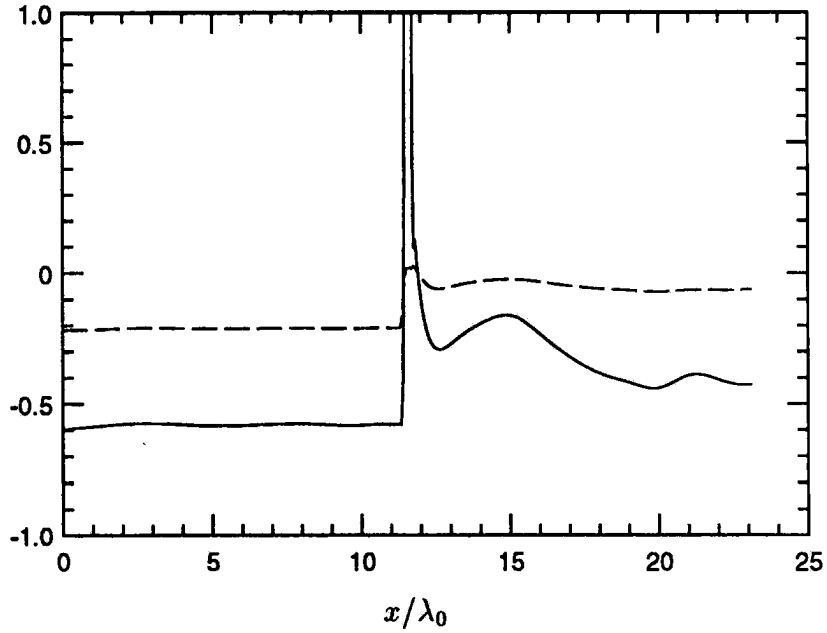


FIGURE 5.15: Variation of the turbulence Reynolds shear stress across the Mach 1.5 shock wave. —— $(\overline{u'v'})$, ---- $(\overline{u'v'}/q^2)$. $\overline{u'v'}$ is normalized by the value of $u_{\rm rms}v_{\rm rms}$ at the inflow.

| | Upstream | Downstream |
|---|---|---|
| $\overline{u'v'}$ | -0.61 | -0.34 |
| $\overline{u'v'}/q^2$ | −0.17 | -0.12 |

TABLE 5.5: Variation of Reynolds shear stress across the Mach 1.2 shock wave at the center streamline ($y/\lambda_0 = 0$). $\overline{u'v'}$ is normalized by the value of $u_{\rm rms}v_{\rm rms}$ at the inflow. The upstream and downstream values are measured at $x/\lambda_0 = 14.5$ and 25 respectively.

shock wave is tabulated in Table 5.5.

We saw in Section 5.4 that turbulence kinetic energy decreased across the Mach 1.2 shock wave due to $\overline{u'T'}$ being positive upstream. However, the decrease in magnitude of shear stress is not a result of positive velocity-temperature correlation. Recall that RDT predicted similar decrease in shear stress magnitude across a normal shock. Also, as shown in figure 5.15, $\overline{u'T'}$ is observed to decrease in magnitude across the Mach 1.5 shock wave although $\overline{u'T'}$ is negative upstream.

Instantaneous fields of $u'v'$ from the Mach 1.5 simulations were examined. The fluctuations were computed with respect to the mean obtained by averaging over the $z-$ direction. The shear stress field upstream of the shock wave was seen to essentially consist of regions of high negative values interspersed with regions of low positive values. Upon passage through the shock wave, the negative regions were observed to be suppressed in magnitude while the positive regions were seen to amplify. The net result is a decrease in shear stress magnitude across the shock wave.

Recall that the decrease in $\overline{u'v'}$ across a normal shock wave was attributed (using RDT) to amplification of the pressure-strain correlation in the equation for $\overline{u'v'}$. A more physically appealing argument is proposed below. Experiments (*e.g.*, Head and Bandopadhyay, 1981) and computations (*e.g.*, Moin and Kim; 1985, Rogers, Moin and Reynolds; 1986) have shown that the vortical structures (away from the wall) in shear flows such as the turbulent boundary layer, channel flow and homogeneous shear flow tend to align at approximately 45° with the direction of the mean flow. That is, distributions of the angle $\theta = \tan^{-1}(\omega'_y/\omega'_x)$ tend to peak at 45° with the direction of the mean flow.

Linear analysis and DNS show that passage through a normal shock tends to amplify the transverse components ($\omega'_y$ and $\omega'_z$) of vorticity, while the streamwise

component stays nearly constant. This implies that vortical structures immediately behind the shock wave are closer to being vertical; *i.e.*, $\theta$ peaks at an angle greater than 45°. This increase in the peak inclination angle would result in a decrease in the magnitude of $\overline{u'v'}$; if the vortical structures were vertical, then $\overline{u'v'}$ would be zero.

## Section 5.6 Thermodynamic fluctuations

The evolution of the thermodynamic fluctuations across the shock wave is considered in this section. Figure 5.16 shows the variation of the pressure, density and temperature fluctuations along the center streamline ($y/\lambda_0 = 0$) of the Mach 1.2 shock wave. All three variables are seen to amplify, with the amplification of the pressure fluctuations noticeably exceeding that of density and temperature immediately behind the shock wave. The *rms* level of pressure fluctuations immediately behind the shock is seen to be about 15 times its upstream value. As observed in the interaction of isotropic turbulence with a shock, the pressure fluctuations decay rapidly behind the shock to attain a far-field ($x/\lambda_0 = 25$) level that is 2.16 times its value at the inflow.

This high level of amplification of pressure fluctuations is explained below. As shown in figure 5.4, $p_{\rm rms}/\overline{p}$ upstream of the shock wave is noticeably smaller than $\rho_{\rm rms}/\overline{\rho}$, $T_{\rm rms}/\overline{T}$ and $q/U$. As a result, the intensity of the pressure field behind the shock wave is determined by the upstream levels of $\rho_{\rm rms}/\overline{\rho}$ and $q/U$; *i.e.*, $p_{\rm rms}/\overline{p_1}$ behind the shock wave scales with the upstream value of $\rho_{\rm rms}/\overline{\rho_1}$ (figure 5.17). This implies that the amplification of pressure fluctuations,

$$\frac{\sqrt{\overline{p'^2_{\rm down}}}}{\sqrt{\overline{p'^2_{\rm up}}}} = \frac{\sqrt{\overline{p'^2_{\rm down}}}/\overline{p_1}}{\sqrt{\overline{\rho'^2_{\rm up}}}/\overline{\rho_1}} \cdot \frac{\sqrt{\overline{\rho'^2_{\rm up}}}/\overline{\rho_1}}{\sqrt{\overline{p'^2_{\rm up}}}/\overline{p_1}} \gg 1. \tag{5.2}$$

Profiles of $p_{\rm rms}/\gamma\overline{P}$, $\rho_{\rm rms}/\overline{\rho}$ and $T_{\rm rms}/\overline{T}$ in the near-field ($x/\lambda_0 = 15.7$) and far-field ($x/\lambda_0 = 25$) behind the Mach 1.2 shock wave are plotted in figures 5.18 and 5.19 respectively. The intensity of pressure fluctuations is seen to be of the same order as that of density and temperature immediately behind the shock wave. However, due to their rapid decay behind the shock wave, the far-field intensity of the pressure fluctuations is seen to be noticeably smaller than density and temperature. As shown in figure 5.20, a similar trend is observed across the Mach 1.5 shock wave.

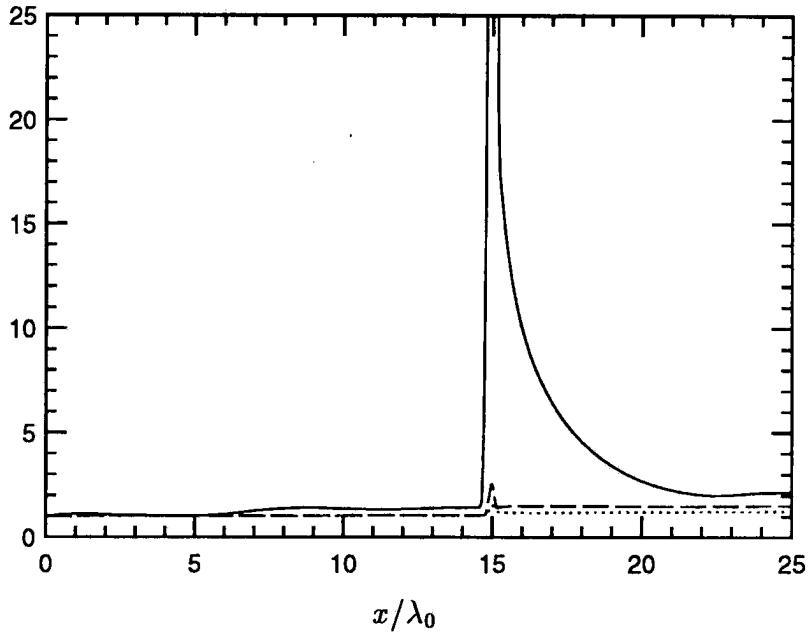


FIGURE 5.16: Streamwise variation of the thermodynamic fluctuations at the center streamline ($y/\lambda_0 = 0$) of the Mach 1.2 shock. ——— ($p_{\rm rms}$), ---- ($\rho_{\rm rms}$), ····· ($T_{\rm rms}$). All variables are normalized by their values at the inflow.

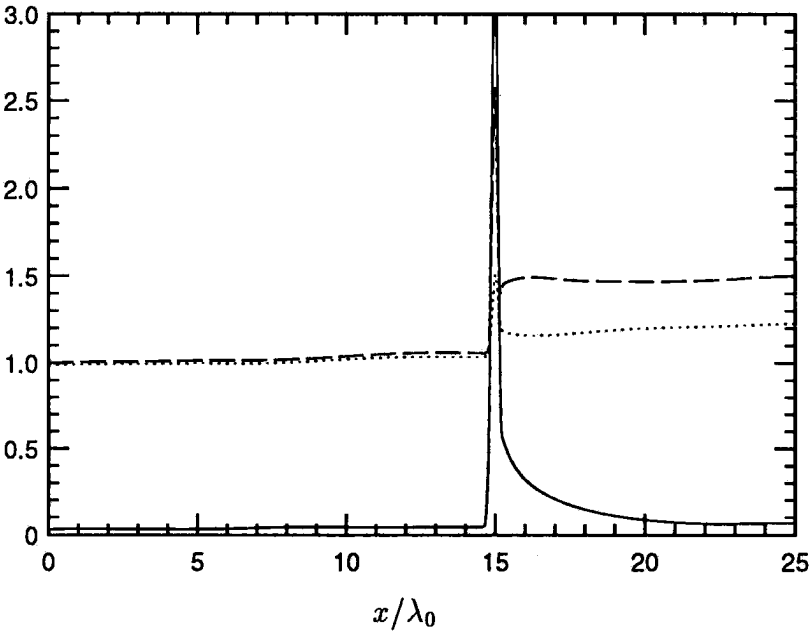


FIGURE 5.17: Streamwise variation of the thermodynamic fluctuations at the center streamline ($y/\lambda_0 = 0$) of the Mach 1.2 shock. ——— ($p_{\rm rms}/\overline{p}_{\rm inflow}$), ---- ($\rho_{\rm rms}/\overline{\rho}_{\rm inflow}$), ····· ($T_{\rm rms}/\overline{T}_{\rm inflow}$). All variables are normalized by the value of $\rho_{\rm rms}/\overline{\rho}$ at the inflow.

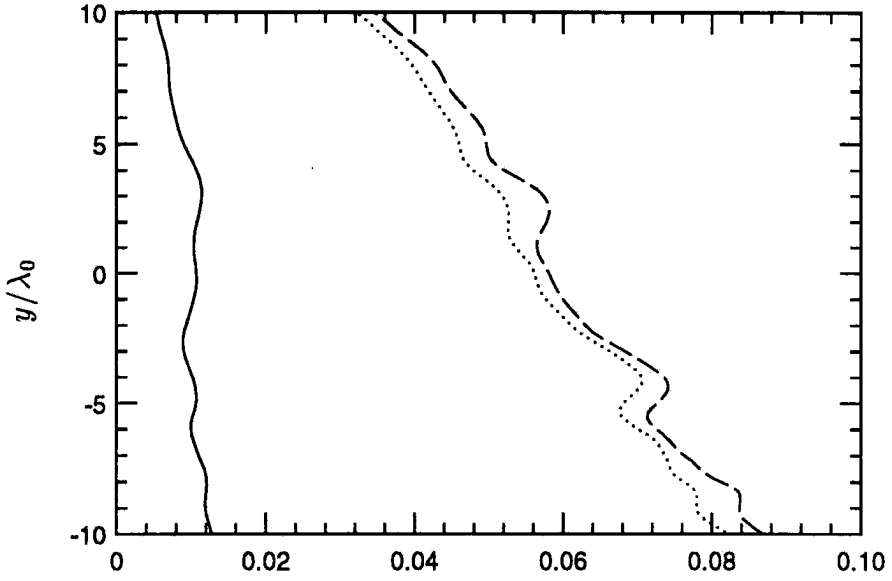


FIGURE 5.18: Profiles of the intensity of the thermodynamic field in the near-field behind the shock ($x/\lambda_0 = 15.7$). —— $(p_{\rm rms}/\gamma\overline{p})$, ---- $(\rho_{\rm rms}/\overline{\rho})$, ····· $(T_{\rm rms}/\overline{T})$.

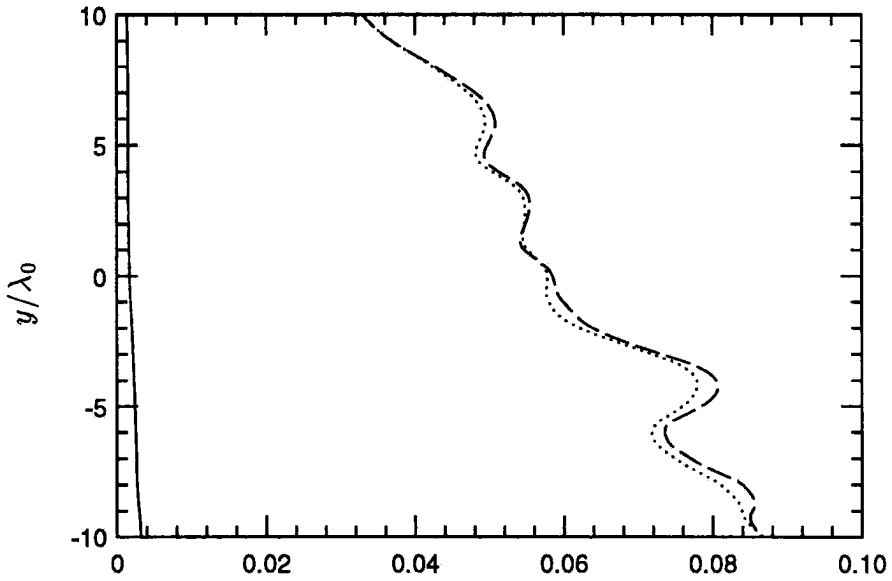


FIGURE 5.19: Profiles of the intensity of the thermodynamic field in the far-field behind the shock ($x/\lambda_0 = 25$). —— $(p_{\rm rms}/\gamma\overline{p})$, ---- $(\rho_{\rm rms}/\overline{\rho})$, ····· $(T_{\rm rms}/\overline{T})$.

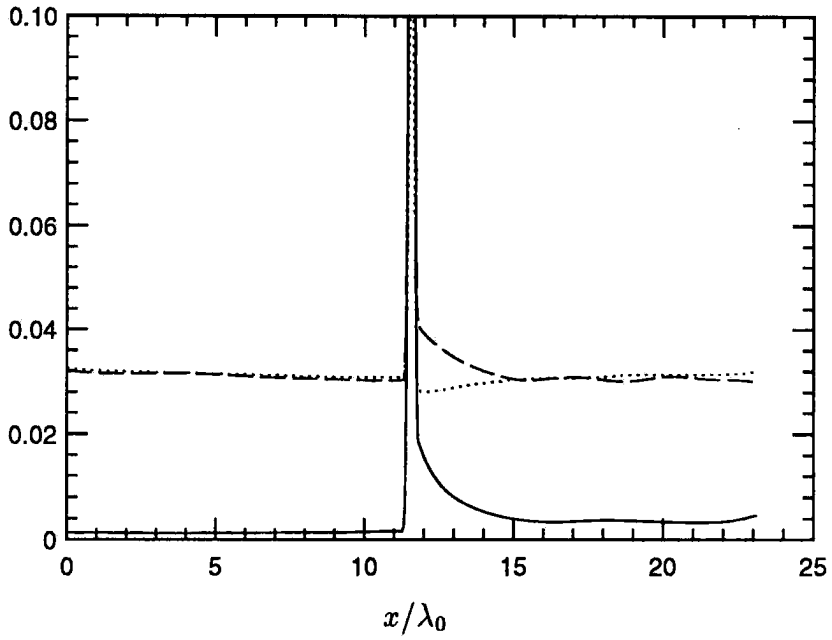


FIGURE 5.20: The intensity of the thermodynamic field across the Mach 1.5 shock wave. —— $(p_{\rm rms}/\gamma\overline{p})$, ---- $(\rho_{\rm rms}/\overline{\rho})$, ····· $(T_{\rm rms}/\overline{T})$.

Passage through the shock wave is seen to affect the velocity-temperature correlation. Plots of the streamwise evolution across the Mach 1.2 shock wave (figures 5.21 and 5.22) show a drop in the magnitude of the correlation between $u'$ and $T'$. Interestingly, the correlation coefficient between $v'$ and $T'$ is seen to increase in magnitude. Using values measured at $x/\lambda_0 = 14.5, 15.7$ and 25 respectively, the values of the correlation coefficients on both sides of the shock wave are tabulated in Table 5.6.

| | Upstream | Near-field | Far-field |
|---|---|---|---|
| $\overline{u'T'}/u_{\rm rms}T_{\rm rms}$ | 0.70 | 0.38 | 0.34 |
| $\overline{v'T'}/v_{\rm rms}T_{\rm rms}$ | −0.64 | -0.76 | -0.74 |
| $\overline{\rho'T'}/\rho_{\rm rms}T_{\rm rms}$ | −0.996 | -0.96 | -0.996 |

TABLE 5.6: Variation of the correlation between the velocity, density and temperature fluctuations across the Mach 1.2 shock wave. The upstream and downstream values are measured at $x/\lambda_0 = 14.5, 15.7$ and 25 respectively.

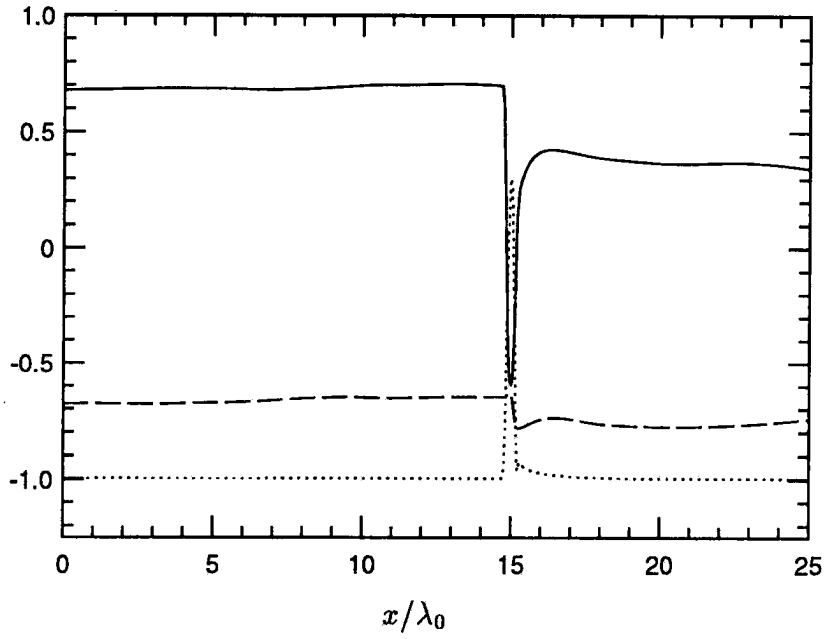


FIGURE 5.21: Streamwise variation of the correlation between the temperature, velocity and density fluctuations at the center streamline ($y/\lambda_0 = 0$) of the Mach 1.2 shock. —— ($\overline{u'T'}/u_{\rm rms}T_{\rm rms}$), ---- ($\overline{v'T'}/v_{\rm rms}T_{\rm rms}$), ····· ($\overline{\rho'T'}/\rho_{\rm rms}T_{\rm rms}$).

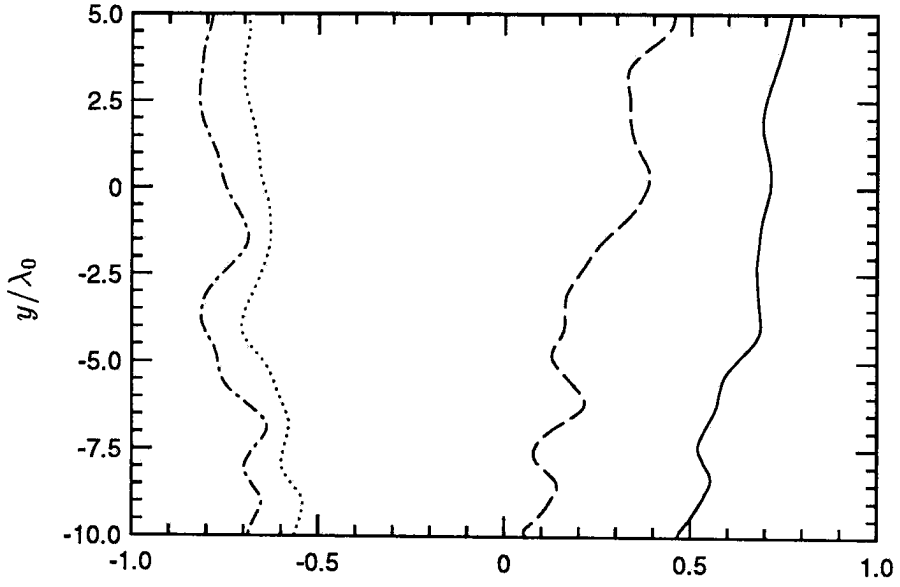


FIGURE 5.22: Profiles of the velocity-temperature correlation on both sides of the Mach 1.2 shock wave. The upstream and downstream values are plotted at $x/\lambda_0 = 14.5$ and 25 respectively. —— (Upstream $\overline{u'T'}/u_{\rm rms}T_{\rm rms}$), ---- (Downstream $\overline{u'T'}/u_{\rm rms}T_{\rm rms}$), ····· (Upstream $\overline{v'T'}/v_{\rm rms}T_{\rm rms}$), —·— (Downstream $\overline{v'T'}/v_{\rm rms}T_{\rm rms}$).

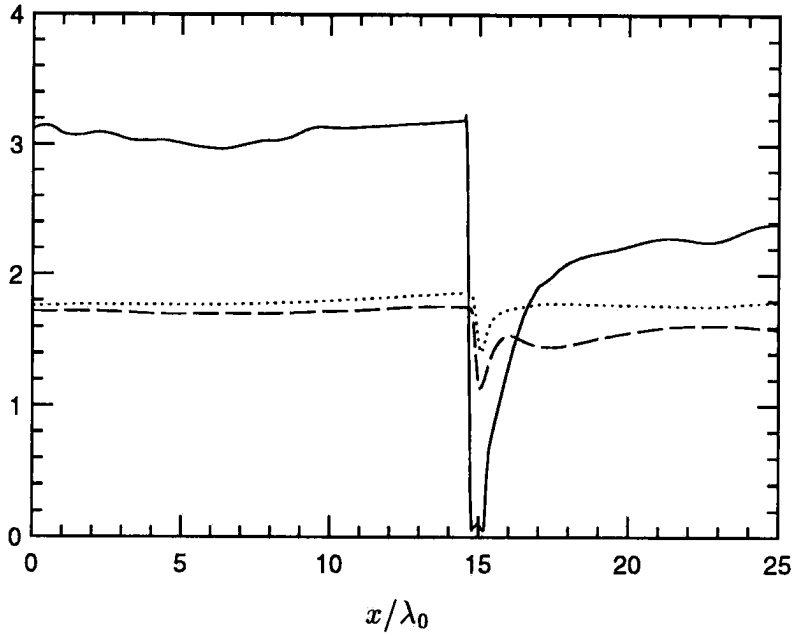


FIGURE 5.23: Variation of the Taylor microscales along the center streamline of the Mach 1.2 shock ($y/\lambda_0 = 0$). —— $(\lambda_1/\lambda_0)$, ---- $(\lambda_2/\lambda_0)$, ····· $(\lambda_3/\lambda_0)$.

Also tabulated, is the correlation coefficient between density and temperature fluctuations. The correlation coefficient is nearly -1 upstream, and drops slightly across the shock due to the appreciable level of pressure fluctuations immediately behind the shock wave. As the pressure field decays behind the shock, the correlation coefficient increase in magnitude to a far-field value of nearly -1, indicating the dominance of entropy fluctuations in the far-field.

## Section 5.7 Turbulence lengthscale

The lengthscales of the turbulent fluctuations are seen to decrease across the shock wave, irrespective of whether the upstream velocity-temperature correlation is positive or negative. Using the Taylor microscale,

$$\lambda_\alpha^2 = \frac{\overline{u'^2_\alpha}}{\overline{(\partial u'_\alpha/\partial x_\alpha)^2}} \tag{5.3}$$

as a representative lengthscale, the streamwise evolution of $\lambda_\alpha$ across the Mach 1.2 and Mach 1.5 shock waves is plotted in figures 5.23 and 5.24 respectively. As observed when the upstream turbulence is isotropic, the microscales in all three directions decrease across the shock, with the shock-normal microscale decreasing

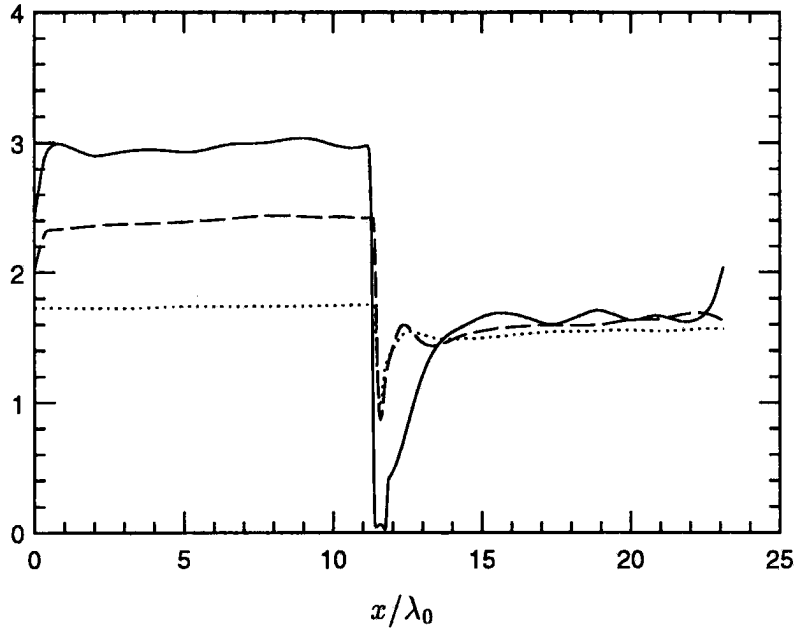


FIGURE 5.24: Variation of Taylor microscales across the Mach 1.5 shock. —— $(\lambda_1/\lambda_0)$, ---- $(\lambda_2/\lambda_0)$, ····· $(\lambda_3/\lambda_0)$.

the most. Interestingly, all three microscales behind the Mach 1.5 shock wave are seen to be equal.

This behavior is different from that observed by experiments on the interaction of a turbulent boundary layer with a shock wave, where an increase in turbulence lengthscale is observed across the shock (Smits and Muck, 1987). The difference can however, be reconciled by noting that a turbulent boundary layer separates upon interacting with a shock wave. The separation would result in an increase in lengthscale of the boundary layer turbulence. Similar increase in lengthscale is observed in incompressible boundary layers upon separation. However, when unbounded turbulent flows interact with a shock, in the absence of separation, the bulk compression across the shock wave would result in a decrease in turbulence lengthscale.

## 5.8 Summary

Results obtained from direct numerical simulation of the interaction of the turbulent shear flow with a normal shock wave were presented in this chapter. Two cases were considered: Mach 1.2 and Mach 1.5 respectively. The sign of the

correlation between $u'$ and $T'$ upstream of the Mach 1.2 shock wave was positive, while that upstream of the Mach 1.5 shock wave was negative. The influence of the shock wave on the mean flow, turbulence kinetic energy, Reynolds shear stress, thermodynamic fluctuations and lengthscales was discussed.

The mean flow was seen to noticeably change across the shock wave, with the change being predicted quite accurately by the Rankine Hugoniot equations for a steady laminar shock. The evolution of the turbulence kinetic energy was observed to be different between the two simulations. While the kinetic energy of the turbulence decreased across the Mach 1.2 shock wave, it amplified considerably across the Mach 1.5 shock. These trends were attributed to the different nature of the upstream entropy fluctuations in the two computations. The observed evolution of turbulence kinetic energy followed the trend predicted by linear analysis, where positive upstream $\overline{u'T'}$ was seen to suppress the kinetic energy while negative upstream correlation was seen to considerably enhance it.

The Reynolds shear stress $\overline{u'v'}$ was observed to *decrease* in magnitude across the shock wave irrespective of the sign of the upstream velocity-temperature correlation. The observed decrease followed the trend predicted by rapid distortion theory. An argument based on the inclination of vortical structures was proposed to explain this decrease in shear stress magnitude across a normal shock wave. Instantaneous fields of shear stress showed that the upstream turbulence was essentially composed of regions of high negative shear stress interspersed with regions of low positive shear stress. Upon passage through the shock, the negative regions were suppressed in magnitude while the positive regions amplified, leading to an overall decrease in shear stress magnitude across the shock wave.

The fluctuations in pressure, density and temperature were observed to amplify across the shock wave, with the amplification of pressure fluctuations far exceeding those of density and temperature. The intensity of pressure fluctuations immediately behind the shock wave was found to be significant. However, due to rapid decay behind the shock wave, the intensity of pressure fluctuations in the far-field was significantly smaller than that of density and temperature; *i.e.*, the far-field was dominated by entropy fluctuations.

# Chapter Six
# Conclusions

We have used direct numerical simulation and linear analysis to study the interaction of a shock wave with a turbulent shear flow. Our study aimed towards a fundamental understanding of shock/turbulence interaction. Of particular interest were factors likely to be important in the interaction of a shock wave with a turbulent boundary layer. The simulations examined the interaction of a normal shock with a turbulent shear flow whose mean velocity gradient and mean Mach number were uniform across mean streamlines. The analyses complement the simulation in identifying and explaining important aspects of the interaction. The salient conclusions drawn from this study are summarized below. Sections 6.1 through 6.3 discuss the influence of the anisotropy of the upstream turbulence, upstream acoustic waves and upstream entropy fluctuations. The applicability of Morkovin's hypothesis across a shock is discussed in Section 6.4. Section 6.5 describes the validity of linear analysis for shock/turbulence interaction. Finally, conclusions drawn from the simulations are summarized in Section 6.6.

## 6.1 Anisotropy of the upstream turbulent fluctuations

Rapid distortion theory shows the strong dependence of shock/turbulence interaction on the anisotropy of the upstream turbulence. The evolution of turbulent fluctuations in a shear flow across a shock is considerably different from that of isotropic turbulence. The anisotropy of the shear flow results in larger amplification of turbulent kinetic energy. If the shock-normal direction is denoted by $x$, the evolution of kinetic energy is strongly influenced by the upstream energy spectrum, $E_{11}(k_1)$ and the upstream value of $\overline{u'^2}/q^2$. Mean shear increases the streamwise lengthscale of the turbulent fluctuations thereby moving $E_{11}$ to lower wavenumbers upstream of the shock wave. Also, turbulent fluctuations in a shear flow have a larger fraction of their energy in the streamwise direction; $\overline{u'^2}/q^2$ in a shear flow is about 0.55 as compared to 0.33 in isotropic turbulence. The RDT equations show that these two factors combine to yield higher amplification of kinetic energy across the shock wave.

Reynolds stress modeling in the RDT limit (*i.e.* only rapid terms are retained) shows that popular models ( *e.g.* Launder, Reece, Rodi, 1975; Speziale,

Sarkar, Gatski, 1991) for the pressure-strain correlation are unable to reproduce these trends. For example, the Launder, Reece, Rodi model considerably underpredicts the amplification of kinetic energy. The lack of dependence on upstream spectral information is likely responsible for this deficiency.

The Reynolds shear stress $\overline{u'v'}$ decreases in magnitude across a normal shock wave. Analysis reveals that amplification of the pressure-strain correlation is responsible for this trend. An explanation based upon the inclination angle of the vortical structures in the shear flow was provided to explain this decrease in shear stress magnitude. Instantaneous shear stress fields from the computations shows that the upstream turbulence is essentially composed of regions of high negative shear stress interspersed with regions of low positive shear stress. Upon passage through the shock, the negative regions are suppressed in magnitude while the positive regions amplify, leading to an overall decrease in shear stress magnitude across the shock wave. Reynolds stress modeling in the RDT limit shows that the Launder-Reece-Rodi model is unable to predict this drop in magnitude; it predicts an increase instead.

## 6.2 The influence of upstream acoustic waves

Supersonic flow in wind-tunnels are likely to have high levels of acoustic fluctuations. The influence of these acoustic waves on shock / turbulence interaction was therefore examined using linear analysis. Acoustic fluctuations differ significantly from vortical fluctuations in their evolution across a shock. The kinetic energy of acoustic fluctuations *decreases* slightly across shocks of moderate strength (upstream Mach number between 1.25 and 1.8). Presence of acoustic waves in the upstream turbulent flow would therefore result in lower levels of kinetic energy amplification over this range of shock strength. The amplification of kinetic energy of acoustic fluctuations significantly exceeds that of vortical fluctuations for mean Mach numbers exceeding 3. In fact, the kinetic energy amplification of acoustic fluctuations is asymptotically unbounded; it varies as $M_1^2$. These trends were explained using linear analysis.

Significant increase in sound level is observed across the shock wave. The sound level increases by 5 to 20 decibels across shocks ranging from Mach 1.5 to Mach 5. Acoustic fluctuations generate vortical fluctuations - 'turbulence' behind the shock wave. The contribution of these vortical fluctuations to the far-field kinetic energy increases as the shock strength increases.

## 6.3 The role of upstream entropy fluctuations

Upstream entropic temperature (or density) fluctuations significantly influence the evolution of turbulent fluctuations across the shock wave. Both, the magnitude of temperature fluctuations and their correlation with the velocity field influence shock/turbulence interaction. Temperature fluctuations that are negatively correlated with the streamwise (shock-normal) velocity significantly increase turbulence intensity, vorticity and sound levels behind the shock wave. Positively correlated fluctuations have a suppressing effect. A simple argument based on the effects of bulk compression and baroclinic torque explains these trends. This explanation was further extended to derive a simple formula that predicts the amount of vorticity produced in the interaction of a shock wave with entropic temperature fluctuations.

Appreciable levels of entropy fluctuations are known to be present in turbulent flows with mean temperature variation (*e.g.* boundary layers, jets and wakes) and reacting flows. For example, measurements in flat plate boundary layers show that temperature and density fluctuations arise largely from entropy fluctuations. The intensity of these fluctuations is measured to be around 5% (in non-hypersonic boundary layers), which is of the same magnitude as the intensity of velocity fluctuations. In addition, the velocity and temperature fluctuations are strongly correlated; measurements and Morkovin's hypothesis show that the correlation coefficient between $u'$ and $T'$ is nearly -1. Our results strongly suggest that upstream temperature and density fluctuations have a large influence on shock wave/boundary layer interaction.

## 6.4 Morkovin's hypothesis across a shock wave

The validity of Morkovin's hypothesis:

$$\frac{\rho_{\text{rms}}}{\overline{\rho}} = \frac{T_{\text{rms}}}{\overline{T}} = (\gamma - 1)M^2 \frac{u_{\text{rms}}}{\overline{U}} \tag{6.1}$$

across a shock wave is questionable. Linear analysis and simulation show that the first part of the hypothesis is a reasonable approximation in the far-field of shock waves of moderate strength ($M_1 < 2.5$). The second part of the hypothesis, which requires that fluctuations in stagnation temperature be small does not hold across the shock. Non-negligible oscillation of the shock front is shown to be responsible.

## 6.5 The validity of linear analysis

Linear analysis seems to be a very useful tool in predicting the interaction of a shock wave with an unsteady field of disturbances. Computations of the interaction of a Mach 1.5 shock wave with plane acoustic and vorticity-entropy waves were compared to analysis. Very good agreement was seen at all incidence angles away from the critical angle. This deviation around the critical angles is explained by noting that it corresponds to transonic flow in suitably transformed coordinates. The primary limitation of linear analysis appears to be in the transonic regime. Strong insensitivity to disturbance amplitude is noted (in the non-transonic regime). Of course, an additional restriction is that the analysis is restricted to very simple mean flow; as a result, application to more complex flows is qualitative.

The one-dimensional compression of homogeneous turbulence has restricted relevance to shock/turbulence interaction. It is useful only in predicting the evolution of an incompressible velocity field across a shock of moderate strength. The interaction of acoustic or entropic fluctuations with a shock is not properly represented. Primary reasons for this deviation are the absence of shock distortion effects, lack of enforcement of the Rankine Hugoniot equations, completely different behavior of pressure fluctuations and absence of baroclinic effects in the linear limit.

## 6.6 Direct numerical simulation

The method of Lee, Lele and Moin (1992) was modified to use an instantaneous realization of a developed temporal simulation to generate turbulent fluctuations at the inflow boundary. This approach is considerably better than the use of random numbers with prescribed energy spectrum.

The interaction of a low Reynolds number ($R_\lambda \sim 30$) turbulent shear flow with Mach 1.2 and Mach 1.5 shock waves was computed. The simulations support the predictions made by linear analysis. The evolution of turbulence kinetic energy across the shock wave is seen to depend on the upstream anisotropy and velocity-temperature correlation. Large levels of amplification (2 to 2.5) is seen when $\overline{u'T'}$ is negative upstream of the shock. Negligible amplification is observed when the upstream correlation is positive.

The shear stress ($\overline{u'v'}$) decreases in magnitude across the shock. The Taylor microscales noticeably decrease across the shock wave. The fluctuations in pressure,

density and temperature amplify across the shock wave, with the amplification of pressure fluctuations far exceeding those of density and temperature. The intensity of pressure fluctuations immediately behind the shock wave is significant. However, due to rapid decay behind the shock wave, the intensity of pressure fluctuations in the far-field is significantly smaller than that of density and temperature; *i.e.*, the far-field thermodynamic field is dominated by entropy fluctuations.

# Appendix A

# Supplement to Chapter Three

This appendix supplements Chapter 3 where linear analysis of a shock wave interacting with a vorticity-entropy wave was performed. Recall that Chapter 3 developed the analysis to a point where the solution was known except for some undetermined coefficients. The procedure for obtaining those coefficients is discussed here.

The form of the solution is reproduced from Chapter 3 (Equations 3.20 and 3.21):

$$
\begin{aligned}
\frac{u_2'}{U_1} &= F\ e^{i\widetilde{k}x} e^{ik(ly-mU_1 t)} + G\ e^{ik(mrx+ly-mU_1 t)} \\
\frac{v_2'}{U_1} &= H\ e^{i\widetilde{k}x} e^{ik(ly-mU_1 t)} + I\ e^{ik(mrx+ly-mU_1 t)} \\
\frac{p_2'}{P_2} &= K\ e^{i\widetilde{k}x} e^{ik(ly-mU_1 t)} \\
\frac{\rho_2'}{\overline{\rho}_2} &= \frac{K}{\gamma}\ e^{i\widetilde{k}x} e^{ik(ly-mU_1 t)} + Q\ e^{ik(mrx+ly-mU_1 t)} \\
\frac{T_2'}{\overline{T}_2} &= \frac{\gamma-1}{\gamma} K\ e^{i\widetilde{k}x} e^{ik(ly-mU_1 t)} - Q\ e^{ik(mrx+ly-mU_1 t)}
\end{aligned}
\qquad (A.1)
$$

$$
\frac{\xi_t}{U_1} = L\ e^{ik\ (ly-mU_1 t)}; \qquad \xi_y = -\frac{l}{m} L\ e^{ik\ (ly-mU_1 t)}.
$$

Recall that the wavenumber $\widetilde{k}$ may be real or complex depending on $\psi_1$ being less or greater than $\psi_c$. The following expression for $\widetilde{k}$ is reproduced from Equations 3.17,3.18 and 3.19:

If $0 < \psi_1 < \psi_c$,

$$
\frac{\widetilde{k}}{k} = \frac{U_1}{U_2}\frac{M_2}{1-M_2^2}\left[ -mM_2 + l\sqrt{\frac{m^2}{l^2} - \frac{U_2^2}{U_1^2}\left(\frac{1}{M_2^2}-1\right)}\right] \qquad (A.2)
$$

If $\psi_c < \psi_1 < \pi/2$, $\widetilde{k} = \widetilde{k_r} + i\ \widetilde{k_i}$ where,

$$
\frac{\widetilde{k_r}}{k} = -m\frac{U_1}{U_2}\frac{M_2^2}{1-M_2^2} \qquad (A.3a)
$$

$$\frac{\widetilde{k_i}}{k} = l\frac{U_1}{U_2}\frac{M_2}{1-M_2^2}\sqrt{\frac{U_2^2}{U_1^2}\left(\frac{1}{M_2^2}-1\right)-\frac{m^2}{l^2}} \qquad (A.3b)$$

The coefficients $F, G, H, I, K, Q$ and $L$ are obtained by substituting the solution into the governing equations behind the shock wave and the boundary conditions at the mean position of the shock front. Since the argument of the solution has been matched to that of the incident disturbance this yields a set of equations relating the coefficients. This system of equations is then solved thereby completing the solution.

The form of the incident disturbance, the governing equations behind the shock wave and the boundary conditions at the shock front are given by Equations 3.2 , 3.3 and 3.4 respectively. Substitution into the x momentum equation yields,

$$U_1(-FikmU_1) + U_2U_1Fi\widetilde{k} = -\frac{1}{\overline{\rho}_2}P_2Ki\widetilde{k} \qquad (A.4)$$

which may be rewritten as

$$F = \frac{a_2^2}{\gamma U_1^2}\frac{\frac{\widetilde{k}}{k}}{m-\frac{\widetilde{k}}{kr}}K \qquad (A.5)$$

For reasons of convenience, a complex variable $\alpha$ is defined such that the above equation becomes:

$$F = \alpha\ K \qquad (A.6)$$

The momentum equation in the $y$ direction yields,

$$U_1(-HikmU_1) + U_2U_1Hi\widetilde{k} = -\frac{1}{\overline{\rho}_2}P_2Kikl \qquad (A.7)$$

Rearranging, we get

$$H = \frac{a_2^2}{\gamma U_1^2}\frac{l}{m-\frac{\widetilde{k}}{kr}}K \qquad (A.8)$$

which is expressed in terms of the complex variable $\beta$ as,

$$H = \beta\ K \qquad (A.9)$$

The acoustic component of the velocity field has already been constrained to satisfy the acoustic equations. As a result, the continuity equation behind the shock wave reduces to the vortical component of the velocity field being solenoidal. This yields,

$$U_1Gikmr + U_1Iikl = 0 \qquad (A.10)$$

which implies,

$$I = -\frac{mr}{l}G \tag{A.11}$$

Prior to substitution, the boundary conditions at the shock wave are written in the following compact form:

$$\frac{u_2' - \xi_t}{U_1} = B_1 \frac{u_1' - \xi_t}{U_1} + B_2 \frac{T_1'}{\overline{T}_1} \tag{A.12a}$$

$$\frac{\rho_2'}{\overline{\rho}_2} = C_1 \frac{u_1' - \xi_t}{U_1} + C_2 \frac{T_1'}{\overline{T}_1} \tag{A.12b}$$

$$\frac{p_2'}{P_2} = D_1 \frac{u_1' - \xi_t}{U_1} + D_2 \frac{T_1'}{\overline{T}_1} \tag{A.12c}$$

$$\frac{v_2'}{U_1} = \frac{v_1'}{U_1} + E_1 \, \xi_y \tag{A.12d}$$

The variables $B_1, B_2, C_1, C_2, D_1, D_2$ and $E_1$ are readily obtained by comparison to Equations 3.4. Substitution of the solution into the above equations yields:

$$F + G - L = B_1(lA_v - L) - B_2 \, A_e \tag{A.13a}$$

$$\frac{K}{\gamma} + Q = C_1(lA_v - L) - C_2 \, A_e \tag{A.13b}$$

$$K = D_1(lA_v - L) - D_2 A_e \tag{A.13c}$$

$$H + I = -mA_v - E_1 \frac{l}{m} L \tag{A.13d}$$

Equations $A.6, A.9, A.11$ and $A.13$ may solved to obtain the coefficients. Rather than solve them directly, we normalize them by the incident vorticity wave and then solve the resulting equations. This involves dividing through the equations by $A_v$ and using a tilde to denote the normalized coefficients; *i.e.*, $\widetilde{L} = L/A_v$. This yields the following set of equations.

$$\widetilde{F} = \alpha \widetilde{K} \tag{A.14a}$$

$$\widetilde{H} = \beta \widetilde{K} \tag{A.14b}$$

$$\widetilde{I} = -\frac{mr}{l}\widetilde{G} \tag{A.14c}$$

$$\widetilde{F} + \widetilde{G} - \widetilde{L} = B_1(l - \widetilde{L}) - B_2 \frac{A_e}{A_v} \tag{A.14d}$$

$$\frac{\widetilde{K}}{\gamma} + \widetilde{Q} = C_1(l - \widetilde{L}) - C_2\frac{A_e}{A_v} \qquad (A.14e)$$

$$\widetilde{K} = D_1(l - \widetilde{L}) - D_2\frac{A_e}{A_v} \qquad (A.14f)$$

$$\widetilde{H} + \widetilde{I} = -m - E_1\frac{l}{m}\widetilde{L} \qquad (A.14g)$$

The ratio $A_e/A_v$ is the ratio of Fourier coefficients of the entropy and vorticity waves. It may be expressed as $A_r e^{i\phi_r}$ where $A_r$ and $\phi_r$ denote the amplitude ratio and phase difference between the entropy and vorticity waves.

Equations $A.14$ are solved first for $\widetilde{L}$. Equation $A.14g$ implies,

$$E_1\frac{l}{m}\widetilde{L} = -m - \widetilde{H} - \widetilde{I} \qquad (A.15)$$

The variables $\widetilde{H}$ and $\widetilde{I}$ need to be expressed in terms of $\widetilde{L}$. Now,

$$\widetilde{K} = D_1(l - \widetilde{L}) - D_2\frac{A_e}{A_v} \qquad (A.16)$$

Substituting for $\widetilde{K}$ in Equation $A.14b$, we get,

$$\widetilde{H} = \beta\left(D_1 l - D_2\frac{A_e}{A_v}\right) - \beta D_1\widetilde{L} \qquad (A.17)$$

The variable $\widetilde{I}$ is expressed in terms of $\widetilde{L}$ as follows. Equation $A.14d$ yields,

$$\widetilde{G} = \widetilde{L}(1 - B_1) - \widetilde{F} + B_1 l - B_2\frac{A_e}{A_v} \qquad (A.18)$$

But,

$$\widetilde{F} = \alpha\widetilde{K} = \alpha D_1(l - \widetilde{L}) - \alpha D_2\frac{A_e}{A_v} \qquad (A.19)$$

This implies,

$$\widetilde{G} = \widetilde{L}(1 - B_1 + \alpha D_1) - \alpha(D_1 l - D_2\frac{A_e}{A_v}) + B_1 l - B_2\frac{A_e}{A_v} \qquad (A.20)$$

The coefficient $\widetilde{I}$ may now be expressed in terms of $\widetilde{L}$ as,

$$\widetilde{I} = -\frac{mr}{l}(1 - B_1 + \alpha D_1)\widetilde{L} - \frac{mr}{l}\left[-\alpha(D_1 l - D_2\frac{A_e}{A_v}) + B_1 l - B_2\frac{A_e}{A_v}\right] \qquad (A.21)$$

Substituting for $\widetilde{H}$ and $\widetilde{I}$ into equation $A.15$ and rearranging yields the following expression for $\widetilde{L}$:

$$\widetilde{L} = \frac{-m - \beta(D_1 l - D_2\frac{A_e}{A_v}) + \frac{mr}{l}[-\alpha(D_1 l - D_2\frac{A_e}{A_v}) + B_1 l - B_2\frac{A_e}{A_v}]}{E_1\frac{l}{m} - \beta D_1 - \frac{mr}{l}(1 - B_1 + \alpha D_1)} \qquad (A.22)$$

Once $\widetilde{L}$ is known, the other coefficients are easily obtained using equations $A.14$. This completes the solution.

# Appendix B

# The Interaction of an Isotropic Field of Acoustic Waves with a Shock Wave

## B.1 Introduction

This appendix uses linear analysis to study the interaction of a shock wave with an isotropic field of acoustic waves. The analysis aims at characterizing the effect of compressibility in the interaction of a compressible turbulent flow with a shock wave. Within the linear framework, a field of acoustic waves would correspond to the dilatational component of a compressible turbulent flow. As discussed in Chapter 3, there is evidence to suggest that compressible effects are negligible in non-hypersonic turbulent boundary layers. However shear flows such as the mixing layer and supersonic jet are known to be significantly affected by compressibility.

Increased level of compressibility in these flows (parametrized by the ratio of kinetic energy in solenoidal and dilatational components) suggests that effects due to the dilatational component would be important in their interaction with a shock wave. Past analytical work related to shock/turbulence interaction (Chapter 1) has considered the interaction of a shock wave with a plane acoustic wave. To the best of our knowledge, the interaction of a field of acoustic waves with a shock wave has not been analyzed before. Our analysis is based upon Moore's (1954) study of the interaction of a shock with a plane acoustic wave. Moore's analysis is extended to study the evolution of an isotropic field of acoustic waves across a shock. The results are then applied to predict the response of a compressible isotropic turbulent flow to a shock.

This appendix is organized as follows. Section B.2 formulates the problem of a plane acoustic wave interacting with a shock. The results are evaluated by comparison to DNS. The analysis is then extended to examine the evolution of an isotropic field of acoustic waves across a shock. The statistics of turbulent kinetic energy and thermodynamic fluctuations behind the shock wave are described in Section B.3. A brief discussion including description of shock wave/compressible turbulence interaction is presented in Section B.4. Summary of the study in Section

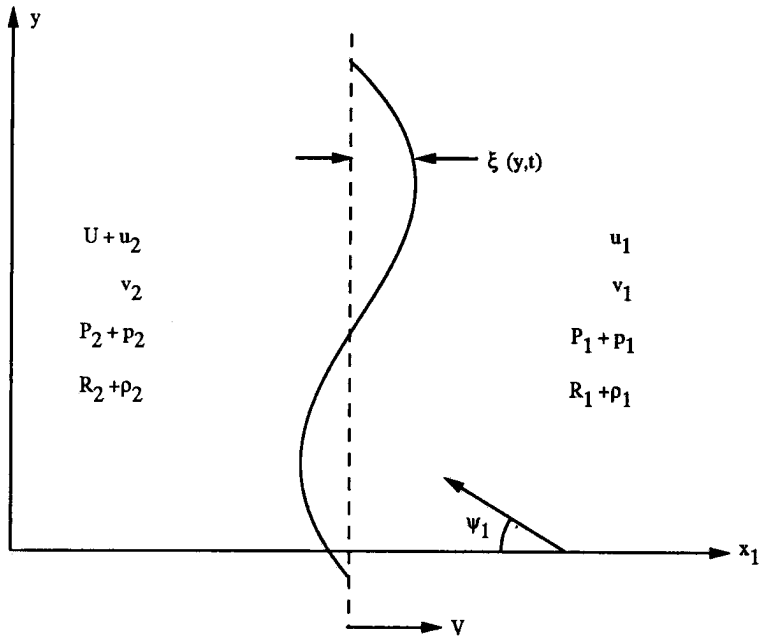


FIGURE B.1: Schematic of the interaction of a shock wave with an acoustic wave that is incident from upstream.

B.5 is followed by the concluding section (B.6) where some of the details of Moore's analysis are outlined.

Parallel may be drawn between Chapter 3 and the following analysis. The notation used below might differ from that in Chapter 3; we have retained Moore's notation and method of analysis for consistency. The work described below is essentially a reproduction of the published article by Mahesh, Lee, Lele and Moin (1995).

## B.2 Formulation of the problem

### B.2.1 The interaction of an acoustic wave with a shock wave

Figure B.1 shows a schematic of the problem. A normal shock propagates at speed $V$ into fluid that is at rest in the mean. The mean velocity behind the shock is denoted by $U$. The subscripts 1 and 2 denote the fluid in front and behind the shock respectively. The fluid at rest is assumed to be perturbed by the weak field of a plane acoustic wave that is incident at angle $\psi_1$ to the shock. The flow field

associated with the acoustic wave is given by:

$$\frac{u_1}{V} = A_1 f\left(\frac{mx_1 - ly + a_1 t}{\lambda_1}\right) \tag{B.1a}$$

$$\frac{v_1}{V} = A_2 f\left(\frac{mx_1 - ly + a_1 t}{\lambda_1}\right) \tag{B.1b}$$

$$\frac{p_1}{P_1} = A_3 f\left(\frac{mx_1 - ly + a_1 t}{\lambda_1}\right) \tag{B.1c}$$

$$\frac{\rho_1}{R_1} = A_4 f\left(\frac{mx_1 - ly + a_1 t}{\lambda_1}\right). \tag{B.1d}$$

Here, $P_1$, $R_1$ and $a_1$ are the mean pressure, density and sound speed in the fluid ahead of the shock while $u_1$ and $v_1$ are the disturbance velocities in the $x_1$ and $y$ directions respectively. The pressure and density fluctuations associated with the incident acoustic wave are denoted by $p_1$ and $\rho_1$. The variables $l$ and $m$ are related to the direction of propagation by $l = \sin\psi_1$ and $m = \cos\psi_1$ and $\lambda_1$ represents the lengthscale of the disturbance. Note that the coordinate system is fixed in the fluid that is at rest, yielding $x_1 = Vt$ at the mean position of the shock wave. The amplitudes of velocity, pressure and density are related through the governing equations for an acoustic wave; *i.e.*,

$$lA_1 = -mA_2; \qquad A_3 = \gamma A_4; \qquad A_1 = -\frac{m}{\gamma M} A_3 \tag{B.2}$$

$M = V/a_1$ is the mean Mach number of the shock wave and $\gamma$ is the ratio of specific heats. Incidence of the acoustic wave causes the shock wave to deform with a profile that matches the profile of the incident wave. The linearized Rankine-Hugoniot equations are used to describe the jump of the disturbance across the disturbed shock. This yields boundary conditions for the flow behind the shock which is described by the Euler equations linearized about the uniform mean flow. The linearized Euler equations are solved in consonance with the boundary conditions to calculate the displacement of the shock wave and the flow field downstream of the shock.

The flow behind the shock wave has two distinct regimes depending upon the angle of incidence of the acoustic wave. The two regimes differ in the nature of the pressure field (and hence, its associated velocity, temperature and density field) behind the shock wave. Over a range of incident angles $0 \leq \psi_1 < \psi_{cl}$ or $\psi_{cu} <$

$\psi_1 \leq \pi$, the pressure field behind the shock is a freely propagating plane acoustic wave. However, if $\psi_{cl} < \psi_1 < \psi_{cu}$, the pressure field behind the shock corresponds to an evanescent wave and decays exponentially. Over both these regimes, the vorticity and entropy waves propagate without decaying. $\psi_{cl}$ and $\psi_{cu}$ are roots of the following equation (Moore, 1954):

$$\left(\frac{a_2}{V}\right)^2 - \left(1 - \frac{U}{V}\right)^2 = \left(\cot\psi_c + \frac{a_1}{V}\csc\psi_c\right)^2. \qquad (B.3)$$

Note that $\psi_{cl}$ and $\psi_{cu}$ depend only on the mean Mach number. The displacement of the shock front has a certain speed of propagation along the shock front due to the unsteady nature of the incident field. Analogous to the classical flexural wall problem in acoustics, (Pierce, 1981) the nature of the downstream pressure field is determined by how the speed of the disturbance compares with the mean speed of sound and velocity downstream of the shock. Moore (1954) illustrates the two regimes geometrically. Ribner (1953) provides an equivalent explanation by noting that the unsteady interaction of an oblique wave with a normal shock can be transformed into the steady interaction of an oblique wave with an oblique shock. In the transformed coordinates, depending upon the incident angle of the wave, the flow behind the oblique shock is either supersonic or subsonic (yielding either a wave equation or Poisson equation for the pressure), which corresponds to the two regimes mentioned above. Alternatively, arguments similar to those in Chapter 3 could be used to demonstrate the existence of two regimes.

The method for solution of the downstream flow field is given by Moore. In the interests of clarity, we reproduce his results at the end of the Appendix in Section B.6. Apart from the existence of two different regimes, note that the velocity field is a linear superposition of acoustic and vortical components. Similarly, the density and temperature fields are superpositions of acoustic and entropic components. The pressure field is associated solely with the acoustic component.

## B.2.2 Comparison of linear analysis to numerical solution

We compare results of the linear analysis to numerical computations of the interaction of a normal shock wave with a plane acoustic wave that is incident from upstream. The computation solves the two-dimensional compressible Navier-Stokes equations in a frame of reference that moves at the mean speed of the shock wave. The sixth order Pade scheme (Lele, 1992b) is used to compute spatial derivatives

and the third order Runge Kutta (Wray, 1986) is used to integrate in time. No shock-capturing or shock-fitting is used to treat the shock wave; its structure is resolved by a non-uniform mesh.

This comparison is intended to complement that by Zang *et al* (1984) who compared the predictions of McKenzie and Westphal's (1968) linear analysis to their numerical solution of the two-dimensional Euler equations using a shock-fitting scheme. Zang *et al* examined the effect of incident angle, shock-strength and the amplitude of the incident disturbance in the interaction of acoustic and vorticity waves with a shock wave. Results were presented only in the freely propagating regime. The dependence on incident angle was examined in the interaction of disturbances of amplitude 0.1% and 10% with a shock wave of Mach number 8. Good agreement was seen away from the critical angle; divergence from the linear analysis prediction was seen within about 20° of the critical angle. The linear analysis predictions were quite robust in terms of dependence on shock strength and disturbance amplitude. For an incident angle of 30°, the linear predictions were valid for disturbance amplitudes as high as 25% for acoustic waves and 100% for vorticity waves and shock waves whose Mach number was close to unity.

We present results of the interaction of a plane acoustic wave ($p_1/P_1 = 2.5\%$) interacting with a shock wave of Mach number 1.5. The Mach number of 1.5 was chosen to be representative of experiments on the shock/turbulence interaction. In the context of Zang *et al*'s results, we only present the dependence on the incident angle. Results are presented in both freely propagating and decaying regimes. Figure B.2 compares the computed values of *rms* dilatation and vorticity with predictions of the linear analysis. Note that $\psi_{cl}$ and $\psi_{cu}$ have values of 97.16° and 154.45° respectively for $M = 1.5$. Excellent agreement is seen except for a region within 25 degrees of the critical angles. As noted by Zang *et al* (for the shock wave of Mach number 8), a decaying pressure field is observed downstream of the shock wave before the critical angle is reached.

A possible reason for deviation of the computed result from the linear analysis around the critical angle is as follows. Within linear analysis, the unsteady interaction of a plane disturbance with a normal shock wave may be transformed into the *steady* interaction of the disturbance with an oblique shock wave. This transformation is an integral part of Ribner's (1953) and Chang's (1957) analysis of the interaction of a shock with a vorticity and entropy wave respectively. While Moore

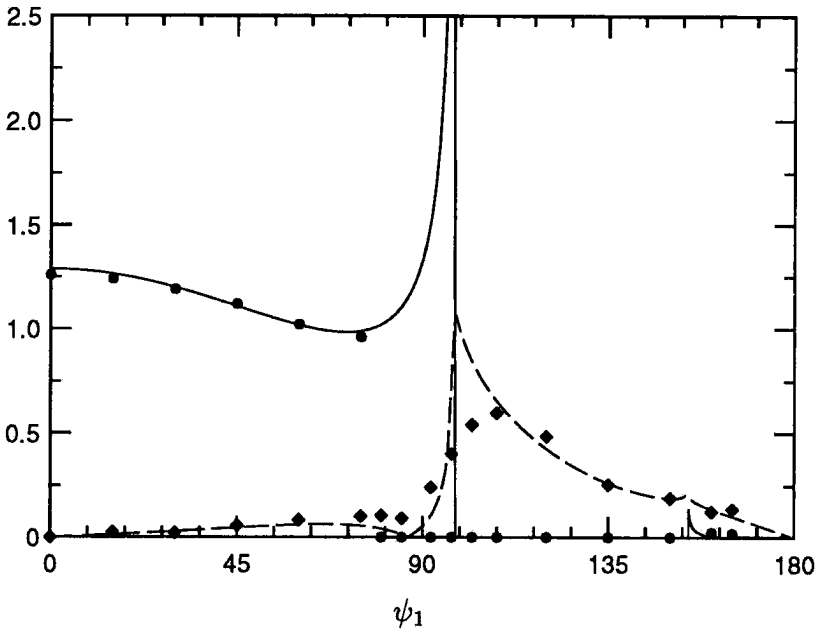


FIGURE B.2: Comparison of the predictions of the linear analysis to computed results. The lines are values obtained from analysis while the symbols represent computed values. All quantities are normalized by $p_1/P_1$. —— $(\theta_2/\theta_1)$, ---- $(\omega_2/\theta_1)$. $\theta_2$ and $\omega_2$ denote the *rms* dilatation and vorticity behind the shock wave respectively.

does not employ this transformation, it exists and involves defining coordinates $x'$ and $y'$ such that

$$x' = x - Vt; \qquad y' = y - \frac{a_1 + mV}{l}t$$

*i.e.*, the flow is observed from a frame of reference that moves at the mean shock speed in the $x$ direction and at speed $(a_1 + mV)/l$ in the $y$ direction. In these transformed coordinates, the governing equations behind the shock wave are the steady Euler equations that are linearized about uniform mean flow at an equivalent Mach number $M_e$ that is given by the relation:

$$M_e^2 = \frac{l^2(V-U)^2 + (a_1 + mV)^2}{a_2^2 l^2}$$

This equivalent Mach number depends upon the Mach number of the normal shock wave and the incident angle of the disturbance and equals unity at the critical angle. As a result, incident angles close to the critical angle correspond to steady transonic flow downstream of the shock wave in the transformed coordinates. It is well known that the linear approximation is inconsistent in the transonic regime. We believe

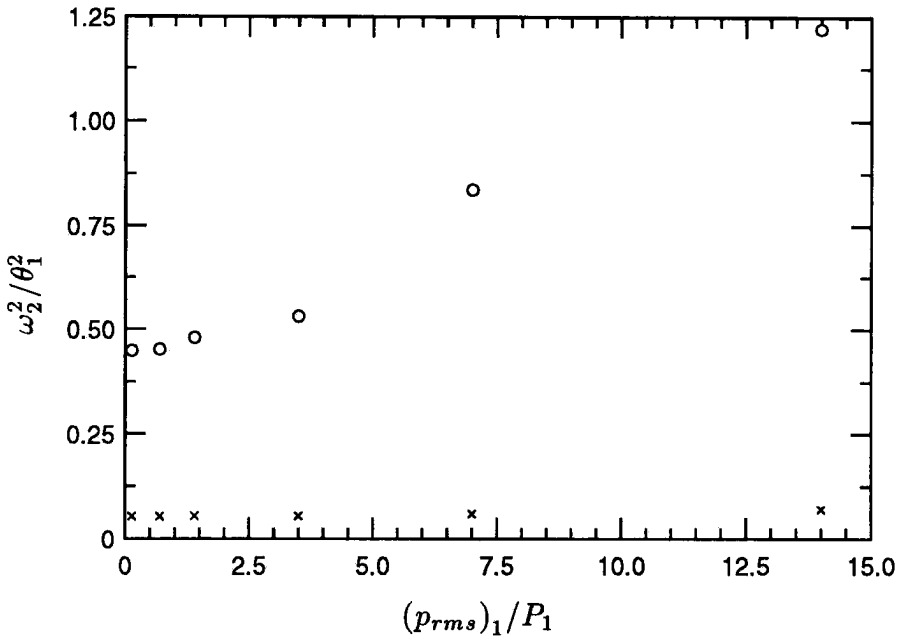


FIGURE B.3: Computed values of the vorticity behind the shock wave as a function of the amplitude of the incident disturbance. The mean Mach number is 1.5. o ($\psi_1 = 100°$), × ($\psi_1 = 60°$).

that use of the transonic small disturbance equations are necessary to accurately represent the interaction around the critical angle.

Further indication of this is provided in Figure B.3, where the dependence of the interaction upon the amplitude of the incident disturbance is examined. The interaction away from the critical angle ($\psi_1 = 60°$) is compared to that close to the critical angle ($\psi_1 = 100°$). The *rms* intensity ($p_{rms}/P$) of the incident pressure fluctuation is varied from 0.14% to 14% in both cases. The vorticity (normalized by the incident dilatation) behind the shock wave is plotted against the amplitude of the incident disturbance in Figure B.3. The variation with the incident amplitude is negligible away from the critical angle. However, significant dependence upon the incident amplitude is seen close to the critical angle. This non-linear behavior around the critical angle is in accordance with the expectation that the transonic small disturbance equations are needed to describe the interaction in that range.

## B.2.3 The interaction of a field of acoustic waves with a shock wave

Moore's analysis is now extended to describe the interaction of an isotropic

field of acoustic waves with the shock wave. The problem is convenient to analyze in cylindrical coordinates. Figure B.4 shows a schematic of the problem in a frame of reference that moves at the speed of the undisturbed shock. The $y-z$ plane corresponds to the shock wave, while the acoustic wave lies in the $x_1 - r$ plane that makes an angle $\phi$ with the $y$ axis. Irrotationality precludes any component of velocity outside this plane. In the $x_1 - r$ plane, the acoustic wave makes an angle $\psi_1$ with the $x_1$ axis. The $x_1 - r$ plane is equivalent to the $x_1 - y$ plane used in Moore's analysis. It is seen from Figure B.4 that

$$u_r = \frac{v}{\cos\phi} = \frac{w}{\sin\phi}; \qquad u_\phi = 0. \tag{B.4}$$

Moore's results are used to obtain the following relations describing the amplitude of the fluctuating field behind the shock for a plane incident wave. Note that we transform to a coordinate system that moves at the mean speed of the shock *i.e.*, our streamwise coordinate becomes $\eta_2 = -[x_2 - (V-U)t]$.

For $0 \leq \psi_1 < \psi_{cl}$ or $\psi_{cu} < \psi_1 \leq \pi$,

$$\frac{|\widehat{p}_2|^2}{{P_2}^2} = \widetilde{K}^2 \, \frac{|\widehat{p}_1|^2}{{P_1}^2} \tag{B.5a}$$

$$\frac{|\widehat{u}_2|^2}{V^2} = \left[\widetilde{F}^2 + \widetilde{G}^2 + 2\widetilde{F}\widetilde{G}\cos\left(\frac{1}{\lambda_2}\frac{a_2}{V}\frac{\eta_2}{1-r}\right)\right] \frac{|\widehat{p}_1|^2}{{P_1}^2} \tag{B.5b}$$

$$\frac{|\widehat{u}_{r2}|^2}{V^2} = \left[\widetilde{H}^2 + \widetilde{I}^2 + 2\widetilde{H}\widetilde{I}\cos\left(\frac{1}{\lambda_2}\frac{a_2}{V}\frac{\eta_2}{1-r}\right)\right] \frac{|\widehat{p}_1|^2}{{P_1}^2} \tag{B.5c}$$

$$\frac{|\widehat{\rho}_2|^2}{{R_2}^2} = \left[\left(\frac{\widetilde{K}}{\gamma}\right)^2 + \widetilde{Q}^2 + 2\frac{\widetilde{K}\widetilde{Q}}{\gamma}\cos\left(\frac{1}{\lambda_2}\frac{a_2}{V}\frac{\eta_2}{1-r}\right)\right] \frac{|\widehat{p}_1|^2}{{P_1}^2} \tag{B.5d}$$

The constants $\widetilde{K}, \widetilde{F}$ and $\widetilde{H}$ are associated with the acoustic component of the flow field. Similarly, $\widetilde{G}$ and $\widetilde{I}$ are associated with the vortical component and $\widetilde{Q}$ corresponds to the entropic component.

If $\psi_{cl} < \psi_1 < \psi_{cu}$, the amplitudes behind the shock are given by:

$$\frac{|\widehat{p}_2|^2}{{P_2}^2} = e^{-2d\eta_2/\lambda_1} \left[\widetilde{K}_{(1)}^2 + \widetilde{K}_{(2)}^2\right] \frac{|\widehat{p}_1|^2}{{P_1}^2} \tag{B.6a}$$

$$\frac{|\widehat{u}_2|^2}{V^2} = \left[T_1 + T_2 + T_3\right] \frac{|\widehat{p}_1|^2}{{P_1}^2} \tag{B.6b}$$

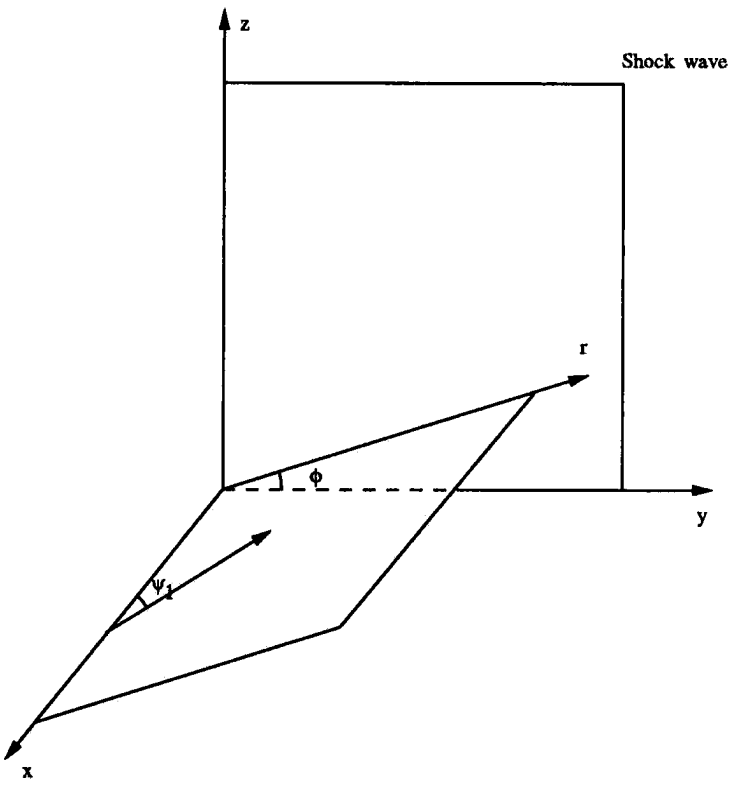


FIGURE B.4: Coordinate system used in analysis of the interaction of a shock wave with an isotropic field of acoustic waves that are incident from upstream.

where,

$$T_1 = \widetilde{G}_{(1)}^2 + \widetilde{G}_{(2)}^2; \qquad T_2 = e^{-2d\eta_2/\lambda_1}\left[\widetilde{F}_{(1)}^2 + \widetilde{F}_{(2)}^2\right]$$

$$T_3 = 2e^{-d\eta_2/\lambda_1}\left[\left(\widetilde{F}_{(1)}\widetilde{G}_{(1)} + \widetilde{F}_{(2)}\widetilde{G}_{(2)}\right)\cos\delta - \left(\widetilde{F}_{(2)}\widetilde{G}_{(1)} - \widetilde{F}_{(1)}\widetilde{G}_{(2)}\right)\sin\delta\right];$$

$$\delta = \frac{c\eta_2}{\lambda_1}\frac{1}{1-r}.$$

The amplitude of $u_{r2}/V$ may be obtained from the expression for $u_2/V$ by replacing $\widetilde{F}_{(1)}, \widetilde{G}_{(1)}, \widetilde{F}_{(2)}$ and $\widetilde{G}_{(2)}$ by $\widetilde{H}_{(1)}, \widetilde{I}_{(1)}, \widetilde{H}_{(2)}$ and $\widetilde{I}_{(2)}$ respectively. The amplitude of $\rho_2/R_2$ may be obtained from the expression for $u_2/V$ by replacing $\widetilde{F}_{(1)}, \widetilde{G}_{(1)}, \widetilde{F}_{(2)}$ and $\widetilde{G}_{(2)}$ by $\widetilde{K}_{(1)}/\gamma, \widetilde{Q}_{(1)}, \widetilde{K}_{(2)}/\gamma$ and $\widetilde{Q}_{(2)}$ respectively.

Analogous to the propagating regime, the constants $\widetilde{K}_{(\alpha)}, \widetilde{F}_{(\alpha)}$ and $\widetilde{H}_{(\alpha)}$ are associated with the acoustic component of the flow field. $\widetilde{G}_{(\alpha)}$ and $\widetilde{I}_{(\alpha)}$ are associated with the vortical component and $\widetilde{Q}_{(\alpha)}$ corresponds to the entropic component.

Note that the solution downstream of the shock wave requires the spectrum of pressure fluctuations ahead of the shock. We assume the incident acoustic field to be isotropic. This combined with the condition of irrotationality requires the upstream spectrum of the velocity fluctuations to be of the form:

$$E_{ij}(\mathbf{k}) = \frac{E(k)}{8\pi k^2}\frac{k_i k_j}{k^2}$$

where $E_{ij}(\mathbf{k})$ is the energy spectrum tensor and $E(k)$ is the three-dimensional energy spectrum. Using the acoustic relation, $A_3 = \gamma M A_1/\cos\psi_1$, and the above expression for the energy spectrum tensor, we get,

$$\frac{|\widehat{p}_1|^2(\mathbf{k})}{{P_1}^2} = \left(\frac{\gamma M}{V}\right)^2 \frac{E(k)}{4\pi k^2} \tag{B.7}$$

Substituting for $|\widehat{p}_1|^2(\mathbf{k})/{P_1}^2$ and integrating over wavenumber space at every streamwise location ($\eta_2$), we get the streamwise evolution of statistics downstream of the shock wave. This integration is done in polar coordinates in the wave number space:

$$k_1 = k\cos\psi_1, \quad k_2 = k\sin\psi_1\cos\phi, \quad k_3 = k\sin\psi_1\sin\phi, \quad \mathrm{d}^3\mathbf{k} = k^2\sin\psi_1\,\mathrm{d}\psi_1\,\mathrm{d}\phi\,\mathrm{d}k$$

where, $k = |\mathbf{k}|$ varies from 0 to $\infty$, $\psi_1$ from 0 to $\pi$ and $\phi$ varies from 0 to $2\pi$. Since the coefficients in the above equations are independent of $\phi$, the integration over $\phi$ can be done analytically for isotropic initial spectra. For example,

$$\frac{v_2^2(\eta_2)}{V^2} = \int \cos^2\phi\,\frac{|\widehat{u}_{r2}(\eta_2,k,\psi_1)|^2}{V^2}\,\mathrm{d}^3\mathbf{k} = \pi\iint_{k\psi_1}\frac{|\widehat{u}_{r2}|^2}{V^2}\,k^2\sin\psi_1\mathrm{d}\psi_1\,\mathrm{d}k$$

The integration over $k$ and $\psi_1$ is performed numerically at every streamwise location. Note that the results depend upon the three dimensional energy spectrum, $E(k)$. We assume the following form for $E(k)$:

$$\frac{E(k)}{V^2} \sim \left(\frac{k}{k_0}\right)^4 e^{-2(\frac{k}{k_0})^2}$$

This form of the spectrum was used by Lee *et al.* (1993,1994*b*) in their analysis of the interaction of isotropic vortical turbulence with a shock wave. There is no data that suggests the chosen spectral dependency for an isotropic field of sound waves.

However, only the inhomogeneous part of the flow-field behind the shock wave is dependent upon the energy spectrum of the incident waves; the far-field ($\eta_2 \rightarrow \infty$) values are *independent* of the shape of the spectrum. We choose the same spectrum as Lee *et al* to allow direct comparison to their results of the inhomogeneous near-field behind the shock wave. Since the inhomogeneous component of the flow-field exponentially decays behind the shock wave, it is the far-field that is of importance and will be examined in detail.

## B.3 Results

### B.3.1 Spatial variation of kinetic energy

The evolution of the kinetic energy behind the shock wave is shown in Figure B.5, where $q^2 = R_{ii}$ is plotted as a function of downstream distance. The inhomogeneous nature of the velocity field is apparent immediately downstream of the shock. Note that the curves for $M = 1.2$ and $M = 2$ are qualitatively different. While $q^2$ decays monotonically for $M = 1.2$, it exhibits rapid nonmonotonic variation for $M = 2$. A similar rapid variation of kinetic energy was observed in the interaction of vortical fluctuations with a shock wave by Lee *et al* (1993). However, in the shock wave/vortical turbulence interaction problem, this variation was observed at all Mach numbers considered.

Equations (B.5) and (B.6) are used to show that this variation of kinetic energy behind the shock wave is a consequence of the acoustic waves that are incident at $\psi_{cl} < \psi_1 < \psi_{cu}$. Recall that the downstream pressure field and hence the velocity field set up by these waves decayed exponentially. Equation ($B.6b$) shows that the downstream kinetic energy over this regime has three components: a homogeneous component associated with the vorticity waves ($T_1$), a monotonically decreasing component due to acoustic waves ($T_2$) and a nonmonotonic component due to the correlation between the vorticity and acoustic waves ($T_3$). Upon integration over all the incident waves, these components combine to produce the rapid evolution immediately downstream of the shock.

As seen from equations ($B.5a$) and ($B.5b$), the kinetic energy associated with waves incident outside this range has homogeneous vortical and acoustic components and a nonmonotonic inhomogeneous component due to the correlation between them. When integrated over all incident waves, this correlation term is however, much smaller than the other components. This is illustrated in Figure B.6 where the

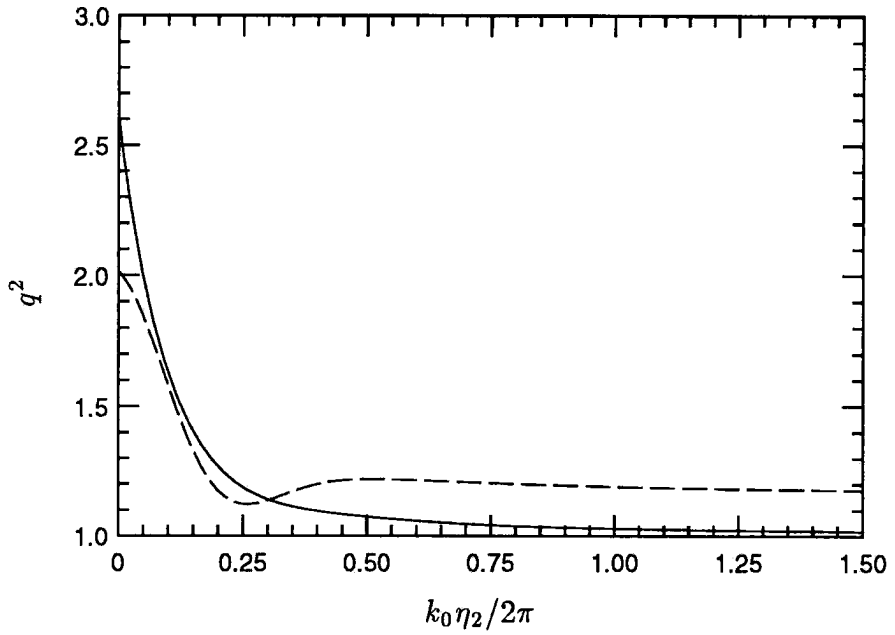


FIGURE B.5: Evolution of $q^2$ behind the shock wave as predicted by linear analysis. $q^2$ is normalized with its upstream value. ——— $(M = 1.2)$, - - - - $(M = 2.0)$.

kinetic energy is decomposed into four components (vortical, acoustic, correlation term for $\psi_{cl} < \psi_1 < \psi_{cu}$ and correlation term outside this regime) for $M = 2.0$. The correlation term associated with waves incident at $\psi_{cl} < \psi_1 < \psi_{cu}$ is seen to produce the rapid nonmonotonic evolution downstream.

A similar decomposition for the $M = 1.2$ shock showed the correlation term to be insignificant resulting in the monotonic evolution of Figure B.5. In our linear analysis calculations, the nonmonotonic downstream variation was observed for shocks whose Mach number exceeded 1.5. In studying the interaction of vortical disturbances with the shock wave, Lee *et al* (1993) erroneously concluded that linear analysis could not reproduce this trend which they had found in the DNS. This error was subsequently corrected and explained by them (Lee *et al*, 1994*a*,1994*b*).

The equation governing the evolution of kinetic energy downstream of the shock wave provides further insight into the spatial evolution of kinetic energy. The Euler equations linearized about uniform mean flow may be rearranged to show that the quantity,

$$I_{\text{total}} = \frac{\gamma M}{2}\left[\frac{q^2}{a^2} + \frac{p^2}{\gamma^2 P^2}\right] + \frac{\overline{pu}}{Pa} \qquad (B.8)$$

is conserved along a mean streamline. $I_{\text{total}}$ changes across the shock wave and

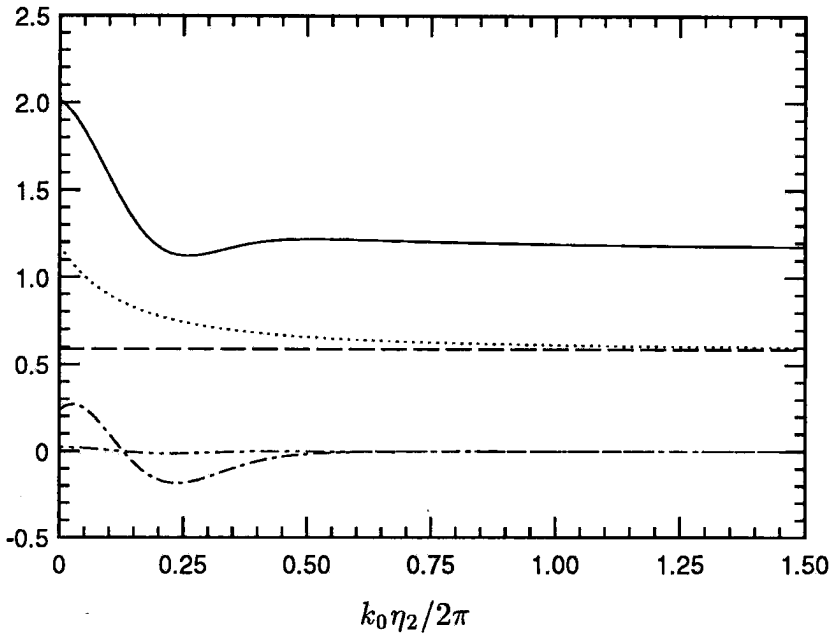


FIGURE B.6: Decomposition of $q^2$ behind the shock wave under linear analysis. The Mach number is 2 and all components are normalized with the upstream value of $q^2$. ——— (Total), ---- (Vortical), ····· (Acoustic), —·— (Correlation for $\psi_{cl} < \psi_1 < \psi_{cu}$), —··— (Correlation for $0 \leq \psi_1 < \psi_{cl}, \psi_{cu} < \psi_1 \leq \pi$ ).

remains unchanged downstream. The $\overline{pu}$ correlation determines the partitioning of $I_{\text{total}}$ between potential and kinetic energy. The spatial uniformity of $I_{\text{total}}$ and the exponential decay of $p^2$ behind the shock wave show that the rapid evolution of $q^2$ behind the shock wave is a result of the rapid change in the partitioning of $I_{\text{total}}$ through the correlation between pressure and the shock-normal component of fluctuating velocity. Decomposition of the $\overline{pu}$ correlation reveals that the rapid evolution of kinetic energy behind the shock wave is produced by the waves that are incident at $\psi_{cl} < \psi_1 < \psi_{cu}$. The far-field values of kinetic energy and pressure are however, determined by the correlation between pressure fluctuations and the *acoustic* component of the velocity field in the *propagating* regime.

## B.3.2 Far-field kinetic energy

As seen from Figure B.5, after a distance that is comparable to the lengthscale (taken as $2\pi/k_0$) of the incident acoustic waves, the kinetic energy asymptotes to its far-field value. The far-field values are independent of the upstream energy spectrum since the inhomogeneous terms drop out in the far-field. As a result, the integration

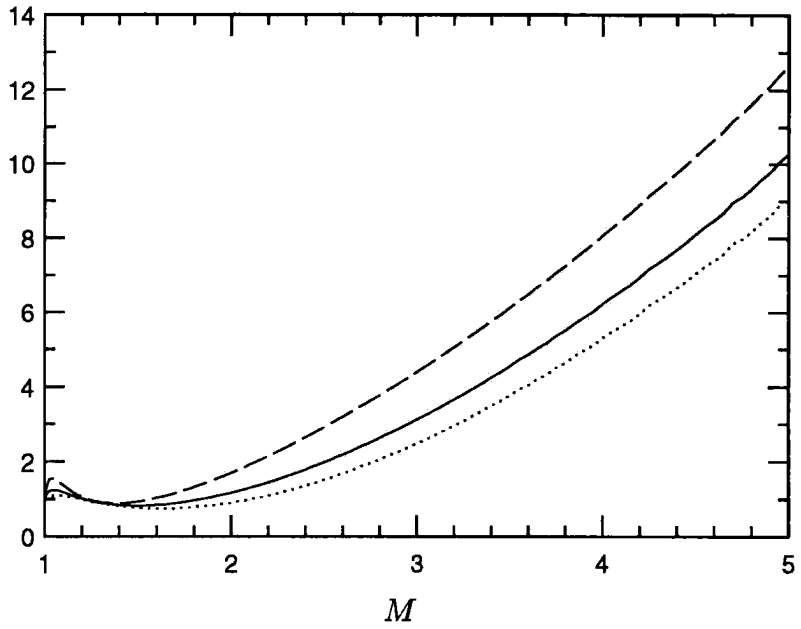


FIGURE B.7: Far-field kinetic energy as a function of Mach number. All components are normalized with their upstream value. ---- $(\overline{u^2})$, ····· $(\overline{v^2} = \overline{w^2})$, —— $(q^2)$.

over $k$ can be performed independently of $\psi_1$ and $\phi$ to give $\int E(k)\, dk = q_0^2/2$. To gauge the effect of shock strength upon the interaction, we examine (Figure B.7) the far-field kinetic energy (normalized with the upstream kinetic energy) as a function of the Mach number of the shock wave. Note that the shock-normal component of kinetic energy is larger than the transverse components for all Mach numbers shown. An interesting feature of the evolution of kinetic energy is that kinetic energy *decreases* slightly across the shock wave over a range of Mach number from 1.25 to 1.80. The transverse components decrease across the shock wave over a wider range of the Mach number. This decrease in kinetic energy across the shock wave is peculiar to the acoustic wave/shock interaction problem. It is not observed in the interaction of vortical fluctuations with the shock wave where under linear analysis, kinetic energy increases across the shock wave for all shock strengths. Also, for $M > 3$, the amplification of kinetic energy is significantly higher than amplification levels seen in the interaction of vortical fluctuations with the shock wave.

The decrease in kinetic energy across the shock wave may be explained by decomposing (Figure B.8) the far-field energy into acoustic and vortical components and examining their dependence on Mach number. Both components are normalized with the upstream kinetic energy. This decomposition of kinetic en-

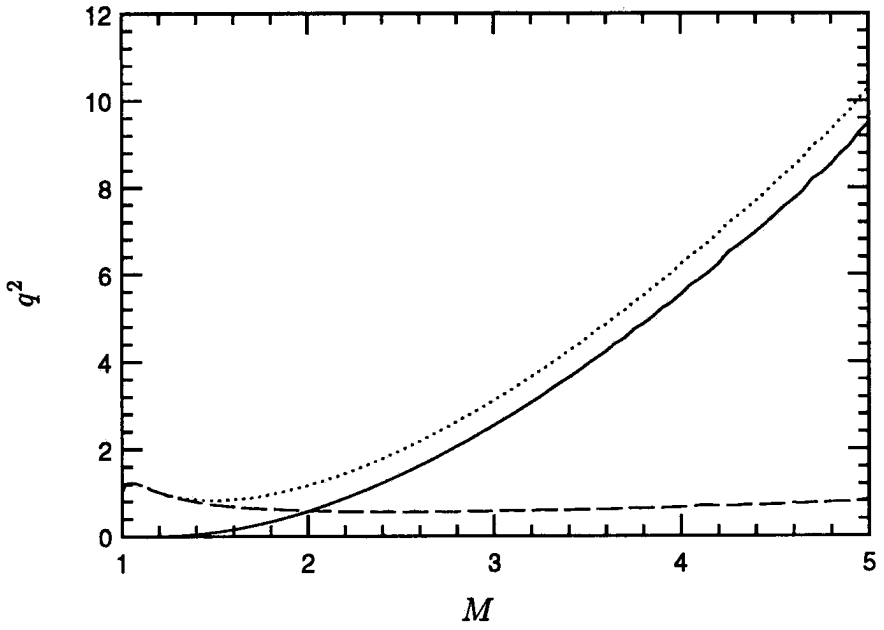


FIGURE B.8: The far-field kinetic energy decomposed into acoustic and vortical components. Both components are normalized with the upstream value of $q^2$. ····· (Total), ——— (Vortical), ---- (Acoustic).

ergy is possible since the correlation between vortical and acoustic components falls to zero in the far-field. Note that the kinetic energy associated with the vortical component increases monotonically with Mach number and *exceeds* the upstream kinetic energy beyond a Mach number of about 2.25. The kinetic energy associated with the acoustic component, however *decreases* across the shock wave for Mach numbers exceeding about 1.2. These two components compete in determining the overall evolution of kinetic energy. For lower Mach numbers, the acoustic component dominates since not enough vorticity is generated downstream, causing the overall kinetic energy to drop. At higher Mach number, the vortical component dominates due to increased generation of vortical fluctuations and the overall kinetic energy rises across the shock. The vortical component of energy exceeds the acoustic component for Mach number exceeding 2.

The decrease of the far-field acoustic kinetic energy with Mach number is explained as follows. As the Mach number increases, $\psi_{cu} - \psi_{cl}$ increases (see Figure B.4 of Moore) and hence a larger fraction of incident waves lie in the range $\psi_{cl} < \psi_1 < \psi_{cu}$. Recall that these waves make no contribution to the far-field acoustic kinetic energy. The only contribution to the far-field acoustic kinetic en-

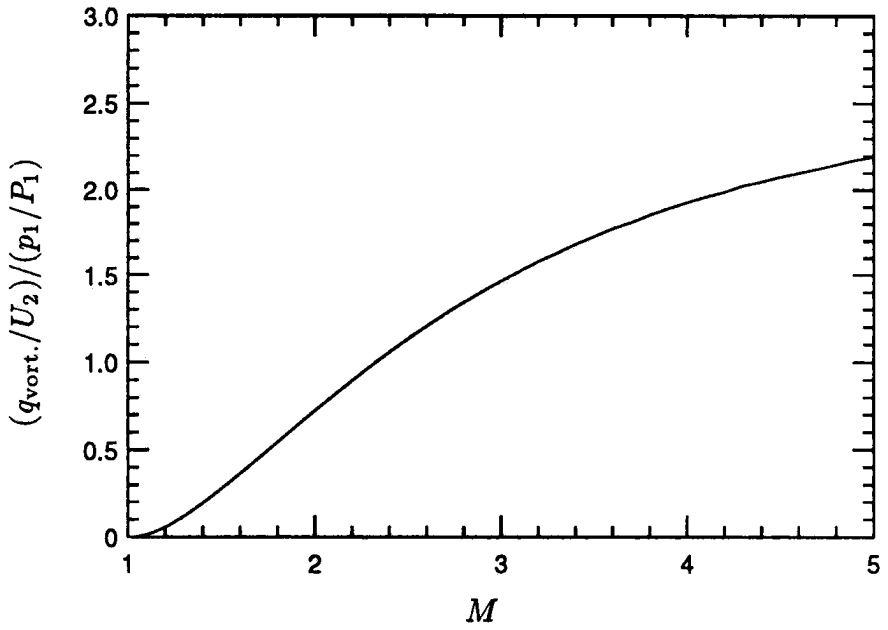


FIGURE B.9: The far-field 'turbulent' intensity compared to the intensity of incident pressure fluctuations. The curve asymptotes to 2.75 ($\gamma = 1.4$).

ergy comes from waves incident outside this range whose amplification increases upon increasing the Mach number. Upon integrating over all incident waves, the net result of these competing factors is to produce (as seen in Figure B.8) a slow decrease (for $M < 3.5$) in the the far-field acoustic kinetic energy. Note that the variation of $\psi_{cl}$ and $\psi_{cu}$ with Mach number is most rapid at lower Mach numbers; in the limit of infinite Mach number, $\psi_{cl}$ and $\psi_{cu}$ are symmetrical about 90° and (for $\gamma = 1.4$), have values of 67.8° and 112.2° respectively.

## B.3.3 The production of turbulence

Having observed the generation of vortical fluctuations - 'turbulence' behind the shock wave, we examine in Figure B.9, the intensity of the turbulence relative to the intensity of the incident pressure fluctuations. Note that $(q_{vort.}/U_2)/(p_1/P_1)$ is of the order 1 for most of the Mach numbers shown. ($U_2 = V - U$ is the mean velocity behind the shock wave if the shock were stationary in the mean) This suggests an interesting possibility in turbulent flows involving multiple shock waves (eg. unadapted supersonic jets). It is known that upon interaction with a shock wave, turbulence generates intense sound. For isotropic turbulence, the intensity of the sound generated $(p_2/P_2)$ scales with the intensity of the incident turbulence $(q_1/U_1)$. In turbulent flows involving multiple shock waves, it is reasonable to

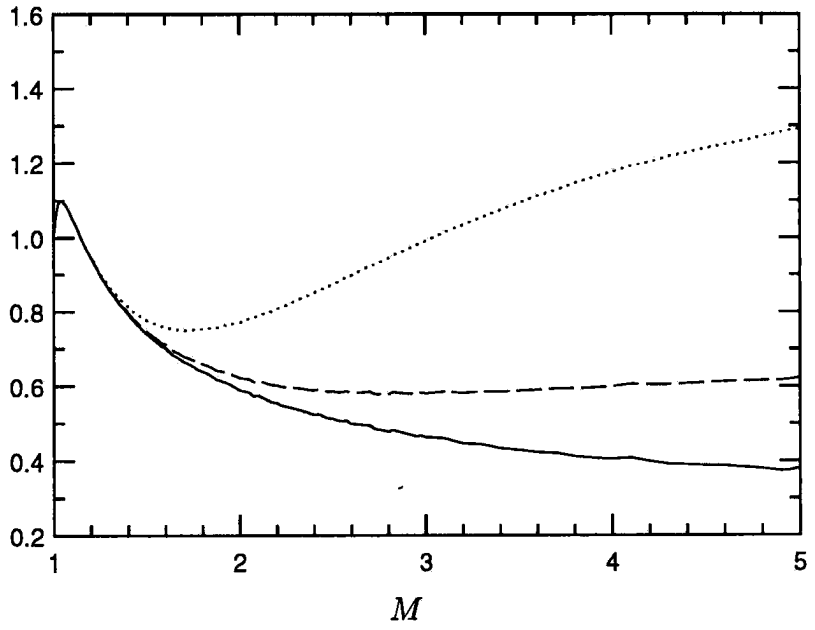


FIGURE B.10: The intensity of pressure, density and temperature fluctuations in the far-field compared to the intensity of incident pressure fluctuations. —— $(p_2/P_2)$, ---- $\gamma(\rho_2/R_2)$, ····· $\gamma/(\gamma-1)(\theta_2/T_2)$. $\theta_2$ and $T_2$ are the rms and mean temperature behind the shock wave respectively. The three curves are normalized with $p_1/P_1$ and asymptote to 0.29, 0.67 and 1.54 respectively ($\gamma = 1.4$).

expect the generated sound waves to interact with the subsequent shock waves. If this happens, Figure B.9 suggests that these acoustic waves can generate significant levels of turbulence through the interaction. We do not mean to suggest that our homogeneous analysis is directly applicable to flows involving shock cells, which are quite inhomogeneous. However, our results suggest that acoustic wave/ shock wave interaction may be a significant generator of turbulence in these flows.

## B.3.4 Thermodynamic fluctuations

Interaction with the shock wave is seen to significantly increase sound levels. Figure B.10 shows the intensity $(p_2/P_2)$ of the far-field pressure fluctuations normalized with the intensity of pressure fluctuations upstream of the shock. Note that the intensity drops, although pressure fluctuations actually amplify across the shock wave. The rise across the shock wave of the far-field sound pressure level (SPL) and the level of acoustic intensity (AIL) in decibels is shown in Figure B.11.

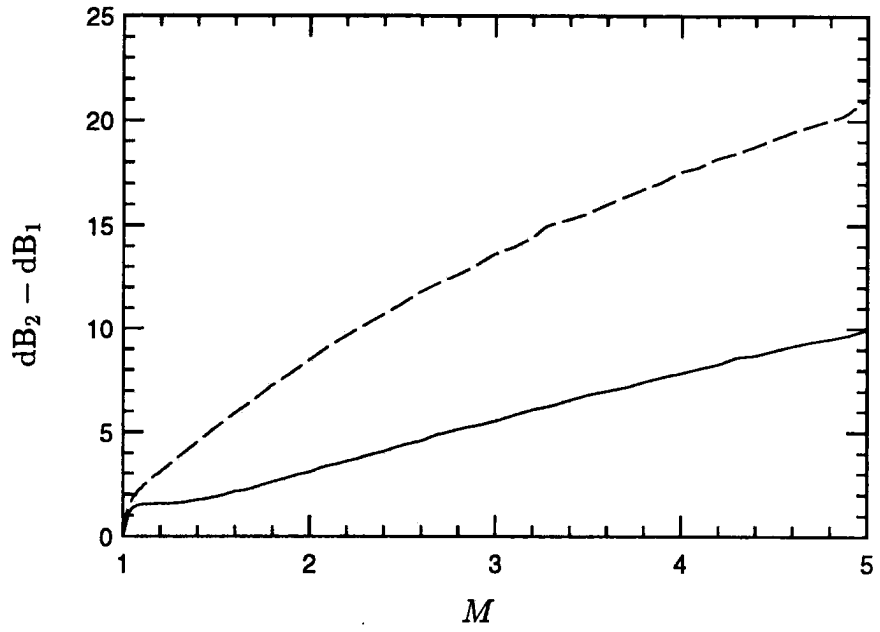


FIGURE B.11: The level of far-field sound behind the shock wave compared to the incident sound level. ---- Sound pressure level, ——— Level of acoustic intensity.

We define,

$$\text{SPL} = 10\log\left[\frac{p^2}{{p_r}^2}\right], \qquad \text{AIL} = 10\log\left[\frac{p^2/Ra}{{p_r}^2/R_r a_r}\right] \tag{B.9}$$

where the subscript $r$ denotes reference values. The rise in the level of sound across the shock wave is independent of the reference values. The increase in sound pressure level varies from 5 to 20 decibels while the rise in acoustic intensity varies from 2 to 10 decibels over the range of Mach numbers shown. Figure B.10 also shows the nature of the thermodynamic fluctuations in the far-field. The density and temperature fluctuations are normalized such that the three curves would collapse if the fluctuations were isentropic. We see that the isentropic relations hold until a Mach number of 1.5, beyond which the entropy fluctuations that are generated at the shock wave become significant relative to the acoustic fluctuations. The increasing importance of the entropy fluctuations in the far-field is due to two factors: increased production of entropy fluctuations at the shock wave and the decrease with Mach number of the far-field intensity of pressure fluctuations. Asymptotically, $(s_2/C_p)/(p_2/P_2)$ equals 1.47 ($\gamma = 1.4$) where $s_2$ is the *rms* entropy behind the shock wave and $C_p$ is the specific heat at constant pressure.

### B.3.5 Asymptotic behavior

Another feature that distinguishes the interaction of sound waves with a shock wave is the asymptotic behavior with respect to Mach number. Linear analysis shows that for incident acoustic waves, quantities such as the ratio of fluctuating kinetic energy, pressure and temperature fluctuations across the shock wave are not bounded but increase as $M^2$. This is easily seen from equations (B.5) and (B.6). The constants (*eg.* $\widetilde{K}$) in the equations have finite values in the limit of infinite Mach number and hence the intensities of velocity, density and pressure fluctuations are bounded for finite intensity of incident pressure fluctuations. However, for a given intensity of pressure fluctuations the incident kinetic energy decreases as $1/M^2$ causing the amplification of kinetic energy to vary as $M^2$ for strong shocks. Similarly, since the mean pressure and temperature ratio varies as $M^2$ for strong shocks, the ratio of pressure and temperature fluctuations are not bounded. Unboundedness of kinetic energy amplification is peculiar to the acoustic wave/shock interaction problem; it is not present when vortical fluctuations interact with the shock wave. We show in Figure B.12 the kinetic energy amplification normalized by $M^2$. Note that the amplification ratios asymptote to finite values when properly scaled with $M^2$.

## B.4. Discussion

### B.4.1 Evaluation of linear analysis

The inviscid linear analysis of Moore (1954) is extended to study the interaction of a three-dimensional isotropic field of acoustic waves with a normal shock wave. The objective of this study is to isolate the effect of acoustic waves on the evolution of a turbulent flow as it interacts with a shock wave. As the level of compressibility of a turbulent flow increases, the effects associated with the acoustic component will become important. Understanding the interaction of acoustic waves with a shock wave is therefore of fundamental importance. The interaction is likely to be especially important in unbounded turbulent flows.

Our use of linear analysis is prompted by its success in past investigations. In the interaction of a single unsteady disturbance with a shock wave, there appear to be four important factors that could cause deviation from linear behavior: proximity of the incident angle to the critical angle, the amplitude of the disturbance being non-negligible relative to the strength of the shock wave, the mean Mach number

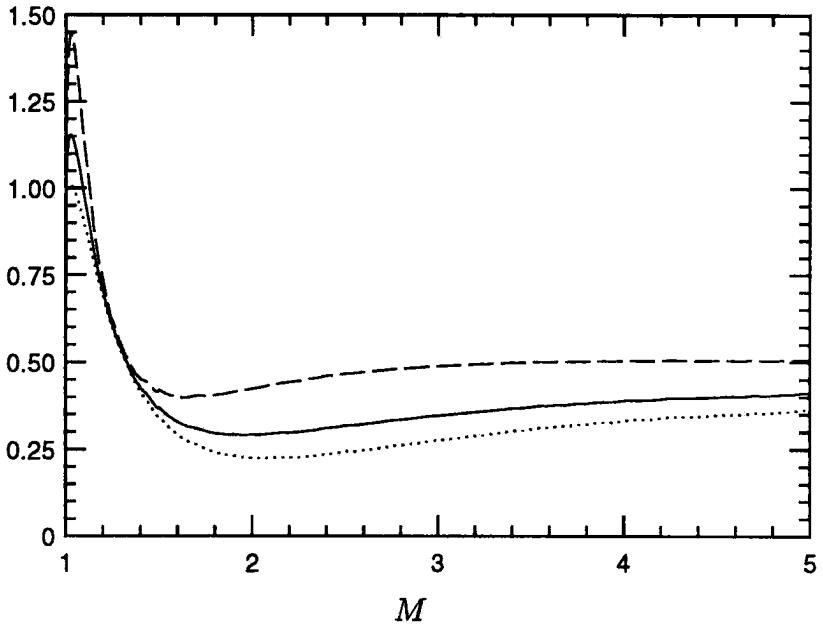


FIGURE B.12: Far-field kinetic energy as a function of Mach number. All components are normalized with the incident energy and $M^2$. ---- $(\overline{u^2}/M^2\ \overline{u_0^2})$, ····· $(\overline{v^2}/M^2\ \overline{v_0^2} = \overline{w^2}/M^2\ \overline{w_0^2})$, —— $(q^2/M^2\ q_0^2)$. The three curves asymptote to 0.49, 0.40 and 0.43 respectively ($\gamma = 1.4$).

being close to unity and finally, viscous effects. Proximity to the critical angle seems to be the most important factor. Our computations of of single acoustic waves interacting with a shock wave disagree with linear analysis around 25 degrees of the critical angle; very good agreement is seen outside this range. Fortunately, in the interaction of a spectrum of waves with a shock wave, the incident waves around the critical angle make only partial contribution to the overall energy. With regard to the amplitude of incident disturbances, results of computations are encouraging. Our computations show good agreement with linear analysis away from the critical angle for disturbance amplitudes varying from 0.14% to 14%. Zang *et al* (1984) show that linear analysis yields good prediction away from the critical angle for acoustic disturbance amplitudes as large as 25%. Meadows *et al* (1994) reach a similar conclusion in their study of the one-dimensional interaction of an acoustic wave with a shock wave. Their comparison of linear analysis to a non-linear Riemann analysis yielded indistinguishable results (to plotting accuracy) for disturbance amplitudes

less than 10%. An effect of increasing disturbance amplitude for a fixed shock strength has been documented by Honkan and Andreopoulous (1992) and Lee *et al* (1992) in the interaction of isotropic turbulence with a normal shock. Both studies reported a decrease in the amplification of kinetic energy as the disturbance amplitude was increased. Honkan and Andreopoulous' experimental study had a shock of mean Mach number 1.24 while Lee *et al*'s numerical results were for a shock wave of mean Mach number 1.2.

## B.4.2 Combined interaction of vortical and acoustic fluctuations

The linearity of the analysis permits the use of superposition to predict the combined interaction of vortical and acoustic fluctuations with a shock wave. Since sound and vorticity travel at different speeds, the correlation between them can be assumed negligible upstream and in the far-field behind the shock wave. The amplification of kinetic energy across the shock wave can therefore be expressed as,

$$\frac{q^2}{q_0^2} = \frac{q_\omega^2 + q_\theta^2}{(q_\omega^2)_0 + (q_\theta^2)_0} \qquad (B.10)$$

where , the subscript '0' represents conditions upstream of the shock and the subscripts $\omega$ and $\theta$ represent the vortical and dilatational components respectively. The amplification ratio in the mixed problem may be expressed in terms of the amplification ratios of vortical and acoustic fluctuations as:

$$\frac{q^2}{q_0^2} = (1 - X) f_\omega + X f_\theta \qquad (B.11)$$

where, $f_\omega = q_\omega^2/(q_\omega^2)_0$, $f_\theta = q_\theta^2/(q_\theta^2)_0$ and $X = (q_\theta^2)_0/q_0^2$ . $X$ is the ratio of acoustic to total kinetic energy upstream of the shock wave. Note that as $X$ varies from 0 to 1, $q^2/q_0^2$ varies from $f_\omega$ to $f_\theta$. Available experiments on the shock/turbulence interaction are in the range of Mach numbers for which the kinetic energy of the acoustic component decreases across the shock wave. Our results suggest that the presence of acoustic waves in these experiments will decrease the amplification of kinetic energy. As noted by Jacquin *et al* (1993), wind-tunnel experiments on the shock/turbulence interaction report lower amplification ratios than shock-tube experiments. They suggest that boundary-layer induced oscillation of the shock wave in the wind-tunnel experiments might be responsible (through an unknown mechanism) for this observation. Our results suggest the alternative scenario that

the lower kinetic energy amplification is a consequence of a significant amount of acoustic waves in the turbulence ahead of the shock wave. A likely source of these sound waves are the shock waves that are generated at the edges of the grid that generates turbulence in the tunnel. Further data is needed to support or discard this scenario.

According to linear analysis (equation B.18), when compressible isentropic turbulence interacts with a shock wave, the evolution of kinetic energy lies between two limits - the pure solenoidal and pure dilatational limits. This behavior is identical to the response of *homogenous* turbulence to one-dimensional compression. As shown by Cambon *et al*, the evolution of kinetic energy when compressible homogeneous turbulence is subjected to one-dimensional compression lies between the solenoidal and the dilatational limits. However an important difference between the shock/turbulence interaction problem and the homogeneous compression problem is the behavior of the turbulence in the dilatational limit. For homogeneous turbulence, Cambon *et al* show that the dilatational limit is characterized by loss of acoustic communication which forces the pressure-strain correlation to zero thereby yielding significantly higher amplification of $q^2$ as compared to solenoidal turbulence. The compressibility-induced decrease in kinetic energy across the shock wave that is seen in the acoustic wave/shock wave interaction for $1.25 < M < 1.8$ is not observed. This is due to the fundamentally different nature of the pressure fluctuations in the two problems.

The difference between the one-dimensional compression of solenoidal turbulence and Ribner's (1954,1987) analysis of solenoidal fluctuations interacting with a shock wave were pointed out by Lee *et al* (1993) and underscored by Jacquin *et al* (1993). Results of the two problems agree for small Mach numbers; for large Mach numbers significantly larger amplification is seen in the homogeneous problem. Jacquin *et al* also compare the compression of homogeneous compressible turbulence to Ribner's analysis and note that the difference between the two problems is greater than pointed out by Lee *et al.* A comparison of the compression of dilatational fluctuations to the interaction of solenoidal fluctuations with a shock wave is not appropriate; comparison should be made to the interaction of dilatational fluctuations with the shock wave. Such comparison would reveal disagreement in the dilatational limit over the entire range of Mach numbers. While the homogeneous problem can approximate the evolution of kinetic energy in the interaction

of solenoidal fluctuations with a shock wave of moderate strength, it is quite inappropriate as the incident turbulence becomes increasingly compressible.

### B.4.3 Comparison to computation

The analysis explains recent observations (Hannapel and Friedrich, 1994) on the interaction of compressible turbulence with a normal shock. Hannapel and Friedrich numerically computed the interaction of low Reynolds number isotropic turbulence ($R_\lambda \sim 4$ upstream of the shock wave) with a normal shock of mean Mach number 2. The fluctuating Mach number was 0.1 at the inflow and the kinetic energy was equally distributed between the vortical and acoustic modes. ($X = 0.5$ in our notation.) They compared this interaction with that of essentially solenoidal turbulence ($X = 0$) of the same fluctuating Mach number. The 'compressible' case displayed increased amplification of vorticity, decreased amplification of velocity components transverse to the shock, decreased reduction of Taylor microscale and decreased amplification of density, temperature and pressure fluctuations across the shock wave.

The computation may suffer from lack of sufficient resolution of the shock front. As a result we do not attempt quantitative comparison. We show that the computation follows the trends predicted by the linear analysis and quote the linear analysis predictions for reference. The higher amplification of the transverse components of vorticity in the compressible case is explained by the generation of vorticity through the acoustic wave/shock wave interaction. Using an expression similar to equation (B.18), the increase in the amplification of vorticity may be shown to be $3g_\theta({\theta_0}^2/{\omega_0}^2)$, where $g_\theta = {\omega_2}^2/{\theta_0}^2$ in the acoustic wave/shock wave interaction problem. Similarly, linear analysis predicts the decrease in transverse velocity and reduction in Taylor microscale. For the interaction of vortical fluctuations with a shock wave, Ribner's analysis yields $u^2/u_0^2 = 1.64$ and $v^2/v_0^2 = 1.66$ across a shock wave of Mach number 2. For dilatational fluctuations, our analysis yields values of 1.69 and 0.9 respectively. Using an expression similar to equation (B.18), we get $u^2/u_0^2 = 1.67$ and $v^2/v_0^2 = 1.28$; *i.e.*, the amplification of $u^2$ is essentially unchanged while the amplification of the transverse velocity drops.

Linear analysis yields values of 0.53 and 0.77 for $\lambda_1/(\lambda_1)_0$ and $\lambda_2/(\lambda_2)_0$ respectively ($\lambda_i$ represents the Taylor microscale in the $i$ direction) for the vortical problem. Corresponding values for the compressible problem are 0.66 and 0.94 respectively. The reduced amplification of thermodynamic fluctuations in the com-

pressible problem (an order lower) is a consequence of the fact that in pure vortical turbulence, the absolute level of incident thermodynamic fluctuations is much lower (zero in the linear limit). The level of thermodynamic fluctuations behind the shock wave, however scale with the incident kinetic energy as a result of which the amplification of thermodynamic fluctuations will be large (undefined in linear analysis).

## B.5. Summary

Inviscid linear analysis was used to study the evolution of fluctuating kinetic energy, sound level and thermodynamic fluctuations in the interaction of an isotropic field of acoustic waves with a normal shock wave. The analysis was an extension of Moore's (1954) study of the interaction of a shock wave with a single acoustic wave. Moore's analysis was evaluated by comparison to numerical computation. Good agreement was seen for angles away from the critical angles. A possible reason for disagreement around the critical angles was proposed. Linear approximation was noted to be inconsistent in this regime; requirement of the transonic small disturbance equations was suggested.

The interaction of an isotropic acoustic field with the shock was noted to be significantly different from that of vortical fluctuations. The kinetic energy of the acoustic fluctuations decreased across the shock wave for Mach numbers between 1.25 and 1.8. For Mach numbers exceeding 3, the kinetic energy amplified by levels that significantly exceeded those found in the interaction of vortical fluctuations with the shock. These trends were explained by decomposing the velocity field into acoustic and vortical components and examining their dependence on the Mach number. Upon interacting with the shock wave, the acoustic waves generated vortical fluctuations whose contribution to the far-field kinetic energy increased with increasing Mach number. The level of sound increased across the shock wave. The rise in the sound pressure level across the shock varied from 5 to 20 decibels for Mach number varying from 1.5 to 5. The fluctuations behind the shock wave were nearly isentropic for Mach number less than 1.5 beyond which the generation of entropy fluctuations became significant.

Finally the analysis was used to describe the combined interaction of isotropic vortical and acoustic fluctuations with a normal shock wave.

## B.6 Details of Moore's analysis

The solution dowstream of the shock wave is given below. The subscript 2 refers to conditions behind the shock wave.

For $0 \leq \psi_1 < \psi_{cl}$ or $\psi_{cu} < \psi_1 \leq \pi$,

$$\frac{1}{A_3}\frac{p_2}{P_2} = \widetilde{K} f\left(\frac{\alpha x_2 + \beta y + a_2 t}{\lambda_2}\right)$$

$$\frac{1}{A_3}\frac{\rho_2}{R_2} = \frac{\widetilde{K}}{\gamma} f\left(\frac{\alpha x_2 + \beta y + a_2 t}{\lambda_2}\right) + \widetilde{Q} f\left(\frac{\frac{m+1/M}{1-r} x_2 - ly}{\lambda_1}\right)$$

$$\frac{1}{A_3}\frac{u_2}{V} = \widetilde{F} f\left(\frac{\alpha x_2 + \beta y + a_2 t}{\lambda_2}\right) + \widetilde{G} f\left(\frac{\frac{m+1/M}{1-r} x_2 - ly}{\lambda_1}\right)$$

$$\frac{1}{A_3}\frac{v_2}{V} = \widetilde{H} f\left(\frac{\alpha x_2 + \beta y + a_2 t}{\lambda_2}\right) + \widetilde{I} f\left(\frac{\frac{m+1/M}{1-r} x_2 - ly}{\lambda_1}\right).$$

The $x_2$ axis is stationary in a frame of reference that moves with speed $U$ yielding, $x_2 = (V - U)t$ at the mean position of the shock wave. Of the two terms that contribute to the velocity, density and temperature, the unsteady term corresponds to the acoustic wave while the steady term corresponds to the vorticity and entropy waves. The coefficients $\widetilde{K}, \widetilde{Q}, \widetilde{G}, \widetilde{H}$ and $\widetilde{I}$ in the above equations are functions of the Mach number of the shock and the angle of incidence and are given below.

If $\psi_{cl} < \psi_1 < \psi_{cu}$, the solution is a bit more complex and is given by:

$$\frac{1}{A_3}\frac{p_2(\eta,\xi)}{P_2} = \widetilde{K}_{(1)}\Phi_{(1)}(\eta,\xi) + \widetilde{K}_{(2)}\Phi_{(2)}(\eta,\xi)$$

$$\frac{1}{A_3}\frac{\rho_2}{R_2} = \frac{1}{\gamma}\frac{p_2}{P_2} + \widetilde{Q}_{(1)} f\left(\frac{\frac{m+1/M}{1-r} x_2 - ly}{\lambda_1}\right) + \widetilde{Q}_{(2)} g\left(\frac{\frac{m+1/M}{1-r} x_2 - ly}{\lambda_1}\right)$$

$$\frac{1}{A_3}\frac{u_2}{V} = \widetilde{F}_{(1)}\Phi_{(1)}(\eta,\xi) + \widetilde{F}_{(2)}\Phi_{(2)}(\eta,\xi) + \widetilde{G}_{(1)} f\left(\frac{\frac{m+1/M}{1-r} x_2 - ly}{\lambda_1}\right) + \widetilde{G}_{(2)} g\left(\frac{\frac{m+1/M}{1-r} x_2 - ly}{\lambda_1}\right)$$

$$\frac{1}{A_3}\frac{v_2}{V} = \widetilde{H}_{(1)}\Phi_{(1)}(\eta,\xi) + \widetilde{H}_{(2)}\Phi_{(2)}(\eta,\xi) + \widetilde{I}_{(1)}f\left(\frac{\frac{m+1/M}{1-r}x_2 - ly}{\lambda_1}\right) + \widetilde{I}_{(2)}g\left(\frac{\frac{m+1/M}{1-r}x_2 - ly}{\lambda_1}\right).$$

Analogous to the propagating regime, $\widetilde{K}_{(\alpha)}, \widetilde{Q}_{(\alpha)}, \widetilde{G}_{(\alpha)}, \widetilde{H}_{(\alpha)}$ and $\widetilde{I}_{(\alpha)}$ are functions of the Mach number of the shock and the angle of incidence and are given below. Also, $\eta$ and $\xi$ are related to $x_2, y$ and $t$ by:

$$\eta = -\frac{d}{\lambda_1}[x_2 - (V-U)t]$$

$$\xi = \frac{1}{\lambda_1}(\alpha x_2 + \beta y + cVt).$$

$\eta$ is thus proportional to the distance behind the shock while $\xi$=constant represents an oblique plane moving at constant velocity. The functions $g, \Phi_{(1)}$ and $\Phi_{(2)}$ are defined as:

$$g(\eta) = \frac{1}{\pi}\int_{-\infty}^{\infty}\frac{f(\tau)}{\tau-\xi}\,d\tau$$

$$\Phi_{(1)} = \frac{1}{\pi}\int_{-\infty}^{\infty} f(\tau)\frac{\eta}{\eta^2+(\tau-\eta)^2}\,d\tau$$

$$\Phi_{(2)} = \frac{1}{\pi}\int_{-\infty}^{\infty} f(\tau)\frac{\tau-\eta}{\eta^2+(\tau-\eta)^2}\,d\tau.$$

Since a homogenous acoustic field may be represented as a superposition of plane waves, we consider $f(x) = e^{ix}$ for which $g, \Phi_{(1)}$ and $\Phi_{(2)}$ are given by:

$$g(\xi) = i\,e^{i\xi}, \quad \Phi_{(1)} = e^{-\eta}e^{i\xi}, \quad \Phi_{(2)} = i\,e^{-\eta}e^{i\xi}$$

Note that if the incident wave is a plane wave, the above equations take on a simple form. The coefficients in the solution are determined as follows.

$$B_1 = -\frac{2}{\gamma+1}\frac{1}{M^2}\left(1-\frac{\gamma-1}{2}M^2\right); \qquad B_2 = \left(\frac{\gamma-1}{\gamma+1}\right)\frac{2}{\gamma M^2}$$

$$C_1 = \frac{2}{1+\frac{\gamma-1}{2}M^2}; \qquad C_2 = \frac{1}{\gamma}\left(1-\frac{\gamma-1}{1+\frac{\gamma-1}{2}M^2}\right)$$

$$D_1 = \frac{2\gamma M^2}{\gamma M^2 - \frac{\gamma-1}{2}}; \qquad D_2 = \frac{M^2-\frac{\gamma-1}{2}}{\gamma M^2 - \frac{\gamma-1}{2}}$$

$$l = \sin\psi_1; \quad m = \cos\psi_1; \quad n = \tan\psi_1$$

$$r = \frac{2}{\gamma+1}\left(1-\frac{1}{M^2}\right); \qquad \left(\frac{a_2}{V}\right)^2 = (1-r)\left(1+\frac{\gamma-1}{2}r\right); \qquad \sigma = \frac{n(1-r)}{1+\frac{1}{Mm}}.$$

For $0 \le \psi_1 < \psi_{cl}$ or $\psi_{cu} < \psi_1 \le \pi$,

$$\chi = \left[1-\frac{r(\gamma+1)(1+\sigma^2)}{2+(\gamma-1)r}\right]^{\frac{1}{2}}$$

$$\widetilde{L} = -\frac{m}{\gamma M}\frac{\left[1+\frac{\gamma+1}{4}\frac{M}{m}\left(\frac{3-\gamma}{\gamma+1}+\frac{\gamma-1}{2}r\right)\right]\chi+\frac{\gamma+1}{4}\left[1-2\frac{\gamma-1}{\gamma+1}\frac{n}{\sigma}-\frac{n\sigma}{1-r}\right](1-r)}{1+\chi-\frac{\gamma+1}{4}r\left(1+\frac{\sigma^2}{1-r}\right)}$$

$$\widetilde{K} = D_1\left(\widetilde{L}+\frac{m}{\gamma M}\right)+D_2$$

$$\widetilde{Q} = C_1\left(\widetilde{L}+\frac{m}{\gamma M}\right)+C_2-\frac{\widetilde{K}}{\gamma}$$

$$m\frac{\lambda_2}{\lambda_1} = \frac{\frac{a_2}{V}(1+\frac{1}{mM})}{(1+\frac{1}{mM})^2+n^2(1-r)^2}\left[1+\sqrt{1-r\frac{1+n^2(1-r)^2/(1+\frac{1}{mM})^2}{1-\frac{\gamma-1}{\gamma+1}(1-r)}}\right]$$

$$\alpha = \frac{1}{1-r}\left[\frac{\lambda_2}{\lambda_1}\left(m+\frac{1}{M}\right)-\frac{a_2}{V}\right]; \qquad \beta = -l\frac{\lambda_2}{\lambda_1}$$

$$\widetilde{F} = -\frac{a_2}{\gamma V}\widetilde{K}\alpha; \qquad \widetilde{H} = -\frac{a_2}{\gamma V}\widetilde{K}\beta$$

$$\widetilde{G} = \widetilde{L}-\widetilde{F}-B_1\left(\widetilde{L}+\frac{m}{\gamma M}\right)-B_2; \qquad \widetilde{I} = \frac{1+1/Mm}{n(1-r)}\widetilde{G}.$$

For $\psi_{cl} \le \psi_1 \le \psi_{cu}$, the coefficients are as follows.

$$c = \frac{m+1/M}{1-V^2(1-r)^2/a_2^2}; \quad \alpha = -\frac{V^2}{a_2^2}(1-r)c; \quad \beta = -l; \quad d = \sqrt{\frac{\alpha^2+l^2-V^2c^2/a_2^2}{1-V^2(1-r)^2/a_2^2}}$$

$$h_1 = -\frac{1-r}{r}\frac{1}{\sigma}\left[\frac{l}{\gamma M}+\left(\frac{m}{\gamma M}B_1+B_2\right)\frac{1}{\sigma}\right]$$

$$h_2 = 1-\frac{1-r}{r}\frac{1-B_1}{\sigma^2}; \qquad h_3 = -\frac{2d(1-r)}{l\sigma(1+\frac{\gamma-1}{2}r)}$$

$$\widetilde{L}_{(1)} = \frac{h_1h_2-(\frac{m}{\gamma M}+\frac{D_2}{D_1})h_3^2}{h_2^2+h_3^2}; \qquad \widetilde{L}_{(2)} = h_3\frac{h_1+(\frac{m}{\gamma M}+\frac{D_2}{D_1})h_2}{h_2^2+h_3^2}$$

$$h_4 = \frac{4}{\gamma+1}\frac{\sigma^2}{1+\sigma^2}; \qquad h_5 = \frac{2rd\sigma(1-r)}{l(1+\sigma^2)}\frac{V^2}{a_2^2}$$

$$\widetilde{F}_{(1)} = h_4\left(\widetilde{L}_{(1)} + \frac{m}{\gamma M} + \frac{D_2}{D_1}\right) - h_5\widetilde{L}_{(2)}; \quad \widetilde{F}_{(2)} = h_5\left(\widetilde{L}_{(1)} + \frac{m}{\gamma M} + \frac{D_2}{D_1}\right) + h_4\widetilde{L}_{(2)}$$

$$\widetilde{H}_{(1)} = \frac{h_4}{\sigma}\left(\widetilde{L}_{(1)} + \frac{m}{\gamma M} + \frac{D_2}{D_1}\right) + \sigma h_5\widetilde{L}_{(2)}$$

$$\widetilde{H}_{(2)} = -\sigma h_5\left(\widetilde{L}_{(1)} + \frac{m}{\gamma M} + \frac{D_2}{D_1}\right) + \frac{h_4}{\sigma}\widetilde{L}_{(2)}$$

$$\widetilde{K}_{(1)} = D_1\left(\widetilde{L}_{(1)} + \frac{m}{\gamma M}\right) + D_2; \qquad \widetilde{K}_{(2)} = D_1\widetilde{L}_{(2)}$$

$$\widetilde{Q}_{(1)} = C_1\left(\widetilde{L}_{(1)} + \frac{m}{\gamma M}\right) + C_2 - \frac{\widetilde{K}_{(1)}}{\gamma}; \qquad \widetilde{Q}_{(2)} = C_1\widetilde{L}_{(2)} - \frac{\widetilde{K}_{(2)}}{\gamma}$$

$$\widetilde{G}_{(1)} = \widetilde{L}_{(1)} - \widetilde{F}_{(1)} - B_1\left(\widetilde{L}_{(1)} + \frac{m}{\gamma M}\right) - B_2; \qquad \widetilde{G}_{(2)} = \widetilde{L}_{(2)}(1-B_1) - \widetilde{F}_{(2)}$$

$$\widetilde{I}_{(1)} = \frac{1+\frac{1}{mM}}{n(1-r)}\widetilde{G}_{(1)}; \qquad \widetilde{I}_{(2)} = \frac{1+\frac{1}{mM}}{n(1-r)}\widetilde{G}_{(2)}.$$

The expression for $\widetilde{H}_{(1)}$ in Moore's paper contains a typographical error; $\widetilde{L}_{(1)} + \frac{m}{\gamma M} + \frac{D_2}{D_1}$ should be replaced by $\widetilde{L}_{(1)} + \frac{n}{\gamma M} + \frac{D_2}{D_1}$. Also, the plots of the constants when $\psi_{cl} \leq \psi_1 \leq \psi_{cu}$ do not agree with the formulae. After repeating Moore's analysis, we conclude that the formulae are correct.

# Appendix C

# Generation of Inflow Turbulence

Spatial simulation of turbulent flows requires specification of 'turbulent' fluctuations at the inflow plane of the computational domain. This appendix describes how inflow turbulence was specified in our calculations. Previous workers ( e.g. Lee, Lele and Moin, 1992; Le and Moin, 1994) have developed methods for this purpose. Their methods differ in detail but are conceptually similar. A field of random numbers subject to certain constraints on the second-order statistics is convected into the domain of the spatial computation. To ensure that the turbulent signal at the inflow is not periodic in time, the field of random numbers is continuously 'jittered'. The method used in our simulations is an extension of that proposed by Lee, Lele and Moin. As opposed to introducing random numbers at the inflow, a separate temporal calculation is conducted. A single developed field from the temporal simulation is then used to generate inflow turbulence. Section C.1 describes the details of the method. The spatial simulation of isotropic turbulence is then considered in Section C.2. Finally, the shear flow computations are discussed in Section C.3.

## C.1 Details of the method

The spatial simulation of isotropic turbulence is used to describe the procedure for specifying inflow 'turbulence'. It will be seen that the procedure may easily be extended to other turbulent flows.

In the spatial simulation of decaying turbulence, the mean flow at the inflow plane is spatially uniform and given by:

$$U = U_1; \qquad \overline{p} = \frac{1}{\gamma}; \qquad \overline{\rho} = 1. \tag{C.1}$$

Turbulent fluctuations in velocity, pressure and density are superposed onto the above mean flow. These turbulent fluctuations are obtained as follows. A temporal simulation with periodic streamwise boundary conditions is first performed. The spanwise boundary conditions in the temporal calculation match those in the spatial simulation (periodic for isotropic turbulence). The mean flow in the temporal simulation is identical to that at the inflow of the spatial computation. The

initial fluctuations are similar to those used by Lee, Lele and Moin (1992); *i.e.*, the velocity field is isotropic and solenoidal with $E(k) \sim (k/k_0)^4 \ \mathrm{e}^{-2(k/k_0)^2}$, while the thermodynamic fluctuations are set to zero.

The temporal simulation is then advanced in time. Consider the turbulence time scale defined as, $\tau_t = \lambda/u_{\mathrm{rms}}$ where, $\lambda$ and $u_{\mathrm{rms}} = \sqrt{\overline{u'^2}}$ are the Taylor microscale and r.m.s. velocity respectively. The velocity derivative skewness, defined as $S_\alpha = \overline{u'^3_\alpha}/[\overline{(\frac{\partial u'_\alpha}{\partial x_\alpha})^2}]^{3/2}$ is known (Tavoularis, Bennett and Corrsin, 1978; Erlebacher *et al.*, 1992) to have a typical value between -0.4 and -0.6 in developed isotropic turbulence. As the temporal simulation is advanced in time, skewness varies from its initial value of 0 (due to the choice of initial conditions) to its developed value. This variation occurs on the order of one turbulence time scale; *i.e.*, $t/\tau_t \sim 1$. An instantaneous realization of the temporal simulation is taken after the skewness reaches its developed value. This instantaneous field is then used to specify turbulence at the inflow of the spatial calculation.

This is done as follows. Fluctuations in velocity, density and pressure are extracted from the turbulent field. The fluctuations are then Fourier transformed in all three directions; *i.e.*, if $f$ denotes fluctuations in a variable, its Fourier transform $\widehat{f}$ is obtained as

$$\widehat{f}(k_1,k_2,k_3) = \frac{1}{N_x N_y N_z} \sum_{x,y,z} f(x,y,z) \ \mathrm{e}^{-i(k_1 x + k_2 y + k_3 z)}. \qquad (C.2)$$

Taylor's hypothesis is then invoked to convect this turbulent field into the spatial domain. The streamwise distance $x$ in equation $C.2$ is therefore expressed as $x = x_0 + U_1 t$, where $x_0$ is taken as 0 without loss of generality. Substituting for $x$ and inverse Fourier transforming yields $f(t,y,z)$; *i.e.*,

$$f(t,y,z) = \sum_{k_1,k_2,k_3} \widehat{f}(k_1,k_2,k_3) \ \mathrm{e}^{i(k_1 U_1 t + k_2 y + k_3 z)}. \qquad (C.3)$$

The above signal may be added onto the mean flow at the inflow. However, $f$ as given by equations C.3 is periodic in time with $(L_x)_{\mathrm{temporal}}/U_1$ being the period. This periodicity may be eliminated if desired, by 'jittering' the signal in Fourier space. Alternatively, the signal could be convected without jittering and statistics collected over one period. Ensemble averaging could then be used to improve statistical convergence.

The turbulent signal at the inflow is jittered as follows. The Fourier coefficient $\widehat{f}$ is first expressed in terms of its amplitude and phase as $|\widehat{f}|_{\rm o}\ {\rm e}^{i\phi_{\rm o}}$ where the subscript 'o' denotes 'old'. The amplitude and phase of the signal are then jittered as follows,

$$|\widehat{f}|_{\rm n} = |\widehat{f}|_{\rm o}\frac{1+\alpha_{\rm amp}c_{\rm amp}}{\sqrt{1+c_{\rm amp}^2/3}};\quad \phi_{\rm n} = \phi_{\rm o}(1+\alpha_{\rm p}c_{\rm p}). \tag{C.4}$$

The variables $\alpha_{\rm amp}$ and $\alpha_{\rm p}$ are random numbers that vary between -1 and +1; $c_{\rm amp}$ and $c_{\rm p}$ are constants that denote the percentage variation. The factor, $\sqrt{1+c_{\rm amp}^2/3}$ in the denominator of $|\widehat{f}|_{\rm n}$ ensures that the r.m.s. level of the signal is maintained. This is easily seen as follows.

Denoting the factor $\sqrt{1+c_{\rm amp}^2/3}$ by $1/K$, we have from equation $C.4$,

$$\widehat{f}_{\rm n} = K\ |\widehat{f}|_{\rm o}\,(1+\alpha_{\rm amp}c_{\rm amp})\ {\rm e}^{i\phi_{\rm o}(1+\alpha_p c_p)}. \tag{C.5}$$

The amplitude of the jittered signal is given by the relation,

$$|\widehat{f}|_{\rm n}^2 = \widehat{f}_n\widehat{f}_n^* = K^2\ |\widehat{f}|_{\rm o}^2\ (1+\alpha_{\rm amp}c_{\rm amp})^2. \tag{C.6}$$

The variable $\alpha_{\rm amp}$ is obtained from a random number generator that has a uniform probability distribution between -1 and +1; *i.e.*, $P(\alpha_{\rm amp}) = 1/2$ (so that $\int_{-1}^{+1} P(\alpha_{\rm amp})\ {\rm d}\alpha_{\rm amp} = 1$). The r.m.s. level of the jittered signal is therefore given by,

$$\begin{aligned}\int_{-1}^{+1} |\widehat{f}_{\rm n}|^2\ P(\alpha_{\rm amp})\ {\rm d}\alpha_{\rm amp} &= \frac{K^2}{2}\ |\widehat{f}_{\rm o}|^2\ \int_{-1}^{+1}(1+\alpha_{\rm amp}c_{\rm amp})^2\ {\rm d}\alpha_{\rm amp}\\ &= K^2\ |\widehat{f}_{\rm o}|^2\left[1+\frac{c_{\rm amp}^2}{3}\right].\end{aligned} \tag{C.7}$$

To ensure that $(f_{\rm n})_{\rm rms} = (f_{\rm o})_{\rm rms}$, we require,

$$K^2\left(1+\frac{c_{\rm amp}^2}{3}\right) = 1 \quad\Rightarrow\quad K = \frac{1}{\sqrt{1+\frac{c_{\rm amp}^2}{3}}}. \tag{C.8}$$

Equation C.3 is used to inverse Fourier transform the jittered Fourier coefficients thereby yielding the turbulent signal at the inflow. The variables $c_{\rm amp}$ and $c_{\rm p}$ are typically chosen as 0.2. The random numbers $\alpha_{\rm amp}$ and $\alpha_{\rm p}$ are a function of $\vec{k}$ and time. The time dependence is introduced by varying $\alpha_{\rm amp}$ and $\alpha_{\rm p}$ at different

instants for different wavenumbers. Each Fourier mode is jittered at one random instant every $N_t$ timesteps where $N_t$ is specified. This ensures temporal smoothness; *i.e.*, it avoids large levels of high frequency contribution (Lee, Moin and Lele 1992).

## C.2. The spatial simulation of decaying turbulence

The procedure described above is applied to compute the spatial decay of isotropic turbulence. The governing equations are the three-dimensional compressible unsteady Navier Stokes equations. As mentioned in Chapter 4, the sixth order Padé scheme is used to compute spatial derivatives while the third order Runge Kutta scheme is used for time advancement. Periodic boundary conditions are specified in the $y$ and $z$ directions. The flow is supersonic and hence all flow variables are specified at the inflow boundary. No boundary conditions are needed at the exit boundary; the governing equations are used to advance the solution there.

The turbulent fluctuations at the inflow boundary are specified as discussed above. A temporal simulation of isotropic turbulence is first conducted. The relevant dimensional and non-dimensional parameters (refer Chapter 4 for notation) at the start of the simulation are listed in Table C.1.

| $L_x$ | $L_y$ | $L_z$ | $N_x$ | $N_y$ | $N_z$ | $Re$ | $R_\lambda$ | $M_t$ | $CFL$ |
|---|---|---|---|---|---|---|---|---|---|
| $3\pi$ | $3\pi$ | $3\pi$ | 81 | 81 | 81 | 750 | 30 | 0.17 | 0.4 |

TABLE C.1: Parameters in the temporal simulation of isotropic turbulence.

The solution is advanced for three turbulence timescales. Figures C.1 and C.2 illustrate the temporal evolution of $q^2$ and the velocity derivative skewness. Note that the plotted skewness is the average of all three velocity derivative skewnesses. Kinetic energy decays by almost a factor of 5. The skewness attains its developed value after about one turbulence timescale.

The instantaneous flow field at $t/\tau_t = 2$ is used to generate inflow turbulence for the spatial simulation. Note that after two eddy turnover times, $R_\lambda$ and $M_t$ are about 15 and 0.11 respectively. The fidelity of the temporal solution is illustrated in Figures C.3 and C.4 where the one-dimensional spectra, $E_{ij}(k_3)$ and two-point correlations, $Q_{ff,\alpha}(r) = \overline{f'(\mathbf{x})f'(\mathbf{x}+r\mathbf{e}_\alpha)}/\overline{f'(\mathbf{x})f'(\mathbf{x})}$ of the velocity field are plotted. Both, the resolution as well as size of the computational domain are seen to be adequate.

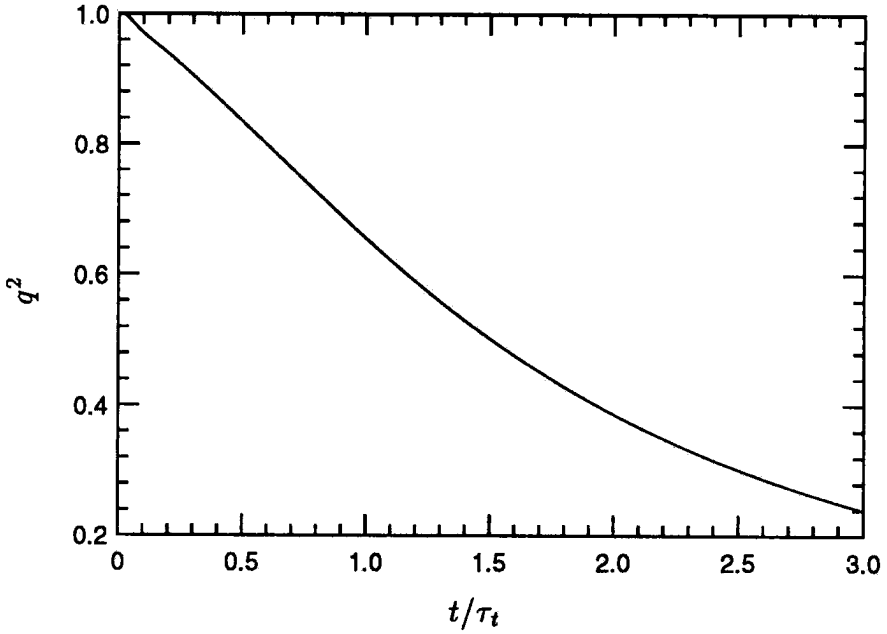


FIGURE C.1: The evolution of kinetic energy in the temporal decay of isotropic turbulence.

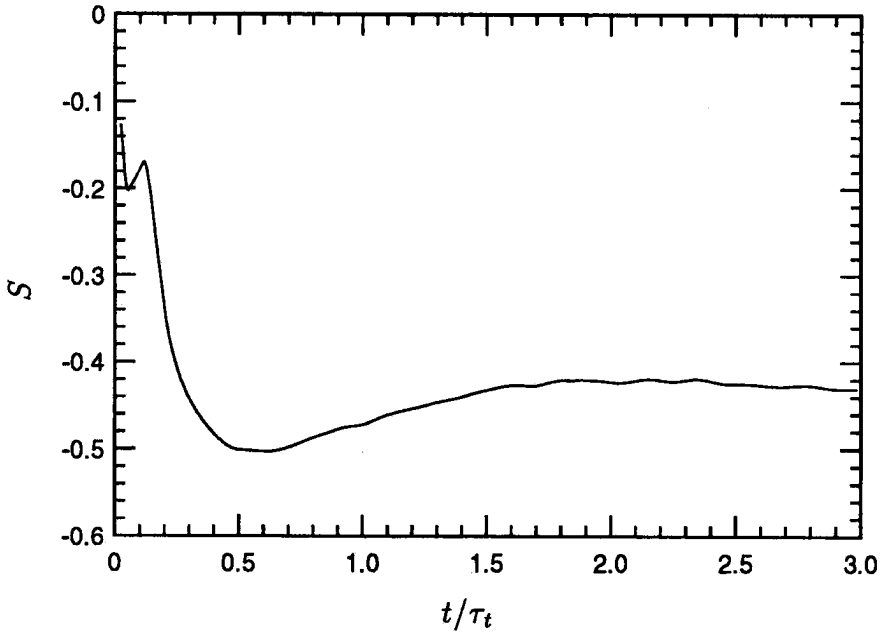


FIGURE C.2: Velocity derivative skewness in the temporal decay of isotropic turbulence.

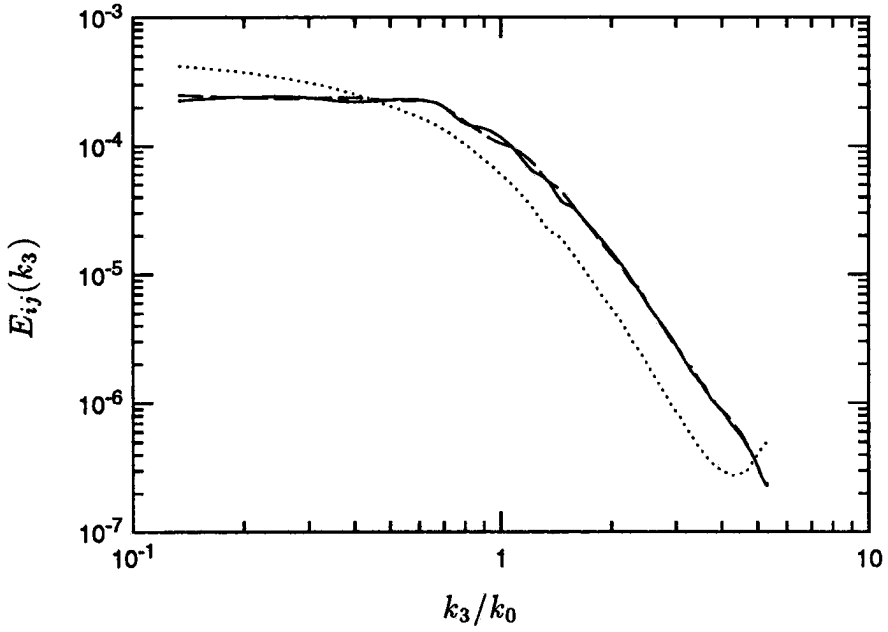


FIGURE C.3: One-dimensional energy spectra from the temporal simulation at $t/\tau_t = 2$. —— $(E_{11})$, ---- $(E_{22})$, ····· $(E_{33})$.

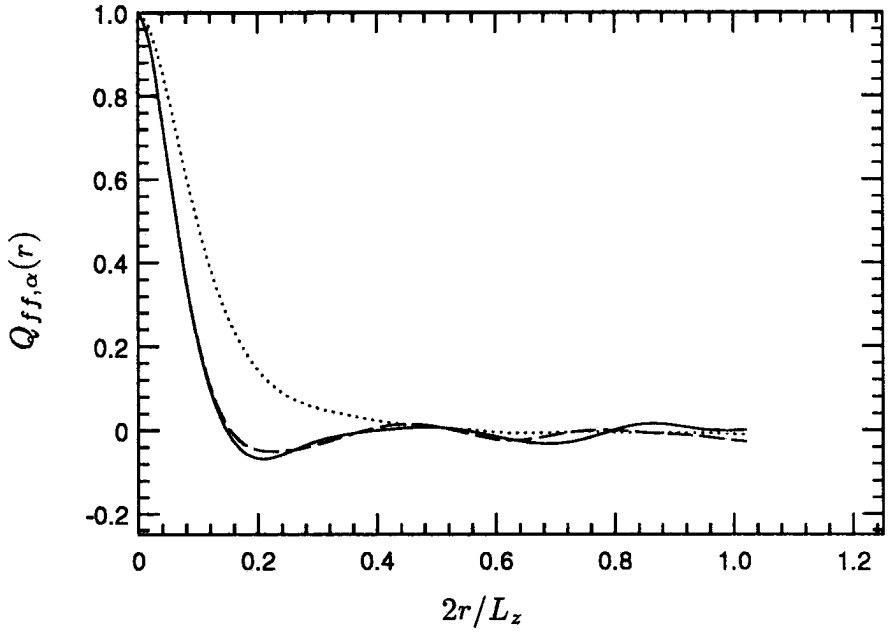


FIGURE C.4: Two-point correlations of the velocity field at $t/\tau_t = 2$. —— $(Q_{11,3})$, ---- $(Q_{22,3})$, ····· $(Q_{33,3})$.

The relevant parameters of the spatial simulation are listed in Table C.2.

| $L_x$ | $L_y$ | $L_z$ | $N_x$ | $N_y$ | $N_z$ | $Re$ | $U_1$ | $c_{amp}$ | $c_p$ |
|---|---|---|---|---|---|---|---|---|---|
| $3\pi$ | $3\pi$ | $3\pi$ | 81 | 81 | 81 | 750 | 1.5 | 0.25 | 0.25 |

TABLE C.2: Parameters in the spatial simulation of decaying turbulence.

The flow is initialized with uniform mean flow on which fluctuations obtained from the temporal simulation are superposed. The spatial calculation is then advanced for two flow-through timescales, $(L_x/U_1)$ to allow initial transients to exit the domain. Statistics are then gathered by averaging over time and the homogeneous directions ($y$ and $z$). The streamwise evolution of $q^2$ and velocity derivative skewness is illustrated in Figures C.5 and C.6. The mean velocity is used to convert streamwise distance into time which is then normalized by the turbulence timescale, $\lambda/u_{rms}$ at the inflow. After a brief transient (about 0.2 eddy turnover times), the skewness reaches a plateau. By comparison, the inflow fluctuations of Lee, Lele and Moin (1992) require about 0.6 turnover times to evolve into 'realistic' turbulence. The use of a developed turbulent field at the inflow is thus seen to considerably reduce the evolution length.

The transient at the inflow is a function of the amount of jitter as well as the level of compressibility ($M_t$). Strictly speaking, the solenoidal and dilatational parts of the inflow turbulence should be convected at different speeds. However, this is not done, in order to keep the computational cost low. The inflow turbulence therefore rapidly adjusts near the inflow boundary. This transition length will increase as the level of dilatational fluctuations in the inflow turbulence increases.

## C.3 The spatial simulation of a shear flow

The procedure discussed above is used to specify inflow turbulence in the spatial simulation of a turbulent shear flow interacting with a shock wave. Since the flow at the inflow boundary is supersonic, all flow variables are specified there. The mean flow at the inflow boundary is the same as in equation 4.1; *i.e.*,

$$U_1(y) = U_0 + S(y + L_y/2), \qquad \overline{p}_1(y) = \frac{1}{\gamma}, \qquad \overline{T}_1(y) = \frac{U_1^2(y)}{(\gamma-1)M_1^2}. \qquad (C.9)$$

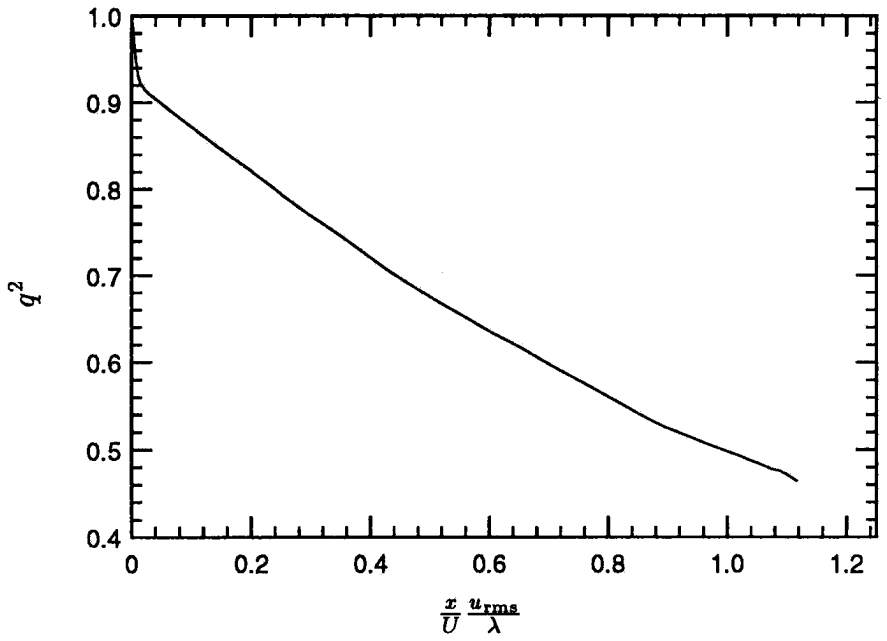


FIGURE C.5: The evolution of kinetic energy in the spatial simulation of isotropic turbulence.

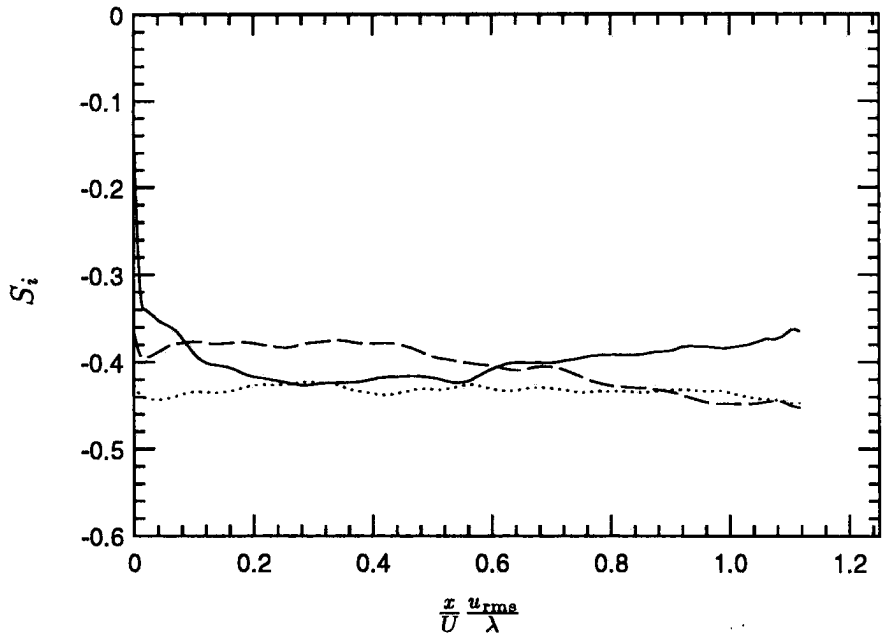


FIGURE C.6: Velocity derivative skewness in the spatial simulation of isotropic turbulence. —— $(S_1)$, ---- $(S_2)$, ····· $(S_3)$.

Fluctuations in velocity, density and pressure are superposed on the mean flow. These fluctuations are obtained from a separate temporal simulation of the shear flow. Details of the temporal simulation are described in Section C.3.1. Use of the temporal simulation to specify inflow turbulence is then discussed briefly in Section C.3.2.

## C.3.1 Temporal simulation of the shear flow

The governing equations are the compressible Navier Stokes equations. The computational mesh is uniform in all three directions. The sixth order Padé scheme and third order Runge Kutta scheme are used for spatial and temporal discretization respectively. Periodic boundary conditions are imposed in the $x$ and $z$ directions while 'sponge regions' are used to approximate non-reflecting boundary conditions at the $y$ boundaries. Details of the sponge are provided in Section 4.8.2. Essentially, a 'cooling' term of the form $-\sigma(\mathbf{U} - \mathbf{U}_{\text{ref.}})$ is added to the right-hand side of the governing equations over a region of width $\delta_{\text{sponge}}$ *near the top and bottom boundaries alone.* The coefficient $\sigma$ is defined to vary smoothly from 0 in the interior to a finite value at the boundary; *i.e.*, if $y_{\text{bot}} = -L_y/2 + \delta_{\text{sponge}}$ and $y_{\text{top}} = L_y/2 - \delta_{\text{sponge}}$ denote the start of the sponge near the bottom and top boundary respectively, then

$$\sigma_{\text{bot/top}} = A_s \left( \frac{|y - y_{\text{bot/top}}|}{\delta_{\text{sponge}}} \right)^n . \qquad (C.10)$$

The exponent $n$ is set to 3 in our calculations. Values used for the parameters $A_s$ and $\delta_{\text{sponge}}$ are listed in Table C.3. Typically, about 15 points are used in each of the two sponge regions. The reference state, $\mathbf{U}_{\text{ref}}$ is the mean flow specified in the initial conditions. The solution in the sponge region is thus forced towards the mean flow. As a result, in addition to giving the $y$ boundaries a non-reflecting character, the sponge regions ensure that the mean shear rate is essentially unchanged.

The initial mean flow is the same as that specified at the inflow of the spatial simulations; *i.e.*,

$$U(y) = U_0 + S(y + L_y/2), \qquad \overline{p}(y) = \frac{1}{\gamma}, \quad \overline{\rho}(y) = \frac{M_1^2}{U^2}. \qquad (C.11)$$

'Turbulent' fluctuations are then superposed onto the above mean flow. The fluctuating velocity field is specified to be isotropic and solenoidal. Initial fluctuations in

the thermodynamic variables are set to zero. The procedure used by Rogallo (1981) is used to generate the initial velocity field whose spectrum is specified to be,

$$E(k) = 16\sqrt{\frac{2}{\pi}}\frac{u_0^2}{k_0}\left(\frac{k}{k_0}\right)^4 \mathrm{e}^{-2\left(\frac{k}{k_0}\right)^2}. \qquad (C.12)$$

The variable $u_0$ determines the rms level of the signal. $k_0$ denotes the wavenumber corresponding to the peak of the spectrum and represents the dominant lengthscale of the turbulence. To ensure consistency with the sponge regions, the above velocity fluctuations are only specified over part of the domain in the $y$ direction. The velocity fluctuations (denoted by $u_i'$) are multiplied by a smooth function that varies from one in the interior to zero at the $y$ boundaries. The instantaneous initial velocity field is therefore given by

$$u_i = \overline{U}_i + \left\{\frac{\tanh[b(y + L_y/2 - \delta)] + \tanh[b(y - L_y/2 + \delta)]}{2}\right\}u_i' \qquad (C.13)$$

where the variables $b$ and $\delta$ are set to equal 10 and .75 respectively.

The initial conditions require specification of the following variables: $U_0, S, M$, $k_0, u_0$ and $Re$. The following non-dimensional parameters are taken into consideration in choosing the above variables (refer to figure C.7):

$$\left(\frac{\Delta U}{U}\right)_{\text{eddy}} = 2\frac{U_2 - U_1}{U_2 + U_1} = \frac{1}{U_1 + Sl/2}$$

$$\left(\frac{\Delta \rho}{\rho}\right)_{\text{eddy}} = 2\frac{M^2/U_2^2 - M^2/U_1^2}{M^2/U_2^2 + M^2/U_1^2} = \frac{1 + 2U_1/Sl}{(U_1/Sl)^2 + (U_1/Sl) + 1/2}$$

$$\frac{\tau_{\text{turbulence}}}{\tau_{\text{mean flow}}} = \frac{\lambda/u_{\text{rms}}}{1/S}$$

$$M_t = \frac{\sqrt{u_i'u_i'}}{\overline{c}} = M\frac{\sqrt{u_i'u_i'}}{U}$$

$$R_\lambda = \frac{\overline{\rho}u_{\text{rms}}\lambda_1}{\overline{\mu}}$$

Figure C.7 shows a sketch of an eddy in the initial turbulent field. The eddy is characterized by lengthscale $l$ in the $y$ direction. In the following discussion, we assume $l = 2\pi/k_0$. Also, subscripts 1 and 2 are used to denote the bottom and top of the eddy. With reference to figure C.7, the parameter, $(\Delta U/U)_{\text{eddy}}$ represents the fractional change in mean velocity across the eddy. $(\Delta U/U)_{\text{eddy}}$ is

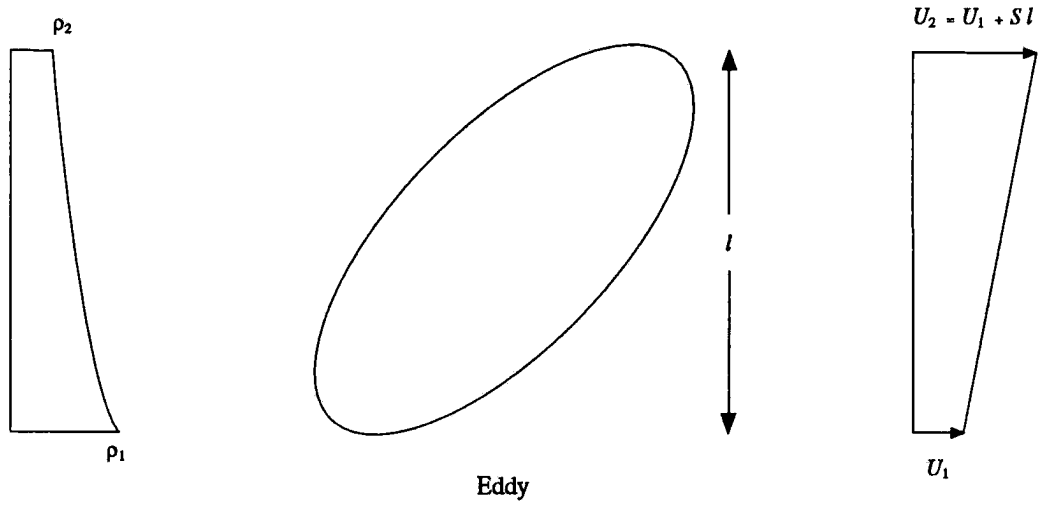


FIGURE C.7: Schematic of the mean gradients over an eddy in the turbulent shear flow.

required to be small if Taylor's hypothesis is to be applied to the above flow to generate inflow turbulence. Note that increasing $U_1$ and decreasing $S$ decreases the value of $(\Delta U/U)_{\text{eddy}}$. Similarly, the parameter, $(\Delta\rho/\rho)_{\text{eddy}}$ represents the fractional change in mean density across the eddy. It is readily seen from equation C.11 that $(\Delta\rho/\rho)_{\text{eddy}}$ is directly related to the fractional change in mean velocity. In turbulence at low $M_t$, the mean density gradient can influence the flow either through the inertial terms (inviscid mechanism), or through the associated gradient in Reynolds number across the eddy. The 'strength' of the turbulence with respect to the mean flow is represented by the parameter $S\lambda/u_{\text{rms}}$ - the ratio of turbulence to mean timescale. The linear 'rapid' limit is approached as $S\lambda/u_{\text{rms}}$ increases. Correspondingly, the effect of mean strain diminishes as $S\lambda/u_{\text{rms}}$ decreases. Finally, the fluctuation Mach number $M_t$ represents the extent to which compressibility might be significant in the flow.

The temporal simulation corresponding to the Mach 1.2 case is considered below. The relevant physical and computational parameters are first tabulated. Results are then presented and statistics of the turbulence specified at the inflow are documented.

The initial field is first generated. Two point correlations of the initial velocity field are checked to ensure that they decay to zero. The initial field is then advanced in time at a CFL number of 0.3. About 13000 timesteps are needed to advance

| $(L_x, L_y, L_z)$ | $(5\pi, 5\pi, 5\pi)$ | $(N_x, N_y, N_z)$ | $(121, 121, 121)$ |
|---|---|---|---|
| $U_0$ | 2 | $S$ | 0.2 |
| $M$ | 1.2 | $u_{\text{rms}}$ | 0.13 |
| $k_0$ | 5 | $Re$ | 2250 |
| $CFL$ | 0.3 | $\delta_{\text{sponge}}/L_y$ | 0.12 |
| $A_s$ | 5 | $(\Delta U/U)_{\text{eddy}}$ | 0.12 |
| $(\Delta\rho/\rho)_{\text{eddy}}$ | 0.24 | $S\lambda/u_{\text{rms}}$ | 0.62 |
| $(M_t)_{\text{centerline}}$ | 0.06 | $(R_\lambda)_{\text{centerline}}$ | 13 |

TABLE C.3: Parameters in the temporal simulation of the shear flow.

to a non-dimensional time of $St = 5.7$. Figure C.8 shows the temporal evolution of turbulent kinetic energy at the centerline ($y = 0$). Note that statistics are computed by averaging over $x$ and $z$. After decaying initially, $\overline{u'^2}$ and $\overline{w'^2}$ are seen to grow with time. Kinetic energy is seen to develop the ordering, $u_{\text{rms}} > w_{\text{rms}} > v_{\text{rms}}$ that is typical of incompressible two-dimensional shear flows (Townsend, 1976).

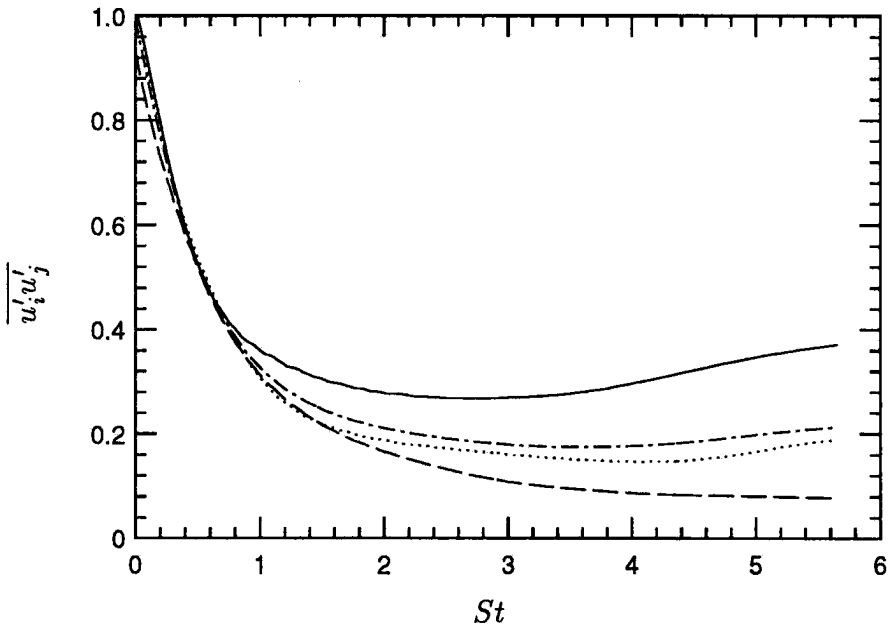


FIGURE C.8: Temporal evolution of turbulence intensities and kinetic energy at the centerline. —— $(\overline{u'^2}/\overline{u_0'^2})$, ---- $(\overline{v'^2}/\overline{u_0'^2})$, ····· $(\overline{w'^2}/\overline{u_0'^2})$, —·— $(q^2/3\overline{u_0'^2})$.

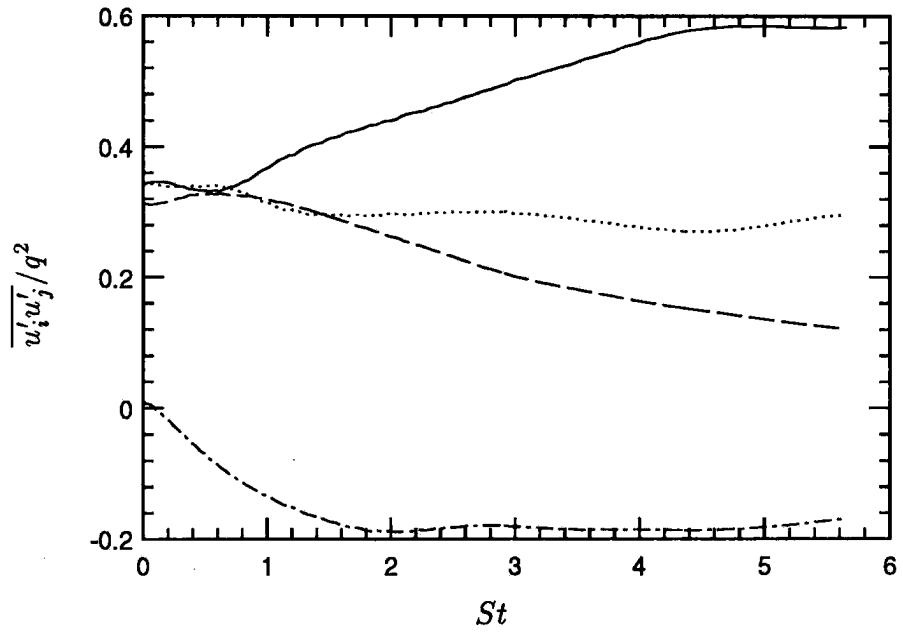


FIGURE C.9: Evolution of $\overline{u_i'u_j'}/q^2$ at the centerline. —— $(\overline{u'^2}/q^2)$, ---- $(\overline{v'^2}/q^2)$, ..... $(\overline{w'^2}/q^2)$, —·— $(\overline{u'v'}/q^2)$.

Also, the non-dimensional shear stresses, $\overline{u_i'u_j'}/q^2$ (figure C.9) develop values typically observed in incompressible shear flows such as the boundary layer and homogeneous shear flow (Moin, 1988). The intensity of temperature and density fluctuations at the centerline is seen to increase with time over the extent of the computation (figure C.10). As seen from figure C.10, $\rho_{\rm rms}/\overline{\rho}$ is very nearly equal to $T_{\rm rms}/\overline{T}$. Also, the intensity of pressure fluctuations is noticeably smaller than that of density and temperature. Note that if the thermodynamic fluctuations were isentropic, then $p_{\rm rms}/\gamma\overline{p} = \rho_{\rm rms}/\overline{\rho} = T_{\rm rms}/(\gamma-1)\overline{T}$. On the other hand, if the thermodynamic fluctuations were entropic in nature, then in the linear limit, $\rho'/\overline{\rho} = -T'/\overline{T}$ and $p' = 0$. The correlation coefficient between density and temperature fluctuations is plotted in figure C.11. The coefficient is seen to be very nearly equal to -1 for times exceeding $St = 0.3$. When combined with the relative intensities of the thermodynamic fluctuations, this suggests that the thermodynamic field is essentially composed of entropy fluctuations.

The thermodynamic field is strongly correlated with the velocity field. Figure C.12 shows the evolution of the velocity-temperature correlation at the centerline. $R_{u'T'}$ is seen to be strongly positive while $R_{v'T'}$ is strongly negative. The sign of $R_{u'T'}$ is opposite to that observed in adiabatic compressible boundary layers

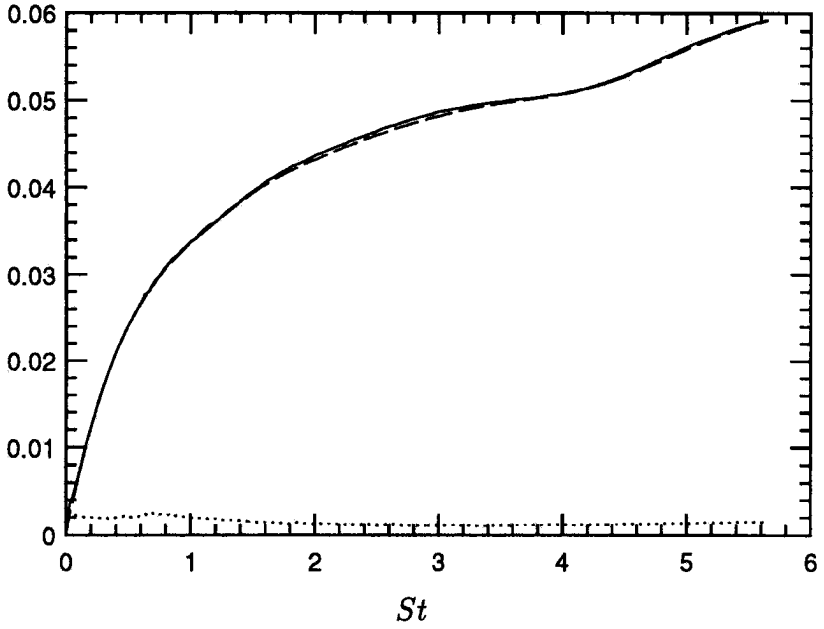


FIGURE C.10: Evolution of thermodynamic fluctuations at the centerline. —— $(\sqrt{\overline{\rho'^2}}/\overline{\rho})$, ---- $(\sqrt{\overline{T'^2}}/\overline{T})$, ····· $(\sqrt{\overline{p'^2}}/\gamma\overline{p})$.

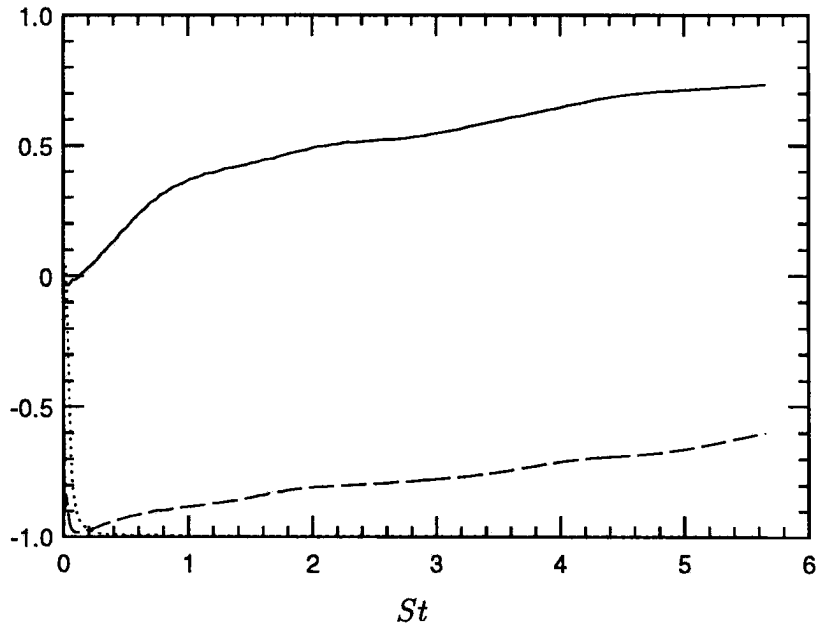


FIGURE C.11: Variation of the correlation of temperature with velocity and density at the center. —— $(\overline{u'T'}/\sqrt{\overline{u'^2}}\sqrt{\overline{T'^2}})$, ---- $(\overline{v'T'}/\sqrt{\overline{v'^2}}\sqrt{\overline{T'^2}})$, ····· $(\overline{\rho'T'}/\sqrt{\overline{\rho'^2}}\sqrt{\overline{T'^2}})$.

layers, where experiments and Morkovin's hypothesis show that $R_{u'T'} \sim -1$. It is easily shown that the reason for this difference is that $U$ and $\overline{T}$ both increase with $y$ in our flow as compared to the adiabatic boundary layer, where $\overline{T}$ decreases with $y$.

Since as seen above, the thermodynamic field is dominated by entropy fluctuations, the linearized equations governing the evolution of velocity and entropy fluctuations in the shear flow are examined below. These equations will be seen to predict the sign of the velocity temperature correlation observed in the simulations. The linearized continuity, momentum and energy equations are given by

$$\frac{\partial \rho'}{\partial t} + U\frac{\partial \rho'}{\partial x} = -v'\frac{\mathrm{d}\overline{\rho}}{\mathrm{d}y} - \overline{\rho}\theta'. \tag{C.14a}$$

$$\frac{\partial u'}{\partial t} + U\frac{\partial u'}{\partial x} = -v'\frac{\mathrm{d}U}{\mathrm{d}y} - \frac{1}{\overline{\rho}}\frac{\partial p'}{\partial x}. \tag{C.14b}$$

$$\frac{\partial v'}{\partial t} + U\frac{\partial v'}{\partial x} = -\frac{1}{\overline{\rho}}\frac{\partial p'}{\partial y}. \tag{C.14c}$$

$$\frac{\partial s'}{\partial t} + U\frac{\partial s'}{\partial x} = -v'\frac{\mathrm{d}\overline{s}}{\mathrm{d}y}. \tag{C.14d}$$

Using $\rho'/\overline{\rho} = -T'/\overline{T}$ and the equation of state yields the following equation for the temperature fluctuations:

$$\frac{\partial T'}{\partial t} + U\frac{\partial T'}{\partial x} = -v'\frac{\mathrm{d}\overline{T}}{\mathrm{d}y} + \overline{T}\theta'. \tag{C.15}$$

The equation for temperature fluctuations may be combined with the momentum equations to obtain the following equations for the velocity-temperature correlation.

$$\frac{\partial}{\partial t}\overline{v'T'} + U\underbrace{\frac{\partial}{\partial x}\overline{v'T'}}_{0} = \underbrace{-\overline{v'^2}\frac{\mathrm{d}\overline{T}}{\mathrm{d}y}}_{\text{negative}} + \underbrace{\overline{Tv'\theta'} - \frac{1}{\overline{\rho}}\overline{T'\frac{\partial p'}{\partial y}}}_{\text{neglect}}. \tag{C.16a}$$

$$\frac{\partial}{\partial t}\overline{u'T'} + U\underbrace{\frac{\partial}{\partial x}\overline{u'T'}}_{0} = \underbrace{-\overline{u'v'}\frac{\mathrm{d}\overline{T}}{\mathrm{d}y}}_{\text{positive}} \underbrace{-\overline{v'T'}\frac{\mathrm{d}U}{\mathrm{d}y}}_{\text{positive}} + \underbrace{\overline{Tu'\theta'} - \frac{1}{\overline{\rho}}\overline{T'\frac{\partial p'}{\partial x}}}_{\text{neglect}}. \tag{C.16b}$$

The 'production' terms in the above equations show the dependence of the sign of the velocity-temperature correlation on the mean gradients. Note that terms associated with $p'$ and $\theta'$ are assumed small as suggested by the computations.

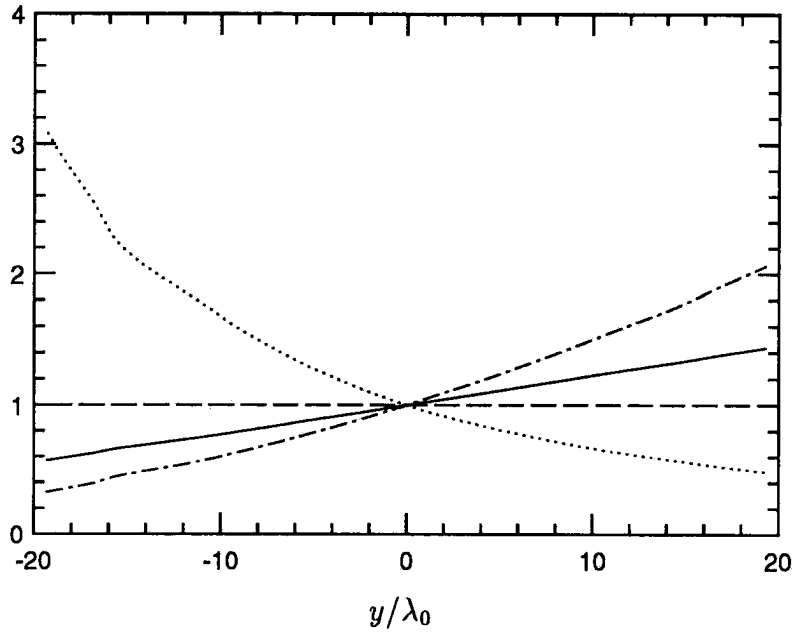


FIGURE C.12: Profiles of the mean flow at $St = 4.58$. All curves are normalized by their values at the centerline. ——— $(U)$, - - - - $(\overline{P})$, ····· $(\overline{\rho})$, —·— $(\overline{T})$.

An instantaneous field from the computation is used to generate inflow turbulence in the spatial simulation with the Mach 1.2 shock wave. The field at $St = 4.58$ is chosen for this purpose. Statistics from this instantaneous realization are presented in detail below. Figure C.12 shows profiles of the mean flow at $St = 4.58$. Note that the mean pressure is very nearly uniform. The maximum deviation of the mean pressure from its value at the centerline is 0.06%. Although not plotted, the mean vertical component of velocity was checked and seen to be 4 orders lower than $U$.

Profiles of turbulent kinetic energy are shown in figure C.13. As expected, kinetic energy levels near the boundary are negligible due to the sponge regions. The profile of $\overline{u'^2}$ suggests that the transverse inhomogeneity introduced at the outer edge of the turbulent region extends until about $y/\lambda_0 = \pm 12$. As a result, we focus on the 'core region' extending from $-12 \leq y/\lambda_0 \leq 12$. Subsequent plots only show this core region. The kinetic energy is seen to be inhomogeneous over this region; figure C.13 shows that kinetic energy decreases with increasing $y$. This trend is consistent with the Reynolds number decreasing with increasing $y$. Although kinetic energy decreases with $y$, the non-dimensional Reynolds stresses $\overline{u_i' u_j'}/q^2$ are nearly uniform as shown in figure C.14.

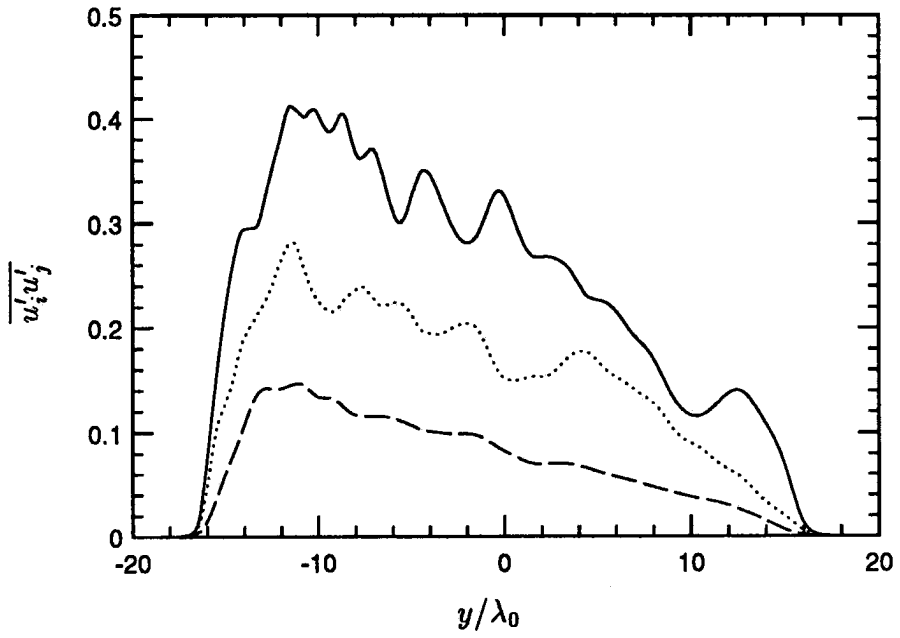


FIGURE C.13: Profiles of kinetic energy at $St = 4.58$. —— $(\overline{u'^2}/\overline{u_0'^2})$, ---- $(\overline{v'^2}/\overline{u_0'^2})$, ..... $(\overline{w'^2}/\overline{u_0'^2})$.

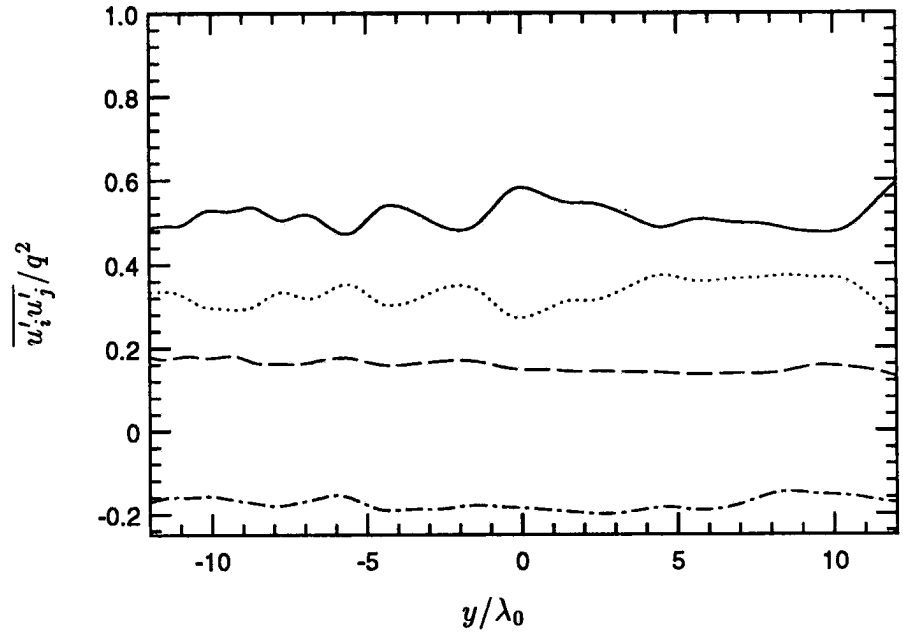


FIGURE C.14: Profiles of $\overline{u_i'u_j'}/q^2$ at $St = 4.58$. —— $(\overline{u'^2}/q^2)$, ---- $(\overline{v'^2}/q^2)$, ..... $(\overline{w'^2}/q^2)$, —·— $(\overline{u'v'}/q^2)$.

Profiles of the thermodynamic fluctuations and their correlation with the velocity field are shown in figures C.15 and C.16 respectively. As previously observed at the centerline, the intensity of pressure fluctuations is noticeably smaller than that of density and temperature. Also, $\rho_{\rm rms}/\overline{\rho}$ is very nearly equal to $T_{\rm rms}/\overline{T}$. The intensities of density and temperature are seen to decrease with increasing $y$. While variaton of Reynolds number across the mean streamlines might partially be responsible, it can be shown that the observed trend is consistent with the variation of $\mathrm{d}\overline{\rho}/\mathrm{d}y$ with $y$.

As seen from equations C.14, the primary source of thermodynamic fluctuations is the stirring of the mean gradients by the turbulent velocity field. As a result, a mixing length argument is used to explain the observed profiles of density and temperature. Denoting the mixing length by $\eta$, we have $\rho' = -\eta \mathrm{d}\overline{\rho}/\mathrm{d}y$. Using equation C.11 to express $\overline{\rho}$ in terms of $U$, yields the following expression:

$$\frac{\rho'}{\overline{\rho}} = 2\eta \frac{S}{U}, \qquad (C.17)$$

which shows that the intensity of density fluctuations decreases with increasing $y$ if $\eta$ is independent of $y$. Similar to $\overline{u_i' u_j'}/q^2$, the velocity temperature correlation is nearly uniform across streamlines. Also, the correlation coefficient between density and temperature fluctuations is nearly -1 on all streamlines in the core region.

The fidelity of the solution is examined in figures C.17 and C.18 respectively. One-dimensional spectra (in the $z$ direction) of density and velocity fluctuations (computed with respect to the instantaneous mean) at the centerline are plotted in figure C.17. The spectra show about 8 decades of decay, indicating adequate resolution. Although not shown, spectra on the other streamlines were also examined and found acceptable. In particular the spectra on the lower streamlines were examined on account of their higher Reynolds number. About 6 decades of decay was observed.

Since mean shear increases the turbulence lengthscales, the turbulent eddies could outgrow the computational domain at large times. Since the streamwise lengthscale is the largest, two-point correlations of the density and velocity field in the streamwise direction are examined to check for adequacy of the domain size. The correlations computed at the centerline are plotted in figure C.18. The magnitude of the correlation is seen to drop to acceptably small levels inside the domain indicating that the domain size is adequate.

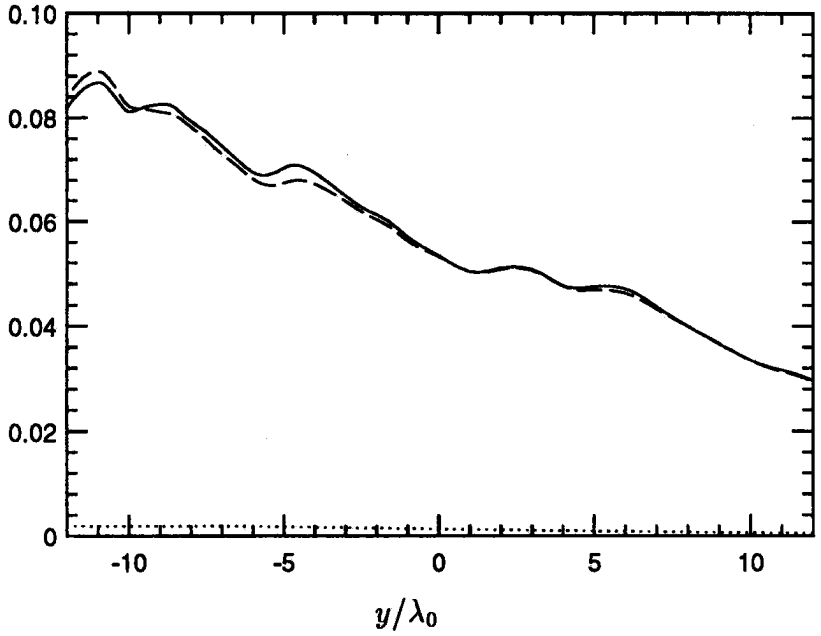


FIGURE C.15: Profiles of thermodynamic fluctuations at $St = 4.58$. —— $(\sqrt{\overline{\rho'^2}}/\overline{\rho})$, ---- $(\sqrt{\overline{T'^2}}/\overline{T})$, ····· $(\sqrt{\overline{p'^2}}/\gamma\overline{p})$.

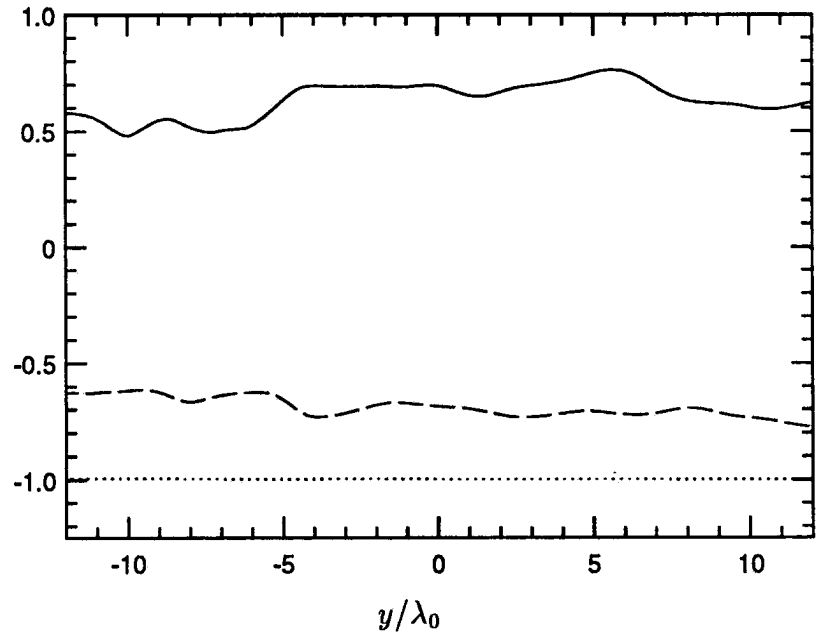


FIGURE C.16: Profiles of the correlation of temperature with velocity and density at $St = 4.58$. —— $(\overline{u'T'}/\sqrt{\overline{u'^2}}\sqrt{\overline{T'^2}})$, ---- $(\overline{v'T'}/\sqrt{\overline{v'^2}}\sqrt{\overline{T'^2}})$, ····· $(\overline{\rho'T'}/\sqrt{\overline{\rho'^2}}\sqrt{\overline{T'^2}})$.

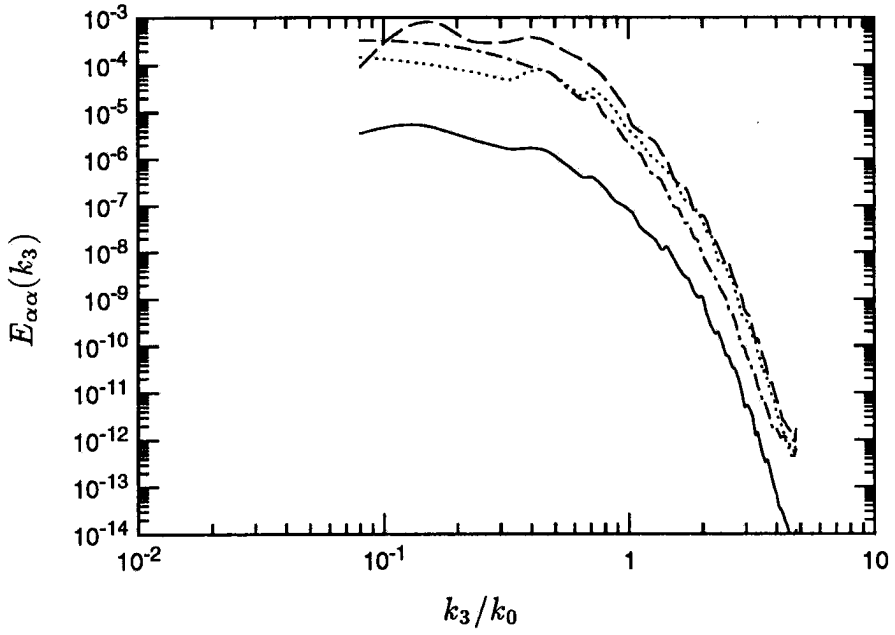


FIGURE C.17: One-dimensional energy spectra at $St = 4.58$. —— $(E_{\rho\rho})$, ---- $(E_{uu})$, ····· $(E_{vv})$, —·— $(E_{ww})$.

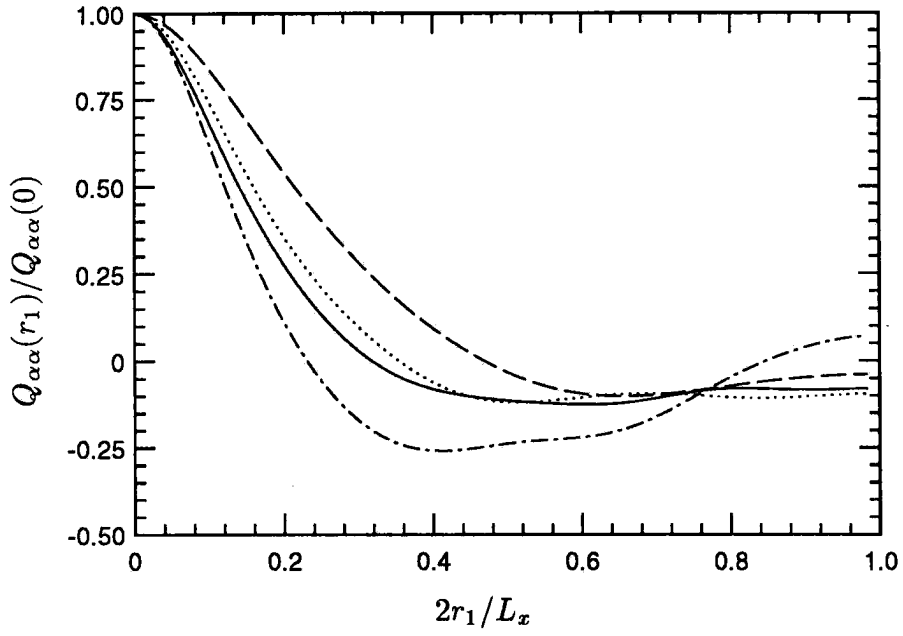


FIGURE C.18: Normalized streamwise two point correlation at $St = 4.58$. —— $(Q_{\rho\rho})$, ---- $(Q_{uu})$, ····· $(Q_{vv})$, —·— $(Q_{ww})$.

## C.3.2 Spatial simulation of the shear flow

As mentioned above, the instantaneous field at $St = 4.58$ is used to generate inflow turbulence in the spatial simulation. The procedure is similar to that discussed in Section C.2. The only significant differences are that the fluctuations are only Fourier transformed in $x$ and $z$ and that the convection velocity is the mean velocity at the center of the domain. Use of a constant convection velocity is needed to ensure that the correlation of the turbulence in the $y$ direction is preserved. However, since turbulent fluctuations are (over small distances) convected by the *local* mean velocity, this will set up streamwise gradients at the inflow. The magnitude of these gradients is determined by the extent to which the mean velocity is uniform over a typical eddy lengthscale in the $y$ direction; *i.e.*, the parameter $(\Delta U/U)_{\text{eddy}}$ is required to be small to reduce transients due to the mean shear. The relevant statistics of the turbulence upstream of the shock wave are documented in Chapter 5 and are not repeated here. Similar to spatially decaying turbulence (section C.2), the inflow disturbances develop statistics similar to the temporal simulation after a small transient.

# Appendix D

# Influence of Entropy Fluctuations on Shock / Turbulence Interaction: Direct Numerical Simulation

Chapter Three used linear analysis to quantify the role of entropy fluctuations on the evolution of a turbulent flow across a shock wave. This appendix considers direct numerical simulation of the problem: *i.e.*, the interaction of a normal shock wave with isotropic turbulence. The appendix is organized as follows. An introduction to the computation is first provided in Section D.1. Section D.2 discusses the relevant numerical details; emphasis is placed upon the inflow and outflow boundary conditions. Results from the simulations are then presented in Section D.3.

## D.1 Introduction

A schematic of the computed flow is shown in Figure D.1. Note that the mean flow upstream of the shock wave is spatially uniform. Also, the shock wave is stationary in the mean. The coordinate system is chosen such that $x$ denotes the streamwise or shock-normal direction, while $y$ and $z$ denote the directions transverse to the mean shock wave. The turbulence upstream of the shock wave is isotropic. The role of upstream entropy fluctuations is examined by performing two different simulations for the same mean Mach number of the shock. In one computation, the upstream turbulence is essentially composed of vortical fluctuations while in the second computation, the upstream turbulence comprises of vorticity and entropy fluctuations that approximately satisfy Morkovin's hypothesis. Contrasting the two calculations allows the role of entropy fluctuations to be studied.

The governing equations are the unsteady, three-dimensional, compressible Navier Stokes equations in the following conservative, non-dimensional form:

$$\frac{\partial \rho}{\partial t} = -\frac{\partial}{\partial x_i}(\rho u_i) \qquad (D.1a)$$

$$\frac{\partial}{\partial t}(\rho u_i) = -\frac{\partial}{\partial x_j}(\rho u_i u_j + p\delta_{ij}) + \frac{\partial \tau_{ij}}{\partial x_j} \qquad (D.1b)$$

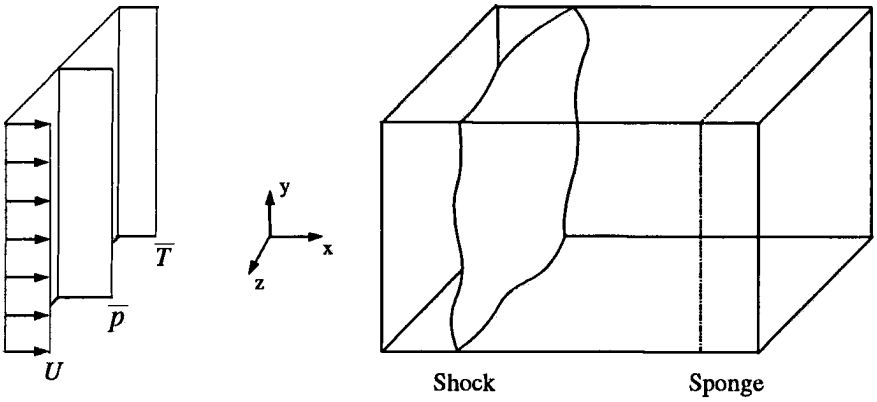


FIGURE D.1: Schematic of the numerical simulation.

$$\frac{\partial E_t}{\partial t} = -\frac{\partial}{\partial x_i}[(E_t + p)u_i] - \frac{\partial q_i}{\partial x_i} + \frac{\partial}{\partial x_j}(u_i \tau_{ij}). \qquad (D.1c)$$

The viscous stress tensor and heat flux vector are given by

$$\tau_{ij} = \frac{\mu}{Re}\left(\frac{\partial u_i}{\partial x_j} + \frac{\partial u_j}{\partial x_i} - \frac{2}{3}\frac{\partial u_k}{\partial x_k}\delta_{ij}\right),$$

$$q_i = -\frac{\mu}{RePr}\frac{\partial T}{\partial x_i}. \qquad (D.2)$$

The variable $E_t$ denotes the total energy, defined as, $E_t = p/(\gamma - 1) + \rho u_i u_i/2$. Note that the mean sound speed, density and dynamic viscosity at the inflow of the domain are used to non-dimensionalize velocity, density and viscosity respectively. The reference lengthscale, $L_r$ is arbitrary and is related to the other reference variables by, $Re = \rho_r c_r L_r/\mu_r$. The fluid is assumed to be an ideal gas with 1.4 as the ratio of specific heats. Dynamic viscosity is related to temperature by a power law with 0.76 being the exponent, and the Prandtl number is assigned a constant value of 0.7.

The computational mesh is uniform in the directions transverse to the shock wave. A non-uniform mesh is used in the streamwise direction, such that points are clustered in the vicinity of the shock. The following analytical mapping is used for this purpose. Using the variable $s$ to denote a uniform mesh from 0 to $L_x$, the

non-uniform mesh is given by

$$\frac{x}{L_x} = \frac{rs + \left(\frac{r-d}{2b}\right) \ln\left[\frac{\cosh b(s-3c/2)\cosh bc/2}{\cosh b(s-c/2)\cosh 3bc/2}\right]}{r + \left(\frac{r-d}{2b}\right) \ln\left[\frac{\cosh b(1-3c/2)\cosh bc/2}{\cosh b(1-c/2)\cosh 3bc/2}\right]}. \qquad (D.3)$$

Typical values for $b, r, d$ and $c$ are 12, 1.95, 0.04 and 0.281 respectively.

A combination of the sixth order Pade scheme (Lele, 1992b) and the sixth order ENO scheme (Shu & Osher 1988, 1989) is used to compute spatial derivatives. The shock-capturing scheme (ENO) is applied only in the streamwise (shock-normal) direction in the vicinity of the shock wave. The sixth order Pade scheme is therefore used to compute all spatial derivatives except the streamwise inviscid fluxes around the shock: the ENO scheme is used to compute those terms. Time advancement is performed using the compact-storage, third order Runge Kutta scheme (Wray, 1986). Since the turbulence is statistically homogeneous transverse to the shock wave, periodic boundary conditions are imposed in those directions. Turbulent fluctuations are superposed onto the mean field at the inflow boundary while non-reflecting boundary conditions are specified at the exit through use of a 'sponge' zone. Details of the inflow and outflow boundary conditions are provided below.

## D.2.1 Inflow turbulence

Since flow upstream of the shock wave is supersonic, all flow variables are specified at the inflow boundary. Turbulent fluctuations in velocity, density and pressure are superposed on the uniform mean flow. These turbulent fluctuations are obtained from a single realization of a separate temporal simulation of decaying turbulence. The temporal simulation (which has periodic boundary conditions in all three directions) is advanced in time until the flow field is developed *i.e.*, the velocity derivative skewness $S_\alpha = \overline{u'^3_\alpha}/[\overline{(\frac{\partial u'_\alpha}{\partial x_\alpha})^2}]^{3/2}$ attains (Tavoularis, Bennett & Corrsin, 1978; Erlebacher *et al.*, 1992) a value between -0.4 and -0.6. Typically this happens after a time, $t \sim \lambda/u_{\rm rms}$. Taylor's hypothesis is then invoked, to convect a single realization of the developed field into the inflow of the spatial simulation. Details of this procedure are described in Appendix C.

The simulations with the shock wave compare two different cases at each Mach number. The two cases differ in the nature of turbulence upstream of the shock wave. While upstream turbulence in one case, (case A) is essentially composed of

vortical fluctuations, a combination of vorticity and entropy fluctuations is present in the other (case B). The upstream entropy field in the second case is required to approximately satisfy the weak form of Morkovin's hypothesis *i.e.*, equation 3.1 is satisfied in the r.m.s. sense. To further ensure that the inflow spectra and r.m.s levels of velocity in both cases are essentially the same, the inflow turbulence in both cases is obtained from the same temporal calculation.

This is done as follows. A temporal simulation of isotropic turbulence is conducted where the initial velocity field has the spectrum $E(k) \sim k^4 e^{-2k^2/k_0^2}$ and zero thermodynamic fluctuations. This simulation is advanced until velocity derivative skewness reaches its developed value. An instantaneous developed flow field is then taken. The thermodynamic fluctuations in this field are nearly isentropic. To generate a realistic flow field of vorticity and entropy fluctuations, the following procedure is carried out. Pressure fluctuations in the stored flow field are set to zero while density fluctuations that satisfy $\rho'/\overline{\rho} = (\gamma - 1)M_{\text{spat.}}^2 u'/U_{\text{spat.}}$ are specified (the subscript spat. denotes spatial). This modified field is then advanced in time. Statistics from the simulation are compared to a parallel simulation where the field without the above modifications is advanced for the same length of time.

As expected from Kovasznay's (1953) modal decomposition, the entropy fluctuations that are introduced do not significantly influence the velocity field. After a brief acoustic transient ($t \sim M_t \lambda/u_{\text{rms}}$), the decay rate of kinetic energy and velocity derivative skewness match that obtained in the simulation without entropy fluctuations. However as expected, the entropy fluctuations decay with time and exhibit increasing deviation from Morkovin's hypothesis. To ensure that the weak formulation of the hypothesis is approximately satisfied by the upstream turbulence, an instantaneous realization is taken immediately after the acoustic transient and used to specify inflow turbulence for case B. A realization at exactly the same instant of time is taken from the temporal simulation without entropy fluctuations and used to specify inflow turbulence in case A.

Consider for example, the temporal simulation used to generate inflow turbulence in the simulation of a Mach 1.29 shock wave interacting with a turbulent flow. The initial velocity field is chosen to have fluctuation Mach number $M_t = \sqrt{q^2}/\overline{c} = 0.22$ and microscale Reynolds number $R_\lambda = u_{\text{rms}}\lambda/\overline{\nu} = 39.5$. A uniform mesh of $81^3$ points is used on a domain of length $2\pi$ in all three directions. The solution is advanced for a period of time, $t = 1.58\tau_t$, where $\tau_t$ is a turbulence

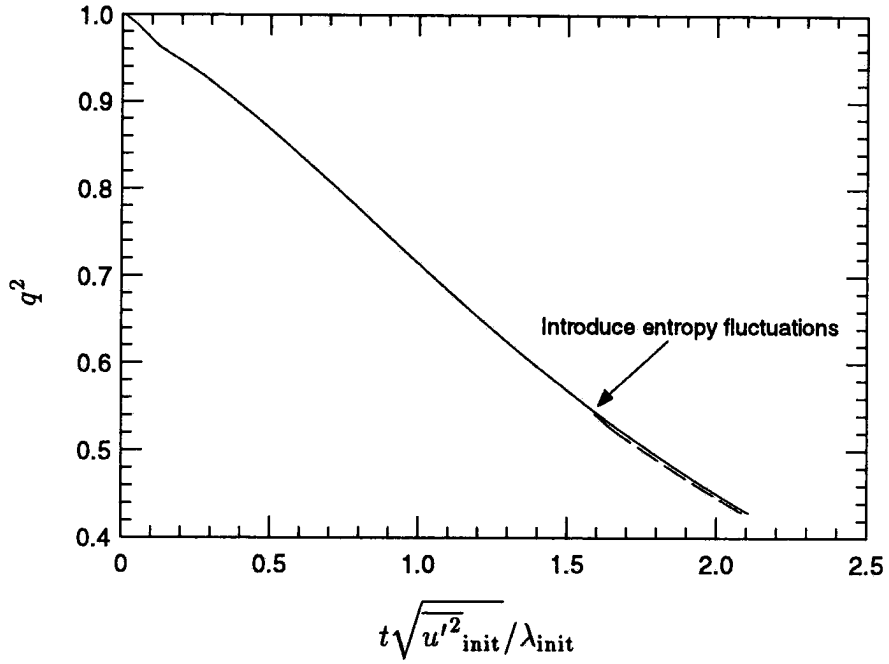


FIGURE D.2: Temporal evolution of turbulence kinetic energy in the decay of isotropic turbulence. ——— (without entropy fluctuations), ---- (with entropy fluctuations).

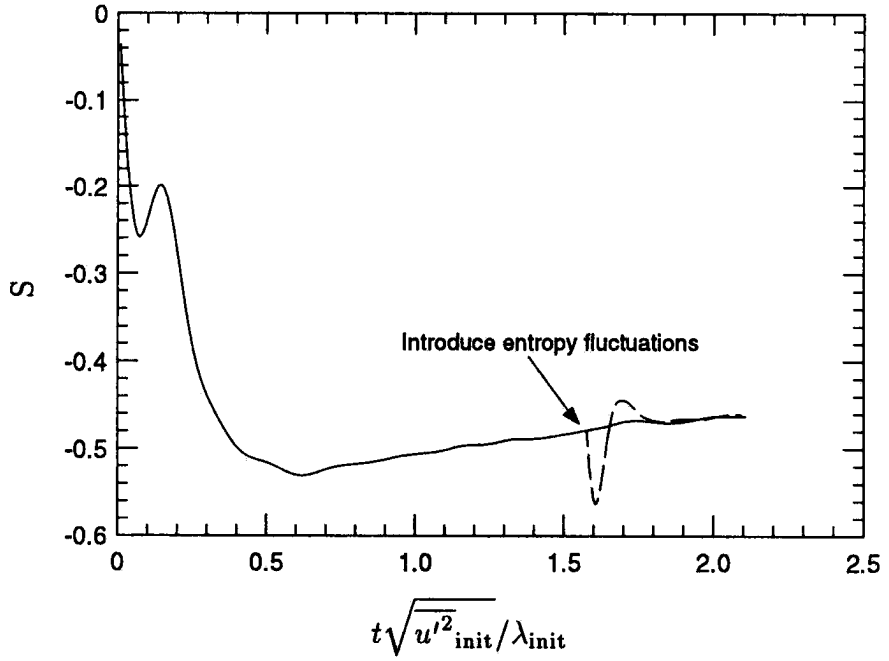


FIGURE D.3: Temporal evolution of velocity derivative skewness in the temporal decay of isotropic turbulence. ——— (without entropy fluctuations), ---- (with entropy fluctuations).

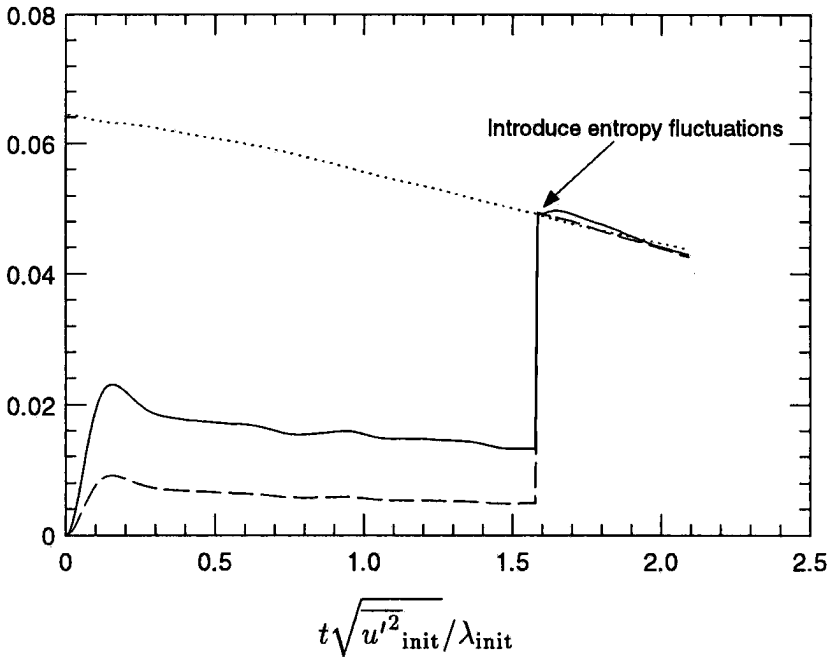


FIGURE D.4:Temporal evolution of r.m.s values of terms in Morkovin's hypothesis in the temporal decay of isotropic turbulence. —— $(\rho_{\text{rms}}/\overline{\rho})$, ---- $(T_{\text{rms}}/\overline{T})$, ····· $([\gamma - 1]M^2_{\text{spat}}u_{\text{rms}}/U_{\text{spat}})$.

time-scale, defined as the ratio of $\lambda$ to $u_{\text{rms}}$ at $t = 0$. As shown in figure D.3, the velocity derivative skewness has attained a value of $-0.48$ by this time. Also, $M_t$ and $R_\lambda$ have dropped to 0.16 and 22.8 respectively.

The solution at the end of the run is then modified to introduce entropy fluctuations as described above. The resulting field is then advanced in time. The temporal evolution of the velocity derivative skewness is compared in figure D.3 to a parallel simulation, where the stored field without any modifications is advanced for the same period of time. After a brief acoustic transient, the skewness is observed to have the same value as the simulation without entropy fluctuations. The temporal evolution of the r.m.s values of the terms in Morkovin's hypothesis in the simulation with entropy fluctuations are shown in figure D.4. The deviation from Morkovin's hypothesis is seen to increase with time. At the end of the simulation the weak form of the hypothesis is approximately satisfied; $\rho_{\text{rms}}/\overline{\rho}, T_{\text{rms}}/\overline{T}$ and $(\gamma-1)M^2_{\text{spat}}u_{\text{rms}}/U$ have values of 0.043, 0.043 and 0.044 respectively. By comparison, $p_{\text{rms}}/\gamma\overline{p}$ is 0.01. Also, $M_t$, $R_\lambda$ and $\theta_{\text{rms}}/\omega_{\text{rms}}$ have values of 0.14, 20.6 and 0.085 respectively; *i.e.*, the solution is dominated by vorticity and entropy fluctuations that approximately

satisfy Morkovin's hypothesis.

The solution at the end of the two runs shown in figures D.3 and D.4 is used to specify inflow turbulence in the spatial simulation involving the shock wave. The fidelity of the temporal simulation is checked by examining energy spectra and two-point correlations of the flow field. One-dimensional spectra of the velocity field show very good agreement between the two cases. The spectra show about five decades of drop-off indicating adequate resolution. Also, two point correlations of the velocity and density field drop off to zero indicating adequate size of computational domain.

## D.2.2 Outflow boundary condition

Approximately non-reflecting boundary conditions are specified at the subsonic outflow boundary. The boundary conditions comprise of a 'sponge layer' in the streamwise direction, followed by a characteristics-based boundary condition (Poinsot & Lele, 1992) at the outflow plane. Boundary conditions involving a sponge layer have been used in the past in a variety of problems: e.g. Givoli (1991), Israeli & Orszag (1981), Colonius, Moin & Lele (1995). The boundary conditions with a sponge were shown (Colonius *et al.*) to yield significantly better results than boundary conditions without the sponge layer.

Accordingly, a 'cooling term' of the form, $-\sigma(\mathbf{U} - \mathbf{U}_{\text{ref}})$ is added to the right-hand side of the governing equations *over the sponge layer alone.* $\mathbf{U}_{\text{ref}}$ denotes the vector of reference variables towards which the solution in the sponge layer is forced. It is obtained from the Rankine-Hugoniot equations for a laminar shock. The coefficient $\sigma(x)$ is a polynomial function; i.e.

$$\sigma(x) = A_s \frac{(x - x_s)^n}{(L_x - x_s)^n} \tag{21}$$

where, $x_s$ and $L_x$ denotes the start of the sponge and the length of the domain respectively. Typical values of $A_s$, $n$ and $(L_x - x_s)/L_x$ used in our simulations are 5, 3 and 0.14 respectively.

The performance of the outflow boundary conditions is illustrated by computing the interaction of a Mach 1.29 shock wave with a plane vorticity-entropy wave, that is incident at 45° from upstream. The ability of the boundary conditions to handle the downstream propagating waves (as predicted by linear analysis) is thus tested. The mean flow parameters, streamwise domain and grid are the same as the

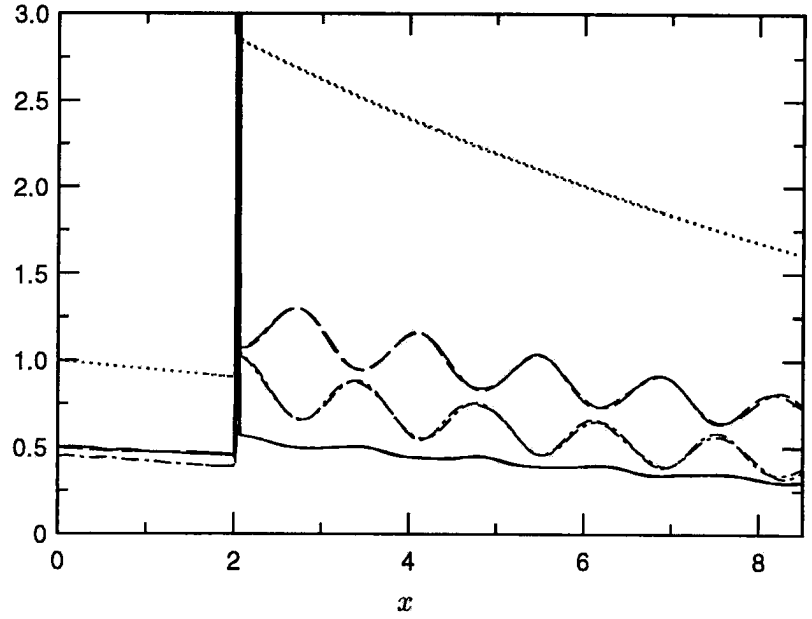


FIGURE D.5:. Spatial evolution of statistics from computation of the interaction of a Mach 1.29 shock wave with a plane vorticity-entropy wave. Results from short and long domain are both plotted. ——— $(\overline{u'^2}/q_{\text{in}}^2)$, ---- $(\overline{v'^2}/q_{\text{in}}^2)$, ····· $(\overline{\omega'^2}/\overline{\omega_{\text{in}}'^2})$, —·— $(\frac{\overline{\rho'^2}}{\overline{\rho_2}^2}/\frac{q_{\text{in}}^2}{\overline{U_1}^2})$. The subscript 'in' denotes inflow.

corresponding turbulent simulation. The extent of the domain in $y$ is set to equal one wavelength of the incident disturbance. A mesh of 231 by 16 points is used to discretize the flow.

The disturbance at the inflow boundary is given by the real part of equation 3.2, where the variables $k, \psi_1, A_v$ and $A_e$ are set to equal 5, 45°, 0.05 and 0.05 respectively. The computation is initialized by a numerically computed steady laminar shock. The disturbance field is then introduced at the inflow boundary. Results are then gathered over each period of the inflow disturbance after one domain flow-through time. The results from successive periods are compared to check if initial transients persist. After a time $\overline{U_1}t/L_x = 3.5$, the transient effects are found negligible and the results have converged.

To evaluate the outflow boundary conditions, the same flow is computed on a domain twice as long behind the shock wave. 1100 points are used in the streamwise direction. The resulting resolution is greater than that in the shorter domain. Results from the two simulations are then compared to each other and linear analysis. Figure D.5 shows the streamwise evolution of kinetic energy, vorticity and

| | Case 1.29A | Case 1.29B |
|---|---|---|
| $M_1$ | 1.29 | 1.29 |
| $R_\lambda$ | 19.1 | 19.1 |
| $M_t$ | 0.14 | 0.14 |
| $\sqrt{q^2}/\overline{U_1}$ | 0.11 | 0.11 |
| $\rho_{\rm rms}/\overline{\rho_1}$ | 0.012 | 0.042 |
| $T_{\rm rms}/\overline{T_1}$ | 0.0042 | 0.041 |
| $p_{\rm rms}/\gamma\overline{P_1}$ | 0.011 | 0.010 |
| $(N_x, N_y, N_z)$ | (231, 81, 81) | (231, 81, 81) |

TABLE D.1: Parameters of the numerical simulations.

density fluctuations in the two computations. Only the 'useful region' $(L_x - x_s)$ of the shorter domain is shown. Good agreement between the two computations is observed, indicating that the non-reflecting nature of the outflow region is acceptable. Some influence of the sponge region (maximum value about 3.5%) on the statistics of $\overline{v'^2}$ and $\overline{\rho'^2}$ is observed immediately upstream of the sponge.

Comparison of the *spatial evolution* of the statistics to inviscid linear analysis is not performed, due to significant viscous decay in the computation. However, the amplification of statistics immediately across the shock wave is compared to that from analysis. Such comparison shows that the error (computed with respect to analysis) in $\overline{u'^2}, \overline{v'^2}, \overline{\omega'^2}$ and $\overline{\rho'^2}$ is 0.8%, 1.6%, 0.8% and 0.5% respectively. Note that in computing shock/turbulence interaction, the fraction of incident waves that lie in the propagating regime pose the primary challenge to outflow boundary conditions. Performance of the outflow boundary for the incidence angle of 45°, suggests that the boundary conditions are quite adequate for the turbulent simulations.

## D.2.3 Simulations performed

The relevant parameters of the turbulent simulations are tabulated in Table D.1. The quoted values of all quantities are those at the inflow. Essentially, the simulations consider the interaction of low Reynolds number turbulence with a Mach 1.29 shock wave. Note that one of the compression-corner experiments (freestream

Mach number 2.9, wedge angle 8°) of Smits and Muck (1987) yields a normal Mach number of 1.29 if one assumes that the entire flow is turned across a single shock.

## D.3 Results

Turbulence statistics are computed by averaging over time and the $y-$ and $z-$ directions. As shown in figure D.6, the mean flow exhibits behavior similar to that observed by Lee *et al.* (1992). The ratios of mean velocity, temperature and pressure across the shock wave are very nearly equal to their corresponding laminar values. An overshoot in pressure and temperature is observed immediately downstream of the shock wave. The mean velocity exhibits a corresponding undershoot, following which, it remains practically constant. However, mean pressure and temperature exhibit a small positive gradient behind the shock wave. The presence of upstream entropy fluctuations has no noticeable effect on the mean flow on both sides of the shock wave. Entropy fluctuations do however, influence the apparent thickness of the shock wave as inferred from the mean flow profiles. The 'mean shock thickness' is larger in the presence of entropy fluctuations; *i.e.*, the mean gradients in the vicinity of the shock are smaller. Given that the 'mean shock thickness' reflects the amplitude of shock oscillation, this indicates an increase in shock motion when the upstream fluctuations satisfy the SRA.

### D.3.1 Turbulence kinetic energy

The presence of upstream entropy fluctuations has a noticeable effect on the evolution of turbulence kinetic energy across the shock wave. Figure D.7 shows the streamwise evolution of turbulence kinetic energy in cases 1.29A and 1.29B. Note that $\overline{v'^2} = \overline{w'^2}$ behind the shock wave due to axisymmetry. The intermittency associated with shock oscillation is seen to cause high fluctuation levels in the vicinity of the shock (Debieve & Lacharme, 1986; Lee *et al.*, 1992) The width of this intermittent region (denoted by $\delta_{\text{inter.}}$) nearly equals the 'mean shock thickness'. Using the mean velocity profile to determine its value, $k_0\delta_{\text{inter.}}$ is approximately 0.3 and 0.4 in cases 1.29A and 1.29B respectively. We focus our attention on the evolution of kinetic energy outside of this intermittent region in the following paragraphs.

As shown in figure D.7, kinetic energy levels behind the shock wave are noticeably higher in case 1.29B. The streamwise component is affected more than the transverse components. Comparison of the peak in the profile of $\overline{u'^2}$ (at $k_0x = 14$) reveals 20% higher levels in case 1.29B. Comparison of $\overline{v'^2}$ at the same location

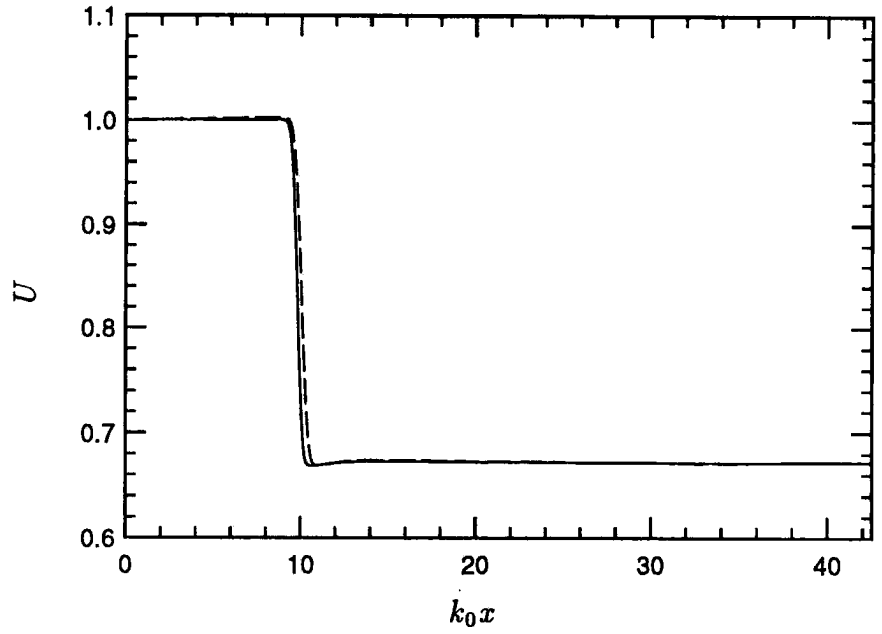


FIGURE D.6a: Streamwise variation of mean velocity. ——— (without entropy fluctuations), ---- (with entropy fluctuations).

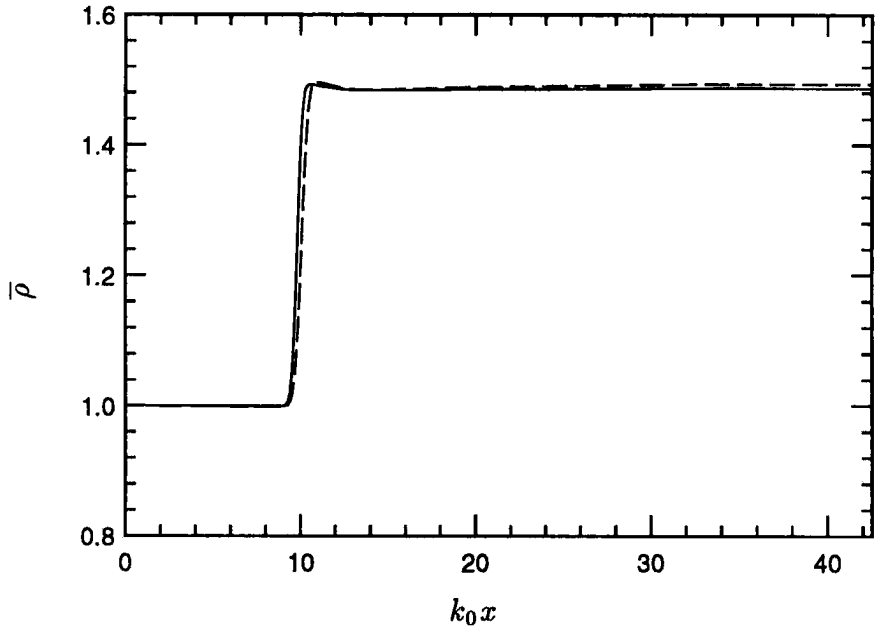


FIGURE D.6b: Streamwise variation of mean density. ——— (without entropy fluctuations), ---- (with entropy fluctuations).

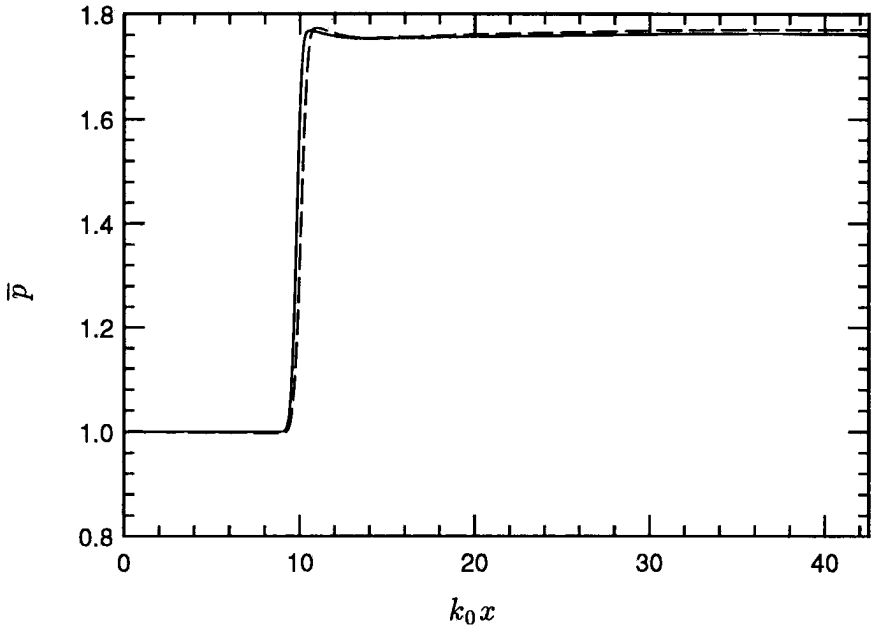


FIGURE D.6c: Streamwise variation of pressure. —— (without entropy fluctuations), ---- (with entropy fluctuations).

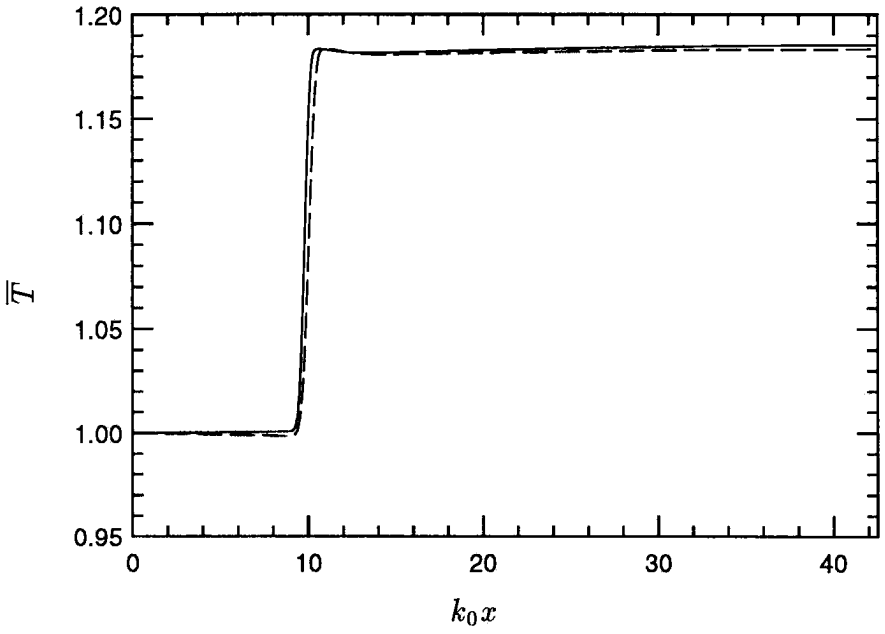


FIGURE D.6d: Streamwise variation of mean temperature. —— (without entropy fluctuations), ---- (with entropy fluctuations).

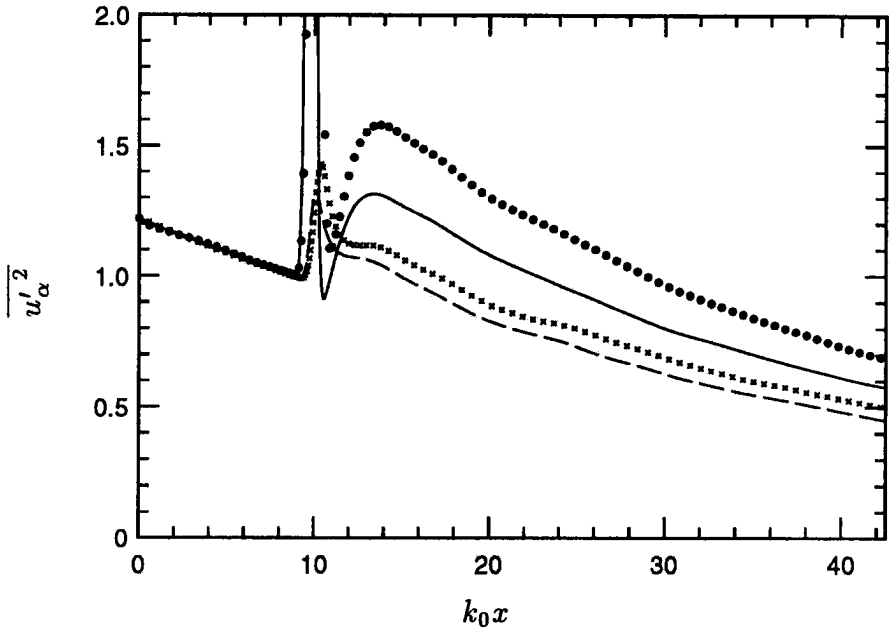


FIGURE D.7: Turbulent kinetic energy from DNS of the Mach 1.29 shock wave. All the curves are normalized by their value immediately upstream of the shock ($k_0 x = 8.97$). ——— , $\overline{u'^2}$: case 1.29A; ---- , $\overline{v'^2}$: case 1.29A; • , $\overline{u'^2}$: case 1.29B; × , $\overline{v'^2}$: case 1.29B.

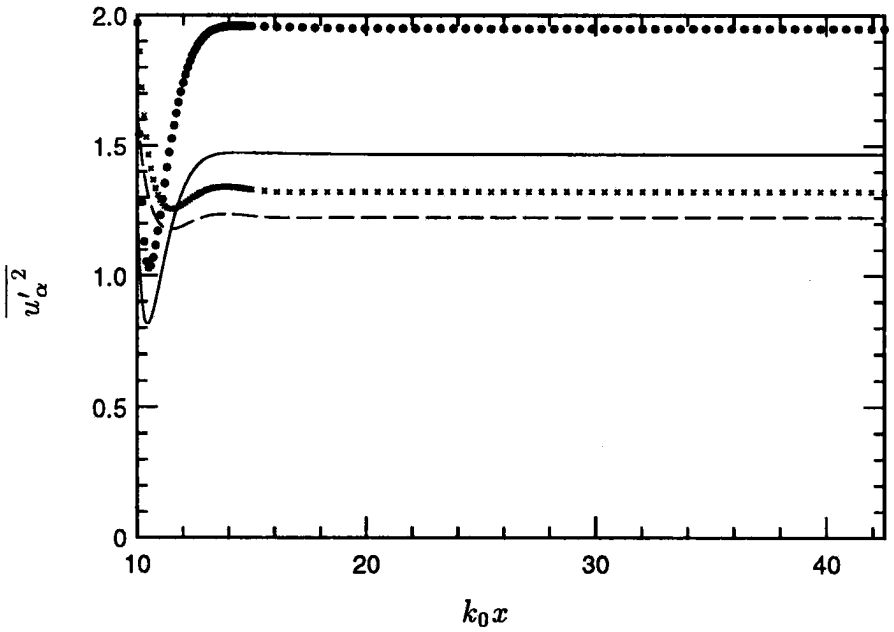


FIGURE D.8: Evolution of turbulence kinetic energy behind a Mach 1.29 shock wave as predicted by linear analysis. All the curves are normalized by their value immediately upstream of the shock. ——— , $\overline{u'^2}$: without entropy fluctuations; ---- , $\overline{v'^2}$: without entropy fluctuations; • , $\overline{u'^2}$: with entropy fluctuations; × , $\overline{v'^2}$: with entropy fluctuations.

shows the level of enhancement to be a modest 7%. As shown in figure D.8, this enhancement in the presence of entropy fluctuations is in agreement with linear analysis. Note that unambiguous quantitative comparison of kinetic energy between analysis and simulation is made difficult by viscous decay in the simulations. Also, the intermittency associated with shock oscillation is not reproduced by the analysis. If the peak levels of kinetic energy behind the shock wave in the simulation and analysis are compared, the linear analysis predictions are seen to be higher - consistent with viscous decay in the simulations. As seen from figure D.8, the amplification of $\overline{u'^2}$ as predicted by linear analysis, is 1.47 and 1.95 in the absence and presence of entropy fluctuations (that satisfy SRA) respectively. The corresponding values for $\overline{v'^2}$ are predicted to be 1.22 and 1.32 respectively. Thus linear analysis predicts a 33% enhancement in the amplification of $\overline{u'^2}$ while amplification of $\overline{v'^2}$ is predicted to increase by about 8%.

## D.3.2 Vorticity fluctuations

All components of vorticity are affected by the upstream presence of entropy fluctuations. As shown in figure D.9, levels of vorticity fluctuations behind the shock wave are higher in case 1.29B. The amplification of $\overline{\omega_2'^2}$ is seen to increase by 8.7% when entropy fluctuations are present upstream of the shock. This increase is qualitatively predicted by linear analysis. The increase in amplification predicted by analysis is much higher - about 19.4%. The primary reason for this difference between analysis and DNS is believed to be the strict imposition of the SRA upstream of the shock in the analysis. The upstream fluctuations in the simulation only approximately satisfy the SRA due to the absence of mean temperature gradients. Further support for this reasoning, is provided by the fact that vorticity amplification in case 1.29A is within 6.3% of analysis while the deviation in case 1.29B is about 16.2%.

DNS shows that, while the transverse components of vorticity monotonically decay behind the shock, the streamwise component increases downstream of the shock wave after remaining practically constant across it. In fact, the peak level of $\overline{\omega_1'^2}$ behind the shock wave in case 1.29B is about 7.1% greater than its upstream value. As noted by Lee *et al.* (1992), this behavior is nonlinear in nature; it is caused by the stretching of vorticity fluctuations by the fluctuating strain rate. In the presence of upstream entropy fluctuations, it is likely that non-linear baroclinic effects might provide additional contribution.

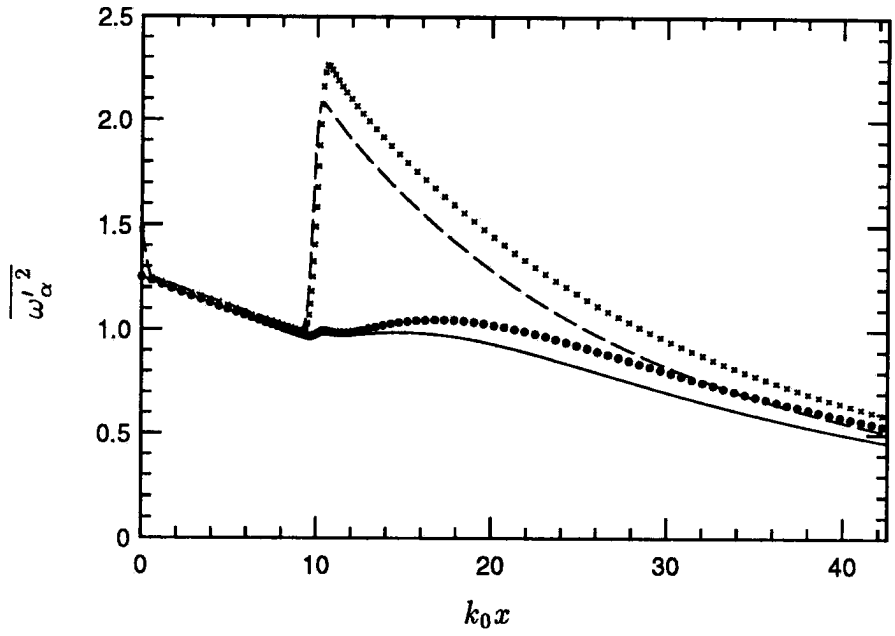


FIGURE D.9: Streamwise evolution of vorticity fluctuations from DNS of the Mach 1.29 shock wave. All the curves are normalized by their value immediately upstream of the shock ($k_0 x = 8.97$). ——— , $\overline{\omega_1'^2}$: case 1.29A; ---- , $\overline{\omega_2'^2}$: case 1.29A; • , $\overline{\omega_1'^2}$: case 1.29B; × , $\overline{\omega_2'^2}$: case 1.29B.

### D.3.3 Thermodynamic fluctuations and Morkovin's hypothesis

The thermodynamic fluctuations behind weak shock waves were noted by Lee *et al.* (1994) to be nearly isentropic. The thermodynamic field in case 1.29A follows this trend; i.e. $p_{\rm rms}/\gamma\overline{p}$, $\rho_{\rm rms}/\overline{\rho}$ and $T_{\rm rms}/(\gamma-1)\overline{T}$ are nearly equal over the entire domain. However, upstream entropy fluctuations were not present in Lee *et al.*'s computations. As might be expected, the downstream thermodynamic field is not isentropic when upstream entropy fluctuations are present. Figure D.10 shows the streamwise evolution of the pressure, density and temperature fluctuations in case 1.29B. The quantity $(\gamma-1)M^2 u_{\rm rms}/U$ is also shown. This allows the weak form of Morkovin's hypothesis to be evaluated across the shock. The corresponding predictions made by linear analysis are shown in figure D.11. Good qualitative agreement is observed between analysis and simulation. The intensity of pressure fluctuations in the near field is seen to be comparable to those of density and temperature. However, pressure fluctuations decay behind the shock wave, thereby causing their far field intensity to be smaller.

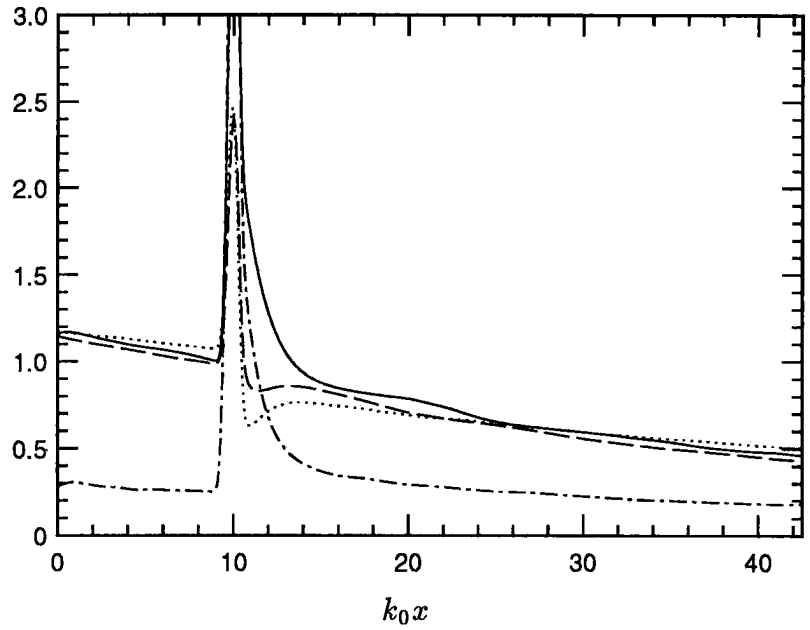


FIGURE D.10: Thermodynamic fluctuations from DNS - case 1.29B. All variables are non-dimensionalized by the value of $\rho_{\rm rms}/\overline{\rho}$ immediately upstream of the shock wave ($k_0x = 8.97$). ——— , $\rho_{\rm rms}/\overline{\rho}$; - - - - , $T_{\rm rms}/\overline{T}$, ····· , $(\gamma-1)M^2u_{\rm rms}/U$; —·— , $p_{\rm rms}/\gamma\overline{p}$.

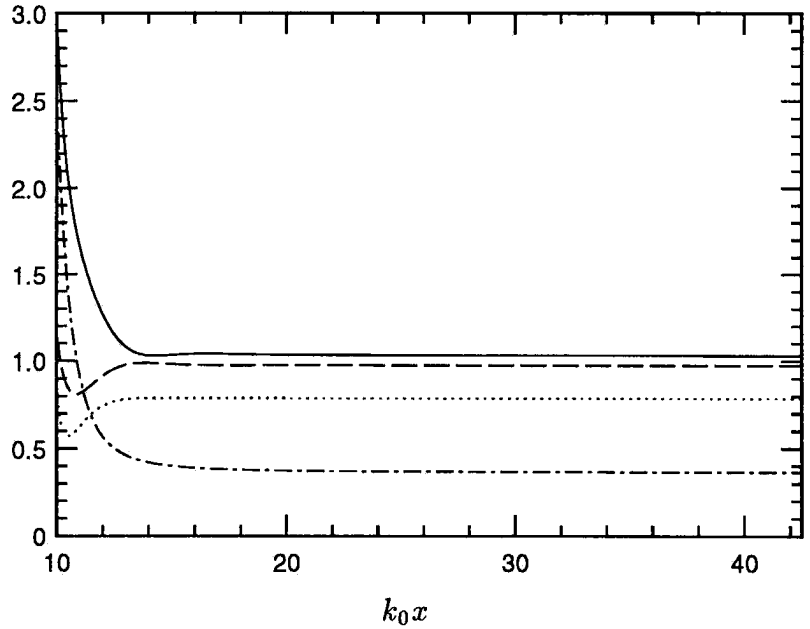


FIGURE D.11: Thermodynamic fluctuations as predicted by linear analysis for case 1.29B. All variables are non-dimensionalized by the value of $\rho_{\rm rms}/\overline{\rho}$ upstream of the shock wave. ——— , $\rho_{\rm rms}/\overline{\rho}$; - - - - , $T_{\rm rms}/\overline{T}$, ····· , $(\gamma-1)M^2u_{\rm rms}/U$; —·— , $p_{\rm rms}/\gamma\overline{p}$.

Considerable deviation from Morkovin's hypothesis is observed in the near field behind the shock. The extent of deviation in the far field is seen to be smaller. Also, the first part of the hypothesis ($\rho_{\rm rms}/\overline{\rho} = T_{\rm rms}/\overline{T}$) is seen to be a better approximation in the far field than the second part, which relates the density and velocity fluctuations. Note that the notion of far field in the simulation is not as precise as that in the analysis. Linear analysis suggests (figure D.11) that the far field values are attained at approximately $k_0 x = 17$. If Morkovin's hypothesis is evaluated at this location in the computation, it shows behavior comparable to analysis. However, the validity of the weak form of the hypothesis is seen to increase with distance downstream of this location. Interestingly, although the *rms* levels of the terms in the hypothesis approach each other, the correlation coefficient between $u'$ and $T'$ does not approach -1. It decreases in magnitude across the shock, and decreases further in magnitude downstream; *e.g.*, the correlation coefficient at $k_0 x = 20$ is -0.54. The exact cause for this trend which is not predicted by analysis, is not known. Perhaps, it is best considered a transient aspect of the return to isotropy problem behind the Mach 1.29 shock wave.

## D.4 Summary

Direct numerical simulation was used to study the influence of entropy fluctuations on the evolution of isotropic turbulence across a Mach 1.29 shock wave. The observed results are in qualitative agreement with the linear analysis of Chapter 3. The presence of upstream entropy fluctuations was observed to increase the amplification of turbulence kinetic energy and vorticity across the shock wave. The computed enhancement was lower than that predicted by linear analysis, presumably due to the imposition of the strict form of Morkovin's hypothesis in the analysis. The turbulence was observed to remain axisymmetric over the length of the domain behind the shock wave. Upstream entropy fluctuations were observed to increase the nonlinear rise in the level of streamwise vorticity fluctuations behind the shock wave. Morkovin's hypothesis was seen to be invalid immediately behind the shock. However, the validity of the hypothesis is seen to increase with distance behind the shock.

# References


ADAMS, M. C. 1949 On shock waves in inhomogeneous flow. *J. Aero. Sci.* **16**, 685-690.

ANDREOPOULOUS, J. & MUCK, K.C. 1987 Some new aspects of the shock-wave boundary layer interaction in a compression ramp corner. *J. Fluid Mech.* **180**, 405-428.

BARRE, S., ALEM, D. & BONNET, J. 1995 Experimental study of a normal shock/homogeneous turbulence interaction. *AIAA Paper 95-0579.*

BATCHELOR, G. K. & PROUDMAN, I. 1954 The effect of rapid distortion of a fluid in turbulent motion. *Quart. J. Mech. Appl. Math.* **7**, 83-103.

BLAISDELL, G.A., MANSOUR, N.N & REYNOLDS, W.C. 1991 Numerical simulations of compressible homogeneous turbulence. *Report No. TF-50*, Department of Mechanical Engineering, Stanford University, Stanford, California .

BRADSHAW, P. 1977 Compressible turbulent shear layers. *Ann. Rev. Fluid Mech.* **9**, 33-54.

BRADSHAW, P. & WONG, F.Y.F 1972 The relaxation of a turbulent shear layer after reattachment. *J. Fluid Mech.* **52**, 113-135.

BURGERS, J.M. 1946 On the transmissions of sound waves through a shock wave. *Koninklijke Nederlandsche Akademie Van Wetenschappen, Proc.* **XLIX**, 273-281.

CAMBON, C., COLEMAN, G.N. & MANSOUR, N.N. 1992 Rapid distortion analysis and direct simulation of compressible homogeneous turbulence at finite Mach number. *J. Fluid Mech.* **257**, 641-665.

CARRIER, G.F. 1949 On the stability of the supersonic flows past a wedge. Quarterly of Applied Mathematics, **6**, 367-378.

CHANG, C.T. 1957 Interaction of a plane shock and oblique plane disturbances with special reference to entropy waves. *J. Aero. Sci.* **24**, 675-682.

CHU, B.T. 1952 On weak interaction of strong shock and Mach waves generated downstream of a shock. *J. Aero. Sci.* **19**, 433-446.

COLEMAN, G.N. & MANSOUR, N.N. 1991 Modeling the rapid spherical compression of isotropic turbulence. *Phys. Fluids A*, **3** (9), 2255-2259.

COLONIUS, T., MOIN, P. & LELE, S.K. 1995 Direct Computation of Aerodynamic Sound. *Report No. TF-65*, Department of Mechanical Engineering, Stanford University, Stanford, California .

CUADRA, E. 1968 Flow perturbations generated by a shock wave interacting with an entropy wave. *AFOSR-UTIAS Symposium on Aerodynamic Noise,* Toronto, 251-271.

DEBIEVE, F.R., GOUIN, H. & GAVIGLIO, J. 1982a Evolution of the Reynolds stress tensor in a shock wave-turbulence interaction. *Indian Journal of Technology* **20**, 90-97.

DEBIEVE, F.R., GOUIN, H. & GAVIGLIO, J. 1982b Momentum and temperature fluxes in a shock wave-turbulence interaction. *Structure of Turbulence in Heat and Mass Transfer* (ed. Z.P. Zaric), Hemisphere, New York.

DEBIEVE, J.F. & LACHARME, J.P. 1986 A shock wave/free-turbulence interaction. *Turbulent Shear Layer / Shock Wave Interactions* (ed. J.Délery), Springer.

DEISSLER, R.G. 1961 Effect of inhomogeneity and of shear flow in weak turbulent fields. *Phys. Fluids* **4**, 1187-1198.

DOLLING, D.S. 1993 Fluctuating loads in shock wave/turbulent boundary layer interaction: tutorial and update. *AIAA Paper 93-0284.*

DUCK, P.W., LASSEIGNE, D.G. & HUSSAINI, M.Y. 1995 On the interaction between the shock wave attached to a wedge and freestream disturbances. *Theoretical and Computational Fluid Dynamics* **7** (2), 119-139.

DURBIN, P.A. & ZEMAN, O. 1992 Rapid distortion theory for homogeneous compressed turbulence with application to modeling. *J. Fluid Mech.* **242**, 349-370.

DUSSAUGE, J.P., MUCK, K.C. & ANDREOPOULOUS, J. 1986 Properties of wall pressure fluctuations in a separated flow over a compression ramp. *Turbulent Shear Layer/Shock Wave Interactions* (ed. J. Delery), Springer, Berlin.

ERENGIL, M.E. & DOLLING, D.S. 1990 Correlation of separation shock motion in a compressible ramp interaction with pressure fluctuations in the incoming boundary layer. *AIAA Paper 90-1646.*

ERENGIL, M.E. & DOLLING, D.S. 1991 Correlation of separation shock motion with pressure fluctuations in the incoming boundary layer. *AIAA J.* **29**, 1868-1877.

ERLEBACHER, G., HUSSAINI, M.Y., SPEZIALE, C.G. & ZANG, T.A. 1992 Towards the large eddy simulation of compressible turbulent flows. *J. Fluid Mech.* **238**, 155-185.

FERNHOLZ, F.F. & FINLEY, P.J. 1981 A further compilation of compressible boundary layer data with a survey of turbulence data. *AGARDograph 263.*

GIDDINGS, T., RUSAK, Z. & COLE, J.D. 1993 Interaction of a weak shock with turbulence. Bulletin of the American Physical Society, **38** (12), 2247-2248.

GIVOLI, D. 1991 Non-reflecting boundary conditions. *J. Comp. Phys.*, **94**, 1-29.

GRAMANN, R.A. & DOLLING, D.S. 1992 Examination of turbulent structures associated with unsteady shock motion in a Mach 5 interaction. *AIAA Paper 92-0744.*

GREEN, J.E. 1970 Interaction between shock waves and turbulent boundary layers. *Prog. Aerosp. Sci.* **11**, 235-340.

HANKEY, W.L. & HOLDEN, M.S. 1975 Two-dimensional shock wave-boundary layer interactions in high speed flows. *AGARDograph 203.*

HANNAPPEL, R. & FRIEDRICH, R. 1994a On the interaction of wave-like disturbances with shocks - two idealizations of the shock/turbulence interaction problem. *Acta Mechanica* **4**, 69-77.

HANNAPPEL, R. & FRIEDRICH, R. 1994 DNS of a M=2 shock interacting with isotropic turbulence. *Proc. First ERCOFTAC Workshop on DNS and LES*, Guildford, Surrey, U.K.

HARTEN, A. & OSHER, S. 1987 Uniformly high-order accurate nonoscillatory schemes, I. *SIAM J. Num. Anal.* **24**, 279-309.

HARTEN, A., ENGQUIST, B., OSHER, S. & CHAKRAVARTHY, S. 1987 Uniformly high-order accurate nonoscillatory schemes, III. *J. Comp. Phys.* **71**, 231-303.

HAYAKAWA, K., SMITS, A.J. & BOGDONOFF, S.M. 1984 Turbulence measurements in a compressible reattaching shear layer. *AIAA J.* **22**, 889-895.

HEAD, M.R. & BANDOPADHYAY, P.R. 1981 New aspects of turbulent boundary-layer structure. *J. Fluid Mech.* **107** 297-338.

HESSELINK, L. & STURTEVANT, B. 1988 Propagation of weak shocks through a random medium. *J. Fluid Mech.* **196**, 513-553.

HIRSCH, C. 1990 *Numerical Computation of Internal and External Flows: Vol. 2* Wiley.

HONKAN, A. & ANDREOPOULOUS, J. 1992 Rapid compression of grid-generated turbulence by a moving shock wave. Phys. Fluids A, **4**, 2562-2572.

HUNT J.C.R. & CARRUTHERS, D.J. 1990 Rapid distortion theory and the 'problems' of turbulence. *J. Fluid Mech.* **242**, 497-532.

HUSSAINI, M.Y., COLLIER, F. & BUSHNELL, D.M. 1986 Turbulence alteration due to shock motion. *Turbulent Shear Layer/Shock Wave Interactions* (ed. J. Delery), Springer, Berlin.

ISRAELI, M. & ORSZAG, S.A. 1981 Approximation of Radiation Boundary Conditions. *J. Comp. Phys.* **41**, 115-135.

JACQUIN, L., BLIN, E. & GEFFROY, P. 1991 Experiments on free turbulence / shock wave interaction. *Proc. Eighth Symp. on Turbulent Shear Flows, Munich* (ed. F.Durst, R.Friedrich, B.E.Launder, F.W.Schmidt, U.Schumann & J.H.Whitelaw), Springer.

JACQUIN, L., CAMBON, C. & BLIN, E. 1993 Turbulence amplification by a shock wave and rapid distortion theory. Phys. Fluids A, **5**, 2539-2550.

JOHNSON, W.R. & LAPORTE, O. 1958 Interaction of cylindrical sound waves with a stationary shock wave. Phys. Fluids, **1**, 82-94.

KANTROWITZ, A. 1947 The formation and stability of normal shock waves in channel flow. *NACA TN 1225.*

KELLER, J. & MERZKIRCH, W. 1990 Interaction of a normal shock wave with a compressible turbulent flow. Exp. Fluids, **8**, 241-248.

KERREBROCK, J.L. 1956 The interaction of flow discontinuities with small disturbances in a compressible fluid. *Ph.D Dissertation, California Institute of Technology.*

KEVLAHAN, N., MAHESH, K. & LEE, S. 1992 Evolution of the shock front and turbulence structures in the shock/turbulence interaction. *Proc. 1992 Summer Program*, Center for Turbulence Research, Stanford, CA.

KORKEGI, R. 1971 Survey of viscous interactions associated with high Mach number flight. *AIAA J.* **9**, 771-784.

KOVASZNAY, L.S.G. 1953 Turbulence in supersonic flow. *J. Aero. Sci.* **20**, 657-682.

KUNTZ, D.W., AMADUCCI, V.A. & ADDY, A.L. 1987 Turbulent boundary layer properties downstream of the shock wave/boundary layer interaction. *AIAA J.* **25**, 668-675.

LANDAU, L.D. & LIFSHITZ, E.M. 1982 Fluid Mechanics. *Course of Theoretical Physics,* Vol. 6, Pergamon Press, 332-333.

LAUNDER, B.E., REECE, G.J. & RODI, W. 1975 Progress in the development of a Reynolds stress turbulence closure. *J. Fluid Mech.* **68**, 537-566.

LAX, P.D. & WENDROFF, B. 1960 System of conservation laws. *Comm. Pure Appl. Math.* **13**, 217-237.

LE, H. & MOIN, P. 1994 Direct numerical simulation of turbulent flow over a backward facing step. *Report No. TF-58*, Department of Mechanical Engineering, Stanford University, Stanford, California.

LEE, M.J. 1989 Distortion of homogeneous turbulence by axisymmetric strain and dilatation. *Phys. Fluids A*, **1**, 1541-1557.

LEE, M.J., KIM, J. & MOIN, P. 1990 The structure of turbulence at high shear rate. *J. Fluid Mech.* **216**, 561-583.

LEE, M.J. & REYNOLDS, W.C. 1985 Numerical experiments on the structure of homogeneous turbulence. *Report No. TF-24*, Department of Mechanical Engineering, Stanford University, Stanford, California.

LEE, S., LELE, S.K. & MOIN, P. 1991 Direct numerical simulation and analysis of shock turbulence interaction. *AIAA Paper 91-0523.*

LEE, S., LELE, S.K. & MOIN, P. 1992 Interaction of isotropic turbulence with a shock wave. *Rep.* TF-52. Department of Mechanical Engineering, Stanford University, Stanford, CA.

LEE, S. 1992 Large eddy simulation of shock turbulence interaction. *Annual Research Briefs, Center for Turbulence Research, Stanford, California*, 73-84.

LEE, S., LELE, S.K. & MOIN, P. 1993 Direct numerical simulation of isotropic turbulence interacting with a weak shock wave. *J. Fluid Mech.***251**, 533-562. Also see Corrigendum, *J. Fluid Mech.*, 264, 373-374.

LEE, S. LELE, S.K. & MOIN, P. 1994 Interaction of isotropic turbulence with a strong shock wave. *AIAA Paper 94-0311.*

LELE, S.K. 1992a Shock jump conditions in a turbulent flow. Phys. Fluids A, **4**, 2900-2905.

LELE, S.K. 1992b Compact finite difference schemes with spectral-like resolution. *J. Comp. Phys.*, **103**, 16-42.

LELE, S.K. 1994 Compressibility Effects on Turbulence. *Ann. Rev. Fluid Mech.* **26**, 211-254.

LEROUX, A.Y. 1977 A numerical conception of entropy for quasi-linear equations. *Math. Comp.* **31**, 848-872.

LIGHTHILL, M.J. 1949 The flow behind a stationary shock. *Phil. Mag. 40, Ser.7,* No. 301, 214-220.

LINDQUIST, D.R. & GILES, M.B. 1991 On the validity of linearized unsteady Euler equations with shock-capturing. *AIAA Paper,* 91-1598-CP.

LOWSON, M.V. 1968 Pressure fluctuations resulting from shock interactions. *J. Sound Vib.* **7**, 380-392.

MAJDA, A. & OSHER, S. 1979 Numerical viscosity and the entropy condition. *Comm. Pure Appl. Math.* **32**, 797-838.

MAHESH, K., LELE, S.K. & MOIN, P. 1993 Shock turbulence interaction in the presence of mean shear: an application of rapid distortion theory. *AIAA Paper 93-0663.*

MAHESH, K., LELE, S.K. & MOIN, P. 1994 The response of anisotropic turbulence to rapid homogeneous one-dimensional compression. Phys. Fluids, **6**, 1052-1062.

MAHESH, K., LEE, S., LELE, S.K. & MOIN, P. 1995 The interaction of an isotropic field of acoustic waves with a shock wave. *J. Fluid Mech.* **300**, 383-407.

MAHESH, K., LELE, S.K. & MOIN, P. 1996 The influence of entropy fluctuations on the interaction of turbulence with a shock wave. Submitted to *J. Fluid Mech.*

MAXEY, M.R. 1982 Distortion of turbulence in flows with parallel streamlines. *J. Fluid Mech.* **124**, 261-282.

MCCLURE, W.B. 1992 An experimental study of the driving mechanism and control of the unsteady shock-induced turbulent separation in a Mach 5 compression corner flow. *Ph.D Dissertation, Dept. of Aerospace Engineering and*

*Engineering Mechanics, The Univ. of Texas at Austin.*

McKENZIE, J.F. & WESTPHAL, K.O. 1968 Interaction of linear waves with oblique shock waves. Phys. Fluids, **11**, 2350-2362.

MEADOWS, K.R., KUMAR, A. & HUSSAINI, M.Y. 1991 Computational study of the interaction between a vortex and a shock wave. *AIAA J.* **29**, 174-179.

MEADOWS, K.R., CAUGHEY, D.A. & CASPER, J. 1993 Computing unsteady shock waves for aeroacoustic applications *AIAA Paper 93-4329.*

MOFFATT, H.K. 1967 The interaction of turbulence with strong wind shear. *Proceedings of the international colloquium on atmospheric turbulence and radio wave propagation*, (ed. A.M. Yaglom and V.I. Tatarsky), Nauka, Moscow.

MOIN, P. 1988 Similarity of Organized Structures in Turbulent Shear Flows. *Near-Wall Turbulence: 1988 Zoran Zaric Memorial Conference* (ed. S.J.Kline and N.H.Afgan), Hemisphere Publishing Corporation.

MOIN, P. & KIM. J. 1985 The structure of the vorticity field in turbulent channel flow. Part 1: Analysis of instantaneous fields and statistical correlations. *J. Fluid Mech.* **155**, 441-464.

MOORE, F.K. 1954 Unsteady Oblique Interaction of a Shock Wave with a Plane Disturbance. *NACA TN 2879.*

MORKOVIN, M.V. 1960 Note on the assessment of flow disturbances at a blunt body traveling at supersonic speeds owing to flow disturbances in the free stream. *J. App. Mech.,* ASME Trans., No. 60-APM-10.

MORKOVIN, M.V. 1961 Effects of compressibility on turbulent flows. *Mecanique de la Turbulence* (ed. A. Favre), 367-380.

NAOT, D., SHAVIT, A. & WOLFSHTEIN, H. 1970 Interactions between components of the turbulent velocity correlation tensor. *Israel J. Tech.* **8**, 259.

PEARSON, J.R.A. 1959 The effect of uniform distortion on weak homogeneous turbulence. *J. Fluid Mech.* **5**, 274-288.

PIERCE, A.D. 1989 *Acoustics: An Introduction to Its Physical Principles and Applications*, Acoustical Society of America, New York.

POINSOT, T.J. & LELE, S.K. 1992 Boundary conditions for direct simulation of compressible viscous reacting flow. *J. Comp. Phys.* **101** (1) 104-129.

PRANDTL, L. 1933 Attaining a steady stream in wind tunnels. *NACA TN* 726.

REYNOLDS, A.J. & TUCKER, H.J. 1975 The distortion of turbulence by general uniform irrotational strain. *J. Fluid Mech.* **68**, 673-693.

RIBNER, H.S. 1953 Convection of a Pattern of Vorticity through a Shock Wave. *NACA TN 2864.*

RIBNER, H.S. & TUCKER, M. 1953 Spectrum of turbulence in a contracting stream. *NACA TN* 1113.

RIBNER, H.S. 1954 Shock-Turbulence Interaction and the Generation of Noise. *NACA TN 3255.*

RIBNER, H.S. 1969 Acoustic energy flux from shock-turbulence interaction. *J. Fluid Mech.* **35**, 299-310.

RIBNER, H.S. 1987 Spectra of noise and amplified turbulence emanating from shock-turbulence interaction. *AIAA J.* **25**, 436-442.

ROBERTS, T.W. 1990 The behavior of flux difference splitting schemes near slowly moving shocks. *J. Comp. Phys.* **90**, 141-160.

ROGALLO, R.S. 1981 Numerical experiments in homogeneous turbulence. *NASA Tech. Memo.* 81315.

ROGERS M.M., MOIN, P. & REYNOLDS, W.C. 1986 The structure and modeling of the hydrodynamic and passive scalar fields in homogeneous turbulent shear flow. *Report No. TF-25*, Department of Mechanical Engineering, Stanford University, Stanford, California.

ROGERSON, A. & MEIBURG, E. 1990 A numerical study of the convergence properties of ENO schemes. *J. Sci. Comp.* **5**, 151-167.

ROTMAN, D. 1991 Shock wave Effects on a Turbulent Flow. *Phys. Fluids A* **3**, 1792-1806.

SAVILL, A.M. 1987 Recent developments in rapid distortion theory. *Ann. Rev. Fluid Mech.* **19**, 531-570.

SELIG, M.S., ANDREOPOULOUS, J., MUCK, K.C., DUSSAUGE, J.P. & SMITS, A.J. 1989 Turbulence structure in a shock wave/turbulent boundary layer interaction. *AIAA J.* **27**, 862-869.

SETTLES, G.S. & DODSON, L.J. 1994 Supersonic and hypersonic shock / boundary -layer interaction database. *AIAA J.* **32**, 1377-1383.

SHU, C.-W. & OSHER, S. 1988 Efficient implementation of essentially non-oscillatory shock-capturing schemes. *J. Comp. Phys.* **77**, 439-471.

SHU, C.-W. & OSHER, S. 1989 Efficient implementation of essentially non-oscillatory shock-capturing schemes, II. *J. Comp. Phys.* **83**, 32-78.

SHU, C.-W. 1990 Numerical experiments on the accuracy of ENO and modified ENO schemes. *J. Sci. Comp.* **5**, 127-149.

SHU, C.-W., ERLEBACHER, G., ZANG, T.A., WHITAKER, D. & OSHER, S. 1991 High order ENO schemes applied to two- and three- dimensional compressible flow. *NASA CP* 187562, Also *ICASE Report No.* 91-38.

SMITS, A.J. & MUCK, K.C. 1987 Experimental study of three shock wave / turbulent boundary layer interactions. *J. Fluid Mech.* **182**, 294-314.

SPEZIALE, C.G., SARKAR, S. & GATSKI, T.B. 1991 Modeling the pressure-strain correlation of turbulence: an invariant dynamical systems approach. *J. Fluid Mech.* **227**, 245-272.

SREENIVASAN, K.R. & NARASIMHA, R. 1978 Rapid distortion of axisymmetric turbulence. *J. Fluid Mech.* **84**, 497-516.

TAVOULARIS, S. & KARNIK, U. 1989 Further experiments on the evolution of turbulent stresses and scales in uniformly sheared turbulence. *J. Fluid Mech.*, **204**, 457-478.

TAVOULARIS, S., BENNETT, J.C. & CORRSIN, S. 1978 Velocity-derivative skewness in small Reynolds number, nearly isotropic turbulence. *J. Fluid Mech.* **176**, 33-66.

TAYLOR, G.I. 1935 Turbulence in a contracting stream. *Z. Agnew. Math. Mech.* **15**, 91.

THOMPSON, K.W. 1987 Time dependent boundary conditions for hyperbolic systems. *J. Comp. Phys.* **68**, 1-24.

THOMPSON, P.A. 1984 *Compressible Fluid Dynamics*, McGraw-Hill, New York.

TOWNSEND, A.A. 1970 Entrainment and the structure of turbulent flow. *J. Fluid Mech.* **41**, 13-46.

TOWNSEND, A.A 1976 *The structure of turbulent shear flow* 2nd edn. Cambridge University Press, Cambridge.

TOWNSEND, A.A. 1980 The response of sheared turbulence to additional distortion. *J. Fluid Mech.* **98**, 171-191.

UBEROI, M.S. 1956 Effect of wind-tunnel contraction on free-stream turbulence. *J. Aero. Sci.* **23**, 754-764.

WOODWARD,P. & COLLELA, P. 1984 The numerical simulation of two - dimensional flow through shocks. *J. Comp. Phys.* **54**, 115-173.

WRAY, A.A. 1986 Very low storage time-advancement schemes. *Internal Rep.* NASA-Ames Research Center, Moffett Field, CA.

YANG, J., KUBOTA, T. & ZUKOSKI, E.E. 1994 A model for characterization of a vortex pair formed by shock passage over a light-gas inhomogeneity. *J. Fluid Mech.* **258**, 217-244.

YEE, H.C. 1987 Upwind and symmetric shock-capturing schemes. *NASA TM 89464.*

ZANG, T.A., HUSSAINI, M.Y. & BUSHNELL, D.M. 1984 Numerical computations of turbulence amplification in shock-wave interactions. *AIAA J.* **22**, 13-21.